Justus-Liebig-Universität Gießen

Fachbereich Medizin

Institut für Medizinische Virologie

Leitung: Prof. Dr. John Ziebuhr

Neue antivirale Strategien gegen Coronaviren

Habilitationsschrift

zur Erlangung der Lehrbefähigung für das Fach

Molekulare Virologie

im Fachbereich Medizin

der Justus-Liebig-Universität Gießen

vorgelegt von

Dr. rer. nat. Christin Müller-Ruttloff

geb. Müller

Gießen, 2024

Die nachfolgende Arbeit nimmt Bezug auf folgende Arbeiten:

Kapitel I:

1 Pfafenrot C*, Schneider T*, **Müller C***, Hung LH, Schreiner S, Ziebuhr J, Bindereif A. Inhibition of SARS-CoV-2 coronavirus proliferation by designer antisense-circRNAs. Nucleic Acids Res. 2021 Dec 2;49(21):12502-12516. doi: 10.1093/nar/gkab1096. PMID: 34850109; PMCID: PMC8643703.

Kapitel II.1:

2 Shaban MS*, **Müller C***, Mayr-Buro C*, Weiser H, Meier-Soelch J, Albert BV, Weber A, Linne U, Hain T, Babayev I, Karl N, Hofmann N, Becker S, Herold S, Schmitz ML, Ziebuhr J, Kracht M. Multi-level inhibition of coronavirus replication by chemical ER stress. Nat Commun. 2021 Sep 20;12(1):5536. doi: 10.1038/s41467-021-25551-1. PMID: 34545074; PMCID: PMC8452654.

Kapitel II.2:

3 **Müller C*,** Schulte FW*, Lange-Grünweller K, Obermann W, Madhugiri R, Pleschka S, Ziebuhr J, Hartmann RK, Grünweller A. Broad-spectrum antiviral activity of the eIF4A inhibitor silvestrol against corona- and picornaviruses. Antiviral Res. 2018 Feb;150:123-129. doi: 10.1016/j.antiviral.2017.12.010. Epub 2017 Dec 16. PMID: 29258862; PMCID: PMC7113723.

4 **Müller C***, Obermann W*, Schulte FW, Lange-Grünweller K, Oestereich L, Elgner F, Glitscher M, Hildt E, Singh K, Wendel HG, Hartmann RK, Ziebuhr J, Grünweller A. Comparison of broad-spectrum antiviral activities of the synthetic rocaglate CR-31-B (-) and the eIF4A-inhibitor Silvestrol. Antiviral Res. 2020 Mar;175:104706. doi: 10.1016/j.antiviral.2020.104706. Epub 2020 Jan 10. PMID: 31931103; PMCID: PMC7114339.

5 **Müller C**, Obermann W, Karl N, Wendel HG, Taroncher-Oldenburg G, Pleschka S, Hartmann RK, Grünweller A, Ziebuhr J. The rocaglate CR-31-B (-) inhibits SARS-CoV-2 replication at non-cytotoxic, low nanomolar concentrations in vitro and ex vivo. Antiviral Res. 2021 Feb;186:105012. doi: 10.1016/j.antiviral.2021.105012. Epub 2021 Jan 8. PMID: 33422611; PMCID: PMC7791309.

6 Obermann W, Friedrich A, Madhugiri R, Klemm P, Mengel JP, Hain T, Pleschka S, Wendel HG, Hartmann RK, Schiffmann S, Ziebuhr J, **Müller C***, Grünweller A*. Rocaglates as Antivirals: Comparing the Effects on Viral Resistance, Anti-Coronaviral Activity, RNA-Clamping on eIF4A and Immune Cell Toxicity. Viruses. 2022 Mar 3;14(3):519. doi: 10.3390/v14030519. PMID: 35336926; PMCID: PMC8950828.

Abkürzungsverzeichnis

ADMET	*absorption, distribution, metabolism, elimination, and toxicity*
AIDS	*acquired immunodeficiency syndrome*
ARDS	akutes Atemnotsyndrom (*acute respiratory distress syndrome*)
AS	antisense
ASO	Antisense-Oligonukleotide
ATF6a	*activating transcription factor* 6
CC_{50}	Zytotoxische Konzentration 50 % (*cytotoxic concentration 50 %)*
CoV	Coronavirus
circRNA	*circular ribonucleic acid*
DAA	*direct acting antiviral*
EC_{50}	Effektive Konzentration 50 % (*effective concentration 50 %)*
EMA	Europäische Arzneimittel-Agentur
ER	endoplasmatisches Retikulum
ERAD	*ER-associated degradation*
ERGIC	*ER Golgi intermediate compartment*
ERQC	*ER quality control*
HBV	Hepatitis-B-Virus
HCoV-229E	humanes Coronavirus 229E
HCV	Hepatitis-C-Virus
HDA	*host-directed antiviral*
HERPUD1	*homocysteine-responsive endoplasmic reticulum-resident ubiquitin-like domain member* 1
inkl.	inklusive
IRE1	*Inositol-requiring enzyme 1*
IFN	Interferon
LNA	*locked nucleic acid*
MERS-CoV	*Middle East respiratory syndrome coronavirus*
MOI	*multiplicity of infection*
NHBE	normalen menschlichen Bronchialepithelzellen
nm	Nanometer
nM	Nanomolar

nts	Nukleotide
PKR	Proteinkinase R
PERK	*Protein kinase R-like endoplasmic reticulum kinase*
pp1a	Polyprotein 1a
pp1ab	Polyprotein 1ab
pfu	*plaque forming units*
RNA	*ribonucleic acid*
RTC	Replikations-/Transkriptionskomplex (*replication/transcription complex*)
SARS-CoV	*severe acute respiratory syndrome coronavirus*
TRS	transkriptionsregulierende Sequenz
u.a.	unter anderem
UPR	*unfolded protein response*
UTR	*untranslated region*
z.B.	zum Beispiel

Inhalt

1. Einleitung

1.1. Coronaviren

Infektionen des Respirationstrakts können durch eine Vielzahl von Erregern hervorgerufen werden. Neben bakteriellen Erregern spielen Viren hierbei eine herausragende Rolle. So gehören beispielsweise auch die seit 1960 beschriebenen humanpathogenen Coronaviren (CoVs) zu den häufigen viralen Erregern dieser Infektionserkrankungen (1). Aktuell sind sieben verschiedene humanpathogene CoVs bekannt: HCoV-229E, HCoV-OC43, HCoV-NL63 und HCoV-HKU-1 führen in der Regel zu Infektionen der oberen Atemwege mit relativ milder Symptomatik, während *Middle East respiratory syndrome* Coronavirus (MERS-CoV), *severe acute respiratory syndrome* Coronavirus (SARS-CoV) und SARS-CoV-2 häufig auch zu schwereren Verläufen einschließlich Pneumonien oder sogar akutem Lungenversagen (*acute respiratory distress syndrome,* ARDS*)* führen können.

Dabei ist SARS-CoV-2 eng verwandt mit SARS-CoV, welches 2002/2003 in China auftrat und zur gleichen Virusspezies innerhalb der Gattung der Betacoronaviren gehört (2).

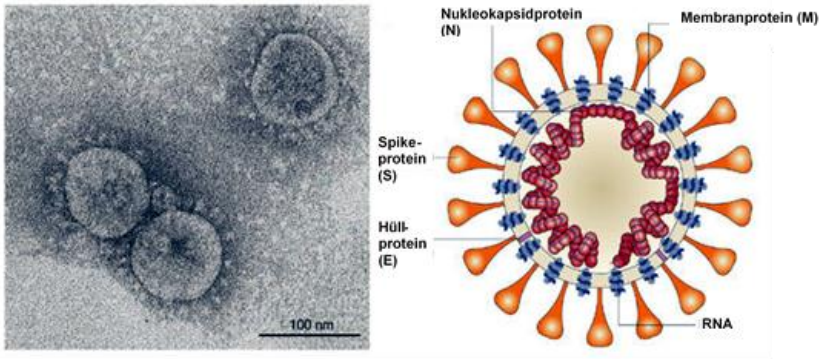

Abbildung 1 *Elektronenmikroskopische und schematische Darstellung eines Coronaviruspartikels. Abbildung modifiziert nach https://jmobraindump.files.wordpress.com/2012/09/coronavirus-structure.jpg)*

Die nahezu kugelförmigen coronaviralen Partikel haben einen Durchmesser von 90-110 nm und besitzen eine Lipidhülle, in der mindestens 3 virale Membranproteine eingelagert sind (Abb.1).

Das Spike-Protein (S-Protein, 180-220 kDa) bildet stabile Trimere und ist für die Rezeptorbindung verantwortlich. Das M-Protein ist das am häufigsten vorkommende Protein in der Virushülle und hat Schlüsselfunktionen bei der Partikelbildung (3). Das Hüllprotein E ist ein kleines integrales Membranprotein, das für die Viruspartikelbildung essentiell zu sein scheint. Das vierte Strukturprotein, das Nukleokapsidprotein N, befindet sich im Inneren des Virions und enkapsidiert das virale RNA-Genom. Das N-

Protein ist phosphoryliert und spielt eine wichtige Rolle bei der viralen Replikation und Transkription (4).

1.2. Genomorganisation und Replikation

Mit ca. 27-32 Kilobasen gehören CoV-Genome zu den größten bekannten viralen RNA-Genomen. Dieses ist am 3'-Ende polyadenyliert und am 5'-Ende durch eine Cap-Struktur geschützt (5). Zudem befinden sich an beiden Enden des viralen Genoms sogenannte 5'- und 3'-untranslatierte Regionen (eng. *untranslated regions,* UTRs) (6).

Nach dem Eintritt der Viruspartikel in die Wirtszelle wird das virale Genom freigesetzt und kann aufgrund seiner positiven (also mRNA-) Polarität und der 5'-terminalen Cap-Struktur nach Bindung an Ribosomen in zwei virale Polyproteine (pp1a und pp1ab) translatiert werden. Die gebildeten Polyproteine werden autoproteolytisch durch viruskodierte Proteasen, die Chymotrypsin-ähnliche Hauptprotease (M^{pro}) sowie eine oder zwei Papain-ähnliche Protease(n) (PL^{pro}), gespalten. Dadurch entstehen insgesamt bis zu 16 sogenannte Nichtstrukturproteine (*non-structural proteins*, nsps). Diese nsps wiederum bilden den Replikations- und Transkriptionskomplex (*replication/transcription complex*, RTC) (7).

Die coronavirale Transkription und Genomreplikation durch den RTC ist ein komplexer Vorgang. Hierbei werden mRNA-Moleküle mit subgenomischer Länge (sogenannte subgenomische RNAs, sgRNAs) sowie Volllängen-Genom-RNAs (genomische RNA, gRNA) hergestellt (8).

Die sgRNAs enthalten einen unterschiedlich langen Teil der Genomsequenz sowie identische 3' und 5'-terminale Enden. Hierbei enthalten alle sg mRNAs sowie auch die gRNAs am 5'-Ende eine identische Sequenz von 65-98 Nukleotiden, die als *leader*-Sequenz bezeichnet wird. Der 5'-*leader* und die 3'-gelegene *body*-Sequenz, die einen oder mehrere ORF(s) enthält, sind durch Transkriptions-regulierende Sequenzen (TRS), welche mehrfach im Genom vorhanden sind, miteinander verbunden. Eines der TRS-Elemente befindet sich unmittelbar 3'-terminal der *leader*-Sequenz, weshalb dieses Element als *leader*-TRS bezeichnet wird. Weitere TRS-Elemente befinden sich unmittelbar vor den verschiedenen ORFs im 3'-terminalen Bereich des Genoms und werden als *body*-TRS bezeichnet.

Diese Elemente spielen eine entscheidende Rolle in der Synthese coronaviraler sgRNAs, welche eine diskontinuierliche Extension während der Minusstrangsynthese einschließt (9). Die Minusstrang-Synthese wird zunächst am 3‘-Ende der genomischen RNA initiiert. Im Bereich der *body*-TRS kommt es dann zu einer Verlangsamung (oder einem Stopp) des Kopiervorgangs. Dadurch kann der virale RTC sowie die bereits synthetisierte Negativstrang-RNA zur *leader*-TRS translozieren und dort die RNA-Synthese fortsetzen und abschließen. Auf diese Weise wird eine Kopie der 5’-*leader*-Sequenz an das 3’-Ende des entstehenden sgRNA angeheftet (10). Die so entstandene Negativstrang-sgRNA dient nun als Matrize zur Generierung von Positivstrang-sgRNAs, welche als mRNA für die Translation der Strukturproteine (sowie weiterer akzessorischer Proteine, die im 3‘-Genombereich kodiert sind)

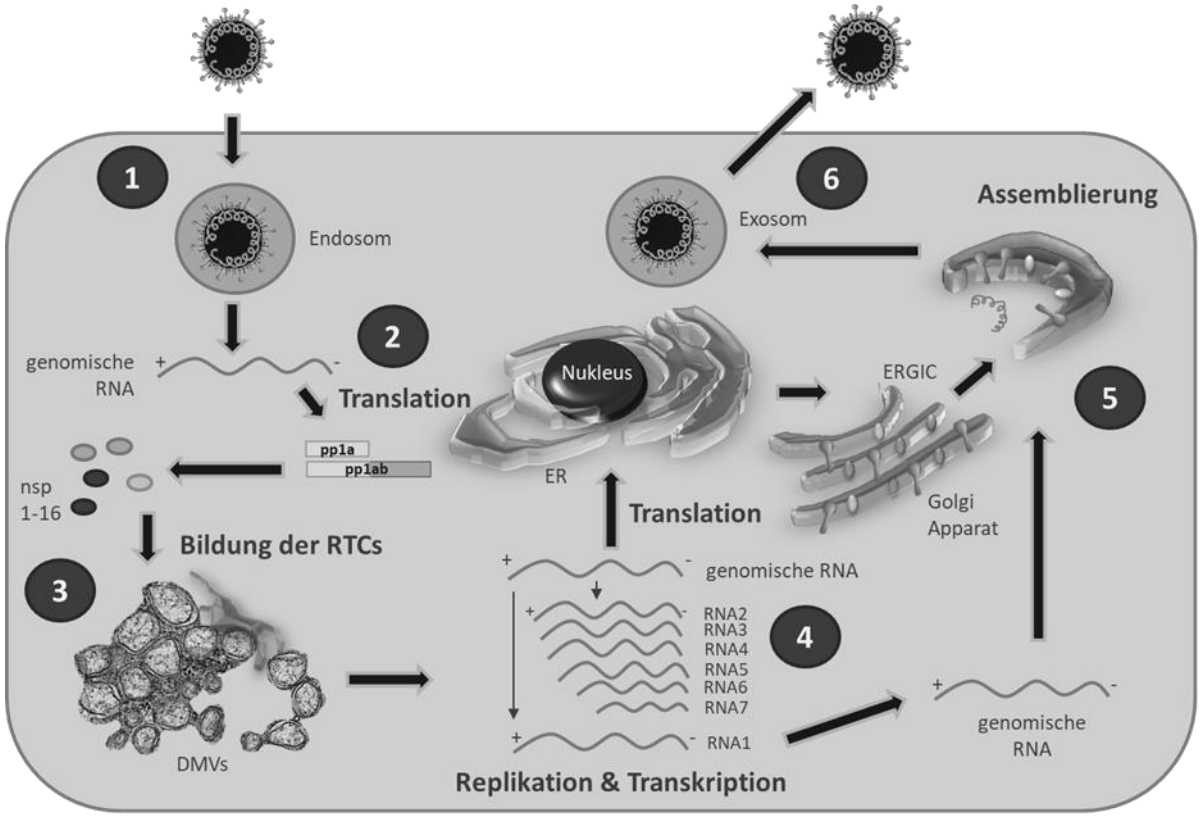

Abbildung 2 *Übersicht über den coronaviralen Replikationszyklus. (1) Das Coronavirus tritt durch rezeptorvermittelte Endozytose (oder direkte Fusion mit der Wirtsmembran, hier nicht dargestellt) in die Wirtszelle ein. (2) Nach der Freisetzung der genomischen RNA mit positiver Polarität (+RNA) wird diese in zwei Polyproteine (pp1a und pp1ab) translatiert, welche proteolytisch in 15-16 nsps prozessiert werden. (3) Die Nichtstrukturproteine bilden dann den RTC, welcher in sogenannten Doppelmembranvesikeln (DMVs) verankert ist. Innerhalb der DMVs findet die RNA-Replikation sowie die Transkription von sg mRNAs statt. (4) Während der Replikation wird zunächst eine negativsträngige Kopie (voller Länge) der Genom-RNA gebildet, welche anschließend als Matrize zur Synthese neuer Genom- +RNAs dient. Während der Transkription wird hingegen ein Set von 6 sgRNAs durch diskontinuierliche Transkription gebildet. Diese sgRNAs kodieren für die Struktur- und akzessorischen Proteine. Während dieses Prozesses werden negativsträngige RNA-Moleküle synthetisiert, die hinsichtlich ihrer Länge am 5‘-Ende variieren, jedoch alle an ihrem 3‘ Ende eine Kopie der genomischen 5‘-leader-Sequenz tragen. Diese sgRNAs negativer Polarität werden anschließend in + sg mRNAs umgeschrieben, die für die Translation der viralen Strukturproteine benötigt werden. (5) Die Assemblierung von Viruspartikeln und der Einbau der Strukturproteine in diese Partikel erfolgt anschließend im intermediären Kompartiment des ER/Golgi-Komplexes (ERGIC). (6) Neu gebildete Virionen werden im Anschluss über Exozytose freigesetzt.*

verwendet wird (11). Die Strukturproteine werden zusammen mit der genomischen RNA an Membranen des Golgi-Komplex zu funktionellen Viruspartikeln verpackt und aus der Zelle ausgeschleust (Abb. 2).

1.3. Pathogenese

Infektionen mit einem der saisonalen CoV führen in den meisten Fällen zu typischen Erkältungssymptomen, jedoch können Ko-Infektionen mit anderen Erregern (insbesondere Rhino-, Parainfluenza- und Enteroviren) oder bestehende Vorerkrankungen (z.B. des Kardiopulmonalsystems) auch zu schwereren Verläufen führen (12).

Auch eine Infektion mit SARS-CoV-2 führt in den meisten Fällen zu einer leichten bis mittelschweren Atemwegserkrankung. Es kann jedoch auch hier zu einem schweren Verlauf mit Dyspnoe oder gar Lungen- und Multiorganversagen kommen. Ähnlich zu einer Infektion mit SARS-CoV (Letalität 10 %) oder MERS-CoV (Letalität 30 %) können solche Infektionen auch eine massive Schädigung des Alveolarepithels verursachen. Zudem weisen Patienten mit COVID-19 und hypoxischem Lungenversagen Anzeichen einer systemischen Hyperinflammation auf (einschließlich der Freisetzung von entzündungsfördernden Zytokinen). Insgesamt liegt die Letalität von SARS-CoV-2 bei ca. 1 %. In 2020 wurden etwa 3-20 % der an COVID-19 Erkrankten stationär behandelt, wovon ein beträchtlicher Teil (ca. 10-30 %) intensivmedizinisch versorgt werden musste (13).
Aufgrund der durchgeführten Impfkampagne und der Entstehung neuer Virusvarianten, die vornehmlich in den oberen Atemwegen replizieren (z.B. Omikron), können diese Werte jedoch aktuell nach unten korrigiert werden.

Die SARS-CoV-2-Pandemie und die bereits wenige Jahre zuvor erfolgten begrenzten Infektionsausbrüche mit bisher unbekannten CoVs zeigen eindrücklich, dass auch zukünftig mit zoonotischen Übertragungen von CoVs aus tierischen Reservoiren auf den Menschen gerechnet werden muss. Dies wird zudem begünstigt durch den Klimawandel, den Handel mit Wildtieren, die zunehmende Urbanisierung und globale Vernetzung (13).

1.4. Antivirale Strategien

In Vorbereitung auf neu auftretende, pandemische CoVs und als Ergänzung zu wirksamen Impfstoffen ist eine Entwicklung antiviraler Medikamente zur Behandlung von coronaviralen Infektionen dringend erforderlich. Insbesondere bei Personen, die aufgrund von einer Immunsuppression (durch andere Grund- oder Begleiterkrankungen oder deren Therapie) keinen ausreichenden Immunschutz nach wiederholten Impfungen aufbauen können. Hinzu kommen Personen, deren Schutz vor Infektion nach gewisser Zeit nachlässt oder die aus verschiedenen Gründen nicht geimpft werden können. Auch im Hinblick auf mögliche Virusvarianten, die von den zugelassenen Impfstoffen nur unzureichend abgedeckt werden, sowie als Vorbereitung auf mögliche neu auftretende CoVs ist eine Entwicklung von antiviralen (Breitband-) Virostatika ratsam (14, 15).

Dabei soll die antivirale Substanz möglichst (**i**) breit verfügbar, (**ii**) nebenwirkungsarm und (**iii**) leicht anwendbar sein (z.B. Verabreichung in oraler oder inhalativer Form). Des Weiteren sollte diese (**iv**) der Entstehung von resistenten Virusvarianten entgegenwirken (15).

Im Allgemeinen ist die Entwicklung antiviraler Arzneimittel ein langwieriger Prozess, der viele Phasen umfasst. Dazu gehören Zielstruktur-Identifizierung und -Screening, *lead*-Generierung und -Optimierung, klinische Studien und letztendlich die Arzneimittelzulassung.

Daher verwundert es nicht, dass noch vor einigen Jahrzehnten nur sehr wenige Medikamente zur Behandlung von Virusinfektionen zugelassen waren. Seitdem hat ein besseres Verständnis der viralen Replikation zur Entwicklung und Anwendung zahlreicher neuer Virostatika geführt (16). Seit der Zulassung des ersten antiviralen Arzneimittels Idoxuridin im Jahr 1963 sind bis heute über 100 Medikamente gegen chronische und akute Virusinfektionen zugelassen und verfügbar (17, 18). Angesichts der großen Zahl humanpathogener Viren muss jedoch einschränkend erwähnt werden, dass wirksame antivirale Therapeutika nur für weniger als ein Dutzend Viren zur Verfügung stehen.

Hierbei wurden die größten Fortschritte in der Therapie von **chronischen Viruserkrankungen** erzielt, die z.B. durch humane Immundefizienz-Viren (HIV), Hepatitis-B-Viren (HBV), Hepatitis-C-Viren (HCV) oder bestimmte Herpesviren verursacht werden.

So sank die Zahl der *acquired immunodeficiency syndrome* (AIDS)-bedingten Todesfälle nach Einführung der antiretroviralen Therapie Mitte der 1990er Jahre um 60-80 % (19). Eine vollständige Elimination von HIV aus dem latenten Zustand und somit eine vollständige Heilung ist jedoch mit den aktuell verfügbaren Medikamenten nicht möglich. Ähnliches gilt für die Therapie von HBV. Trotz einer verfügbaren Impfung sind nahezu 3 % der Weltbevölkerung chronisch mit HBV infiziert. Die derzeitige Behandlung der chronischen Hepatitis B mit pegyliertem Interferon oder Nukleos(t)ide-Analoga kann die HBV-Replikation zwar unterdrücken und den Krankheitsverlauf verlangsamen, eine Heilung ist jedoch in den meisten Fällen nicht möglich (20).

Im Gegensatz zu HIV und HBV, kann heutzutage, 25 Jahre nach seiner Entdeckung, eine chronische HCV-Infektion in 95 % der Fälle geheilt werden. Dieser Meilenstein der Medizingeschichte ist durch die Entwicklung einer speziellen antiviralen Kombinationstherapie möglich (21). Damit ist eine HCV-Infektion die einzige chronische Viruserkrankung, die durch eine antivirale Therapie komplett ausgeheilt werden kann (22).

Neben chronischen Infektionen können auch einige **akute virale Infektionen** behandelt werden. Akute virale Infektionen werden überwiegend von RNA-Viren hervorgerufen. Bei der Therapie sind mehrere Herausforderungen zu beachten. Zum einen muss der Wirkstoff (sehr) frühzeitig vergeben werden. Zum anderen sind RNA-Viren aufgrund ihrer Mutationsrate sehr wandelbar, wodurch Resistenzbildungen möglich sind. Ein Beispiel hierfür ist die Behandlung der akuten Influenza mit Amantadinen, welche das virale M2-Membranprotein hemmen. Aufgrund der schnellen Resistenzentwicklung sind Amantadine inzwischen nicht mehr zur Therapie empfohlen (23).

1.5. Virus- und wirtsgerichtete Virostatika

Generell können antivirale Therapieoptionen in zwei verschiedene Strategien unterteilt werden: **virusgerichtete Virostatika** (auch direkt wirkende Virostatika, *direct acting*

antivirals (DAAs)) oder **wirtsgerichtete Virostatika** (*host directed antivirals* (HDAs)) (24-26).

DAAs setzen am Virus direkt an und wirken unmittelbar hemmend auf bestimmte virale Enzyme. Dahingegen setzen **HDAs** am Wirtsorganismus an und hemmen zelluläre Faktoren, die für die Virusvermehrung essenziell sind. Zudem können zelluläre Abwehrmechanismen frühzeitig therapeutisch aktiviert werden, um eine Virusausbreitung zu verhindern.

Beide Strategien werden in den folgenden Kapiteln am Beispiel anti-coronaviraler Medikamente genauer beschrieben.

1.6. Virusgerichtete Virostatika gegen SARS-CoV-2

Im Prinzip können alle Schritte des viralen Replikationszyklus vom Eintritt bis zur Freisetzung und die daran beteiligten viralen Proteine als molekulare Ziele für die antivirale Therapie angesehen werden. In diesem Abschnitt werden aufgrund ihrer Bedeutung für diese Arbeit hauptsächlich Eintritts-, Protease-, und Polymerase-Inhibitoren besprochen, welche gegen SARS-CoV-2 entwickelt und zugelassen wurden.

1.6.1. Eintritts-Inhibitoren

Bereits der erste Schritt im viralen Replikationszyklus, die Rezeptor-vermittelte Aufnahme des Viruspartikels in die Zielzelle, kann als antiviraler Angriffspunkt verwendet werden (27). Neben Fusions-Inhibitoren kann auch gezielt die Bindung viraler Partikel an die Zielzelle unterbunden werden. Hierfür werden zum Beispiel **neutralisierende Antikörper** verwendet. Diese binden spezifisch an die Rezeptor-bindende Domäne (RBD) im Spikeprotein und blockieren so die Bindung und Aufnahme des Viruspartikels sowie letztendlich eine Infektion des Wirts (28). Allerdings unterscheiden sich diese hochspezifischen, monoklonalen Antikörper enorm in ihrer Wirkempfindlichkeit gegenüber verschiedenen Virusvarianten. Antikörper, welche z.B. gegen die Alpha-, Beta-, Gamma- und Delta-Varianten von SARS-CoV-2 entwickelt wurden, weisen eine teilweise stark reduzierte Wirksamkeit gegenüber den aktuell zirkulierenden Omikron-Virusvarianten auf (29, 30). Daher sind z.B. die zu Beginn der Pandemie zugelassenen monoklonalen Antikörper gegen SARS-CoV-2 Casirivimab/Imdevimab, Tixagevimab/Cilgavimab und Sotrovimab nicht mehr zur Behandlung empfohlen (31, 32). Zudem ist die Herstellung monoklonaler

Antikörper relativ kosten- und zeitaufwändig. Des Weiteren muss, um eine möglichst hohe Wirksamkeit zu erzielen, die therapeutische Gabe sehr früh nach Infektion (oder Kontakt) einmalig intravenös erfolgen. Daher dient diese Therapieoption vor allem als Postexpositionsprophylaxe (z.B. bei einem Ausbruch in einem Pflegeheim) oder kommt bei ausgeprägter Immunschwäche (z.B. nach Transplantation) zur Geltung (33, 34).

1.6.2. Protease-Inhibitoren

Viele Viren kodieren in ihrem Genom eine oder mehrere Proteasen. Diese prozessieren virale Polyproteinvorläufer und sind essenziell für die Freisetzung funktionsfähiger viraler Proteine (35). Die meisten viralen Proteasen besitzen eine eng definierte Substratspezifität für virale (und gelegentlich auch wenige zelluläre) Substrate. Daher sind synthetische Peptidomimetika, die mit einer hohen Bindeaffinität die natürlichen Substrate einzelner viraler Proteasen nachahmen, potente antivirale Kandidaten in der Arzneimittelforschung (36). Diese werden unter anderem erfolgreich gegen HIV (Bsp. Amprenavir, Lopinavir) (37) oder SARS-CoV-2 (Bsp. Paxlovid) eingesetzt (38).

Paxlovid ist eine Kombination aus dem viralen 3CL-Protease (M^{pro}) Inhibitor **Nirmatrelvir** und dem Cytochrom P450 3A- und P-Glykoprotein-Inhibitor Ritonavir (38). Cytochrom P450 3A oxidiert körperfremde Moleküle, wie Toxine und Medikamente, wodurch diese ihre Wirkung verlieren (39). P-Glykoprotein ist ein Effluxtransportprotein, welches aktiv Fremdstoffe aus der Zelle in den Extrazellularraum pumpt (40). Durch die Inhibition dieser leberspezifischen Enzyme über 4-5 Tage, agiert Ritonavir als pharmakokinetischer Verstärker und die Metabolisierung von Arzneimitteln wie Nirmatrelvir wird verringert. Das heißt auch, dass ohne Ritonavir bei einer oralen Verabreichung von Nirmatrelvir keine wirksamen antiviralen Konzentrationen im Zielgewebe erreicht werden (38). Darüber hinaus erhöht jedoch die Verwendung von Ritonavir auch die Konzentrationen anderer Medikamente (z.B. Statine, Antiarrhythmika, Neuroleptika, Sedativa, Antikonvulsiva), wodurch sich das Risiko von Arzneimitteltoxizitäten erheblich erhöht (41, 42).
Dadurch wird Paxlovid für bestimmte Patientengruppen obsolet, darunter auch für Risikogruppen, die eigentlich am meisten von einer anticoronaviralen Behandlung profitieren würden. Obwohl Paxlovid in der Zulassungsstudie einen hohen Nutzen

gegen die Erkrankung COVID-19 aufweist, wird bisher Paxlovid aufgrund der zahlreichen klinisch bedeutsamen Arzneimittelinteraktionen nur wenig verwendet. Des Weiteren könnte es zukünftig zur Entstehung Nirmatrelvir-resistenter Virusvarianten kommen. Hinweise darauf geben *In-vitro*-Studien, in denen SARS-CoV-2 nach 30facher Passage in Anwesenheit von Nirmatrelvir eine Resistenzentwicklung aufwies. Im Vergleich zum Ursprungsvirus waren die angepassten Virusvarianten *in vitro* 33- bis 50-fach weniger sensitiv gegenüber einer Behandlung mit Nirmatrelvir (43).

1.6.3. Polymerase-Inhibitoren

Fast alle Viren kodieren für virale Polymerasen, die eine zentrale Schlüsselrolle in der Replikation und Transkription des viralen Genoms einnehmen. Daher zählen Polymerasen zu den attraktivsten Zielen für die Entwicklung antiviraler Medikamente (44). Ausgehend von der Funktion und der Struktur der viralen Polymerasen gibt es zwei Haupttypen von Polymeraseinhibitoren: (**i**) nichtkompetitive, allosterische Inhibitoren, welche die Polymerase-Aktivität teilweise oder vollständig unterbinden und (**ii**) Nukleosid- und Nukleotid-Analoga (36). Letztere werden zunächst von der Wirtszelle triphosphoryliert, um als aktiver Inhibitor mit natürlichen Nukleosidtriphosphaten zu konkurrieren und (nach Einbau) die Strangsynthese zu terminieren oder (bei der nachfolgenden Gegenstrangsynthese) die Entstehung von Mutationen zu begünstigen. Beispiele hierfür sind **Remdesivir** bzw. **Molnupiravir** (45, 46).

Remdesivir wurde ursprünglich gegen Ebolaviren entwickelt, zeigt jedoch eine breite Wirksamkeit gegen eine Vielzahl verschiedener Viren *in vitro* (45, 47). Daher wurde im Rahmen der SARS-CoV-2-Pandemie 2020 per Notfallzulassung Remdesivir als erstes Medikament zur Behandlung von COVID-19 zugelassen. Remdesivir gilt bis heute als Therapiealternative zu Paxlovid [35, 36]. Das Arzneimittel darf angewendet werden bei Patienten mit Pneumonie und erforderlicher zusätzlicher Sauerstoffgabe (jedoch keine invasive Beatmung) oder bei Patienten mit einem erhöhten Risiko für einen schweren COVID-19-Verlauf (48). Hierbei wird Remdesivir bis spätestens 7 Tage nach Symptombeginn intravenös über 5 Tage gegeben, was im Frühstadium der Erkrankung bei ambulanten Patienten oft eine hohe Hürde darstellt. Daher wird Remdesivir trotz seiner nachgewiesenen Wirksamkeit nur selten eingesetzt.

Zudem konnte (ähnlich zu Nirmatrelvir) bereits gezeigt werden, dass eine Punktmutation in der RNA-abhängigen RNA-Polymerase nsp12 (E802D) zu einer Remdesivir-Resistenz *in vitro* (49) sowie in immunkomprimierten Patienten *in vivo* (50) führt.

Molnupiravir ist das orale Prodrug eines synthetischen Nukleosid-Analogons (N4-Hydroxycytidin) mit einer (gegenüber Remdesivir) guten Bioverfügbarkeit. Es hemmt die virale RNA-Replikation durch Akkumulation von Mutationen im viralen Genom (letale Mutagenese) (29, 42, 46). Daher gilt Molnupiravir als potenziell mutagen bzw. teratogen, wodurch es bei Schwangeren oder Jugendlichen unter 18 Jahren kontraindiziert ist. Obwohl Molnupiravir in vorläufigen klinischen Studien nahezu eine Halbierung der Hospitalisierungs- und Sterberate zeigte (51, 52) und daher eine Notfallzulassung in Deutschland in Betracht gezogen wurde, konnte der klinische Nutzen letztendlich nicht überzeugend nachgewiesen werden (53). In der Gesamtschau der verfügbaren Daten verringerte Molnupiravir das Risiko einer Krankenhauseinweisung oder eines Todesfalls nicht. Zudem konnte auch keine Verkürzung der Krankheitsdauer bestätigt werden. Daher wurde der Zulassungsantrag von Molnupiravir nach negativer Bewertung der Europäischen Arzneimittel-Agentur (EMA) abgelehnt (54). Daher darf Molnupiravir seit dem 24. Februar 2023 nicht mehr ärztlich verordnet oder abgegeben werden.

Zusammenfassend sind DAAs aufgrund ihrer selektiven Wirkung auf virale Proteine relativ nebenwirkungsarm. Allerdings können Medikamenten-resistente Virusvarianten durch den Selektionsdruck einer antiviralen Therapie in z.B. immunsupprimierten oder chronisch erkrankten Patienten entstehen, die eine Behandlung mit dem entsprechenden Medikament obsolet macht (24). Zudem sind einige virale Proteine (vor allem des RTCs) stark konserviert, wodurch speziell entwickelte Inhibitoren oftmals für eine Virusfamilie oder Virusgenera verwendet werden können. Möglicherweise erschwert dies jedoch ein „*drug repurposing*“ bei z.B. neu auftretenden viralen Erregern bei denen noch keine antivirale Therapie vorhanden ist.

1.7. Wirtsgerichtete Virostatika gegen SARS-CoV-2

Wie oben dargelegt, wurden antivirale Medikamente traditionell entwickelt, indem man direkt auf wesentliche Virus-kodierte Faktoren abzielte. Diese Strategie scheiterte

jedoch –langfristig gesehen– häufig an einer Resistenzentwicklung. Als mögliche Alternative wird deshalb die Inhibition von Wirtsfaktoren betrachtet, die für die Replikation unterschiedlicher Viren einer Virusgattung oder sogar einer ganzen Virusfamilie von essentieller Bedeutung sind. Von besonderem Interesse ist dabei auch die Aussicht, möglicherweise ein breit wirksames Virostatikum mit einer erhöhten Barriere für die Entwicklung und Selektion Arzneimittel-resistenter Mutationen entwickeln zu können (55).

Generell gehen Viren während der Replikation zahlreiche Wechselwirkungen mit Wirtsfaktoren und -wegen ein. Durch den technologischen Fortschritt konnten so bereits mehrere Wirtsfaktoren identifiziert werden, die für die Replikation spezifischer Viren (oder sogar Virusfamilien) wesentlich, aber für den Wirt (zumindest kurzfristig) entbehrlich sind.
Präklinische Beispiele der Wirkstoffentwicklung gegen SARS-CoV-2 sind hierbei **ACE2-Antagonisten** (56) oder **Hemmstoffe der TMPRSS2-Protease** (57), welche den Eintritt von SARS-CoV-2 in die Zelle unterbinden. Zudem könnten weitere Wirtsfaktoren, welche beispielsweise an der Proteintranslation, der Lipidsynthese oder der posttranslationalen Modifikation viraler Proteine (z.B. Glykosylierung, Phosphorylierung, ADP-Ribosylierung usw.) beteiligt sind, als mögliche Zielstrukturen dienen (15, 24).

Darüber hinaus könnten auch antivirale Abwehrmechanismen des Wirts in geeigneter Weise beeinflusst werden, um den Infektionsverlauf günstig zu beeinflussen. Dies geschieht in der Regel durch die Gabe von Typ-1- und Typ-3-**Interferon** oder künstlichen Oligonukleotiden, welche spezialisierte Rezeptoren des angeborenen Immunsystems (z.B. RIG-1, Toll-like-Rezeptoren) aktivieren (24). Im Gegensatz zu einer Aktivierung des Immunsystems kann dieses auch unterdrückt werden. Manche Virusinfektionen (inkl. SARS-CoV-2) lösen bei einem schweren Verlauf eine sogenannte überschießende inflammatorische Reaktion (Zytokinsturm) aus. Daher zählt das Glukokortikoid **Dexamethason**, welches entzündungshemmend und immunsuppressiv wirkt, zur Behandlungsstrategie bei invasiv beatmeten COVID-19-Patienten. Hierbei handelt es sich jedoch lediglich um eine supportive Therapie, die sich nicht gegen das Virus selbst richtet (58).

2. Zielsetzung

Für viele Virusinfektionen, insbesondere auch für CoV-bedingte Atemwegsinfektionen, stehen kaum bzw. unzureichende antivirale Therapieoptionen zur Verfügung, die für die meisten Patienten ohne Einschränkungen und Risiken eingesetzt werden könnten. Zu Beginn der COVID-19-Pandemie wurden hauptsächlich Medikamente, die bereits zur Behandlung anderer viraler Erkrankungen geprüft und zugelassen waren (z.B. Remdesivir), eingesetzt. Da diese umgewidmeten Wirkstoffe (sogenannte *repurposed drugs*) nicht speziell für SARS-CoV-2 optimiert wurden, war deren Wirkungen oftmals **limitiert** (15). Zudem sind viele der zugelassenen Therapiemöglichkeiten für SARS-CoV-2-Infektionen nur noch **begrenzt wirksam** (z.B. monoklonale Antikörper) oder haben **starke Nebenwirkungen oder Einschränkungen**, die ihren klinischen Einsatz stark reduzieren (z.B. Molnupiravir, Paxlovid).

Aus diesen Erwägungen ergibt sich, dass die gezielte Entwicklung weiterer Wirkstoffe und Therapieoptionen gegen SARS-CoV-2, aber auch gegen andere CoVs sowie RNA-Viren anderer Familien, dringend erforderlich bleibt.

Ziel der in diese Schrift aufgenommenen Studien war es daher, innovative antivirale Ansätze speziell gegen CoVs zu identifizieren und zu charakterisieren. Diese zielen entweder direkt auf das Virus oder auf spezifische Wirtsfaktoren bzw. -mechanismen, die für die Virusreplikation zwingend erforderlich sind. Im Besonderen wurden dabei folgende Fragestellungen bearbeitet:

1) Virus-gerichtete antivirale Therapie:

   a. Kann die virale Replikation mit Hilfe von zirkulären Antisense-RNAs (circRNAs), welche spezifisch an coronavirale 5'-nichttranslatierte Regionen (5' UTRs) binden, unterdrückt werden?

2) Wirts-gerichtete antivirale Therapie:

   a. Wie und in welchem Umfang kann die coronavirale Replikation durch die Beeinflussung zellulärer ER-Stress-Signalwege beeinträchtigt werden?
   b. Welche Auswirkungen hat die gezielte Hemmung des Translationsinitiationsfaktors eIF4A auf die Replikation verschiedener RNA-Viren?

3. Ergebnisse und Diskussion

3.1. Virusgerichtete Virostatika: circRNAs

Dieses Kapitel nimmt Bezug auf folgende Publikation:

> *Pfafenrot C*, Schneider T*, **Müller C***, Hung LH, Schreiner S, Ziebuhr J, Bindereif A. Inhibition of SARS-CoV-2 coronavirus proliferation by designer antisense-circRNAs. Nucleic Acids Res. 2021 Dec 2;49(21):12502-12516. doi: 10.1093/nar/gkab1096. PMID: 34850109; PMCID: PMC8643703.*

3.1.1. Coronavirale 5'UTR als antivirale Zielstruktur

Das coronavirale Genom enthält an seinen 5‘- und 3'-Enden untranslatierte Regionen, die hoch konservierte RNA-Sekundärstrukturen enthalten. Diese werden als 5’- bzw. 3'-UTR bezeichnet. Die 5'-UTR hat wichtige biologische Funktionen in der viralen Replikation, Transkription, Translation und Verpackung des Genoms (6, 59-61). Daher ist die gezielte Beeinflussung der 5‘-UTR ein vielversprechender antiviraler Ansatz, der im folgenden Abschnitt näher erläutert wird (30, 62-64).

3.1.2. Zirkuläre Antisense-Oligonukleotide gegen SARS-CoV-2

Sogenannte *Antisense* (AS)-Ansätze stellen eine klassische, sequenzbasierte RNA-Interferenz dar (62, 63, 65). Hierbei entsteht eine Wechselwirkung von kurzen Stücken komplementärer RNA (z.B. unter Verwendung von AS-Oligonukleotiden (ASOs) oder *locked nucleic acids* (LNAs)) mit den Ziel-mRNAs. Dies hat eine Modulation der Ziel-RNA-Struktur, -Stabilität, -Translation und/oder des mRNA-Spleißens zur Folge.

In dieser Studie untersuchten wir das antivirale Potenzial nicht-kodierender, **zirkulärer RNAs** (*circular* RNAs, circRNAs) mit kovalent verbundenen 5'- und 3'-Enden (66), indem wir zum ersten Mal den klassischen ASO-Ansatz mit synthetischen kurzen circRNAs kombinierten (67).

Dabei wurden artifizielle AS-circRNAs gegen die strukturell konservierte 5'-UTR (inkl. der gut zugänglichen Subregion des 5’-*leaders*) der SARS-CoV-2-Genom-RNA entwickelt. Um eine stabile Interaktion zu garantieren, wurde hierbei eine AS-Sequenz von mindestens 30 komplementären Nukleotiden verwendet. Hierbei wurden insgesamt neun AS-circRNAs mit einer Länge zwischen 40 und 76 Nukleotiden (nts) eingesetzt, die an verschiedene Bereiche der SARS-CoV-2 5’-UTR binden (siehe Abb. 3).

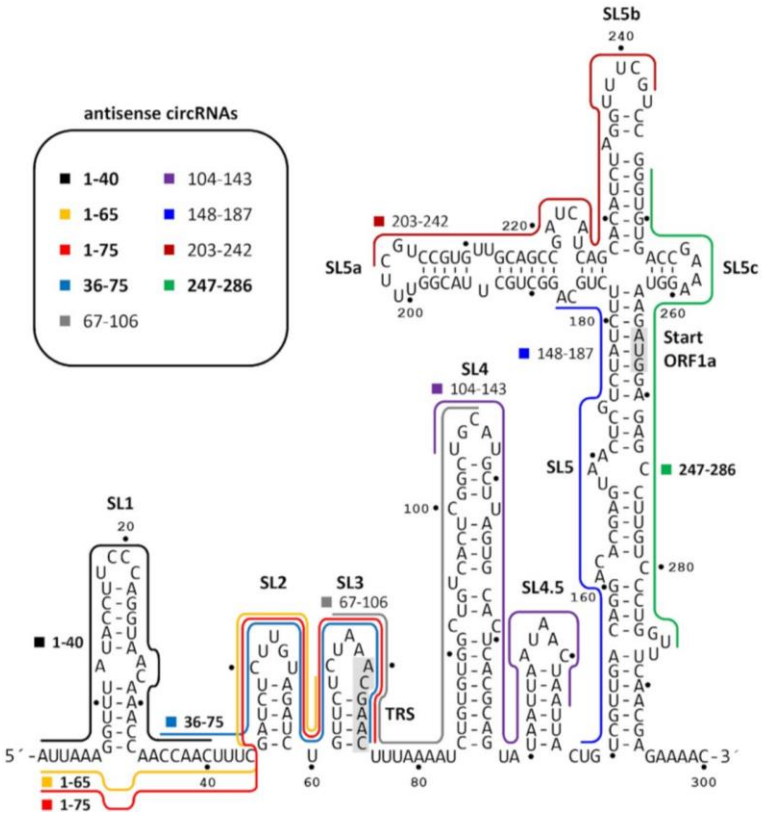

Abbildung 3 *Übersicht der entwickelten AS-circRNAs, die durch komplementäre Basenpaarung an die SARS-CoV-2-RNA binden. Die Zielregionen der AS-circRNAs innerhalb des 5'-Leaders (nts 1-75) und der 5'-UTR von SARS-CoV-2 (nts 1-265) sind zusammen mit dem Sekundärstrukturmodell dieser Region dargestellt. Das TRS-Kernelement (nts 70-75) und das AUG-Startcodon von ORF1a (nts 266-268) sind grau schattiert. Abbildung modifiziert nach Pfafenrot et al., 2021.*

Nach der Identifizierung von AS-circRNAs, die die SARS-CoV-2-Translation wirksam in Reporterassays *in vitro* hemmten (67), wurde deren antivirale Aktivität in SARS-CoV-2-infizierten Zellen analysiert. Zu diesem Zweck wurden ausgewählte circRNAs in drei verschiedenen Konzentrationen transfiziert und 24h später die Zellen mit SARS-CoV-2 infiziert. Im Vergleich zu den verwendeten Kontrollen (unbehandelte, mock-transfizierte oder Kontroll-circRNA-transfizierte Zellen) reduzierten die circRNAs, welche die Region 1-75 nts binden, signifikant die virale Replikation (Abb. 4A-C).
Zudem wurden die lineare und zirkuläre Version der 1-75nt AS-RNA verglichen (Abb. 4D). Hierbei zeigte die zirkuläre Version einen längeren antiviralen Effekt als die lineare Version. Dies deutete auf eine höhere Stabilität der verwendeten circRNA gegenüber der linearen Version hin.

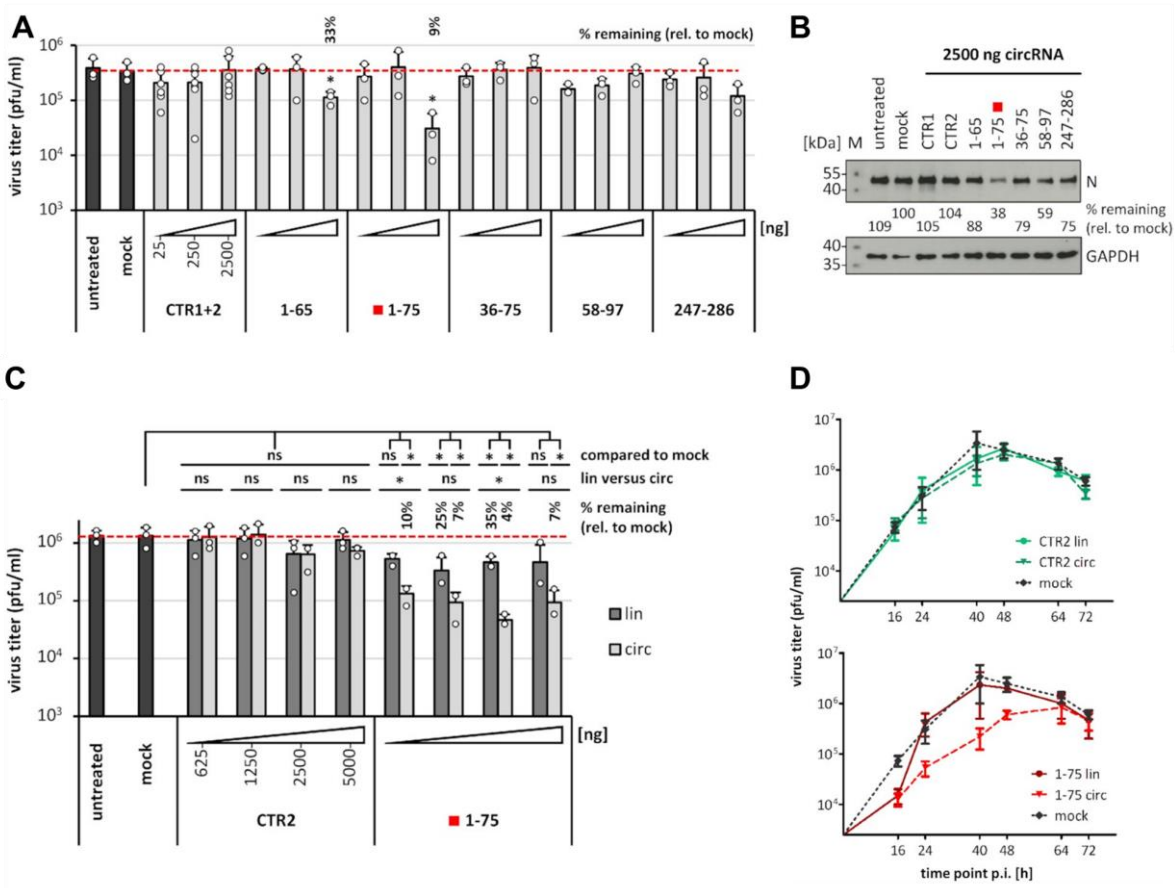

Abbildung 4 *Hemmung der SARS-CoV-2-Replikation durch AS-circRNA. (A) Vero E6-Zellen wurden mit steigenden circRNA-Konzentrationen transfiziert (25, 250 und 2500 ng pro Assay; hellgrau; wie unter dem Diagramm angegeben). Nach 24 Stunden wurden die Zellen mit SARS-CoV-2 (MOI = 0,1 pfu/Zelle) infiziert. Die Virustiter wurden mittels Plaque-Assays der Zellkulturüberstände 24 Stunden nach der Infektion gemessen (Mittelwert und Standardabweichungen von drei Experimenten sind angegeben, *P < 0,05, ns = nicht signifikant, zweiseitiger t-Test). Unbehandelte (ohne RNA und Transfektionsreagenz) und mock-behandelte Zellen (ohne RNA, aber mit Transfektionsreagenz) dienten als Kontrollen. (B) Assays zur viralen Proteinsynthese: Die Western-Blot-Analyse des viralen Nukleokapsidproteins (N) bestätigt die Verringerung der viralen Proteinakkumulation in Zellen, die mit spezifischen AS-circRNAs behandelt wurden. Vero E6-Zellen, die mit 2500 ng der jeweiligen circRNAs transfiziert wurden, wurden geerntet, lysiert und gleiche Proteinmengen mittels Western Blotting analysiert, wobei das Nukleokapsidprotein als Marker für die virale Proteinakkumulation verwendet wurde. GAPDH wurde als Ladekontrolle verwendet. M, Proteinmarker (Größen in kDa). (C) Dosisabhängige antivirale Wirkung der circRNA AS1-75 im Vergleich zu ihrem linearen Gegenstück. Vero E6-Zellen wurden mit steigenden Mengen (625, 1250, 2500 und 5000 ng) der AS_1-75 circRNA (hellgrau) oder des linearen Gegenstücks (dunkelgrau) transfiziert und infiziert (MOI = 0,1 pfu/Zelle). Virustiter wurden 24 h p.i. mittels Plaque-Assays bestimmt (Mittelwert und Standardabweichungen von drei Experimenten, *P < 0,05, ns = nicht signifikant, zweiseitiger t-Test). Als Kontrollen wurden unbehandelte (ohne RNA und Transfektionsreagenz) und mock-behandelte Zellen (ohne RNA, aber mit Transfektionsreagenz) verwendet sowie Transfektionen mit linearer oder zirkulärer Kontroll-RNA (CTR2). (D) Zeitliche Dauer der antiviralen Aktivität von AS_1-75 circRNA. Vero E6-Zellen wurden mit AS_1-75 circRNA oder ihrem linearen Gegenstück (unteres Feld; in rot) transfiziert und infiziert (MOI = 0,1 pfu/Zelle) (Mittelwert und SEM von drei Experimenten). Zur Bestimmung des Virustiters in den Kulturüberständen, die zu den angegebenen Zeitpunkten (16-72 Stunden nach der Infektion) gesammelt wurden, wurden Plaque-Assays durchgeführt. Als Kontrollen wurden mock-behandelte Zellen (ohne RNA, aber mit Transfektionsreagenz) verwendet (oberes und unteres Feld; in schwarz), sowie Transfektionen mit linearer oder zirkulärer Kontroll-RNA (CTR2; oberes Feld; in grün). Abbildung modifiziert nach Pfafenrot et al., 2021.*

Zusätzlich zu der Standard-Zelllinie Vero E6 konnten wir die antivirale Wirkung der AS_1-75 circRNA auch in einem biologisch relevanteren *Ex-vivo*-Zellkultursystem bestätigen (67). Hierbei wurden isolierte, primäre, humane Atemwegsepithelzellen für 4 Wochen unter *Air/liquid-interface*-Bedingungen ausdifferenziert. Anschließend

wurden die Zellen mit AS_1-75 circRNA transfiziert und mit SARS-CoV-2 infiziert. Auch in diesem System konnte eine signifikante Reduktion der viralen Replikation durch die spezifisch bindende AS_1-75 circRNA bestätigt werden (67).
Da Mutationen im Genom neu auftretender Virusvarianten von großer Bedeutung für die Virusausbreitung in Populationen mit teilweise vorbestehender Immunität sind, haben wir auch untersucht, ob die Aktivität der AS_1-75 circRNA durch Einzelpunktmutationen in der viralen Zielsequenz beeinflusst wird. Hierbei wurden anhand von Sequenzanalysen fünf häufig auftretende Punktmutationen (21C→T, 34A→T, 35A→T, 36C→T, 66C→T) im Reporterassay analysiert. Dabei wurden keine signifikanten Unterschiede in der Hemmung zum Wildtyp-Reporter beobachtet. Unsere Daten deuteten darauf hin, dass die Aktivität der AS_1-75 circRNA erstaunlich robust und unempfindlich gegenüber einzelnen Punktmutationen ist (67).

Zusammenfassend konnten wir demonstrieren, dass durch die spezifische komplementäre Bindung einer circRNA an die 5‘-terminale Region des SARS-CoV-2-Genoms unterschiedliche Schritte der viralen Replikation beeinträchtigt werden können (67). Dazu zählt die Translationsinitiierung, die virale Genomreplikation, die Synthese der 5′-*leader*-haltigen subgenomischen RNAs, die RNA-Stabilität und möglicherweise auch die RNA-Verpackung.
Somit könnten Designer-AS-circRNAs zukünftig als eine neue Generation vielseitig einsetzbarer RNA-Therapeutika entwickelt werden, deren Sequenzen – bei Bedarf – leicht an virale Fluchtmutanten angepasst werden könnten.

3.1.3. Ausblick: circRNAs

Die Verwendung von AS-RNA-basierten Therapien ist nicht gänzlich neu. Diverse AS-Oligonukleotide sind bereits für die Behandlung von viralen Erkrankungen sowie zur Behandlung verschiedener menschlicher Erbkrankheiten (z.B. Amyloidose, spinale Muskelatrophie etc.) zugelassen (68).

Ein Beispiel hierfür ist das seit 2017 in Deutschland zugelassene ASO Nusinersen (69). Dieses wird aktuell zur Therapie der häufigsten genetisch bedingten neuromuskulären Erkrankung, der 5q-assoziierten spinalen Muskelatrophie, intrathekal verabreicht. Das ASO verändert den Spleißvorgang des *Survival-motor-neuron*-2-Gens, wodurch der Krankheitsverlauf deutlich verlangsamt wird (70). Neben

Nusinersen sind auch die ASOs Inotersen bei Erwachsenen mit hereditärer Transthyretin-Amyloidose (71) und Volanesorsen bei Patienten mit Chylomikronämie-Syndrom (72) in Deutschland zur Behandlung zugelassen.

Zudem rücken RNA-Therapeutika auch zunehmend in den Fokus antiviraler Therapieoptionen (73). Beispielsweise wurde bereits 1999 der Wirkstoff Fomivirsen zur Behandlung von Cytomegalovirus-assoziierter Retinitis bei HIV-Trägern mit erworbener Immunschwäche zugelassen. Hierbei handelt es sich um ein synthetisches 21-Nukleotid-Phosphorothioat-Oligodesoxynukleotid. Dieses wurde komplementär zur viralen mRNA-Sequenz eines Cytomegalovirusproteins konzipiert. Trotz der bestätigten Wirksamkeit wurde Fomivirsen aufgrund des geringen klinischen Bedarfs nach Einführung der hochaktiven antiretroviralen Therapie am Ende der 1990er Jahre aus wirtschaftlichen Gründen vom Markt genommen (74). Aktuell befinden sich jedoch antivirale, RNA-basierte Medikamente gegen Influenzaviren (75) und Hepatitis-B-Viren (76) in klinischen Phase-I/II-Studien.

Hinsichtlich der Behandlung von CoVs sind aktuell nur vorklinische Daten verfügbar (77, 78). Auf eine Wirksamkeit *in vivo* weisen jedoch Tierversuchsergebnisse mit dem murinen CoV (*mouse hepatitis virus*, MHV) und SARS-CoV-2 hin. Hier konnte unter Verwendung von speziellen ASOs die MHV-Replikation reduziert und somit die virusbedingten Gewebeschädigungen in infizierten Mäusen verringert werden (78). Für SARS-CoV-2 konnten Vora et al. zeigen, dass eine intranasale Behandlung mit ASOs, welche ebenfalls gegen die 5'UTR (speziell den *stem loop* 1) von SARS-CoV-2 gerichtet waren, die infizierten Mäuse vor einem tödlichen Verlauf schützte (79).

Eine erfolgreiche Weiterentwicklung von ASOs zu einem RNA-basierten Arzneimittel ist jedoch mit vielen Herausforderungen verbunden. Zum einen ist RNA sehr instabil und kann leicht durch Nukleasen abgebaut werden. Zudem aktivieren RNA-Moleküle das angeborene Immunsystem und die RNA-Moleküle weisen aufgrund ihrer hohen negativen Ladungsdichte eine geringe Penetration der Zellmembranen auf. Daher müssen geeignete Verpackungsstrategien wie Liposomen, Nanopartikel, Polymere oder Vektor-Systeme entwickelt und verwendet werden (80). Allerdings ermöglicht die RNA-Technologie auch eine schnelle Anpassung an z.B. neue Virus(sub)typen und könnte daher in Zukunft für neu auftretende Viruserkrankungen genutzt werden.

Kapitel II

3.2. Wirtsgerichtete Virostatika: Thapsigargin

Dieses Kapitel nimmt Bezug auf:

> *Shaban MS*, **Müller C***, Mayr-Buro C*, Weiser H, Meier-Soelch J, Albert BV, Weber A, Linne U, Hain T, Babayev I, Karl N, Hofmann N, Becker S, Herold S, Schmitz ML, Ziebuhr J, Kracht M. Multi-level inhibition of coronavirus replication by chemical ER stress. Nat Commun. 2021 Sep 20;12(1):5536. doi: 10.1038/s41467-021-25551-1. PMID: 34545074; PMCID: PMC8452654*.

3.2.1. ER-Stress und seine Regulierungsmechanismen

Das endoplasmatische Retikulum (ER) ist entscheidend an der Proteinbiosynthese sowie der anschließenden Qualitätskontrolle beteiligt. Dazu zählt die korrekte Faltung, sowie der Transport und der Abbau von Proteinen (81).

Dabei führt eine Anhäufung ungefalteter oder fehlgefalteter Proteine im ER-Lumen zu ER-Stress und zur Aktivierung der *unfold protein response* (UPR), wodurch die Proteinsynthese verlangsamt und die Faltungsfähigkeit erhöht wird. Infolgedessen kann die zelluläre Proteinhomöostase wiederhergestellt werden, was zum Überleben der Zelle führt. Wenn dieser Ausgleichsmechanismus versagt, können bestimmte ER-Stress-Signalwege auch oxidativen Stress auslösen, was zum Zelltod führen kann (81, 82).

ER-Stress wird hauptsächlich über drei Sensoren reguliert: die Proteinkinase R (PKR)-ähnliche ER-Kinase (PERK), das *inositol-requiring protein 1α* (IRE1α) und den zyklischen AMP-abhängigen Transkriptionsfaktor 6α (ATF6α). PERK und IRE1α sind Ser/Thr-Kinasen, deren konservierte N-Termini in Richtung des ER-Lumens ausgerichtet sind (83). In nicht-gestressten Zellen bindet BiP, ein HSP70-Chaperon, an ATF6α sowie PERK und IRE1α. Dadurch werden z.B. PERK und IRE1α in einem inaktiven monomeren Zustand gehalten (84, 85). Bei verstärkter Bindung von BiP an fehlgefaltete Proteine wird BiP sowohl von PERK als auch von IRE1α freigesetzt, was zu einer (indirekten) Aktivierung der beiden Kinasen durch Oligomerisierung und Trans(auto)phosphorylierung führt (86-88). ATF6a wird nach der Dissoziation von BiP proteolytisch gepalten und agiert als Transkriptionsfaktor im Zellkern (89).

Die daraufhin angeschalteten Zielgene der UPR können mit Proteinfaltung, ERAD, oxidativem Stress, Autophagie, mitochondrialer Dysfunktion und Stoffwechselwegen in Zusammenhang gebracht werden (90).
ER-Stress kann durch eine Vielzahl an Faktoren ausgelöst werden. Dazu zählt auch die Infektion durch verschiedene Pathogene inklusive CoVs (91).

3.2.2. Thapsigargin, ein chemischer ER-Stress-Induktor und pan-coronaviraler Inhibitor

Obwohl auch CoVs im Zuge ihrer Replikation ER-Stress induzieren, konnten wir zeigen, dass der pharmakologische ER-Stress- und UPR-Induktor **Thapsigargin** eine dosisabhängige antivirale Wirkung auf die Replikation von CoVs ausübt. Thapsigargin ist ein nichtkompetitiver Inhibitor der Ca^{2+}-ATPase des sarko- bzw. endoplasmatischen Retikulums (SERCA) und wird aus der Pflanze *Thapsia garganica* gewonnen (92). Thapsigargin reduzierte die virale Replikation von drei verschiedenen CoVs (HCoV-229E, MERS-CoV und SARS-CoV-2) in einem niedrigen nanomolaren Bereich in vier verschiedenen Zelltypen, darunter auch in differenzierten menschlichen Bronchialepithelzellen (93).
Es konnte auch gezeigt werden, dass Thapsigargin die HCoV-229E-Replikation in Huh-7- und MRC-5-Zellen (Abb. 5A-C) reduzierte und so die BiP- und IRE1α-Spiegel wiederhergestellt werden konnten (Abb. 5C). Darüber hinaus wurde die antivirale Wirkung von Thapsigargin auf MERS-CoV-infizierten Huh-7-Zellen (Abb. 5D/E) und auf SARS-CoV-2-infizierten Vero E6-Zellen analysiert (Abb. 5F/G). Dabei wurde die Replikation von MERS-CoV und SARS-CoV-2 mit einer EC_{50} von 4,8 bzw. 260 nM unterdrückt. Dies ergab Selektivitätsindizes (SI, CC_{50}/EC_{50}) von 1229 für MERS-CoV bzw. 70 (bestimmt mittels MTT Assay) bis 78 (bestimmt mittels ATPlite Assay) für SARS-CoV-2 (93).

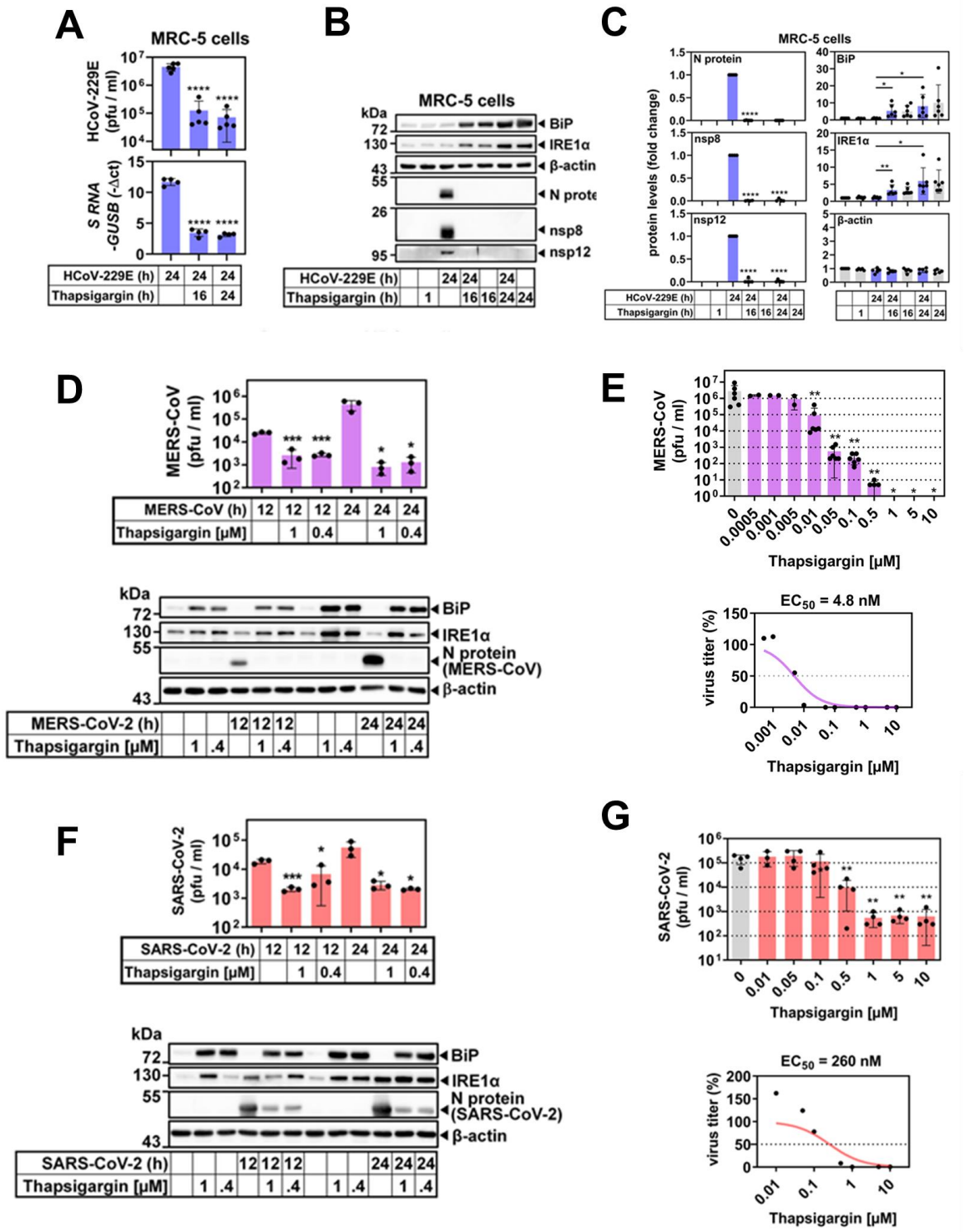

Abbildung 5 *Hemmung der CoV-Replikation durch Thapsigargin. (A-C) Humane embryonale MRC-5-Lungenfibroblasten wurden mit HCoV-229E infiziert und (A) die korrespondierenden Virustiter (oberes Diagramm, fünf biologisch unabhängige Experimente) und die Expression viraler S-Gen-kodierender RNAs (unteres Diagramm, vier biologisch unabhängige Experimente) ermittelt. (B+C) Expression von Virus- und Wirtszellproteinen. (B) zeigt einen repräsentativen Immunoblot von Gesamtzellextrakten und (C) die Quantifizierung aus mindestens vier biologisch unabhängigen Experimenten. (D-G) Infektion von Huh-7-Zellen oder Vero E6-Epithelzellen mit MERS-CoV (MOI = 0,5; D+E) oder SARS-CoV-2 (MOI = 0,5. F+G) für 12 h oder 24 h in Gegenwart/Abwesenheit von 0,4 μM oder 1 μM Thapsigargin. (D+F) Virale Titer und repräsentative Bilder der entsprechenden Expression von MERS-CoV/SARS-CoV-2-Nukleokapsid- (N) bzw. Wirtszellproteinen (drei biologisch unabhängige Experimente). (E) Dosisabhängige Inhibition der MERS-CoV-2-Replikation durch Thapsigargin in Huh-7-Zellen, die mit einer MOI von 0,5 infiziert wurden (oberes Diagramm, zwei oder mehr biologisch unabhängige Experimente) und die geschätzte EC_{50}-Konzentration, die aus den Mittelwerten berechnet*

*wurde (unteres Diagramm). (G) Dosisabhängige Unterdrückung der SARS-CoV-2-Replikation durch Thapsigargin in Vero E6-Zellen, die mit einer MOI von 0,5 infiziert wurden (obere Grafik, drei oder mehr biologisch unabhängige Experimente) und die geschätzte EC_{50}-Konzentration aus den Mittelwerten (untere Grafik). Alle Balkendiagramme zeigen Mittelwerte ± s.d.; Sternchen kennzeichnen p-Werte (*p ≤ 0,05, **p ≤ 0,01, ***p ≤ 0,001, ****p ≤ 0,0001), die durch zweiseitige ungepaarte t-Tests ermittelt wurden. Abbildung modifiziert nach Shaban et al., 2021.*

3.2.3. Thapsigargin blockiert die CoV-Replikation ex vivo

Um diese Beobachtungen in einem physiologisch relevanteren System zu bestätigen, wurden Zellkulturen von differenzierten normalen menschlichen Bronchialepithelzellen (NHBE) angelegt (94). Nach der anfänglichen Expansion wurden die Zellen unter *Air/liquid-interface*-Konditionen in verschiedene Atemwegszelltypen differenziert. Dies wurde durch Fluoreszenzmikroskopie unter Verwendung von geeigneten Antikörpern zum Nachweis von *tight junctions* und Markerproteinen, die für Becher-, Flimmer- bzw. Basalzellen spezifisch sind, validiert (Abb. 6A/B). Wie in Abb. 6C gezeigt, hemmte Thapsigargin die Replikation aller drei CoVs (HCoV-229E, MERS-CoV, SARS-CoV-2) in NHBE-Zellen, die von verschiedenen Spendern stammten, dosisabhängig. Die Lebensfähigkeit der Zellen nach der Thapsigargin-Behandlung (beurteilt durch Messung der Integrität der Epithel-Monolayer mittels TEER) lag nach 72 Stunden zwischen 70 und 80 % (93). Ähnlich wie bei den zuvor verwendeten Zelllinien erwies sich SARS-CoV-2 als etwas weniger empfindlich gegenüber der Behandlung mit Thapsigargin. Wichtig ist jedoch, dass in Gegenwart von 1 µM Thapsigargin bei keinem der drei CoVs zu späteren Zeitpunkten p.i. infektiöse Viruspartikel nachweisbar waren (Abb. 6C).

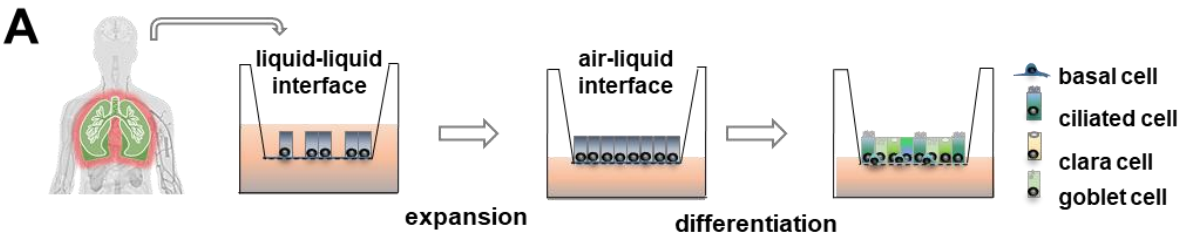
A
liquid-liquid interface
air-liquid interface
expansion
differentiation
basal cell
ciliated cell
clara cell
goblet cell

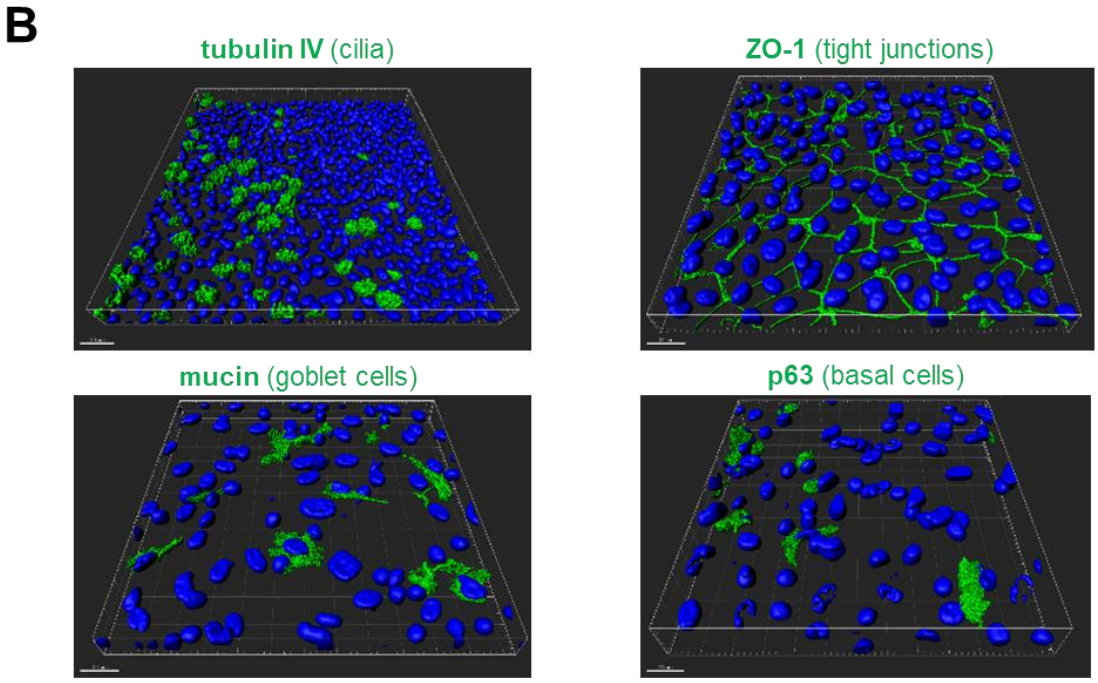
B
tubulin IV (cilia)
ZO-1 (tight junctions)
mucin (goblet cells)
p63 (basal cells)

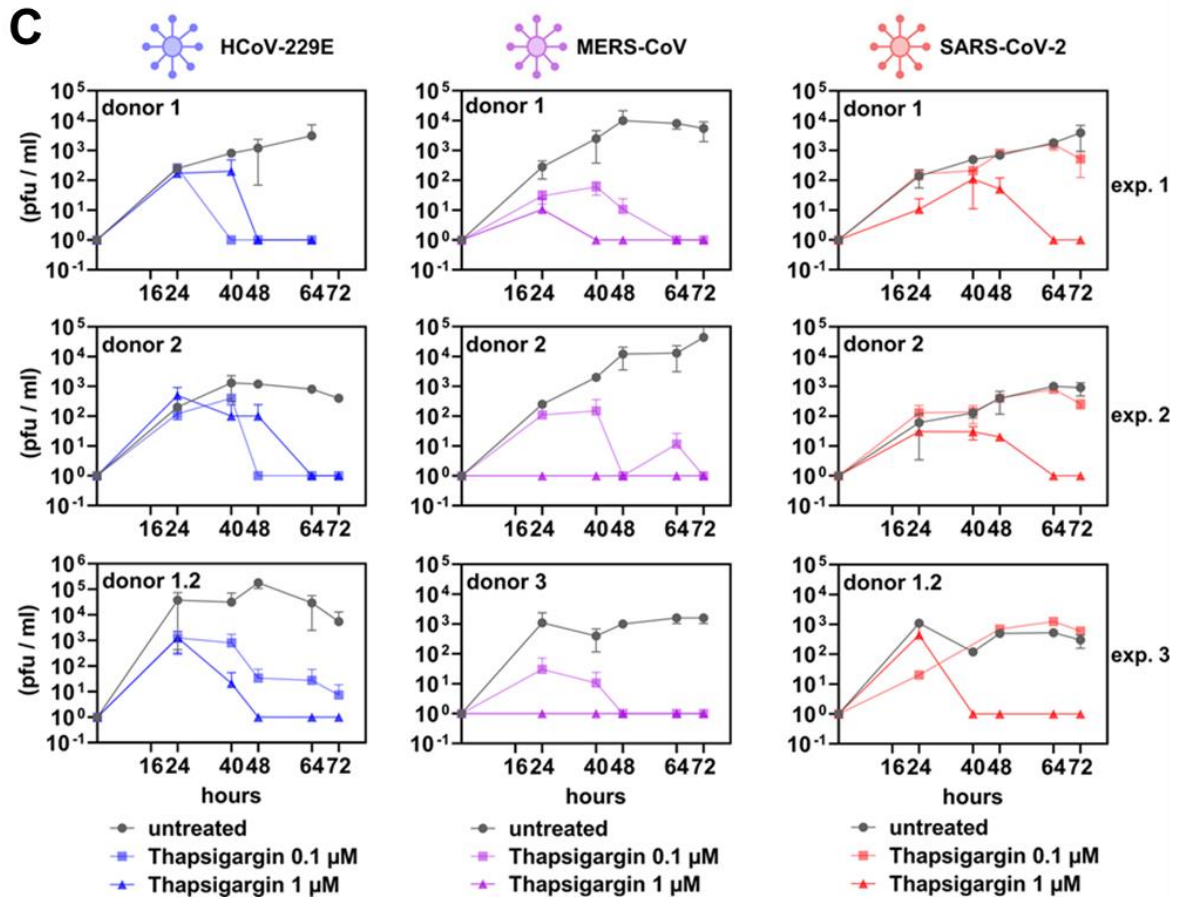
C
HCoV-229E
MERS-CoV
SARS-CoV-2
donor 1
donor 2
donor 1.2
donor 3
exp. 1
exp. 2
exp. 3
(pfu / ml)
hours
untreated
Thapsigargin 0.1 µM
Thapsigargin 1 µM

Abbildung 6 *Hemmung der CoV-Replikation durch Thapsigargin in primären NHBEs. (A) Schematische Darstellung der Expansion in einer Liquid/liquid-Interphase (LLI) und die anschließende Differenzierung in einer Air/liquid-Interphase (ALI) normaler menschlicher Bronchialepithelzellen (NHBE). (B) Dreidimensionale Rekonstruktion der Immunfluoreszenzanalyse (z-Stapel) repräsentativer NHBE-Zellen, die mit spezifischen Antikörpern gegen die angegebenen Differenzierungsmarker gefärbt wurden. (C) NHBE-Zellen wurden unbehandelt gelassen oder mit dem jeweils angegebenen CoV (MOI = 3) infiziert und bis zu drei Tage lang mit Thapsigargin (0,1 oder 1 µM) behandelt. Die Überstände wurden zu fünf Zeitpunkten p.i. gesammelt und die Virustiter mittels Plaque-Assays bestimmt. Die Daten repräsentieren drei biologisch unabhängige Experimente mit NHBE-Zellen, die von zwei bzw. drei unabhängigen Spendern stammen. Dargestellt sind Mittelwerte ± s.d. von technischen Duplikaten. Für HCoV-229E und MERS-CoV wurden die Zellen von Spender 1 ein zweites Mal ausplattiert und differenziert, um ein zusätzliches unabhängiges Experiment durchzuführen (bezeichnet als Spender 1.2). Abbildung modifiziert nach Shaban et al., 2021.*

3.2.4. Molekularer Wirkmechanismus von Thapsigargin

Die antiviralen Wirkmechanismen von Thapsigargin liegen auf unterschiedlichen Ebenen.

Generell führen CoVs zu einem sogenannten *host cell shut-off*, wodurch die zelluläre Proteinbiosynthese zu 90 % reduziert wird. Dieser Translationsstillstand wird durch die Gabe von Thapsigargin aufgehoben.

Zudem konnten wir anhand der durchgeführten Proteom-Studien keine Deregulierung einzelner, sondern vielmehr multipler Signalwege festgestellt werden. Diese tragen in der Summe wahrscheinlich zu einer schützenden Reaktion in infizierten Zellen bei. Bei genauerer Analyse induzierte die Gabe von Thapsigargin in CoV-infizierten Zellen die Expression von 120 Proteinen. Darunter befanden sich Faktoren, die intrazelluläre Membranprozesse (Vesikeltransport und -biogenese) und den ER-assoziierten Proteinabbau (ERAD, ERQC) regulieren. Ein Beispiel ist die starke Hochregulierung des zentralen ERAD-Faktors *homocysteine-responsive endoplasmic reticulum-resident ubiquitin-like domain member 1* (HERPUD1) sowie von Enzymen, welche an der Ubiquitinierung beteiligt sind (u.a. Ubiquilins). Des Weiteren zeigte sich auch eine starke Deregulierung des Autophagie-Adaptorproteins SQSTM1 (auch p62) unter Thapsigargin-Behandlung (93).

Dies deutet auf eine starke Herunterregulation der selektiven Autophagie nach einer Thapsigargin-Behandlung hin. Obwohl die Rolle von Autophagieprozessen für die coronavirale Replikation bislang nicht abschließend geklärt ist, deuten die vorliegenden Daten und weitere bereits publizierte Studien auf eine Stimulation der selektiven Autophagie zu bestimmten Zeitpunkten der coronaviralen Replikation hin (95, 96). Vermutlich werden Autophagieprozesse oder damit assoziierte Mechanismen zur Bildung der membranösen replikativen Organellen benötigt (97-99). Es konnte so unter anderem gezeigt werden, dass LC-3, ein Autophagosommarker, mit viralen

replikativen Organellen in SARS-CoV-infizierten Zellen kolokalisiert (95). Aus der Literatur ist unter anderem bekannt, dass Thapsigargin über einen bislang unbekannten Mechanismus auch die Fusion von Autophagosomen mit Lysosomen blockiert (100, 101). Es ist daher möglich, dass ein solcher Mechanismus die korrekte Fusion von Autophagosomen mit intrazellulären Vesikeln während des gesamten Replikationszyklus verhindert und so möglicherweise auch Membranfusionsereignisse, die für die Bildung der replikativen Organellen benötigt werden, unterbindet (8). Allerdings zeigen auch mehrere Studien, dass die Vermehrung von SARS-CoV und MHV nicht durch die Deletion wichtiger Autophagie-Faktoren wie ATG7 und ATG5, die für die Bildung von Autophagosomen essenziell sind, beeinflusst wird (102, 103). Dies könnte darauf hinweisen, dass die Bildung replikativer Organellen nicht unbedingt eine vollständig intakte Autophagiemaschinerie benötigt, sondern vielmehr (in Abhängigkeit vom jeweils beteiligten CoV) bestimmte Autophagie-Komponenten/Faktoren involviert sind (99, 104).

Zudem handelt es sich bei Thapsigargin um einen Inhibitor der SERCA-Ca^{2+}-Pumpe, wodurch ein Anstieg der zytoplasmatischen Ca^{2+}-Spiegel erzielt wird. Daher könnte der antivirale Mechanismus auch im Zusammenhang mit der Modulation zellulärer Ca^{2+}-Konzentrationen stehen (105). Eine kürzlich durchgeführte Studie konnte zeigen, dass Kalziumkanalblocker, die vielfältig in der Klinik als Blutdrucksenker (z.B. Amlodipin) verwendet werden, die Replikation von SARS-CoV-2 *in vitro* hemmen (106). Dies unterstreicht eine mögliche Bedeutung der Ca^{2+}-Signalwege für die virale Replikation und deren Bedeutung für zukünftige antivirale Medikamente.

Abschließend kann festgehalten werden, dass die durchgeführte bioinformatische Analyse der Massenspektrometrie-Daten und die weiteren Ergebnisse dieser Studie nur vorläufige Schlussfolgerungen zum genauen antiviralen Wirkmechanismus zulassen. Weitere mechanistische Studien sind erforderlich und sollten sich insbesondere auf die genaue Rolle von ER, UPR, ER-Stress, Autophagie, ERAD und die Beteiligung einzelner Faktoren wie SERCA in der Replikation von CoV konzentrieren. Hierbei könnten auch die pharmakologische oder genetische Manipulation weiterer einzelner Signalkomponenten (z.B. PERK) der oben genannten Signalwege wichtige Einblicke ermöglichen. Eine Mikroskopie-basierte (Ko-)Lokalisation dieser Komponenten könnte zudem hilfreich sein, deren mögliche

Beteiligung an der viralen Replikation zu validieren. Diese Studien könnte auch durch eine zeitabhängige Zugabe von Thapsigargin vor- bzw. nach der Infektion ergänzt werden (107, 108). Des Weiteren sind auch Passagierungsexperimente in Anwesenheit von Thapsigargin sinnvoll, um mögliche Resistenzentwicklungen zu untersuchen (107).

3.2.5. Ausblick: Thapsigargin

Die Ergebnisse der oben dargestellten Studie bieten neue und interessante Einblicke in die Beteiligung von ER- und UPR-Signalwegen an der coronaviralen Replikation. Im Ergebnis dieser Arbeiten konnte eine signifikante pan-anticoronavirale Wirkung des ER-Stress-Induktors Thapsigargin nachgewiesen werden (93).

Die Verwendung von Thapsigargin als Medikament in der Krebstherapie wird bereits seit vier Jahrzehnten untersucht (109). Zudem ist die Synthese und Herstellung von Thapsigargin gut etabliert (110). Jedoch stellt die zu erwartende *In-vivo*-Toxizität ein mögliches Hindernis für einen Einsatz als Medikament dar. Ermutigende Daten einer kurzfristigen Behandlungsoption zeigt jedoch eine Studie mit Influenzavirus-infizierten und Thapsigargin-behandelten Mäusen (111). Trotzdem sind weitere *In-vivo*-Daten erforderlich, um Pharmakokinetik, Wirksamkeit und Toxizität anhand von Tiermodellen umfassend bewerten zu können. Dazu gehört auch die Anwendung von Thapsigargin in geeigneten SARS-CoV-2-Tiermodellen.

Generell könnte eine systemische Thapsigargin-vermittelte Toxizität durch sehr niedrige Einzeldosen oder eine spezifische topische bzw. inhalative Anwendung adressiert werden. Alternativ könnte auch eine geeignete Prodrug entwickelt werden, bei der Thapsigargin und bestimmte Komponenten gekoppelt wird, welche die toxischen Nebenwirkungen begrenzen (112). So wurde beispielsweise Mipsagargin, eine inaktive Prodrug von Thapsigargin, entwickelt. Mipsagargin muss zunächst durch eine bestimmte gewebespezifische Protease gespalten werden, bevor der Wirkstoff aktiv wird. Hierbei maskiert ein Peptid die zytotoxische Aktivität, welches erst durch spezifisch in Prostatakarzinom-Zellen gebildete Proteasen abgespalten wird. Dadurch wird ein direkter und weitgehend spezifischer Effekt auf die Tumorzellen erzielt. Gegenwärtig befindet sich Mipsagargin in klinischen Phase-I/II-Studien zur Therapie des Prostatakarzinoms (113-116).

Ein ähnlicher Mechanismus wäre auch für Thapsigargin-Derivate, welche ausschließlich z.B. von viralen Proteasen gespalten werden, möglich. Durch diesen Mechanismus wäre die Freisetzung des Wirkstoffes auf Virus-infizierte Zellen beschränkt.

3.3. Wirtsgerichtete Virostatika: Rocaglate

Dieses Kapitel nimmt Bezug auf:

> ***Müller C****, Schulte FW*, Lange-Grünweller K, Obermann W, Madhugiri R, Pleschka S, Ziebuhr J, Hartmann RK, Grünweller A. Broad-spectrum antiviral activity of the eIF4A inhibitor silvestrol against corona- and picornaviruses. Antiviral Res. 2018 Feb;150:123-129. doi: 10.1016/j.antiviral.2017.12.010. Epub 2017 Dec 16. PMID: 29258862; PMCID: PMC7113723.*
>
> ***Müller C****, Obermann W*, Schulte FW, Lange-Grünweller K, Oestereich L, Elgner F, Glitscher M, Hildt E, Singh K, Wendel HG, Hartmann RK, Ziebuhr J, Grünweller A. Comparison of broad-spectrum antiviral activities of the synthetic rocaglate CR-31-B (-) and the eIF4A-inhibitor Silvestrol. Antiviral Res. 2020 Mar;175:104706. doi: 10.1016/j.antiviral.2020.104706. Epub 2020 Jan 10. PMID: 31931103; PMCID: PMC7114339.*
>
> ***Müller C****, Obermann W, Karl N, Wendel HG, Taroncher-Oldenburg G, Pleschka S, Hartmann RK, Grünweller A, Ziebuhr J. The rocaglate CR-31-B (-) inhibits SARS-CoV-2 replication at non-cytotoxic, low nanomolar concentrations in vitro and ex vivo. Antiviral Res. 2021 Feb;186:105012. doi: 10.1016/j.antiviral.2021.105012. Epub 2021 Jan 8. PMID: 33422611; PMCID: PMC7791309.*
>
> *Obermann W, Friedrich A, Madhugiri R, Klemm P, Mengel JP, Hain T, Pleschka S, Wendel HG, Hartmann RK, Schiffmann S, Ziebuhr J,* ***Müller C****, Grünweller A*. Rocaglates as Antivirals: Comparing the Effects on Viral Resistance, Anti-Coronaviral Activity, RNA-Clamping on eIF4A and Immune Cell Toxicity. Viruses. 2022 Mar 3;14(3):519. doi: 10.3390/v14030519. PMID: 35336926; PMCID: PMC8950828.*

3.3.1. Der zelluläre Translationsinitationsfaktor eIF4a als antivirale Zielstruktur

Die zelluläre DEAD-Box-RNA-Helikase eIF4A ist eine Schlüsselkomponente des zellulären eukaryotischen Translationsinitiationskomplexes eIF4F, welche für das Aufwinden stabiler RNA-Sekundärstrukturen und die Einleitung der Translation benötigt wird (Abb. 7). Natürliche und synthetische **Rocaglate** gehören zu einer gut etablierten Verbindungsklasse von Inhibitoren des eIF4A (117). Diese Stoffgruppe von

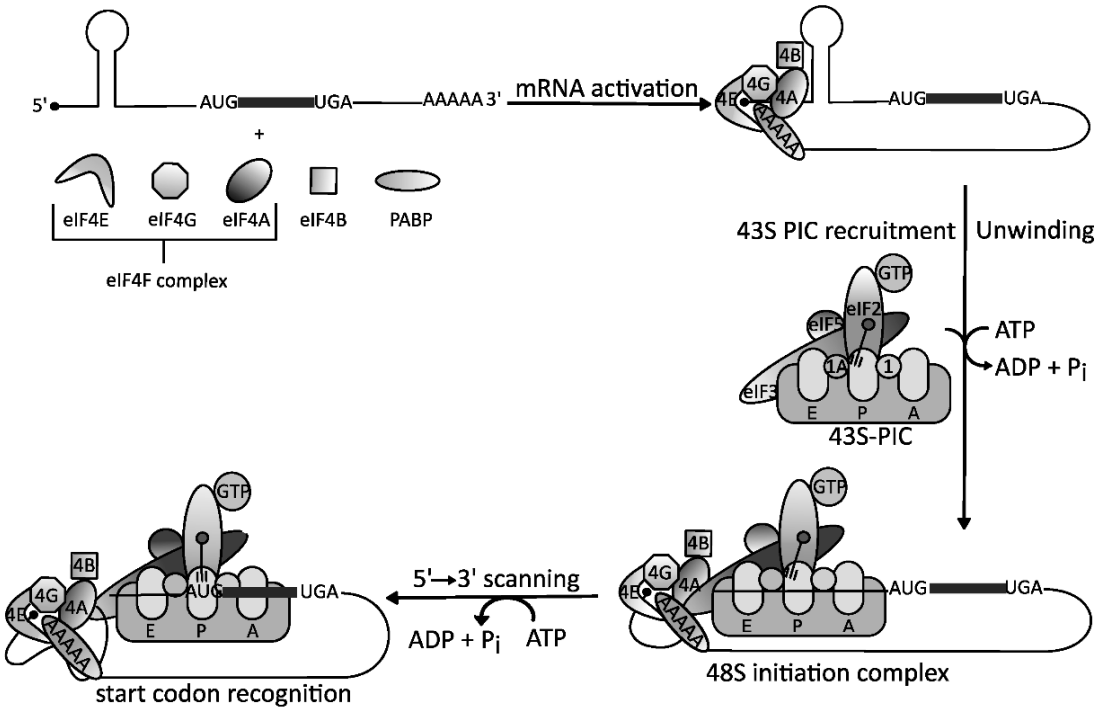

Abbildung 7 *Schematische Darstellung des eukaryotischen Translationsinitiationsmechanismus. Auf die Bindung des heterotrimeren eIF4F-Komplexes an die 5'-Cap-Struktur von mRNAs folgt die Aufspaltung stabiler RNA-Sekundärstrukturen durch die DEAD-Box-RNA-Helikase eIF4A. Dies ermöglicht die Bindung des 43S-Präinitialkomplexes, der die 5'-untranslatierten Regionen (5'-UTRs) abtastet, um das Startcodon AUG zu identifizieren. Abbildung modifiziert nach Taroncher-Oldenburg et al.. 2021.*

Flavaglinen weist eine charakteristische Cyclopenta[b]benzofuranstruktur auf. Im Allgemeinen klammern Rocaglate reversible mRNAs mit stark strukturierten 5'-UTRs an die Oberfläche von eIF4A und beeinträchtigen dadurch die Translation (Abb. 8). Die Wirkung beschränkt sich dabei vor allem auf die Translation stark strukturierter (und dadurch eIF4A-abhängiger) viraler mRNAs. Es gibt jedoch auch einige zelluläre mRNAs, die stabile RNA-Sekundärstrukturen und/oder Polypurin-haltige Sequenzabschnitte in ihren 5'-UTRs besitzen und deshalb eine erhöhte eIF4A-Abhängigkeit aufweisen. Die Wirkung von Rocaglaten beschränkt sich vermutlich auf etwa 300 zelluläre mRNAs, darunter eine Vielzahl protoonkogener mRNAs mit langen, strukturierten 5'-UTRs (118, 119). Aus diesem Grund und wegen ihres günstigen Sicherheitsprofils werden Rocaglate seit Jahrzehnten als potentielle Krebsmedikamente untersucht und weiterentwickelt (120-123).

Neben einigen protoonkogenen mRNAs besitzen auch eine Vielzahl von RNA-Viren umfangreiche RNA-Sekundärelemente in den viralen 5’-UTRs (124). Daher ist die Initiation der Translation viraler Proteine oftmals abhängig von der eIF4A-Aktivität (125). Diese Hypothese wird im folgenden Abschnitt näher analysiert und diskutiert.

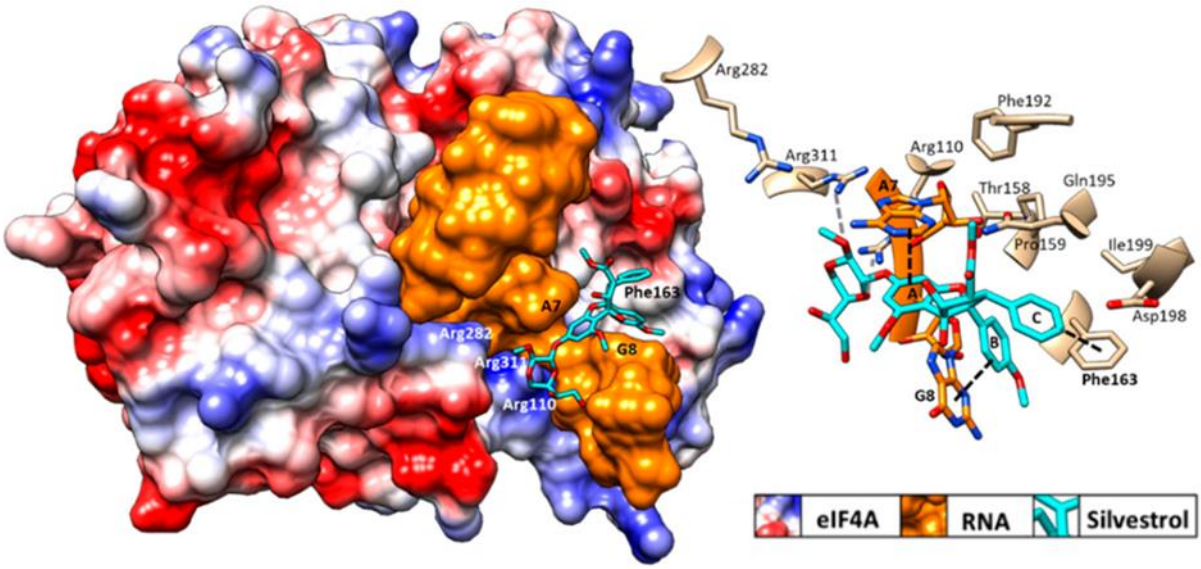

Abbildung 8 *Strukturbasierte Computermodellierung von Silvestrol und seiner Bindung an einen eIF4A-RNA-Komplex (PDB: 5ZC9). Der Dioxan-Anteil von Silvestrol bindet zusätzliche Argininresten auf der Oberfläche von eIF4A und kann so eine Brücke über das RNA-Substrat schlagen, um die RNA fest an eIF4A zu binden. UCSF (University of California, San Francisco) Chimera wurde für die grafische Darstellung und elektrostatische Oberflächenfärbung von eIF4A verwendet (blau: positiv geladen, rot: negativ geladen). Abbildung modifiziert nach Taroncher-Oldenburg et al., 2021.*

3.3.2. Antivirale Breitbandwirkung von Rocaglaten

In den letzten Jahren untersuchten wir eingehend die hemmende Wirkung von eIF4A-Inhibitoren auf die (corona)virale Replikation (126-129). In diesem Zusammenhang konnten wir erstmals bestätigen, dass eine pharmakologische eIF4A-Inhibition die *In-vitro*-Translation verschiedener (Reportergen-)mRNAs mit hochstrukturierten viralen 5'-UTRs unterdrücken (126-128). In Übereinstimmung mit diesen Daten konnte die Replikation verschiedener RNA-Viren, die strukturierte 5'-UTRs enthalten, dosisabhängig beeinträchtigt werden (126-134) (Abb. 9). Hierbei wurde das natürliche Rocaglat Silvestrol sowie das synthetische Rocaglat CR-1-31-B (auch CR-31-B (-)) verwendet. Beide Rocaglate weisen eine vergleichbare Wirksamkeit im nanomolaren Bereich auf (127, 128) (Abb. 9).

Dies ist vor allem deshalb von Bedeutung, weil das natürlich vorkommende Rocaglat Silvestrol nicht in kommerziell herstellbaren Mengen aus der Aglaia-Pflanze gewonnen werden kann. Zudem ist eine synthetische Herstellung von Silvestrol sehr zeit- und kostenaufwendig (135, 136). Daher wurde im weiteren Verlauf der hier dargestellten Arbeiten bevorzugt das strukturell vereinfachte Analog CR-1-31-B verwendet (127).

virus	virus family	cell system	Silvestrol		CR-1-31-B		citation
			CC_{50}	EC_{50}	CC_{50}	EC_{50}	
EBOV	*Filoviridae*	human macrophages	90.5	2	n.d.	n.d.	Biedenkopf et al., 2017
LASV	*Arenaviridae*	murine hepatocytes	>5000	50.73	>5000	36.11	Müller et al., 2020
CCHFV	*Nairoviridae*	murine hepatocytes	>5000	28.53	>5000	20.04	Müller et al., 2020

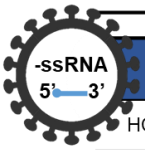

virus	virus family	cell system	Silvestrol		CR-1-31-B		citation
			CC_{50}	EC_{50}	CC_{50}	EC_{50}	
HCoV-229E	*Coronaviridae*	MRC-5	>10000	3	>5000	2.88	Müller et al., 2018; 2020
MERS-CoV	*Coronaviridae*	MRC-5	>10000	1.3	>5000	1.87	Müller et al., 2018; 2020
SARS-CoV-2	*Coronaviridae*	Vero E6	n.d.	n.d.	>100	1.82	Müller et al., 2021
CHIKV	*Togaviridae*	293T	>100	1.89	n.d.	n.d.	Henss et al., 2018
HEV (replicon system)	*Hepeviridae*	Huh 7.5	>100	4-6.6	n.d.	n.d.	Todt et al., 2018
ZIKV	*Flaviviridae*	A549	9.42	1.08	19.34	1.13	Müller et al., 2018

virus	virus family	cell system	Silvestrol		CR-1-31-B		citation
			CC_{50}	EC_{50}	CC_{50}	EC_{50}	
PV	*Picornaviridae*	MRC-5	>10000	20	n.d.	n.d.	Müller et al. 2018
HRV	*Picornaviridae*	MRC-5	>10000	100	n.d.	n.d.	Müller et al. 2018

Abbildung 9 *Zytotoxische Konzentration 50 (CC_{50}) und wirksame Konzentration 50 (EC_{50}), ermittelt für Zellen, die mit dem natürlichen (Silvestrol) oder synthetischen (CR-1-31-B) Rocaglat behandelt und mit dem angegebenen Virus infiziert (EC_{50}) wurden bzw. uninfiziert blieben (CC_{50}). Die Werte sind als nanomolare Konzentrationen angegeben. EBOV: Ebola-Virus; LASV: Lassa-Fieber-Virus; CCHFV: Hämorrhagisches Krim-Kongo-Fieber-Virus; HCoV-229E: Humanes Coronavirus 229E; MERS-CoV: Middle East respiratory syndrome Coronavirus, CHIKV: Chikungunya-Virus; HEV: Hepatitis-E-Virus; ZIKV: Zika-Virus; PV: Poliovirus; HRV: Humanes Rhinovirus. Abbildung modifiziert nach Taroncher-Oldenburg et al., 2021.*

Insbesondere konnten wir zeigen, dass natürliche und synthetische Rocaglate die Replikation von HCoV-229E, MERS-CoV und SARS-CoV-2 bereits in einem niedrigen nanomolaren Bereich reduzierten, während die zytotoxischen Konzentrationen in den in dieser Studie verwendeten Zellsystemen im mikromolaren Bereich lagen (126-128) (Abb. 9). Dies führt zu hohen Selektivitätsindizes von bis zu 1000 und weist auf ein breites therapeutisches Fenster für eine Anwendung dieser Verbindungen hin. Außerdem wurde die Replikation aller drei CoVs in primären NHBEs dosisabhängig und ohne größere Zytotoxizität gehemmt (126, 127) (Abb. 10).

Anhand dieser Daten kann von einer Zelltyp-unabhängigen, pan-anticoronaviralen Aktivität ausgegangen werden.

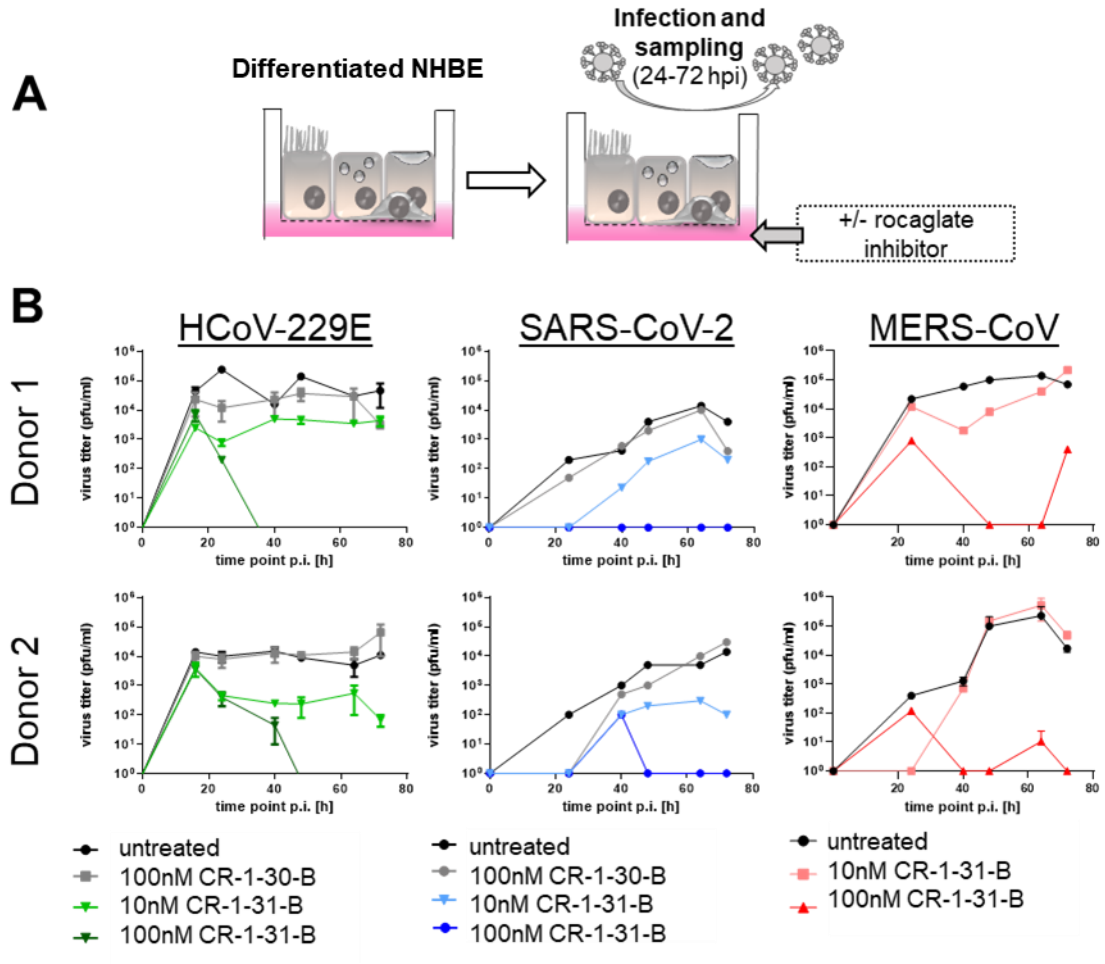

Abbildung 10 *Wachstumskinetik von drei verschiedenen CoVs (HCoV-229E (grün), SARS-CoV-2 (blau) und MERS-CoV (rot)) in differenzierten NHBEs, die mit den angegebenen Konzentrationen des synthetischen Rocaglates CR-1-31-B aus dem basalen Kompartiment infiziert und behandelt wurden (A). Als Kontrolle wurden NHBEs, die mit dem jeweiligen Virus infiziert waren, unbehandelt gelassen (schwarze Linie) oder mit dem inaktiven Enantiomer von CR-1-31-B behandelt, das als CR-1-30-B dargestellt ist (graue Linie). (B) Virale Titer wurden mittels Plaque-Assay für die angegebenen Zeitpunkte p.i. bestimmt.*

3.3.3. Resistenzentwicklung in Gegenwart von Rocaglaten

In einer weiteren Studie untersuchten wir eine mögliche Medikamenten-Resistenzentwicklung von CoVs gegenüber Rocaglaten anhand des saisonalen HCoV-229E (137). Hierbei wurde HCoV-229E in Anwesenheit steigender Konzentrationen von Rocaglaten passagiert und im Anschluss die passagierten Viruspopulationen im Vergleich zum Ausgangsvirus auf (**i**) mögliche Mutationen und (**ii**) eine möglicherweise geänderte Sensitivität gegenüber Rocaglaten nach Passagierung in Rocoglat-haltigen Medien untersucht (Abb. 11A). In dem dafür gewählten experimentellen Set-Up konnten keine Resistenzmutationen detektiert werden (Abb. 11B). Zudem konnte keine gesteigerte Empfindlichkeit gegenüber den verwendeten Rocaglaten beobachtet werden (Abb. 11C). Dies deutet auf eine hohe

genetische Barriere für Fluchtmutationen gegen antivirale Wirkstoffe hin, die auf das Wirtsprotein eIF4A abzielen (137).

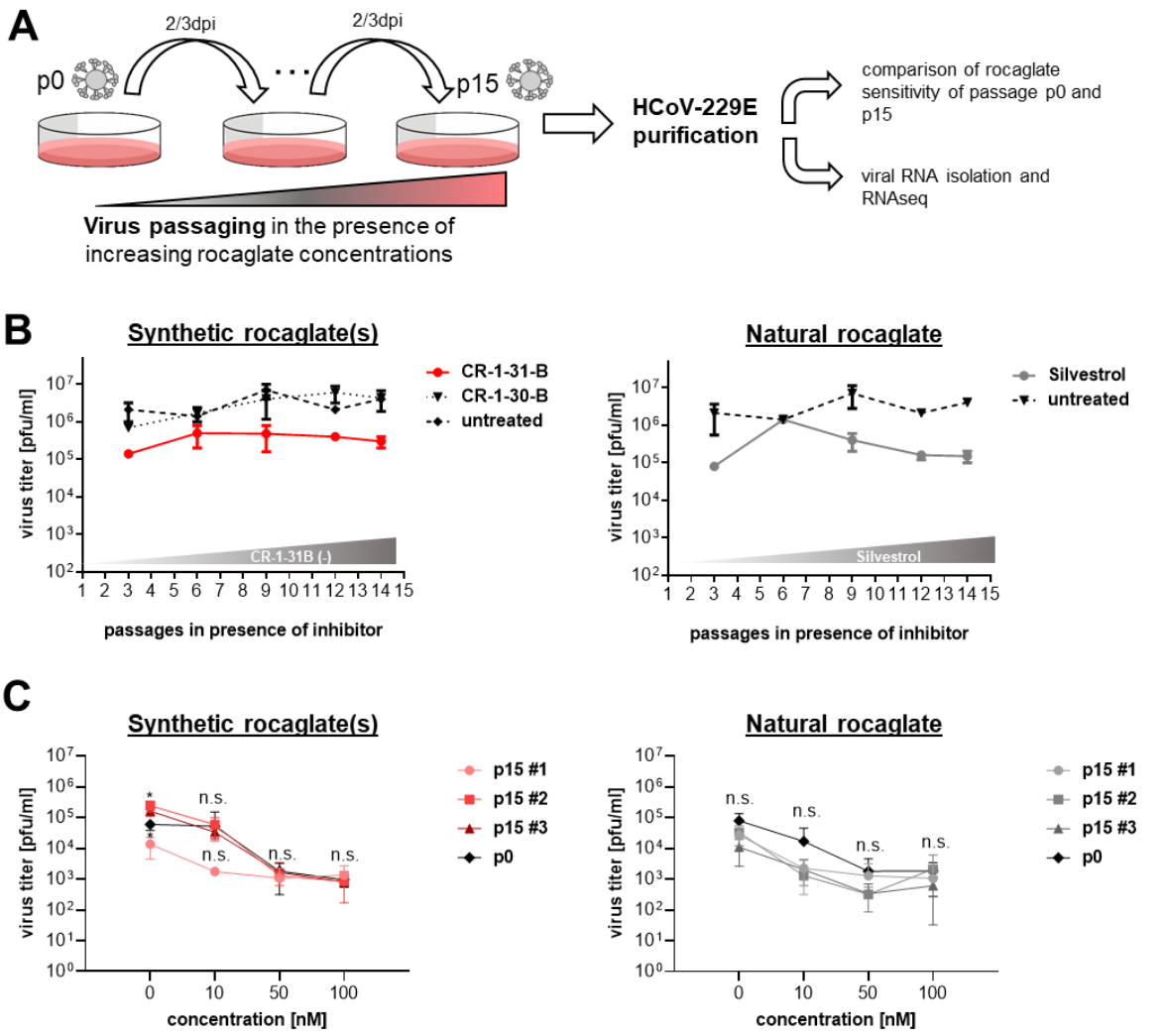

Abbildung 11 *Passage von HCoV-229E in Gegenwart steigender Konzentrationen von Silvestrol oder CR-1-31-B. (A) Schematische Darstellung des experimentellen Ablaufs. (B) MRC-5-Zellen wurden, wie in (A) gezeigt infiziert und behandelt, und die Virustiter im Überstand wurden mittels Plaque-Assay bestimmt (n = 3). (C) MRC-5-Zellen wurden mit HCoV-229E von p0 (nicht passagiert) bis p15 (seriell passagiert, wie in Tafel (B) gezeigt) mit einer MOI von 0,1 infiziert und 24 Stunden lang entweder mit den angegebenen Konzentrationen von CR-1-31-B oder Silvestrol behandelt oder für den gleichen Zeitraum unbehandelt gelassen. Die Virustiter wurden dann mittels Plaque-Assays bestimmt (n = 3). Die Signifikanzniveaus im Vergleich zu p0 wurden mit dem ungepaarten t-Test ermittelt und sind wie folgt angegeben: *: p < 0,05; n.s.: nicht signifikant. Fehlerbalken zeigen SD. Abbildung modifiziert nach Obermann et al., 2021.*

3.3.4. Ausblick: Rocaglate

Die RNA-Helikase eIF4A ist in der Krebsforschung ein vielfach charakterisiertes und erfolgversprechendes Zielmolekül (138), während sie in der Entwicklung von antiviralen Wirkstoffen bisher nur wenig Beachtung fand.

Insgesamt zeigt das Spektrum der hier dargestellten eIF4A-abhängigen, Rocaglat-sensitiven RNA-Viren das Potenzial dieser Verbindungsklasse als Breitband-Virostatikum. Eine gute Wirksamkeit gegen neu- oder wiederauftretende RNA-Viren kann deshalb auch für Erreger zukünftiger Ausbrüche als wahrscheinlich gelten. Zudem konnte die antivirale Aktivität von Rocaglaten bereits in Hepatitis-E-Virus-infizierten Mäusen *in vivo* bestätigt werden (133). Die inzwischen verfügbaren Daten liefern in ihrer Gesamtheit zahlreiche Hinweise dafür, dass eIF4A für die Replikation einer Vielzahl von Viren unerlässlich ist und somit als geeignete Zielstruktur für antiviral wirksame Verbindungen genutzt werden kann (125, 139).

Die erfolgreiche Weiterentwicklung solcher Verbindungen als antivirale Therapeutika ist jedoch an eine Reihe weiterer experimenteller, finanzieller, klinischer und regulatorischer Herausforderungen gebunden. Dazu zählen Studien zur Bestimmung der Absorptions-, Verteilungs-, Stoffwechsel-, Eliminations- und Toxizitätseigenschaften (*absorption, distribution, metabolism, elimination, and toxicity*, ADMET) eines Wirkstoffs im Zusammenhang mit einem geeigneten Tiermodell (140).

Erste Studien zu den pharmakokinetischen Eigenschaften des natürlichen Rocaglates Silvestrol zeigten bei intraperitonealer Verabreichung eine 100 %ige systemische Verfügbarkeit in Leber, Milz und Niere (jedoch nicht im Gehirn). Allerdings lag die Bioverfügbarkeit (Absorptionsrate am Wirkort) unter 2 %. Bei einer intravenösen Gabe betrug die Plasmastabilität etwa 75 % (141). Zudem wurden für das synthetische Rocaglat CR-1-31-B im onkologischen Kontext bereits eine Vielzahl von Parametern zur Genotoxizität, Absorption, Metabolisierung und Bioverfügbarkeit erhoben (142). Da es sich bei CR-1-31-B jedoch um ein *public domain molecule* handelt, ist der Handlungsfreiraum für eine weitere klinische Entwicklung in Zukunft eingeschränkt. Im Rahmen der SARS-CoV-2-Pandemie 2020 wurde allerdings interessanterweise erstmals ein weiteres synthetisches Rocaglat mit dem Namen **Zotatifin** (eFT226) als Virostatikum in COVID-19-Patienten klinisch erprobt (Clinicaltrials.gov; Identifier NCT04632381, (120)). Zotatifin befindet sich zum einen in einer klinischen Phase-1/2-Studie gegen fortgeschrittene Erkrankungen mit soliden Tumoren (Clinicaltrials.gov; Identifier NCT04092673) (143), zum anderen wurde eine klinische Phase-1b-Studie in Patienten mit mildem COVID-19-Verlauf durchgeführt. Hierbei wurde in einer doppelblinden, randomisierten, placebokontrollierten Dosissteigerungsstudie 27

SARS-CoV-2-positiven Patienten 0,01-0,035 mg/kg Zotatifin subkutan verabreicht. Die verabreichte Dosis wurde laut Angaben des Herstellers *Effector Therapeutics* gut vertragen und ein antiviraler Effekt konnte nachgewiesen werden (144). Somit wurde der Grundstein für die weitere Entwicklung von Rocaglaten als potenzielle antivirale Medikamente gelegt. Anhand der geringen verabreichten Wirkstoffkonzentrationen kann jedoch eine starke antivirale Wirkung im Zielgewebe der Virusinfektion bezweifelt werden. Daher würde sich auch hier eine Verabreichung hoher Einzeldosen als Aerosol für die Zukunft anbieten.

Generell bietet die Verabreichung von antiviralen Arzneimitteln mittels Inhalation mehrere Vorteile gegenüber herkömmlichen (oralen oder intravenösen) Therapien. Dazu gehören (**i**) die Vermeidung des leberspezifischen *first-pass* Effekts, (**ii**) ein schnelles Einsetzen hoher lokaler Wirkstoffkonzentrationen im Zielgewebe der Lunge und (**iii**) minimale systemische Nebenwirkungen. Obwohl die Inhalation von Aerosolen eine attraktive Option bietet, müssen dabei eine Vielzahl pharmakokinetischer und pharmakodynamischer Parameter berücksichtigt werden. Dazu gehören u.a. die Formulierung, Stabilität, Deposition, Absorption, Zytotoxizität und antivirale Wirksamkeit der verwendeten Wirkstoffe.

Um diese Parameter im Einklang mit dem 3R-Prinzip (*reduction, replacement, refinement* von Tierversuchen) zu optimieren, ist gegenwärtig geplant, zukünftig das *Ex-vivo*-Atemwegsepithelmodell mit dem *In-vitro*-Verneblersystem ALICE-CLOUD (Air-Liquid Interface Cell Exposure-Cloud; Vitrocell®) (145, 146) zu nutzen.
Die so generierten Daten sollen klären, ob und wie vernebelte antivirale Wirkstoffe die Replikation von respiratorischen Viren (insbesondere SARS-CoV-2) in den Atemwegen hemmen können. Zudem dienen diese als Grundlage für weiterführende Tierstudien.

4. Zusammenfassung und Ausblick

Seit Beginn der SARS-CoV-2-Pandemie wurden eine Vielzahl potentiell anticoronaviral wirksamer Verbindungen untersucht und einige auch zu Medikamenten weiterentwickelt und zur Therapie zugelassen. Hierbei bilden vor allem Paxlovid und Remdesivir die Hauptsäulen der antiviralen Therapie. Beide Medikamente haben jedoch gewisse Limitierungen, die ihren Einsatz bei bestimmten Patientengruppen und klinischen Konstellationen einschränken.

Im Zuge der hier vorgestellten Arbeiten sind drei weitere mögliche antivirale Therapiestrategien gegen SARS-CoV-2 (und weitere Viren) untersucht worden:

1) DAA: **AS-circRNA,** welche speziell auf die 5‘-*leader*-Region der SARS-CoV-2-5‘-UTR abzielt und somit effizient die Replikation von SARS-CoV-2 unterdrückt.
2) HDA: **Thapsigargin**, ein ER-Stress-Modulator, welcher im nM-Bereich die Replikation von drei verschiedenen CoVs inhibiert.
3) HDA: **Rocaglate**, welche als eIF4A-Inhibitoren als Breitband-Virostatikum eingesetzt werden könnten, da sie effizient die Replikation des Ebolavirus, Zikavirus, Chikungunyavirus, Krim-Kongo-Fieber-Virus, Lassavirus, Hepatitis-E-Virus und verschiedener CoVs hemmen.

Alle ausgewählten Wirkstoffkandidaten wurden in der präklinischen experimentellen Phase eingehend auf ihre Wirksamkeit speziell gegen CoVs untersucht. Alle drei Ansätze zeigten hierbei vielversprechende Wirksamkeiten *in vitro* und *ex vivo*.
Trotz der Fülle vielversprechender präklinischer Daten in unterschiedlichen Zellkultursystemen können diese Systeme die tatsächlichen komplexen Wechselwirkungen von Viren mit einem infizierten Organismus nur teilweise abbilden (147). Zudem können Wirkstoffeigenschaften wie Bioverfügbarkeit, Serumkonzentrationen, Halbwertszeiten und Zugänglichkeit zum Zielgewebe nach systemischer oder topischer Applikation nur *in vivo* beurteilt werden. Daher sind zusätzliche *Proof-of-concept*- und PK/PD-Studien *in vivo* in geeigneten Tiermodellen notwendig, um die vorgeschlagenen Ansätze in Zukunft weiterentwickeln zu können (148).

Hierbei ist auch die richtige Wahl des Modellorganismus für das jeweilige Virus von besonderer Bedeutung (149). Für SARS-CoV-2 stehen unter anderem diverse Maus-, Hamster- und Frettchen-Modellen zur Verfügung (148-152).

Letztendlich ist jedoch für die Bewertung der antiviralen Wirksamkeit die Nutzung von mindestens zwei Tiermodellen, einschließlich nichtmenschlicher Primaten, ratsam (149). Obwohl der Umgang mit nichtmenschlichen Primaten unter BSL-3-Bedingungen sehr aufwendig und kostenintensiv ist, stellen diese ein unentbehrliches Modell für die Prüfung therapeutischer Wirkstoffe (wie am Beispiel von Remdesivir (153) und Molnupiravir (154) gezeigt) vor dem Eintritt in klinische Studien dar.

Aus diesen Gründen ist eine genaue Planung und Durchführung der nächsten Schritte unabdingbar. Um eine erfolgreiche Übertragung der grundlagenwissenschaftlichen Erkenntnisse der hier vorgelegten Arbeit in Zukunft zu gewährleiten, ist eine Zusammenarbeit mit einer Produktentwicklungs-Infrastruktur notwendig. Diese unterstützt aktiv die Überführung in die klinische Anwendung. Hierzu zählt auch die Bewertung von toxikologischen, pharmakologischen und pharmakokinetischen Eigenschaften der Wirkstoffe in geeigneten Tiermodellen, eine Herstellung der Wirkstoffe nach international gültigen GLP- und GMP-Regeln und die Testung auf Stabilität und Darreichungsform. Ein solcher Austausch ist in Zukunft mit der *Translational Project Management Office* des Deutschen Zentrums für Infektionsforschung angedacht.

Letztendlich ist die translationale Entwicklung der oben genannten Ansätze (von „*bench to bedside*“) ein langwieriger und kostenintensiver Prozess. Realistisch betrachtet ist in jedem weiteren Evaluationsschritt eine negative Bewertung der Behandlungsstrategie möglich, welche zu einer Terminierung der Wirkstoffentwicklung führen könnte.

Trotzdem ist die Erforschung neuer Wirkstrategien auch in Zukunft sinnvoll, um mit möglichst innovativen Ansätzen neue antivirale Behandlungsoptionen zu entwickeln. Vor allem der Ansatz eines Breitband-Virostatikum bei neu-auftretenden Infektionskrankheiten sollte hierbei verfolgt werden. Da sich hierbei aufgrund ihres breiten Wirkspektrums HDAs anbieten, ist zukünftig eine engere Verzahnung mit der

Medizinalchemie (Leadoptimierung von z.B. Thapsigargin) und Pharmakologie (alternative Verabreichungsformen z.B. topisch als Aerosol bei respiratorischen Viren) unabdingbar.

5. Referenzen

1. Tyrrell DAJ, Bynoe ML. 1965. Cultivation of a Novel Type of Common-Cold Virus in Organ Cultures. Bmj-British Medical Journal 1:1467-+.
2. Gorbalenya AE, Baker SC, Baric RS, de Groot RJ, Drosten C, Gulyaeva AA, Haagmans BL, Lauber C, Leontovich AM, Neuman BW, Penzar D, Perlman S, Poon LLM, Samborskiy DV, Sidorov IA, Sola I, Ziebuhr J, Grp CS. 2020. The species Severe acute respiratory syndrome-related coronavirus: classifying 2019-nCoV and naming it SARS-CoV-2. Nature Microbiology 5:536-544.
3. Vennema H, Godeke GJ, Rossen JWA, Voorhout WF, Horzinek MC, Opstelten DJE, Rottier PJM. 1996. Nucleocapsid-independent assembly of coronavirus-like particles by co-expression of viral envelope protein genes. Embo Journal 15:2020-2028.
4. Schelle B, Karl N, Ludewig B, Siddell SG, Thiel V. 2006. Nucleocapsid protein expression facilitates coronavirus replication. Nidoviruses: Toward Control of Sars and Other Nidovirus Diseases 581:43-48.
5. Lai MMC, Stohlman SA. 1981. Comparative-Analysis of Rna Genomes of Mouse Hepatitis Viruses. Journal of Virology 38:661-670.
6. Madhugiri R, Fricke M, Marz M, Ziebuhr J. 2016. Coronavirus cis-Acting RNA Elements. Advances in Virus Research, Vol 96: Coronaviruses 96:127-163.
7. Ziebuhr J. 2005. The coronavirus replicase. Coronavirus Replication and Reverse Genetics 287:57-94.
8. V'kovski P, Kratzel A, Steiner S, Stalder H, Thiel V. 2021. Coronavirus biology and replication: implications for SARS-CoV-2. Nature Reviews Microbiology 19:155-170.
9. Sawicki SG, Sawicki DL. 1995. Coronaviruses use discontinuous extension for synthesis of subgenome-length negative strands. Adv Exp Med Biol 380:499-506.
10. Zuniga S, Sola I, Alonso S, Enjuanes L. 2004. Sequence motifs involved in the regulation of discontinuous coronavirus subgenomic RNA synthesis. J Virol 78:980-94.
11. Sawicki SG, Sawicki DL, Siddell SG. 2007. A contemporary view of coronavirus transcription. J Virol 81:20-9.
12. Ziebuhr J. 2016. Coronaviren, p 479-482. *In* Suerbaum S, Burchard G-D, Kaufmann SHE, Schulz TF (ed), Medizinische Mikrobiologie und Infektiologie doi:10.1007/978-3-662-48678-8_58. Springer Berlin Heidelberg, Berlin, Heidelberg.
13. Lamers MM, Haagmans BL. 2022. SARS-CoV-2 pathogenesis. Nat Rev Microbiol 20:270-284.
14. Pardi N, Weissman D. 2020. Development of vaccines and antivirals for combating viral pandemics. Nature Biomedical Engineering 4:1128-1133.
15. https://www.leopoldina.org/fileadmin/redaktion/Publikationen/Nationale_Empfehlungen/2021_Stellungnahme_Antivirale_Substanzen.pdf.
16. De Clercq E. 2002. Strategies in the design of antiviral drugs. Nature Reviews Drug Discovery 1:13-25.
17. De Clercq E, Li GD. 2016. Approved Antiviral Drugs over the Past 50 Years. Clinical Microbiology Reviews 29:695-747.
18. Tompa DR, Immanuel A, Srikanth S, Kadhirvel S. 2021. Trends and strategies to combat viral infections: A review on FDA approved antiviral drugs. Int J Biol Macromol 172:524-541.

19. McColl ER, Kojovic D, Piquette-Miller M. 2018. Battling the HIV/AIDS Epidemic: Triumphs and Barriers. Clin Pharmacol Ther 104:1042-1046.
20. Feld JJ, Lok AS, Zoulim F. 2023. New Perspectives on Development of Curative Strategies for Chronic Hepatitis B. Clin Gastroenterol Hepatol 21:2040-2050.
21. Manns MP, Maasoumy B. 2022. Breakthroughs in hepatitis C research: from discovery to cure. Nature Reviews Gastroenterology & Hepatology 19:533-550.
22. Parlati L, Hollande C, Pol S. 2021. Treatment of hepatitis C virus infection. Clin Res Hepatol Gastroenterol 45:101578.
23. Dong G, Peng C, Luo J, Wang C, Han L, Wu B, Ji G, He H. 2015. Adamantane-resistant influenza a viruses in the world (1902-2013): frequency and distribution of M2 gene mutations. PLoS One 10:e0119115.
24. Kumar N, Sharma S, Kumar R, Tripathi BN, Barua S, Ly H, Rouse BT. 2020. Host-Directed Antiviral Therapy. Clinical Microbiology Reviews 33.
25. Bauer L, Lyoo H, van der Schaar HM, Strating JRPM, van Kuppeveld FJM. 2017. Direct-acting antivirals and host-targeting strategies to combat enterovirus infections. Current Opinion in Virology 24:1-8.
26. Kaufmann SHE, Dorhoi A, Hotchkiss RS, Bartenschlager R. 2018. Host-directed therapies for bacterial and viral infections. Nature Reviews Drug Discovery 17:35-56.
27. Pattnaik GP, Chakraborty H. 2020. Entry Inhibitors: Efficient Means to Block Viral Infection. J Membr Biol 253:425-444.
28. O'Brien MP, Hou PJ, Weinreich DM. 2021. Subcutaneous REGEN-COV Antibody Combination to Prevent Covid-19 REPLY. New England Journal of Medicine.
29. https://www.rki.de/DE/Content/InfAZ/N/Neuartiges_Coronavirus/COVRIIN_Dok/Antivirale_Therapie_Fruehphase.pdf?__blob=publicationFile.
30. Cox M, Peacock TP, Harvey WT, Hughes J, Wright DW, Consortium C-GU, Willett BJ, Thomson E, Gupta RK, Peacock SJ, Robertson DL, Carabelli AM. 2023. SARS-CoV-2 variant evasion of monoclonal antibodies based on in vitro studies. Nat Rev Microbiol 21:112-124.
31. Mader AL, Tydykov L, Gluck V, Bertok M, Weidlich T, Gottwald C, Stefl A, Vogel M, Plentz A, Kostler J, Salzberger B, Wenzel JJ, Niller HH, Jantsch J, Wagner R, Schmidt B, Gluck T, Gessner A, Peterhoff D. 2022. Omicron's binding to sotrovimab, casirivimab, imdevimab, CR3022, and sera from previously infected or vaccinated individuals. iScience 25:104076.
32. Planas D, Saunders N, Maes P, Guivel-Benhassine F, Planchais C, Buchrieser J, Bolland WH, Porrot F, Staropoli I, Lemoine F, Péré H, Veyer D, Puech J, Rodary J, Baela G, Dellicour S, Raymenants J, Gorissen S, Geenen C, Vanmechelen B, Wawina-Bokalanga T, Martí-Carrerasi J, Cuypers L, Sève A, Hocqueloux L, Prazuck T, Rey F, Simon-Lorrière E, Bruel T, Mouquet H, André E, Schwartz O. 2022. Considerable escape of SARS-CoV-2 Omicron to antibody neutralization. Nature 602:671-+.
33. Song R, Zeng G, Yu J, Meng X, Chen X, Li J, Xie X, Lian X, Zhang Z, Cao Y, Yin W, Jin R. 2023. Post-exposure prophylaxis with SA58 (anti-SARS-COV-2 monoclonal antibody) nasal spray for the prevention of symptomatic COVID-19 in healthy adult workers: a randomized, single-blind, placebo-controlled clinical study. Emerg Microbes Infect 12:2212806.
34. Chames P, Van Regenmortel M, Weiss E, Baty D. 2009. Therapeutic antibodies: successes, limitations and hopes for the future. Br J Pharmacol 157:220-33.

35. Majerova T, Konvalinka J. 2022. Viral proteases as therapeutic targets. Molecular Aspects of Medicine 88.
36. Lou ZY, Sun YN, Rao ZH. 2014. Current progress in antiviral strategies. Trends in Pharmacological Sciences 35:86-102.
37. Llibre JM, Imaz A, Clotet B. 2013. From TMC114 to Darunavir: Five Years of Data on Efficacy. Aids Reviews 15:112-121.
38. Owen DR, Allerton CMN, Anderson AS, Aschenbrenner L, Avery M, Berritt S, Boras B, Cardin RD, Carlo A, Coffman KJ, Dantonio A, Di L, Eng H, Ferre R, Gajiwala KS, Gibson SA, Greasley SE, Hurst BL, Kadar EP, Kalgutkar AS, Lee JC, Lee J, Liu W, Mason SW, Noell S, Novak JJ, Obach RS, Ogilvie K, Patel NC, Pettersson M, Rai DK, Reese MR, Sammons MF, Sathish JG, Singh RSP, Steppan CM, Stewart A, Tuttle JB, Updyke L, Verhoest PR, Wei LQ, Yang QY, Zhu YA. 2021. An oral SARS-CoV-2 M-pro inhibitor clinical candidate for the treatment of COVID-19. Science 374:1586-+.
39. Wilkinson GR. 1996. Cytochrome P4503A (CYP3A) metabolism: prediction of in vivo activity in humans. J Pharmacokinet Biopharm 24:475-90.
40. Lin JH, Yamazaki M. 2003. Role of P-glycoprotein in pharmacokinetics: clinical implications. Clin Pharmacokinet 42:59-98.
41. Marzolini C, Kuritzkes DR, Marra F, Boyle A, Gibbons S, Flexner C, Pozniak A, Boffito M, Waters L, Burger D, Back DJ, Khoo S. 2022. Recommendations for the Management of Drug-Drug Interactions Between the COVID-19 Antiviral Nirmatrelvir/Ritonavir (Paxlovid) and Comedications. Clin Pharmacol Ther 112:1191-1200.
42. https://www.rki.de/DE/Content/InfAZ/N/Neuartiges_Coronavirus/Therapie/AWMF_STAKOB_Stellungnahme_Arzneimittel.pdf?__blob=publicationFile.
43. Iketani S, Mohri H, Culbertson B, Hong SJ, Duan Y, Luck MI, Annavajhala MK, Guo Y, Sheng Z, Uhlemann AC, Goff SP, Sabo Y, Yang H, Chavez A, Ho DD. 2023. Multiple pathways for SARS-CoV-2 resistance to nirmatrelvir. Nature 613:558-564.
44. Tsai CH, Lee PY, Stollar V, Li ML. 2006. Antiviral therapy targeting viral polymerase. Current Pharmaceutical Design 12:1339-1355.
45. Lo MK, Albarino CG, Perry JK, Chang S, Tchesnokov EP, Guerrero L, Chakrabarti A, Shrivastava-Ranjan P, Chatterjee P, McMullan LK, Martin R, Jordan R, Gotte M, Montgomery JM, Nichol ST, Flint M, Porter D, Spiropoulou CF. 2020. Remdesivir targets a structurally analogous region of the Ebola virus and SARS-CoV-2 polymerases. Proc Natl Acad Sci U S A 117:26946-26954.
46. Sheahan TP, Sims AC, Zhou ST, Graham RL, Pruijssers AJ, Agostini ML, Leist SR, Schafer A, Dinnon KH, Stevens LJ, Chappell JD, Lu XT, Hughes TM, George AS, Hill CS, Montgomery SA, Brown AJ, Bluemling GR, Natchus MG, Saindane M, Kolykhalov AA, Painter G, Harcourt J, Tamin A, Thornburg NJ, Swanstrom R, Denison MR, Baric RS. 2020. An orally bioavailable broad-spectrum antiviral inhibits SARS-CoV-2 in human airway epithelial cell cultures and multiple coronaviruses in mice. Science Translational Medicine 12.
47. Sheahan TP, Sims AC, Graham RL, Menachery VD, Gralinski LE, Case JB, Leist SR, Pyrc K, Feng JY, Trantcheva I, Bannister R, Park Y, Babusis D, Clarke MO, Mackman RL, Spahn JE, Palmiotti CA, Siegel D, Ray AS, Cihlar T, Jordan R, Denison MR, Baric RS. 2017. Broad-spectrum antiviral GS-5734 inhibits both epidemic and zoonotic coronaviruses. Sci Transl Med 9.
48. Sun D. 2020. Remdesivir for Treatment of COVID-19: Combination of Pulmonary and IV Administration May Offer Aditional Benefit. AAPS J 22:77.

49. Szemiel AM, Merits A, Orton RJ, MacLean OA, Pinto RM, Wickenhagen A, Lieber G, Turnbull ML, Wang S, Furnon W, Suarez NM, Mair D, da Silva Filipe A, Willett BJ, Wilson SJ, Patel AH, Thomson EC, Palmarini M, Kohl A, Stewart ME. 2021. In vitro selection of Remdesivir resistance suggests evolutionary predictability of SARS-CoV-2. PLoS Pathog 17:e1009929.
50. Gandhi S, Klein J, Robertson AJ, Pena-Hernandez MA, Lin MJ, Roychoudhury P, Lu P, Fournier J, Ferguson D, Mohamed Bakhash SAK, Catherine Muenker M, Srivathsan A, Wunder EA, Jr., Kerantzas N, Wang W, Lindenbach B, Pyle A, Wilen CB, Ogbuagu O, Greninger AL, Iwasaki A, Schulz WL, Ko AI. 2022. De novo emergence of a remdesivir resistance mutation during treatment of persistent SARS-CoV-2 infection in an immunocompromised patient: a case report. Nat Commun 13:1547.
51. Jayk Bernal A, Gomes da Silva MM, Musungaie DB, Kovalchuk E, Gonzalez A, Delos Reyes V, Martin-Quiros A, Caraco Y, Williams-Diaz A, Brown ML, Du J, Pedley A, Assaid C, Strizki J, Grobler JA, Shamsuddin HH, Tipping R, Wan H, Paschke A, Butterton JR, Johnson MG, De Anda C, Group MO-OS. 2022. Molnupiravir for Oral Treatment of Covid-19 in Nonhospitalized Patients. N Engl J Med 386:509-520.
52. Fischer WA, Eron JJ, Holman W, Cohen MS, Fang L, Szewczyk LJ, Sheahan TP, Baric R, Mollan KR, Wolfe CR, Duke ER, Azizad MM, Borroto-Esoda K, Wohl DA, Coombs RW, Loftis AJ, Alabanza P, Lipansky F, Painter WP. 2022. A phase 2a clinical trial of molnupiravir in patients with COVID-19 shows accelerated SARS-CoV-2 RNA clearance and elimination of infectious virus. Science Translational Medicine 14.
53. Strizki JM, Grobler JA, Murgolo N, Fridman A, Johnson MG, Du J, Carmelitano P, Brown ML, Paschke A, De Anda C. 2023. Virologic Outcomes with Molnupiravir in Non-hospitalized Adult Patients with COVID-19 from the Randomized, Placebo-Controlled MOVe-OUT Trial. Infect Dis Ther doi:10.1007/s40121-023-00891-1.
54. https://www.bfarm.de/DE/Arzneimittel/Arzneimittelinformationen/lagevrio-ablehnung-zulassung.html;jsessionid=BEB044439CF2510F9BDD42C5F1196E0A.intranet262?nn=471278.
55. Tripathi D, Sodani M, Gupta PK, Kulkarni S. 2021. Host directed therapies: COVID-19 and beyond. Curr Res Pharmacol Drug Discov 2:100058.
56. Zhang HR, Lv PJ, Jiang JR, Liu YH, Yan RX, Shu SA, Hu B, Xiao H, Cai K, Yuan S, Li Y. 2023. Advances in developing ACE2 derivatives against SARS-CoV-2. Lancet Microbe 4:e369-e378.
57. Hoffmann M, Hofmann-Winkler H, Smith JC, Kruger N, Arora P, Sorensen LK, Sogaard OS, Hasselstrom JB, Winkler M, Hempel T, Raich L, Olsson S, Danov O, Jonigk D, Yamazoe T, Yamatsuta K, Mizuno H, Ludwig S, Noe F, Kjolby M, Braun A, Sheltzer JM, Pohlmann S. 2021. Camostat mesylate inhibits SARS-CoV-2 activation by TMPRSS2-related proteases and its metabolite GBPA exerts antiviral activity. Ebiomedicine 65.
58. Group RC, Horby P, Lim WS, Emberson JR, Mafham M, Bell JL, Linsell L, Staplin N, Brightling C, Ustianowski A, Elmahi E, Prudon B, Green C, Felton T, Chadwick D, Rege K, Fegan C, Chappell LC, Faust SN, Jaki T, Jeffery K, Montgomery A, Rowan K, Juszczak E, Baillie JK, Haynes R, Landray MJ. 2021. Dexamethasone in Hospitalized Patients with Covid-19. N Engl J Med 384:693-704.

59. Madhugiri R, Karl N, Petersen D, Lamkiewicz K, Fricke M, Wend U, Scheuer R, Marz M, Ziebuhr J. 2018. Structural and functional conservation of cis-acting RNA elements in coronavirus 5 '-terminal genome regions. Virology 517:44-55.
60. Ziv O, Price J, Shalamova L, Kamenova T, Goodfellow I, Weber F, Miska EA. 2020. The Short- and Long-Range RNA-RNA Interactome of SARS-CoV-2. Molecular Cell 80:1067-+.
61. Kim D, Kim S, Park J, Chang HR, Chang J, Ahn J, Park H, Park J, Son N, Kang G, Kim J, Kim K, Park MS, Kim YK, Baek D. 2021. A high-resolution temporal atlas of the SARS-CoV-2 translatome and transcriptome. Nature Communications 12.
62. Bennett CF, Swayze EE. 2010. RNA Targeting Therapeutics: Molecular Mechanisms of Antisense Oligonucleotides as a Therapeutic Platform. Annual Review of Pharmacology and Toxicology 50:259-293.
63. Bennett CF, Krainer AR, Cleveland DW. 2019. Antisense Oligonucleotide Therapies for Neurodegenerative Diseases. Annual Review of Neuroscience, Vol 42 42:385-406.
64. Le TK, Paris C, Khan KS, Robson F, Ng WL, Rocchi P. 2021. Nucleic Acid-Based Technologies Targeting Coronaviruses. Trends in Biochemical Sciences 46:351-365.
65. Crooke ST, Witztum JL, Bennett CF, Baker BF. 2018. RNA-Targeted Therapeutics. Cell Metabolism 27:714-739.
66. Wilusz JE. 2018. A 360 degrees view of circular RNAs: From biogenesis to functions. Wiley Interdiscip Rev RNA 9:e1478.
67. Pfafenrot C, Schneider T, Muller C, Hung LH, Schreiner S, Ziebuhr J, Bindereif A. 2021. Inhibition of SARS-CoV-2 coronavirus proliferation by designer antisense-circRNAs. Nucleic Acids Research 49:12502-12516.
68. Baldassarre A, Paolini A, Bruno SP, Felli C, Tozzi AE, Masotti A. 2020. Potential use of noncoding RNAs and innovative therapeutic strategies to target the 5'UTR of SARS-CoV-2. Epigenomics 12.
69. Albrechtsen SS, Born AP, Boesen MS. 2020. Nusinersen treatment of spinal muscular atrophy - a systematic review. Dan Med J 67.
70. Hoy SM. 2021. Nusinersen: A Review in 5q Spinal Muscular Atrophy. CNS Drugs 35:1317-1328.
71. Benson MD, Waddington-Cruz M, Berk JL, Polydefkis M, Dyck PJ, Wang AK, Plante-Bordeneuve V, Barroso FA, Merlini G, Obici L, Scheinberg M, Brannagan TH, 3rd, Litchy WJ, Whelan C, Drachman BM, Adams D, Heitner SB, Conceicao I, Schmidt HH, Vita G, Campistol JM, Gamez J, Gorevic PD, Gane E, Shah AM, Solomon SD, Monia BP, Hughes SG, Kwoh TJ, McEvoy BW, Jung SW, Baker BF, Ackermann EJ, Gertz MA, Coelho T. 2018. Inotersen Treatment for Patients with Hereditary Transthyretin Amyloidosis. N Engl J Med 379:22-31.
72. Witztum JL, Gaudet D, Arca M, Jones A, Soran H, Gouni-Berthold I, Stroes ESG, Alexander VJ, Jones R, Watts L, Xia S, Tsimikas S. 2023. Volanesorsen and triglyceride levels in familial chylomicronemia syndrome: Long-term efficacy and safety data from patients in an open-label extension trial. J Clin Lipidol 17:342-355.
73. Zhu YR, Zhu LY, Wang X, Jin HC. 2022. RNA-based therapeutics: an overview and prospectus. Cell Death & Disease 13.
74. Jabs DA, Griffiths PD. 2002. Fomivirsen for the treatment of cytomegalovirus retinitis. Am J Ophthalmol 133:552-6.

75. Beigel JH, Voell J, Munoz P, Kumar P, Brooks KM, Zhang JB, Iversen P, Heald A, Wong M, Davey RT. 2018. Safety, tolerability, and pharmacokinetics of radavirsen (AVI-7100), an antisense oligonucleotide targeting influenza a M1/M2 translation. British Journal of Clinical Pharmacology 84:25-34.
76. Hui RWH, Mak LY, Seto WK, Yuen MF. 2022. RNA interference as a novel treatment strategy for chronic hepatitis B infection. Clinical and Molecular Hepatology 28:408-424.
77. Neuman BW, Stein DA, Kroeker AD, Churchill MJ, Kim AM, Kuhn P, Dawson P, Moulton HM, Bestwick RK, Iversen PL, Buchmeier MJ. 2005. Inhibition, escape, and attenuated growth of severe acute respiratory syndrome coronavirus treated with antisense morpholino oligomers. J Virol 79:9665-76.
78. Burrer R, Neuman BW, Ting JP, Stein DA, Moulton HM, Iversen PL, Kuhn P, Buchmeier MJ. 2007. Antiviral effects of antisense morpholino oligomers in murine coronavirus infection models. J Virol 81:5637-48.
79. Vora SM, Fontana P, Mao TY, Leger V, Zhang Y, Fu TM, Lieberman J, Gehrke L, Shi M, Wang LF, Iwasaki A, Wu H. 2022. Targeting stem-loop 1 of the SARS-CoV-2 5' UTR to suppress viral translation and Nsp1 evasion. Proceedings of the National Academy of Sciences of the United States of America 119.
80. Paunovska K, Loughrey D, Dahlman JE. 2022. Drug delivery systems for RNA therapeutics. Nat Rev Genet 23:265-280.
81. Wang M, Kaufman RJ. 2016. Protein misfolding in the endoplasmic reticulum as a conduit to human disease. Nature 529:326-335.
82. Hetz C, Papa FR. 2018. The Unfolded Protein Response and Cell Fate Control. Molecular Cell 69:169-181.
83. Wu HX, Ng BSH, Thibault G. 2014. Endoplasmic reticulum stress response in yeast and humans. Bioscience Reports 34:321-330.
84. Pobre KFR, Poet GJ, Hendershot LM. 2019. The endoplasmic reticulum (ER) chaperone BiP is a master regulator of ER functions: Getting by with a little help from ERdj friends. Journal of Biological Chemistry 294:2098-2108.
85. Bertolotti A, Zhang YH, Hendershot LM, Harding HP, Ron D. 2000. Dynamic interaction of BiP and ER stress transducers in the unfolded-protein response. Nature Cell Biology 2:326-332.
86. Cui WJ, Li JZ, Ron D, Sha BD. 2011. The structure of the PERK kinase domain suggests the mechanism for its activation. Acta Crystallographica Section D-Biological Crystallography 67:423-428.
87. Carrara M, Prischi F, Nowak PR, Ali MMU. 2015. Crystal structures reveal transient PERK luminal domain tetramerization in endoplasmic reticulum stress signaling. Embo Journal 34:1589-1600.
88. Kopp MC, Larburu N, Durairaj V, Adams CJ, Ali MMU. 2019. UPR proteins IRE1 and PERK switch BiP from chaperone to ER stress sensor. Nature Structural & Molecular Biology 26:1053-+.
89. Mori K, Ogawa N, Kawahara T, Yanagi H, Yura T. 2000. MRNA splicing-mediated C-terminal replacement of transcription factor Hac1p is required for efficient activation of the unfolded protein response. Proceedings of the National Academy of Sciences of the United States of America 97:4660-4665.
90. Chen XY, Shi CR, He MH, Xiong SQ, Xia XB. 2023. Endoplasmic reticulum stress: molecular mechanism and therapeutic targets. Signal Transduction and Targeted Therapy 8.
91. DeDiego ML, Nieto-Torres JL, Jimenez-Guardeno JM, Regla-Nava JA, Alvarez E, Oliveros JC, Zhao J, Fett C, Perlman S, Enjuanes L. 2011. Severe acute

respiratory syndrome coronavirus envelope protein regulates cell stress response and apoptosis. PLoS Pathog 7:e1002315.
92. Rasmussen U, Broogger Christensen S, Sandberg F. 1978. Thapsigargine and thapsigargicine, two new histamine liberators from Thapsia garganica L. Acta Pharm Suec 15:133-40.
93. Shaban MS, Muller C, Mayr-Buro C, Weiser H, Meier-Soelch J, Albert BV, Weber A, Linne U, Hain T, Babayev I, Karl N, Hofmann N, Becker S, Herold S, Schmitz ML, Ziebuhr J, Kracht M. 2021. Multi-level inhibition of coronavirus replication by chemical ER stress. Nat Commun 12:5536.
94. Jonsdottir HR, Dijkman R. 2015. Characterization of human coronaviruses on well-differentiated human airway epithelial cell cultures. Methods Mol Biol 1282:73-87.
95. Prentice E, McAuliffe J, Lu X, Subbarao K, Denison MR. 2004. Identification and characterization of severe acute respiratory syndrome coronavirus replicase proteins. J Virol 78:9977-86.
96. Prentice E, Jerome WG, Yoshimori T, Mizushima N, Denison MR. 2004. Coronavirus replication complex formation utilizes components of cellular autophagy. J Biol Chem 279:10136-41.
97. Ji M, Li M, Sun L, Deng H, Zhao YG. 2023. DMV biogenesis during beta-coronavirus infection requires autophagy proteins VMP1 and TMEM41B. Autophagy 19:737-738.
98. Liang H, Luo D, Liao H, Li S. 2022. Coronavirus Usurps the Autophagy-Lysosome Pathway and Induces Membranes Rearrangement for Infection and Pathogenesis. Front Microbiol 13:846543.
99. Maier HJ, Britton P. 2012. Involvement of autophagy in coronavirus replication. Viruses 4:3440-51.
100. Ganley IG, Wong PM, Gammoh N, Jiang XJ. 2011. Distinct Autophagosomal-Lysosomal Fusion Mechanism Revealed by Thapsigargin-Induced Autophagy Arrest. Molecular Cell 42:731-743.
101. Ganley IG, Wong PM, Jiang XJ. 2011. Thapsigargin distinguishes membrane fusion in the late stages of endocytosis and autophagy. Autophagy 7:1397-1399.
102. Zhao Z, Thackray LB, Miller BC, Lynn TM, Becker MM, Ward E, Mizushima NN, Denison MR, Virgin HWt. 2007. Coronavirus replication does not require the autophagy gene ATG5. Autophagy 3:581-5.
103. Schneider M, Ackermann K, Stuart M, Wex C, Protzer U, Schatzl HM, Gilch S. 2012. Severe acute respiratory syndrome coronavirus replication is severely impaired by MG132 due to proteasome-independent inhibition of M-calpain. J Virol 86:10112-22.
104. Reggiori F, Monastyrska I, Verheije MH, Cali T, Ulasli M, Bianchi S, Bernasconi R, de Haan CA, Molinari M. 2010. Coronaviruses Hijack the LC3-I-positive EDEMosomes, ER-derived vesicles exporting short-lived ERAD regulators, for replication. Cell Host Microbe 7:500-8.
105. Saurav S, Tanwar J, Ahuja K, Motiani RK. 2021. Dysregulation of host cell calcium signaling during viral infections: Emerging paradigm with high clinical relevance. Mol Aspects Med 81:101004.
106. Zhang LK, Sun Y, Zeng H, Wang Q, Jiang X, Shang WJ, Wu Y, Li S, Zhang YL, Hao ZN, Chen H, Jin R, Liu W, Li H, Peng K, Xiao G. 2020. Calcium channel blocker amlodipine besylate therapy is associated with reduced case fatality rate of COVID-19 patients with hypertension. Cell Discov 6:96.

107. Lundin A, Dijkman R, Bergstrom T, Kann N, Adamiak B, Hannoun C, Kindler E, Jonsdottir HR, Muth D, Kint J, Forlenza M, Muller MA, Drosten C, Thiel V, Trybala E. 2014. Targeting membrane-bound viral RNA synthesis reveals potent inhibition of diverse coronaviruses including the middle East respiratory syndrome virus. PLoS Pathog 10:e1004166.
108. Muller C, Hardt M, Schwudke D, Neuman BW, Pleschka S, Ziebuhr J. 2018. Inhibition of Cytosolic Phospholipase A(2)alpha Impairs an Early Step of Coronavirus Replication in Cell Culture. J Virol 92.
109. Jaskulska A, Janecka AE, Gach-Janczak K. 2020. Thapsigargin-From Traditional Medicine to Anticancer Drug. Int J Mol Sci 22.
110. Chan K, Robert F, Oertlin C, Kapeller-Libermann D, Avizonis D, Gutierrez J, Handly-Santana A, Doubrovin M, Park J, Schoepfer C, Da Silva B, Yao M, Gorton F, Shi JW, Thomas CJ, Brown LE, Porco JA, Pollak M, Larsson O, Pelletier J, Chio IIC. 2019. eIF4A supports an oncogenic translation program in pancreatic ductal adenocarcinoma. Nature Communications 10.
111. Goulding LV, Yang J, Jiang Z, Zhang H, Lea D, Emes RD, Dottorini T, Pu J, Liu J, Chang KC. 2020. Thapsigargin at Non-Cytotoxic Levels Induces a Potent Host Antiviral Response that Blocks Influenza A Virus Replication. Viruses 12.
112. Zhao ZM, Ukidve A, Kim J, Mitragotri S. 2020. Targeting Strategies for Tissue-Specific Drug Delivery. Cell 181:151-167.
113. Doan NTQ, Paulsen ES, Sehgal P, Moller JV, Nissen P, Denmeade SR, Isaacs JT, Dionne CA, Christensen SB. 2015. Targeting thapsigargin towards tumors. Steroids 97:2-7.
114. Mahalingam D, Peguero J, Cen PT, Arora SP, Sarantopoulos J, Rowe J, Allgood V, Tubb B, Campos L. 2019. A Phase II, Multicenter, Single-Arm Study of Mipsagargin (G-202) as a Second-Line Therapy Following Sorafenib for Adult Patients with Progressive Advanced Hepatocellular Carcinoma. Cancers 11.
115. Mahalingam D, Wilding G, Denmeade S, Sarantopoulas J, Cosgrove D, Cetnar J, Azad N, Bruce J, Kurman M, Allgood VE, Carducci M. 2016. Mipsagargin, a novel thapsigargin-based PSMA-activated prodrug: results of a first-in-man phase I clinical trial in patients with refractory, advanced or metastatic solid tumours. British Journal of Cancer 114:986-994.
116. Isaacs JT, Brennen WN, Christensen SB, Denmeade SR. 2021. Mipsagargin: The Beginning-Not the End-of Thapsigargin Prodrug-Based Cancer Therapeutics. Molecules 26.
117. Chu J, Zhang W, Cencic R, Devine WG, Beglov D, Henkel T, Brown LE, Vajda S, Porco JA, Jr., Pelletier J. 2019. Amidino-Rocaglates: A Potent Class of eIF4A Inhibitors. Cell Chem Biol 26:1586-1593 e3.
118. Hwang BY, Su BN, Chai HB, Mi QW, Kardono LBS, Afriastini JJ, Riswan S, Santarsiero BD, Mesecar AD, Wild R, Fairchild CR, Vite GD, Rose WC, Farnsworth NR, Cordell GRA, Pezzuto JM, Swanson SM, Kinghorn AD. 2004. Silvestrol and episilvestrol, potential anticancer rocaglate derivatives from Aglaia silvestris. (vol 69, pg 3350, 2004). Journal of Organic Chemistry 69:6156-6156.
119. Kim S, Hwang BY, Su BN, Cha HB, Mi QW, Kinghorn AD, Wild R, Swanson SM. 2007. Silvestrol, a potential anticancer rocaglate derivative from Aglaia foveolata, induces apoptosis in LNCaP cells through the mitochondrial/apoptosome pathway without activation of executioner caspase-3 or -7. Anticancer Research 27:2175-2183.
120. Ernst JT, Thompson PA, Nilewski C, Sprengeler PA, Sperry S, Packard G, Michels T, Xiang A, Tran C, Wegerski CJ, Eam B, Young NP, Fish S, Chen J,

Howard H, Staunton J, Molter J, Clarine J, Nevarez A, Chiang GG, Appleman JR, Webster KR, Reich SH. 2020. Design of Development Candidate eFT226, a First in Class Inhibitor of Eukaryotic Initiation Factor 4A RNA Helicase. Journal of Medicinal Chemistry 63:5879-5955.
121. Bordeleau ME, Robert F, Gerard B, Lindqvist L, Chen SM, Wendel HG, Brem B, Greger H, Lowe SW, Porco JA, Jr., Pelletier J. 2008. Therapeutic suppression of translation initiation modulates chemosensitivity in a mouse lymphoma model. J Clin Invest 118:2651-60.
122. Kogure T, Kinghorn AD, Yan I, Bolon B, Lucas DM, Grever MR, Patel T. 2013. Therapeutic potential of the translation inhibitor silvestrol in hepatocellular cancer. PLoS One 8:e76136.
123. Patton JT, Lustberg ME, Lozanski G, Garman SL, Towns WH, Drohan CM, Lehman A, Zhang XL, Bolon B, Pan L, Kinghorn AD, Grever MR, Lucas DM, Baiocchi RA. 2015. The translation inhibitor silvestrol exhibits direct anti-tumor activity while preserving innate and adaptive immunity against EBV-driven lymphoproliferative disease. Oncotarget 6:2693-2708.
124. Kiening M, Ochsenreiter R, Hellinger HJ, Rattei T, Hofacker I, Frishman D. 2019. Conserved Secondary Structures in Viral mRNAs. Viruses-Basel 11.
125. Taroncher-Oldenburg G, Muller C, Obermann W, Ziebuhr J, Hartmann RK, Grunweller A. 2021. Targeting the DEAD-Box RNA Helicase eIF4A with Rocaglates-A Pan-Antiviral Strategy for Minimizing the Impact of Future RNA Virus Pandemics. Microorganisms 9.
126. Muller C, Obermann W, Karl N, Wendel HG, Taroncher-Oldenburg G, Pleschka S, Hartmann RK, Grunweller A, Ziebuhr J. 2021. The rocaglate CR-31-B (-) inhibits SARS-CoV-2 replication at non-cytotoxic, low nanomolar concentrations in vitro and ex vivo. Antiviral Res 186:105012.
127. Muller C, Obermann W, Schulte FW, Lange-Grunweller K, Oestereich L, Elgner F, Glitscher M, Hildt E, Singh K, Wendel HG, Hartmann RK, Ziebuhr J, Grunweller A. 2020. Comparison of broad-spectrum antiviral activities of the synthetic rocaglate CR-31-B (-) and the eIF4A-inhibitor Silvestrol. Antiviral Res 175:104706.
128. Muller C, Schulte FW, Lange-Grunweller K, Obermann W, Madhugiri R, Pleschka S, Ziebuhr J, Hartmann RK, Grunweller A. 2018. Broad-spectrum antiviral activity of the eIF4A inhibitor silvestrol against corona- and picornaviruses. Antiviral Res 150:123-129.
129. Biedenkopf N, Lange-Grunweller K, Schulte FW, Weisser A, Muller C, Becker D, Becker S, Hartmann RK, Grunweller A. 2017. The natural compound silvestrol is a potent inhibitor of Ebola virus replication. Antiviral Res 137:76-81.
130. Glitscher M, Himmelsbach K, Woytinek K, Johne R, Reuter A, Spiric J, Schwaben L, Grunweller A, Hildt E. 2018. Inhibition of Hepatitis E Virus Spread by the Natural Compound Silvestrol. Viruses-Basel 10.
131. Henss L, Scholz T, Grunweller A, Schnierle BS. 2018. Silvestrol Inhibits Chikungunya Virus Replication. Viruses-Basel 10.
132. Pedroni L, Dellafiora L, Varra MO, Galaverna G, Ghidini S. 2022. In silico study on the Hepatitis E virus RNA Helicase and its inhibition by silvestrol, rocaglamide and other flavagline compounds. Scientific Reports 12.
133. Todt D, Moeller N, Praditya D, Kinast V, Friesland M, Engelmann M, Verhoye L, Sayed IM, Behrendt P, Dao Thi VL, Meuleman P, Steinmann E. 2018. The natural compound silvestrol inhibits hepatitis E virus (HEV) replication in vitro and in vivo. Antiviral Res 157:151-158.

134. Praditya DF, Klohn M, Bruggemann Y, Brown LE, Porco JA, Zhang W, Kinast V, Kirschning A, Vondran FWR, Todt D, Steinmann E. 2022. Identification of structurally re-engineered rocaglates as inhibitors against hepatitis E virus replication. Antiviral Research 204.
135. Adams TE, El Sous M, Hawkins BC, Hirner S, Holloway G, Khoo ML, Owen DJ, Savage GP, Scammells PJ, Rizzacasa MA. 2009. Total synthesis of the potent anticancer Aglaia metabolites (-)-silvestrol and (-)-episilvestrol and the active analogue (-)-4'-desmethoxyepisilvestrol. J Am Chem Soc 131:1607-16.
136. El Sous M, Khoo ML, Holloway G, Owen D, Scammells PJ, Rizzacasa MA. 2007. Total synthesis of (-)-episilvestrol and (-)-silvestrol. Angew Chem Int Ed Engl 46:7835-8.
137. Obermann W, Friedrich A, Madhugiri R, Klemm P, Mengel JP, Hain T, Pleschka S, Wendel HG, Hartmann RK, Schiffmann S, Ziebuhr J, Müller C, Grünweller A. 2022. Rocaglates as Antivirals: Comparing the Effects on Viral Resistance, Anti-Coronaviral Activity, RNA-Clamping on eIF4A and Immune Cell Toxicity. Viruses 14:519.
138. Shen L, Pelletier J. 2020. Selective targeting of the DEAD-box RNA helicase eukaryotic initiation factor (eIF) 4A by natural products. Natural Product Reports 37:609-616.
139. Schulz G, Victoria C, Kirschning A, Steinmann E. 2021. Rocaglamide and silvestrol: a long story from anti-tumor to anti-coronavirus compounds. Natural Product Reports 38:18-23.
140. Pellegatti M. 2012. Preclinical in vivo ADME studies in drug development: a critical review. Expert Opinion on Drug Metabolism & Toxicology 8:161-172.
141. Saradhi UVRV, Gupta SV, Chiu M, Wang J, Ling YH, Liu ZF, Newman DJ, Covey JM, Kinghorn AD, Marcucci G, Lucas DM, Grever MR, Phelps MA, Chan KK. 2011. Characterization of Silvestrol Pharmacokinetics in Mice Using Liquid Chromatography-Tandem Mass Spectrometry. Aaps Journal 13:347-356.
142. Schiffmann S, Gunne S, Ulshofer T, Henke M, Roser LA, Schneider AK, Cinatl J, Thomas D, Schreiber Y, Wagner PV, Grunweller A, Parnham MJ. 2022. In Vitro Safety, Off-Target and Bioavailability Profile of the Antiviral Compound Silvestrol. Pharmaceuticals (Basel) 15.
143. Meric-Bernstam F, Sharma M, Sommerhalder D, Skeel RT, El-Khoueiry AB, Caswell-Jin JL, Patel PH, Rosen E. 2022. First-in-human phase 1/2 dose escalation and expansion study evaluating first-in-class eIF4A inhibitor zotatifin in patients with solid tumors. Journal of Clinical Oncology 40.
144. https://investors.effector.com/news-releases/news-release-details/effector-therapeutics-completes-enrollment-second-three-cohorts.
145. Sengupta A, Dorn A, Jamshidi M, Schwob M, Hassan W, De Maddalena LL, Hugi A, Stucki AO, Dorn P, Marti TM, Wisser O, Stucki JD, Krebs T, Hobi N, Guenat OT. 2023. A multiplex inhalation platform to model in situ like aerosol delivery in a breathing lung-on-chip. Front Pharmacol 14:1114739.
146. Artzy-Schnirman A, Hobi N, Schneider-Daum N, Guenat OT, Lehr CM, Sznitman J. 2019. Advanced in vitro lung-on-chip platforms for inhalation assays: From prospect to pipeline. Eur J Pharm Biopharm 144:11-17.
147. Mead BE, Karp JM. 2019. All models are wrong, but some organoids may be useful. Genome Biol 20:66.
148. Munoz-Fontela C, Widerspick L, Albrecht RA, Beer M, Carroll MW, de Wit E, Diamond MS, Dowling WE, Funnell SGP, Garcia-Sastre A, Gerhards NM, de Jong R, Munster VJ, Neyts J, Perlman S, Reed DS, Richt JA, Riveros-Balta X, Roy CJ, Salguero FJ, Schotsaert M, Schwartz LM, Seder RA, Segales J, Vasan

SS, Henao-Restrepo AM, Barouch DH. 2022. Advances and gaps in SARS-CoV-2 infection models. PLoS Pathog 18:e1010161.
149. Chu H, Chan JF, Yuen KY. 2022. Animal models in SARS-CoV-2 research. Nat Methods 19:392-394.
150. McCray PB, Jr., Pewe L, Wohlford-Lenane C, Hickey M, Manzel L, Shi L, Netland J, Jia HP, Halabi C, Sigmund CD, Meyerholz DK, Kirby P, Look DC, Perlman S. 2007. Lethal infection of K18-hACE2 mice infected with severe acute respiratory syndrome coronavirus. J Virol 81:813-21.
151. Hassan AO, Case JB, Winkler ES, Thackray LB, Kafai NM, Bailey AL, McCune BT, Fox JM, Chen RE, Alsoussi WB, Turner JS, Schmitz AJ, Lei T, Shrihari S, Keeler SP, Fremont DH, Greco S, McCray PB, Jr., Perlman S, Holtzman MJ, Ellebedy AH, Diamond MS. 2020. A SARS-CoV-2 Infection Model in Mice Demonstrates Protection by Neutralizing Antibodies. Cell 182:744-753 e4.
152. Leist SR, Dinnon KH, 3rd, Schafer A, Tse LV, Okuda K, Hou YJ, West A, Edwards CE, Sanders W, Fritch EJ, Gully KL, Scobey T, Brown AJ, Sheahan TP, Moorman NJ, Boucher RC, Gralinski LE, Montgomery SA, Baric RS. 2020. A Mouse-Adapted SARS-CoV-2 Induces Acute Lung Injury and Mortality in Standard Laboratory Mice. Cell 183:1070-1085 e12.
153. Williamson BN, Feldmann F, Schwarz B, Meade-White K, Porter DP, Schulz J, van Doremalen N, Leighton I, Yinda CK, Perez-Perez L, Okumura A, Lovaglio J, Hanley PW, Saturday G, Bosio CM, Anzick S, Barbian K, Cihlar T, Martens C, Scott DP, Munster VJ, de Wit E. 2020. Clinical benefit of remdesivir in rhesus macaques infected with SARS-CoV-2. Nature 585:273-276.
154. Johnson DM, Brasel T, Massey S, Garron T, Grimes M, Smith J, Torres M, Wallace S, Villasante-Tezanos A, Beasley DW, Comer JE. 2023. Evaluation of molnupiravir (EIDD-2801) efficacy against SARS-CoV-2 in the rhesus macaque model. Antiviral Res 209:105492.

6. Danksagung

An dieser Stelle möchte ich mich herzlich bei allen bedanken, die zum Gelingen dieser Arbeit beigetragen haben.

Ein ganz besonderer Dank gebührt **Prof. John Ziebuhr** für seine langjährige Unterstützung und das entgegengesetzte Vertrauen. Besonders möchte ich hier die stetige Diskussionsbereitschaft und die hervorragende wissenschaftliche Zusammenarbeit anmerken, ohne die ich sicherlich nicht zu der Wissenschaftlerin geworden wäre, die ich heute bin.

Zudem möchte ich mich bei allen Mitarbeitern des Instituts für Medizinische Virologie (insbesondere Prof. **Stephan Pleschka**, Frau **Nadja Karl** und Herrn **Florian Salisch**) sowie bei den zahlreichen Kooperationspartnern (besonders **Prof. Arnold Grünweller**, **Prof. Michael Kracht** und **Prof. Albrecht Bindereif**) bedanken.

Abschließend möchte ich mich für die finanzielle Unterstützung der Forschungsarbeiten insbesondere beim Deutschen Zentrum für Infektionsforschung bedanken.

7. Anhang

Pfafenrot C*, Schneider T*, **Muller C***, Hung LH, Schreiner S, Ziebuhr J, Bindereif A. 2021. Inhibition of SARS-CoV-2 coronavirus proliferation by designer antisense-circRNAs. Nucleic Acids Research 49:12502-12516.

Shaban MS*, **Muller C***, Mayr-Buro C*, Weiser H, Meier-Soelch J, Albert BV, Weber A, Linne U, Hain T, Babayev I, Karl N, Hofmann N, Becker S, Herold S, Schmitz ML, Ziebuhr J, Kracht M. 2021. Multi-level inhibition of coronavirus replication by chemical ER stress. Nat Commun 12:5536.

Muller C*, Schulte FW*, Lange-Grunweller K, Obermann W, Madhugiri R, Pleschka S, Ziebuhr J, Hartmann RK, Grunweller A. 2018. Broad-spectrum antiviral activity of the eIF4A inhibitor silvestrol against corona- and picornaviruses. Antiviral Res 150:123-129.

Muller C*, Obermann W*, Schulte FW, Lange-Grunweller K, Oestereich L, Elgner F, Glitscher M, Hildt E, Singh K, Wendel HG, Hartmann RK, Ziebuhr J, Grunweller A. 2020. Comparison of broad-spectrum antiviral activities of the synthetic rocaglate CR-31-B (-) and the eIF4A-inhibitor Silvestrol. Antiviral Res 175:104706.

Muller C, Obermann W, Karl N, Wendel HG, Taroncher-Oldenburg G, Pleschka S, Hartmann RK, Grunweller A, Ziebuhr J. 2021. The rocaglate CR-31-B (-) inhibits SARS-CoV-2 replication at non-cytotoxic, low nanomolar concentrations in vitro and ex vivo. Antiviral Res 186:105012.

Obermann W, Friedrich A, Madhugiri R, Klemm P, Mengel JP, Hain T, Pleschka S, Wendel HG, Hartmann RK, Schiffmann S, Ziebuhr J, **Müller C***, Grünweller A*. 2022. Rocaglates as Antivirals: Comparing the Effects on Viral Resistance, Anti-Coronaviral Activity, RNA-Clamping on eIF4A and Immune Cell Toxicity. Viruses 14:519.

12502–12516 *Nucleic Acids Research, 2021, Vol. 49, No. 21* *Published online 24 November 2021*
https://doi.org/10.1093/nar/gkab1096

Inhibition of SARS-CoV-2 coronavirus proliferation by designer antisense-circRNAs

Christina Pfafenrot[1,†], Tim Schneider[1,†], Christin Müller[2,†], Lee-Hsueh Hung[1], Silke Schreiner[1], John Ziebuhr[2] and Albrecht Bindereif[1,*]

[1]Institute of Biochemistry, Justus Liebig University of Giessen, 35392 Giessen, Germany and [2]Institute of Medical Virology, Justus Liebig University of Giessen, 35392 Giessen, Germany

Received June 25, 2021; Revised October 18, 2021; Editorial Decision October 19, 2021; Accepted October 27, 2021

ABSTRACT

Circular RNAs (circRNAs) are noncoding RNAs that exist in all eukaryotes investigated and are derived from back-splicing of certain pre-mRNA exons. Here, we report the application of artificial circRNAs designed to act as antisense-RNAs. We systematically tested a series of antisense-circRNAs targeted to the SARS-CoV-2 genome RNA, in particular its structurally conserved 5′-untranslated region. Functional assays with both reporter transfections as well as with SARS-CoV-2 infections revealed that specific segments of the SARS-CoV-2 5′-untranslated region can be efficiently accessed by specific antisense-circRNAs, resulting in up to 90% reduction of virus proliferation in cell culture, and with a durability of at least 48 h. Presenting the antisense sequence within a circRNA clearly proved more efficient than in the corresponding linear configuration and is superior to modified antisense oligonucleotides. The activity of the antisense-circRNA is surprisingly robust towards point mutations in the target sequence. This strategy opens up novel applications for designer circRNAs and promising therapeutic strategies in molecular medicine.

INTRODUCTION

Coronaviruses are positive-strand RNA viruses with large polycistronic genomes of around 30 kb, which have been extensively studied since the 2003 SARS outbreak [severe acute respiratory syndrome, reviewed in (1)]. Following receptor-mediated coronavirus entry into susceptible host cells, the two large open reading frames (ORFs), 1a and 1b, located in the 5′-terminal two-thirds of the capped and polyadenylated coronavirus genome, are translated, resulting in two polyproteins that are processed by viral proteases to produce nonstructural proteins that direct viral RNA synthesis (2). Translation requires the 5′-untranslated region (UTR) of the genome RNA, which for SARS-CoV-2 comprises nucleotides 1–265 [for secondary structure models, see (3,4)].

Subsequently, the viral genome RNA serves as a template for negative-strand RNA synthesis. Two types of minus-strand RNAs are produced: first, full-length copies of the plus-strand RNA that are used as templates for the production of new genome RNAs, and second, a set of 5′-coterminal subgenomic (sg) minus-strand RNAs of varying length. The vast majority of sg-minus-strand RNAs carry at their 3′-end an 'antileader' sequence, i.e. a complement of the leader sequence located at the 5′-end of the genome, which they acquire in a process called 'discontinuous extension' of minus strands. The sg-minus strands serve as templates for the production of a nested set of sg-mRNAs that share a common 5′-leader sequence (75 nts in SARS-CoV-2, plus a few nucleotides upstream of the translation start codon of the first ORF in the respective mRNA). This unusual process of discontinuous (minus-strand) RNA synthesis is guided by pairing between complements of the conserved transcription-regulatory sequences (TRS) located upstream of the various ORFs in the 3′-region of the genome ('body-TRS') and the TRS located immediately downstream of the 5′ leader ['leader-TRS', reviewed in (5), and studied by transcriptomics for SARS-CoV-2 (6)].

The current COVID-19 pandemic, with its dramatic worldwide impact on human health and economy, is caused by SARS-CoV-2, which emerged in late 2019 in China. The SARS-CoV-2 genome was sequenced in early 2020 (7,8), and currently there are intense worldwide efforts to develop and apply new therapeutic strategies to fight this life-threatening disease. Most of these approaches focus on, first, small-molecule drugs targeting viral enzymes (nucleoside analogs, protease inhibitors and others), and second, on antibodies interfering with virus entry, in particular virus-receptor interactions. In addition, immunomodulatory agents are being used and a large number of SARS-CoV-2 vaccines (including virus vector-

*To whom correspondence should be addressed. Tel: +49 641 9935420; Fax: +49 641 9935419; Email: albrecht.bindereif@chemie.bio.uni-giessen.de
†The authors wish it to be known that, in their opinion, the first three authors should be regarded as Joint First Authors.

and mRNA-based vaccines) are being developed and tested, many of which providing promising new approaches to prevent or treat COVID-19 more effectively (9).

However, alternative novel strategies should also be considered and pursued. Antisense approaches represent such a classical line of sequence-based interference and have been investigated for the last 30 years [for reviews, see (10–13)]. By targeting specific RNA sequences, antisense approaches aim to modulate RNA structure and activity, mRNA splicing, translation, or stability. Best known examples are antisense oligonucleotides (ASO), with incorporated modified positions, such as 2′-*O*-methyl (2′-OMe), 2′-*O*-methoxyethyl (2′-MOE) nucleotides, locked nucleic acids (LNA), morpholino or other modifications, which can increase RNA base-pairing, metabolic stability, and/or delivery. As a result of antisense research over several decades, ASO-based therapies have been advanced to the stage of approved drugs used in certain genetic diseases (14). Regarding antiviral strategies, earlier studies had evaluated HIV-Tat peptide-coupled morpholino ASO against SARS-CoV and the related mouse hepatitis virus (MHV) (15,16). Here, we investigated the antiviral potential of circular RNAs (circRNAs) as a basis for presenting antisense-RNA sequences, exploiting the unusual metabolic stability of circRNAs to develop them into a new line of RNA-based antiviral therapeutics.

CircRNAs are a large class of RNAs with covalently joined 5′ and 3′ ends that exist in all eukaryotes investigated so far and have been known for more than four decades [(17); reviewed in (18–20)]. More recently, circRNAs were rediscovered as a large class of noncoding RNAs, based on deep sequencing (21–23). The most common type of circRNAs consists of one or several adjacent exons derived from pre-mRNAs. Biogenesis of exonic circRNAs relies on a kind of alternative splicing (24). Functionally, however, circRNAs have remained largely unexplored, except for a few examples of validated miRNA sponges (23,25), which are embedded in regulatory RNA networks (26,27). Several other hypothetical roles have been proposed for circRNAs, for example protein sponging and antisense activity (28). Based on their unusually high stability, circRNAs provide an attractive basis for constructing designer circRNAs in biotechnological applications [see, for example, (29–31)].

Here, we combined for the first time the classical antisense (AS)-RNA approach with synthetic short circRNAs, integrating antisense sequences into a circRNA backbone. Our overall aim was to interfere with SARS-CoV-2 genome expression and viral proliferation by specifically targeting the structurally conserved 5′-UTR of SARS-CoV-2. Based on structure-guided design and a systematic functional screen of a series of AS-circRNAs, we identified a highly accessible subregion in the SARS-CoV-2 5′-leader that could be efficiently targeted by specific AS-circRNAs, resulting in 90% reduction of viral replication in cell culture. Functional antisense activity was consistently higher when the antisense sequence was presented within a circRNA rather than as a corresponding linear RNA. Compared with 2′-OMe- and 2′-MOE-modified antisense oligonucleotides, unmodified antisense-circRNA was superior in its activity; finally, it was surprisingly robust towards point mutations in the target sequence.

In conclusion, our work establishes AS-circRNAs as a novel molecular approach suitable to target and functionally regulate specific RNAs, therefore opening up promising new avenues to develop highly specific, flexible and efficient therapeutic strategies in molecular virology and medicine.

MATERIALS AND METHODS

AS-circRNA design

Antisense target sequences (40–75 nts) were selected based on the SARS-CoV-2 5′-UTR secondary structure (3,4), as well as the presence of specific sequence elements (e.g. 5′-leader, TRS, AUGs). Randomized sequences of equal length (40–75 nts) were used as controls.

RNAs for *in vitro* circularization were composed of a constant backbone sequence, in which the individual antisense target or control sequences were inserted. The constant backbone consists of six complementary nucleotides on either 5′ and 3′ ends of the RNA, followed by four non-complementary nucleotides creating overhanging ends and allowing stem-loop formation and efficient ligation. For enhanced flexibility, and to assure stem loop formation, a spacer of three unrelated nucleotides was added between the constant backbone and the antisense or control sequences on each side (for sequences, see Supplementary Table S1). These sequences were ordered as oligonucleotides (Sigma-Aldrich) including a T7 promoter, and subsequently annealed to yield templates for *in vitro* transcription.

For endogenous overexpression of antisense-circRNAs, oligonucleotide cassettes (see Supplementary Table S1) were cloned into the pAV-U6+27-Tornado-Broccoli vector (32), using the SacII and NotI restriction sites, and replacing the Broccoli aptamer sequence. Again, to allow enhanced flexibility a spacer of unrelated nucleotides was inserted, in this case two nucleotides upstream, and five nucleotides downstream of the AS or control sequence. Since internal poly(U) stretches longer than $(U)_4$, including single nucleotide interruptions, would terminate RNA polymerase III, such sequences were changed by single T→A mutations (see Supplementary Table S1).

In vitro transcription, circularization, gel purification and RNase R treatment of antisense-RNAs

RNAs were transcribed from annealed DNA-oligonucleotide templates (see Supplementary Table S1), using the HighScribe™ T7 high-yield RNA synthesis kit (NEB) in the presence of ATP, CTP, UTP, and GTP (each at 7.5 mM), GMP (30 mM GMP; Merck), and RNaseOut (Thermo Fisher Scientific) for 2 h at 37°C. The DNA template was digested by addition of RQ1 DNase (2 U per reaction, Promega), and incubation for 30 min at 37°C. Transcripts were purified using the Monarch RNA purification kit (NEB) and quantified by the Qubit™ RNA broad-range assay kit (Thermo Fisher Scientific).

For circularization, 60 μg transcribed RNA was incubated with 100 U of T4 RNA ligase (Thermo Fisher Scientific) in 1× T4 RNA ligase buffer, supplemented with 0.1 mg/ml BSA and RNaseOut (Thermo Fisher Scientific),

overnight at 16°C in a final volume of 200 µl. RNA was recovered by phenol/chloroform extraction (Roth) and ethanol precipitation.

Gel purification was performed as described (33). To validate the circular conformation, 250 ng of gel-purified circular or linear RNA was incubated with or without 2 U of RNase R (Biozym; 30 min at 37°C). After digestion, 200 ng of RNAs were separated in a 10% denaturing polyacrylamide gel and visualized by ethidium bromide staining.

Luciferase reporter constructs

5′-UTR (nts 1–265) and 5′-leader (nts 1–75) sequences of SARS-CoV-2 (NC_045512.2) were cloned into pcDNA5-CMV-FF (34) containing the Firefly reporter ORF. Additionally, for the 5′-UTR construct, 24 nucleotides of the ORF1a sequence were included, and, for the 5′-leader construct, 25 nucleotides of the S (spike) ORF, followed in either reporter by the Firefly ORF (for a schematic, see Figure 1A). For the construction of 5′-leader constructs carrying point mutations, oligo cassettes with corresponding nucleotide changes were ordered (Sigma-Aldrich) and cloned in front of the Firefly reporter ORF. Point mutations were selected based on their occurrence frequency and annotation within the ViGTK database (https://www.biosino.org/ViGTK).

Transfection of *in vitro*-transcribed RNAs and Tornado-based circRNA expression constructs; luciferase reporter assays and RT-qPCR

HeLa cells were cultured in DME-medium supplemented with 10% FBS (Gibco) at 37°C and 5% CO_2. For luciferase reporter assays, 1×10^5 cells were seeded per well (12-well plate). RNA transfections were done using Lipofectamine 2000, and Tornado-plasmid transfections with Turbofect reagent, both in a total volume of 1 ml medium/well (Thermo Fisher Scientific). For AS-circRNA screening, cells were transfected either with 1 µg of individual circRNAs, or with a combination of two circRNAs (0.5 µg of each). For titration experiments, different amounts (100, 250, 500, 750, 1000 ng) of circular or corresponding linear RNAs (CTR2 and 1–75 RNA) were used.

To compare the efficiency of AS-circRNAs and ASOs (2′-OMe or 2′-MOE modified; SeqLab), 1 µg of circRNA and a molar equivalent of the corresponding ASOs were used. Control ASOs carry the same modifications as the ASOs tested (for sequence information, see Supplementary Table S1).

For Tornado-circRNA screening, cells were transfected with 1 µg of plasmid DNA. Culture medium was always changed 1 h prior and 4 h after transfection. After one day, cells were co-transfected with 50 ng of 5′-UTR or 5′-leader luciferase reporter plasmids (see above), together with 5 ng of pRL-SCV40 Renilla-reporter (Promega). At 24 h post-transfection, cells were washed three times with PBS (Gibco), and lysed in 250 µl Lysis-Juice (PJK). Luminescence was measured for Firefly and Renilla luciferase (Beetle- and Renilla-Juice kits, respectively; PJK), using a Centro LB 960 Luminometer (Berthold Technologies). Relative luciferase activities were calculated as a ratio of the Firefly and Renilla raw values, with three technical replicates per sample and a total of three independent biological replicates.

For detection of Firefly mRNA expression levels by RT-qPCR, HeLa cells were seeded and transfected as described above. After one day, cells were co-transfected with 50 ng of 5′-leader luciferase reporter plasmid, together with 5 ng of pRL-SCV40 Renilla-reporter (Promega). 24 h post-transfection, cells were washed three times with PBS (Gibco), and lysed by addition of TRIzol reagent (Thermo Fisher Scientific), and the RNA was purified using the RNeasy kit (Qiagen), followed by DNase digestion with RQ1 DNase (Promega) to remove remaining plasmid DNA. Reverse transcription was performed, using 500 ng total RNA with the qScript cDNA synthesis kit (Quantabio). Real-time qPCR was carried out using the Luna qPCR Reaction Mix (NEB) on a StepOne thermocycler (Thermo Fisher Scientific). Firefly and Renilla reporter mRNAs were amplified by specific primer pairs (see Supplementary Table S1). All reactions were performed in technical and biological triplicates; fold-changes (relative to reporter transfection, but without RNA transfection) were calculated using the ΔΔCt method with average cycle threshold (Ct) values, and Firefly mRNA expression was normalized to Renilla mRNA levels.

Viral infection, plaque assays and immunofluorescence

Vero E6 cells were cultured in DME-medium supplemented with 10% FBS and 100 U/ml penicillin and 100 µg/ml streptomycin (Gibco) at 37°C and 5% CO_2. Cells were seeded with a density of 0.5×10^5 per well (24-well plate). RNA transfections were done using Lipofectamine 2000 in a total volume of 0.5 ml medium/well (Thermo Fisher Scientific). For AS-circRNA screening, cells were transfected either with increasing amounts of individual circular RNAs, or their linear counterpart (between 25 and 5000 ng per assay, as described in Results and the figures). Culture medium was exchanged 1 h prior and 4 h after transfection. 24 h post-transfection, cells were inoculated with SARS-CoV-2 at a multiplicity of infection (MOI) of 0.1 pfu/cell at 33°C. At 1 h post-infection, the inoculum was replaced with fresh medium. Virus-containing supernatants were collected at 24 h post-infection, and virus titers were determined by plaque assays (35).

For durability assays (Figure 3E, Supplementary Figure S4), 3×10^5 Vero E6 cells were seeded per well (6-well plate) one day before transfection or infection.

For transfection of RNA prior to viral infection, 5 µg of respective RNAs was transfected, using Lipofectamine 2000 in a total volume of 1 ml medium/well (Thermo Fisher Scientific). The medium was replaced by 2 ml fresh medium after 4 h. 24 h post-transfection, cells were inoculated with SARS-CoV-2 at an MOI of 0.1 pfu/cell at 33°C. At 1 h post-infection, the inoculum was replaced with fresh medium, and cells were subsequently incubated for a total of 72 h.

For transfection post infection, cells were inoculated with SARS-CoV-2 at an MOI of 0.1 pfu/cell at 33°C. At

1 h post-infection, the inoculum was replaced with fresh medium, and 5 μg of respective RNAs was transfected, using Lipofectamine 2000 in a total volume of 1 ml medium per well (Thermo Fisher Scientific). The medium was replaced by 2 ml fresh medium after four hours, followed by incubation of cells for a total of 72 h.

Virus-containing supernatants were collected at 16, 24, 40, 48, 64 and 72 h post-infection or transfection, and virus titers were determined by plaque assays (35).

Cryopreserved normal human bronchial epithelial (NHBE) cells of a non-smoking, healthy donor were obtained from Lonza (CC-2540, Batch No. 18TL269120). The undifferentiated cells were seeded on collagen IV-coated transwell plates (CLS3470-48EA; Corning Costar) and grown in a 1:1 mixture of DMEM (Thermo Fisher Scientific) and BEBM (CC-3171; Lonza), supplemented with BEGM Bronchial Epithelial Single Quots Kits (CC-4175, Lonza) and retinoic acid (74 nM; R2625; Sigma-Aldrich), with medium exchange every second day. After reaching confluence, the cells were cultivated for five (Experiment #1) or seven weeks (Experiment #2) under air–liquid conditions for full differentiation into pseudo-stratified human airway epithelia. The medium from the basolateral compartment was renewed every second day, and the apical surface was washed weekly with PBS (Thermo Fisher Scientific).

The differentiation status of NHBE cells was further validated via immunofluorescence, using antibodies against ZO-1 (Invitrogen, #40-2200, 1:100), mucin 5AC (abcam, #ab198294, 1:100), tubulin IV (abcam, #ab179509, 1:100) and Alexa Fluor 488-coupled F(ab')2 goat anti rabbit IgG (H + L) antibody (Invitrogen, #A-11070, 1:500). Images were acquired by confocal laser-scanning microscopy (Leica TCS SP5), and data were processed, using the Imaris 8.4 software package (Bitplane).

For transfection, the apical surface of the cells was washed three times with 150 μl PBS, and afterwards 5 μg RNA was transfected in a total volume of 125 μl using Lipofectamine 2000 (Thermo Fisher Scientific). Four hours post-transfection, the cells were washed three times with 150 μl PBS. After 24 h the cells were infected with SARS-CoV-2 (MOI of 3 pfu/cell) for 1 h. Afterwards, the inoculum was removed, and at the indicated time points, the apical surface of the cells was incubated with 150 μl/well PBS for 15 min at 33°C, followed by plaque assays to determine virus titers in the supernatants.

Subcellular fractionation

HeLa cells were seeded with a density of 8×10^5 cells per 6-cm plate and transfected with 3 μg of *in vitro* produced linear or circular RNA or with 4 μg of Tornado-plasmids, using Lipofectamine 2000 in a total volume of 4 ml medium/plate. After 24 h, cells were harvested, and 2×10^6 cells subjected to fractionation, using the NE-PER Nuclear and Cytoplasmic Extraction kit (Thermo Fisher Scientific). RNA for Northern blot analysis was prepared from 75% of the nuclear and cytoplasmic fractions using TRIzol LS (Ambion), while 25% was saved for Western blotting (see below).

Western blot

Viral protein accumulation was analyzed by Western blot of Vero E6 cell lysates, previously transfected with 2.5 μg of circRNAs and infected with SARS-CoV-2 at an MOI of 0.1 pfu/cell at 33°C. Total protein lysates obtained at 24 h post-infection were heat-denatured in SDS-loading buffer (50 mM Tris–HCl pH 6.8, 2% SDS, 10% glycerol, 2.5% 2-mercaptoethanol, and 0.05% bromophenol blue) at 95°C for 10 min. Following separation by SDS-polyacrylamide gel electrophoresis (PAGE; 10%), proteins were blotted onto a nitrocellulose membrane (BioRad). Viral proteins were immunostained overnight with rabbit anti-SARS nucleocapsid protein (N, 200-401-A50; Rockland Immunochemicals, 1:500) or mouse anti-GAPDH antibody (monoclonal antibody G8795, GAPDH-71.1; Sigma-Aldrich, 1:5000) and appropriate secondary antibodies (HRP-conjugated anti-rabbit (A0545-1ML) or anti-mouse (A9044-2ML), Sigma-Aldrich, each 1:10,000). The blots were developed using the Lumi-Light Western-Blotting Substrate (Roche). Western blot signals were estimated by densitometry, using GelAnalyzer 19.1 software.

For subcellular fractionation, 1.25% of cytoplasmic or nuclear fractions were analyzed by SDS-PAGE (10%) and Western blotting through detection of hnRNP A1 (monoclonal antibody, sc-32301, 4B10; Santa Cruz Biotechnology, 1:2000) and GAPDH (monoclonal antibody G8795, GAPDH-71.1; Sigma-Aldrich,1:5000).

Northern blot

All Northern blots were performed as previously described (36).

Denaturing polyacrylamide Northern blot. For detection of *in vitro* produced linear and circular RNAs transfected in HeLa or Vero-E6 cells, 1 μg of total RNA or 20% of cytoplasmic/nuclear fractions was used, and for Tornado-derived circRNAs 250 ng of total RNA or 20% of cytoplasmic/nuclear fraction. Samples were separated on a 10% denaturing polyacrylamide gel, transferred to a nylon membrane (Hybond-N+; Amersham) by semi-dry blotting, and crosslinked by UV light (0.125 mJ/cm^2 at 254 nm). Membranes were subsequently hybridized with DIG-UTP-labeled (DIG RNA Labeling Mix, Roche) riboprobes in NorthernMax hybridization buffer (Thermo Fisher Scientific) at 60°C. For *in vitro* produced RNAs, CTR2 or 1–75 specific riboprobes were used that are able to detect both circular and linear molecules. For detection of Tornado circRNAs, a circular-junction-specific probe was used. For oligonucleotide and riboprobe sequences, see Supplementary Table S1. Probe detection with alkaline phosphatase-conjugated anti-DIG-Fab fragments (11093274910, Roche) and CDP-Star chemiluminescence substrate was done as described (Roche).

RNase R and RNase H treatment. To confirm circularity of the detected Tornado-derived circRNAs, 250 ng of total RNA were either incubated with 5 U/μg RNase R (Biozym) in 1x RNase R buffer for 1 h at 37°C, or with 50 ng

of antisense DNA-oligonucleotide in 1x RNase H buffer for 20 min at 37°C, followed by addition of 1 U RNase H (NEB) and incubation for 40 min at 37°C. To assess whether the effect of AS-circRNAs is based on a blocking or cleavage mechanism, 3 μg of total RNA from previously transfected HeLa cells (5 μg circRNA, 500 ng 5′-leader reporter) were incubated with 600 ng antisense DNA-oligonucleotide and RNase H-treated (see above). Samples were analyzed by denaturing polyacrylamide Northern blot as described above.

Glyoxal Northern blot. For detection of the SARS-CoV-2 genome and subgenomic RNAs, 3 μg of total RNA from previously transfected (5 μg *in vitro* produced linear or circular RNAs per 3×10^5 cells on a 6-well plate, in 1 ml total volume), and infected (at 24 h post-infection; MOI = 0.1 pfu/cell) Vero E6 cells were mixed with glyoxal loading buffer (Ambion) and incubated for 30 min at 50°C. RNAs were separated by 1% agarose gel electrophoresis in 1x MOPS buffer, transferred to a nylon membrane (Hybond-N+, Amersham), and hybridized with a DIG-labelled riboprobe complementary to the 3′-UTR common to the positive-strand viral genome as well as the subgenomic RNAs (SARS-CoV-2 genome positions 29,535 to 29,848; for the probe sequence, see Supplementary Table S1; NorthernMax hybridization buffer; Thermo Fisher Scientific; 68°C). The same procedure was used for detection of the full-length 5′-leader reporter transcript: 3 μg of total RNA from previously transfected HeLa cells (5 μg circRNA, 500 ng 5′-leader reporter) were treated and separated as described above, followed by probing with a DIG-labeled riboprobe (position 1 to 997 of the reporter-derived transcript, see Supplementary Table S1). Probe detection was performed as described above.

RNA-Seq and data analysis

For global analysis of viral genome and subgenomic RNA abundance after transfection of *in vitro* produced linear or circular RNA, 3×10^6 Vero E6 cells were seeded in a 6-well plate 1 day before transfection. 5 μg of respective *in vitro* produced RNA was transfected in 1 ml total volume, using Lipofectamine 2000. At 24 h post-transfection, cells were inoculated with SARS-CoV-2 at an MOI of 0.1 pfu/cell at 33°C. At 24 h post-infection, RNA was isolated by TRIzol extraction (Ambion). 1 μg of total RNA, together with 2 μl of a 1:100 dilution of ERCC standard (Ambion) as spike-in, was used to perform poly(A)-selection (NEBNext® Poly(A) mRNA Magnetic Isolation Module; NEB), followed by library preparation (NEBNext Ultra II Directional RNA Library Prep Kit for Illumina; NEB). Libraries were sequenced on an Illumina NextSeq 500 platform (single-read, 150 bp). RNA-seq data were deposited in the Sequence Read Archive (PRJNA693241) of NCBI. Sequence reads were aligned to the SARS-CoV-2 reference genome sequence (NC_045512.2) using STAR (37). Positions of the transcription regulatory sequences (TRS) and subgenomic RNAs (sgRNAs) were based on the SARS-CoV-2 transcriptome tracks (6).

To quantitate the total viral RNA accumulation in each sample (Figure 4B), and to calculate the read coverage in the nine segments across the SARS-CoV-2 viral genome (Figure 4C), the number of uniquely mapped sequence reads of each sample were normalized with the corresponding number of total sequenced reads (mock: 33.4 mio; CTR2_lin: 49.5 mio; CTR2_circ: 66.4 mio; 1–75_lin: 46.5 mio; 1–75_circ: 40.1 mio). For the read coverage across the viral genome, the terminal regions were not used (positions 1–75 and the 3′-terminal 50 nucleotides), due to their low representation.

RESULTS

Design of AS-circRNAs targeting SARS-CoV-2 RNA

To develop new RNA-based therapeutics for antiviral strategies, we designed and tested artificial small circRNAs containing antisense-RNA sequences that target SARS-CoV-2 RNA. We focussed on the 5′-UTR, because its RNA secondary structure is relatively well characterized and highly conserved (2,3), and there is evidence for important functions of the 5′-UTR on multiple levels, including viral genome replication (38) and transcription [subgenomic RNA (sgRNA) synthesis, (5,6)], translational initiation (39), RNA stability (3) and, potentially, RNA packaging (40). To screen for functional antisense sequences and optimal SARS-CoV-2 targets in the 5′-UTR, we initially used two separate luciferase reporter systems (Figure 1A).

First, to assess effects of antisense-circRNAs (AS-circRNAs) on the 5′-UTR of the viral genome, the first 265 nucleotides of the SARS-CoV-2 genome including the ORF1a translation start codon and the first 24 nucleotides of ORF1a, were fused in-frame with the luciferase ORF, resulting in the '5′-UTR' reporter construct (Figure 1A).

Second, to determine effects on the 5′-UTR of viral sgRNAs, the 5′-terminal 75 nucleotides of the SARS-CoV-2 genome were used, comprising the common 'leader' sequence (including the TRS element), which is present on all sgRNAs. That region, followed by 25 nucleotides with AUG start codon and 5′-terminal coding sequence of the S protein, were fused to the luciferase ORF, resulting in the '5′-leader' reporter (Figure 1A).

We selected the exact positioning of the antisense sequences according to the current secondary structure model of the 5′-UTR and 5′-leader regions, containing three highly conserved stem-loop RNA structures [SL 1–3, (3,4)]. Our previous work on AS-circRNAs had indicated that perfect base-pairing between circRNA and target over at least 30 nucleotides was required for stable interaction (Silke Schreiner and Christina Pfafenrot, unpublished observations).

On this basis, a series of six short AS-circRNAs, between 66 and 76 nts in length and with 40–50 nts of antisense sequence, was designed to specifically target the SARS-CoV-2 5′-UTR regions (named according to target boundaries; for a schematic representation and exact SARS-CoV-2 target boundaries, see Figure 1A and B; antisense sequences are listed in Supplementary Table S1). AS-circRNA 1–40 targets the 5′-terminal 40 nucleotides of the SARS-CoV-2 genome (and sgRNAs), including SL1; AS-circRNA 1–65 targets the 5′-terminal 65 nucleotides, but omits the complete 27-nucleotide SL1, and AS-circRNA 1–75 extends this base-pairing interaction by

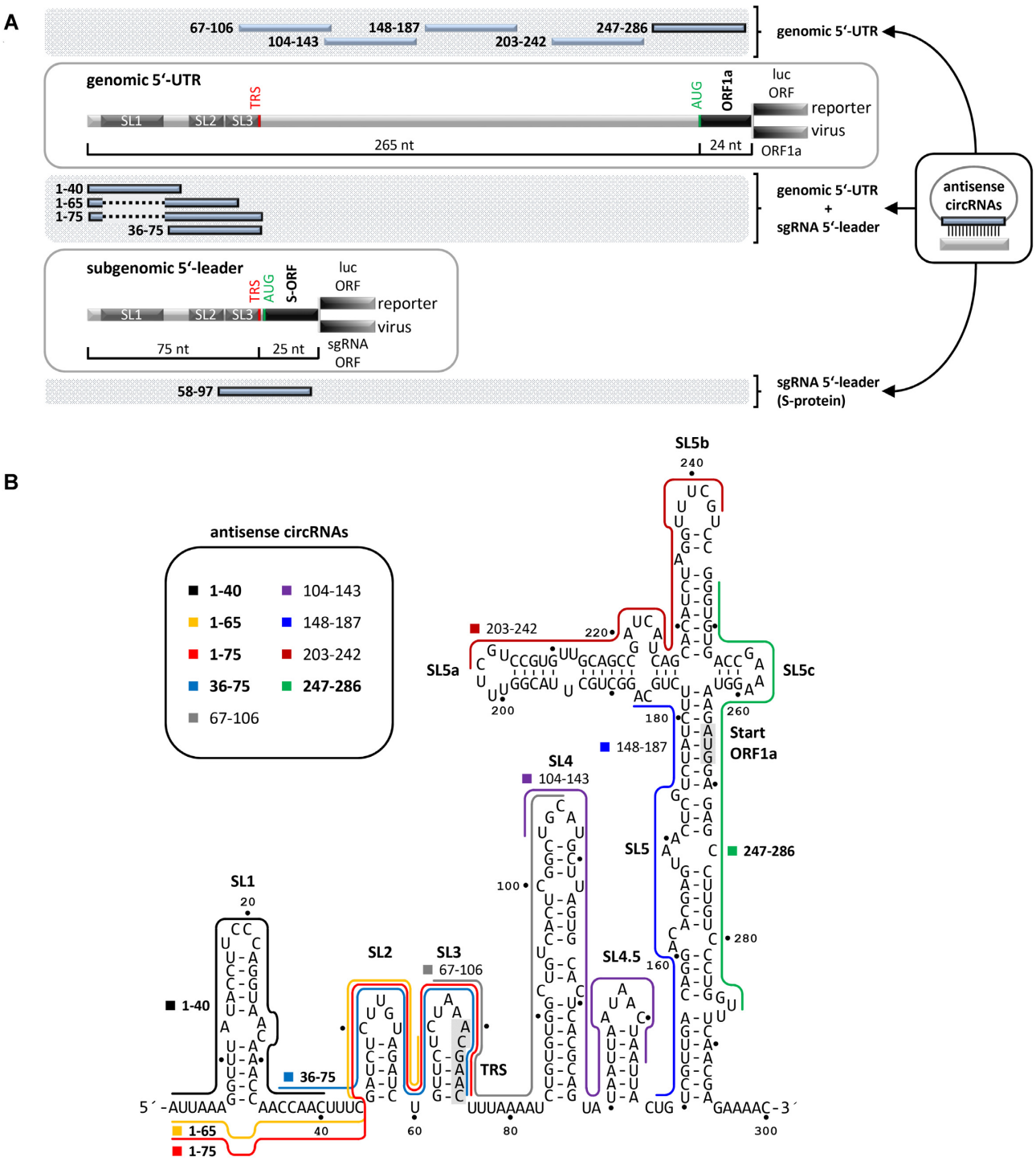

Figure 1. Design of AS-circRNA targeting SARS-CoV-2 RNA. (**A**) Schematic representation of the 5′-UTR (top, nts 1–265) and 5′-leader (bottom; nts 1–75) sequences, targeted by AS-circRNAs, either in a luciferase-reporter (luc), or in the viral SARS-CoV-2 context (ORF1a or S). Target regions of individual AS-circRNAs are represented as blue bars with nucleotide coordinates. The conserved 5′-terminal stem-loop elements (SL1-3) are indicated, as well as the transcription regulatory sequence (TRS) of the 5′-leader. Note that the target regions of AS_1–65 and AS_1–75 circRNAs omit the first stem–loop (SL1), represented as a dashed line. (**B**) Target regions of AS-circRNAs within the 5′-leader (nts 1–75) and 5′-UTR of SARS-CoV-2 (nts 1–265), represented in the context of the secondary structure model of this region [nts 1–300; (3,4)]. For a schematic representation, see panel **A**. The core TRS element (nts 70–75) and the AUG start codon of ORF1a (nts 266–268) are shaded in grey. Note that AS_58–97 circRNA is not included, since it overlaps with the ORF of the S protein.

ten nucleotides, including the TRS element. AS-circRNA 36–75 again was designed to base-pair with the single-stranded region between SL1 and 2, and the less stable SLs 2 and 3, including the TRS element. These four AS-circRNAs have in common that they can base-pair with both the SARS-CoV-2 genomic RNA and all eight major sgRNAs (sgRNAs 2–9) produced in infected cells.

In addition, two AS-circRNAs were designed to specifically target either the ORF1a translation start site, along with flanking regions (in the SARS-CoV-2 genome RNA), or the ORF encoding the viral S protein (in sgRNA 2): AS-circRNA 247–286 spans the 3′-terminal region of the genomic 5′-UTR region and the first 21 nucleotides of the ORF1a, whereas AS-circRNA 58–97 targets SL3, the TRS element and the first 21 nucleotides of the S-protein ORF (Figure 1A). As control and for normalization of luciferase activities, two non-specific circRNAs were used in these experiments, each comprising a randomized sequence of 40 nucleotides instead of the antisense sequences.

Synthetic AS-circRNAs inhibit translation of SARS-CoV-2 reporter constructs

We initially used AS-circRNAs transiently overexpressed in HeLa cells by the so-called Tornado system [Twister-Optimized RNA for Durable Overexpression, see (32)] which relies on an RNA polymerase III-driven and self-cleaving expression cassette, combined with circularization by endogenous RtcB tRNA ligase (Supplementary Figure S1A). One day after transfection of the circRNA expression constructs, either genomic 5′-UTR or subgenomic 5′-leader reporters were transfected, followed by luciferase assays (Supplementary Figure S1B). Overexpression at similarly high levels of all ten SARS-CoV-2 5′-UTR/5′-leader specific AS-circRNAs, as well as of two control circRNAs, was confirmed by Northern blot analysis (Supplementary Figure S1C). In addition, circular configuration was stringently established by RNase H cleavage assays (for AS_1–75 circRNA), and cellular distribution between nucleus and cytoplasm was characterized (for AS_1–75 and CTR2 circRNAs, see Supplementary Figure S1DE). Based on reporter assays with both the genomic (5′-UTR) and subgenomic (5′-leader) constructs, all of these overexpressed anti-SARS-CoV-2 circRNAs, except for AS_67–106 and AS_104–143, were found to reduce luciferase expression to levels between 50 to 60% (Supplementary Figure S1F). Since the four AS-circRNAs against the 5′-leader region (nucleotides 1–75) as well as three AS-circRNAs upstream of or spanning the ORF1a translation initiation site (nucleotides 148–286) reduced reporter expression most profoundly, we decided to focus our subsequent analysis on these regions.

However, the Tornado-based circRNA expression system results in massive overexpression, in the order of 10^6 copies per cell (31), and one cannot rule out effects due to linear precursors or side-products. Therefore we switched for all following assays to synthetic AS-circRNAs transfected in mammalian cells, which is advantageous, because it is a biochemically well-defined system; for example, transfected circRNA quantities can be titrated and the effects of circular and linear forms can be directly compared with each other.

AS-circRNAs were produced *in vitro*, based on transcription by T7 RNA polymerase and circularization by T4 RNA ligase, followed by gel purification (Figure 2A). Each circRNA was designed such that the antisense sequence was linked to a common short stem–loop (6 perfect base-pairs with two overhanging ends that were joined by ligation). The antisense region and the stem–loop are connected by two three-nucleotide linkers, to allow a more flexible presentation of the antisense sequence.

To functionally characterize this series of AS-circRNAs, we first tested their ability to inhibit translation in the two luciferase reporter systems (for a flowchart of analysis, see Figure 2B): HeLa cells were first transfected with circRNA; after 24 h, the reporter construct was transfected and, after another 24 h, luciferase activities were measured.

For quality control and evidence of circularity, purified AS-circRNAs (as well as their linear counterparts) were characterized by denaturing PAGE (Figure 2C): Note that all of these relatively short circRNAs are RNase R resistant, in contrast to the corresponding linear RNAs, and that the circular configuration results in slower mobility relative to the linear form, demonstrating circularity. Regarding cellular distribution after transfection, AS-circRNAs as well as their linear counterparts were detected predominantly in the cytoplasmic compartment (where coronavirus replication is localized), as shown for AS_1–75 and control linear and circular RNAs (Supplementary Figure S2).

Comparing the two reporters, 5′-UTR versus 5′-leader, corresponding effects of AS-circRNAs were observed for the first four AS-circRNAs that target the 5′-terminal region, nucleotides 1–75 (AS_1–40, AS_1–65, AS_1–75, and AS_36–75; see Figure 2D): Only in case of the longest version, AS_1–75, which excludes stem-loop 1, both reporters were strongly reduced in translation (to 39 and 18% residual level, respectively). The two shorter AS-circRNAs (AS_1–40 and AS_1–65) showed smaller or insignificant activities. The strong effect of AS_1–75 circRNA is not simply due to extended base-pairing, since the shorter AS_36–75 was almost as strong as AS_1–75: reduction to 57 and 29%, respectively, for the two reporters.

Moving from the 5′-end to the regions overlapping the translation start codons for the ORF1a and the S-gene, we assayed AS_247–286 circRNA (for the genomic 5′-UTR reporter) and AS_58–97 circRNA (for the 5′-leader reporter): Both had strong effects on reporter activity (reduction to 15% and 54%, respectively). The use of AS-circRNAs (AS_247–286 and AS_58–97) targeting the AUG start codon regions (of ORF1a and S-gene, respectively) in combination with circRNAs targeting the 5′-terminal leader region did not further increase the inhibitory action on reporter translation (see three combinations for each of the two reporters, Figure 2D).

To address the important question of whether the circular configuration of the AS-circRNA is important for inhibitory activity, we compared the two AS-circRNAs with the strongest inhibitory effects with their linear counterparts: AS_1–75 and AS_247–286, using the 5′-UTR reporter, and AS_1–75 and AS_36–75, using the 5′-leader reporter (Figure 2E). To provide additional support for the specificity of the inhibition, we also

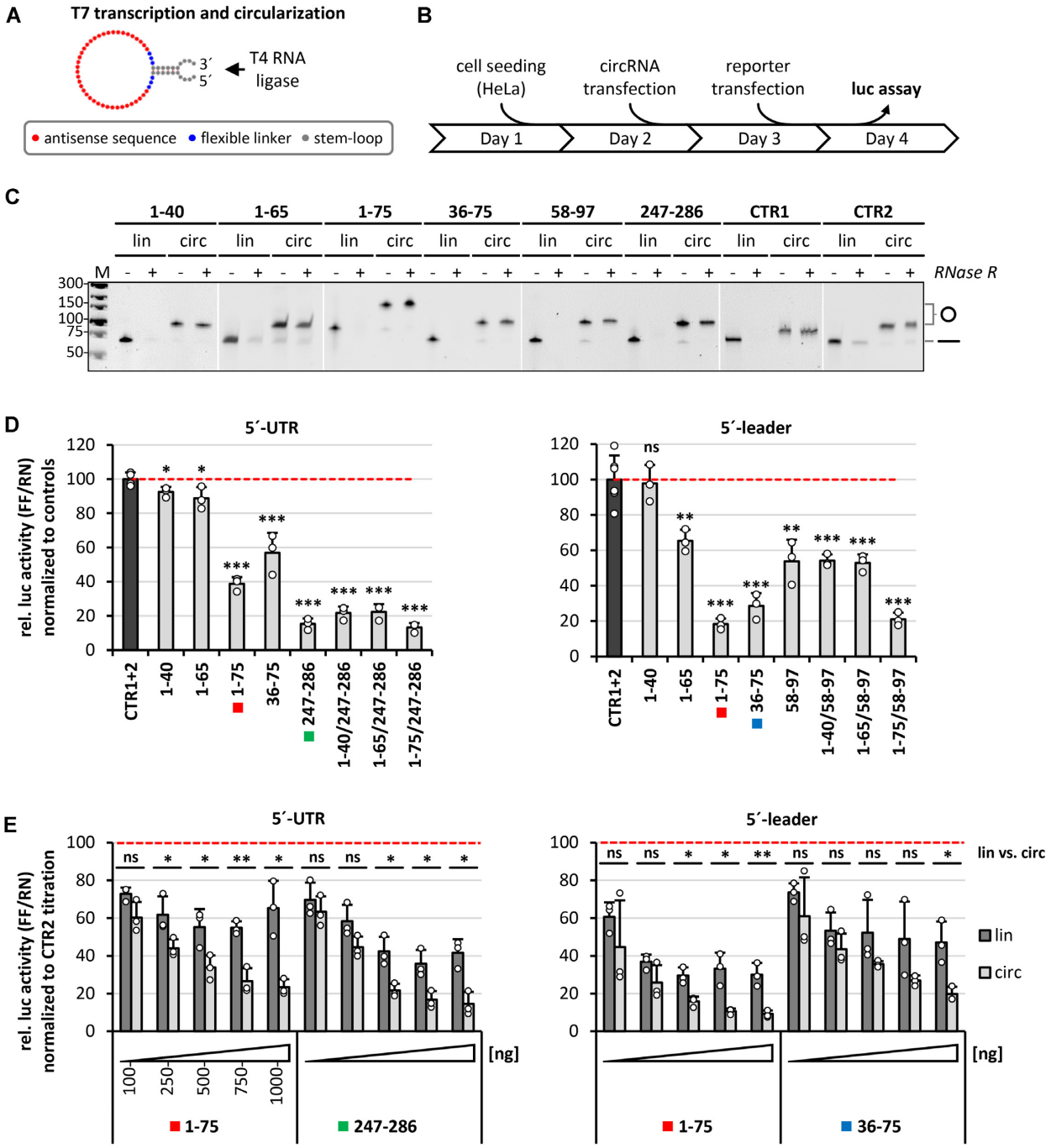

Figure 2. Screening of active AS-circRNAs: 5′-UTR and 5′-leader reporter assays. (**A**) Design of synthetic AS-circRNAs. CircRNAs were produced by *in vitro* T7 transcription and subsequent circularization by T4 RNA ligase. Each circular RNA is composed of a stem–loop with overhangs for efficient ligation (grey), a short stretch of unrelated nucleotides for enhanced flexibility (blue), and the antisense sequence (red). (**B**) Experimental workflow for luciferase reporter assays in HeLa cells transfected with synthetic circRNAs. (**C**) AS-circRNA synthesis. RNase R treatment and aberrant electrophoretic migration confirm the circularity of the produced circRNAs. Gel-purified linear and circular RNAs (lin/circ) were treated with RNase R, or left untreated (–/+), and analyzed by denaturing polyacrylamide electrophoresis and ethidium bromide staining. Mobilities of circular (o) and linear (–) forms are marked. *M*, DNA markers (sizes in bp). (**D**) Luciferase reporter assays reveal regions accessible to AS-circRNAs, based on the repression of luciferase activity by specific SARS-CoV-2 5′-UTR (left) and 5′-leader reporter constructs (right). HeLa cells were transfected with the respective circRNA (as indicated below the diagram) or a combination thereof (e.g. AS.1–40/247–286). The color code highlights those AS-circRNAs that were analyzed in more detail in panel E. After 24 h, the respective reporter was transfected (5′-UTR or 5′-leader), and relative luciferase activities (ratio of Firefly and Renilla expression) were measured, normalized to control circRNAs CTR1 and 2 (mean and standard deviations of three replicates, $*P < 0.05$, $**P < 0.005$, $***P < 0.001$, ns = not significant, two-sided *t*-test). **(E)** Dose dependence and comparison of circular versus linear configuration of selected antisense-RNA regions. HeLa cells were transfected with increasing amounts (100–1000 ng per assay) of circRNAs (light gray), or their linear counterparts (dark grey; as indicated below the diagram). After 24 h, the respective reporter constructs were transfected (5′-UTR or 5′-leader), and relative luciferase activities (Firefly/Renilla expression ratios) were measured, normalized to control circRNA CTR2 (mean and standard deviations of three replicates, $*P < 0.05$, $**P < 0.005$, $***P < 0.001$, ns = not significant, two-sided *t*-test).

measured dosis-dependent reduction in reporter activity for the selected RNAs, with doses ranging between 100 and 1000 ng per assay. For each of the four setups, we observed clear dosis-dependent effects, in particular for the circular configuration. Under the conditions used, maximal activities were attained with 750–1000 ng of AS-circRNA per assay, whereas the inhibition with linear counterparts leveled off at 500 ng and above. Importantly, the circRNAs were consistently more potent than their linear counterparts. At higher concentrations, the circRNA caused a more than 2-fold stronger reduction of reporter activity than the corresponding linear RNA. This superior inhibitory efficacy of the AS-circRNAs may be due to differential stabilities or intracellular localizations of the transfected RNAs, their intrinsic antisense activity, base-pairing potential, structural properties, or a combination thereof.

We conclude that, based on two separate reporters and AS-circRNA transfection in HeLa cells, both the 5′-leader- and the AUG-start codon-proximal regions can be efficiently targeted by AS-circRNAs, resulting in strong translational inhibition down to 10% residual level.

Inhibition of SARS-CoV-2 proliferation by designer AS-circRNAs

Following the identification of specific AS-circRNAs that effectively inhibit translation of reporter RNAs, we sought to corroborate key findings of our study by using SARS-CoV-2-infected cells. To this end, the set of AS-circRNAs we had characterized in our reporter assays, except for inactive AS_1–40, as well as two control RNAs, were transfected in Vero E6 cells, which are permissible for SARS-CoV-2 infection and allow the production of infectious virus progeny (for a flowchart, see Figure 3A). Each AS-circRNAs was transfected in three different quantities (25, 250 and 2500 ng per assay), and 24 h later, cells were infected with SARS-CoV-2 at an MOI of 0.1 pfu/cell. 24 h post-infection, cell culture supernatants were collected, and virus titers were determined by plaque assays to assess the antiviral effects of individual AS-circRNAs on viral replication in cell culture (Figure 3B).

Compared to the controls (untreated cells, mock-transfected cells, two different control AS-circRNAs), the three AS-circRNAs targeting the untranslated leader region differentially affected virus titers: The strongest effect on viral proliferation was measured for AS_1–75, a reduction to 9% of control level, consistent with the strong effect observed in the previous reporter assays (compare Figures 3B and 2D). The shortened version of this circRNA, AS_1–65, still had a moderate, but significant effect on virus titers (reduction to 33% compared to untreated control cells), whereas AS_36–75 had no significant effect (Figure 3B). In contrast to the initial reporter assays, AS_58–97, designed as specific for the subgenomic mRNA encoding the S protein, and AS_247–286, targeting the genomic region including the ORF1a start codon, did not significantly reduce virus titers (Figure 3B). Based on these results, we focussed our further analysis on the AS_1–75 circRNA, which targets both viral genomic and all subgenomic RNA species.

To obtain additional evidence for inhibition of viral replication, we also measured viral protein synthesis by Western blotting, using SARS-CoV-2 nucleocapsid (N) protein-specific antibodies (Figure 3C). Clearly, compared to the controls (untreated, mock, CTR 1 and 2) and four other AS-circRNAs, intracellular accumulation of viral N protein was most profoundly reduced in the cells treated with AS_1–75 circRNA, consistent with the observed inhibitory effects of this particular circRNA on the production of infectious virus progeny.

Finally, we compared effects of circular and linear versions of the antisense sequence of AS_1–75 in their efficiency on viral proliferation, using an extended range of RNA quantities (625–5000 ng per assay; see Figure 3D). We observed a strong and dosis-dependent antiviral effect of AS_1–75 circRNA, with virus titers reduced down to 4% (at 2500 ng per assay); at an even higher dose (5000 ng), virus titers were reduced to 7%, perhaps reflecting some toxic effects at this high circRNA quantity or suboptimal ratios of circRNA to transfection reagent. In contrast, control AS-circRNA had no significant effect. Comparing the effects of circular versus linear RNAs, we observed at all quantities assayed, that circRNA was clearly superior to the corresponding linear version, consistent with our results from reporter assays (see above and Figure 2E).

In addition to the general workflow (Figure 3A), in which we monitored the increase of virus titers until 24 h post-infection, we addressed the question of whether the antiviral effect of AS_1–75 circRNA persists for longer time periods (Figure 3E): We determined virus titers in the culture supernatants of cells transfected with linear versus circular AS_1–75 RNA (along with appropriate controls) and collected at six time points from 16 to 72 h post-infection. Whereas effects of linear and circular control RNA (CTR2) did not significantly differ from the mock control, AS_1–75 circRNA caused a significant reduction of virus titers, especially between 24 to 48 h post-infection. This antiviral effect was specific for the circular configuration and indicates durability of the effect over at least two days under the conditions used. Finally, combining virus titer measurements from several assays of the antiviral effect of AS_1–75 circRNA (all measured at 24 h post-infection and based on Figures 3B, D, E), we estimated an EC_{50} value in the 20–50 nM range for this most effective AS-circRNA (Supplementary Figure S3).

Furthermore, to answer the question whether AS_1–75 circRNA also shows an effect in cells already infected with virus, additional experiments were performed in reverse order of circRNA transfection and virus infection (see Supplementary Figure S4): One hour after virus infection, linear or circular AS_1–75 RNA (together with appropriate controls) was transfected, and virus titers were determined in the culture supernatants at six time points after RNA transfection, from 16 to 72 h post-infection. We chose a one-hour interval between virus infection and circRNA transfection, as used in many published studies. Binding and uptake of virus particles is a relatively fast process (for example, see reference 41). Therefore, one hour is sufficient for establishment of the viral infection, and at the same time, we avoid any potential problems with dying cells, which at later time points would accumulate, obscure any effects, and

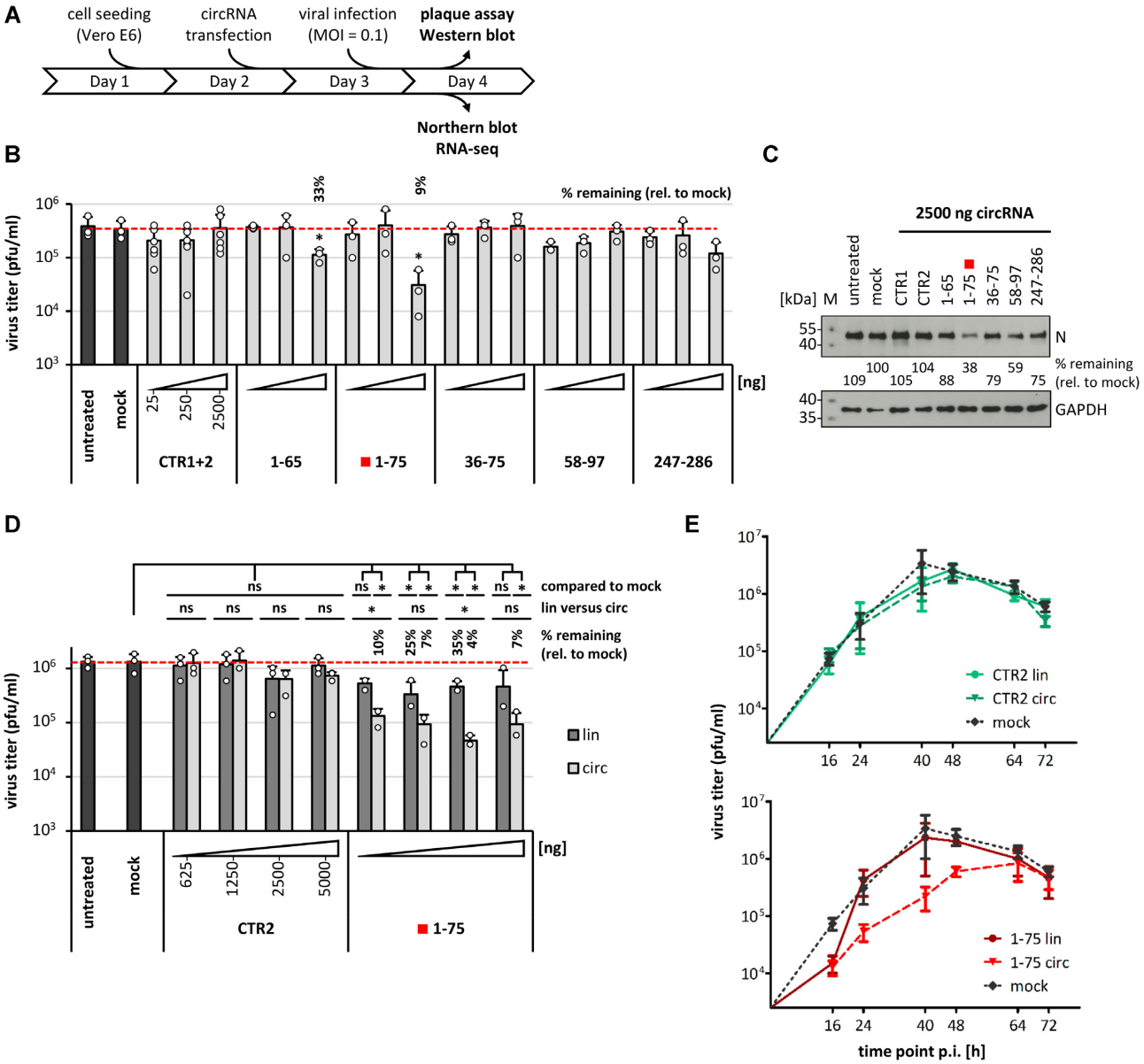

Figure 3. Inhibition of SARS-CoV-2 proliferation by AS-circRNAs: viral infection assays. (**A**) Experimental workflow for viral infection assays using Vero E6 cells. (**B**) Screening of AS-circRNAs by virus titer assays identifies AS_1–75 as the most effective antiviral circRNA. Vero E6 cells were transfected with increasing quantities of circRNAs (25, 250 and 2500 ng per assay; light gray; as indicated below the diagram). After 24 h, cells were infected with SARS-CoV-2 (MOI = 0.1 pfu/cell). The effects on virus titers were measured by virus plaque assays using cell cutlure supernatants collected at 24 h post-infection (mean and standard deviations of three experiments, $*P < 0.05$, ns = not significant, two-sided *t*-test). Untreated (without RNA and transfection reagent) and mock-treated cells (without RNA, but with transfection reagent) served as controls. Residual virus titers of significantly affected samples are indicated as 'percent remaining' relative to mock treatment. (**C**) Viral protein synthesis assays: Western blot analysis of the viral nucleocapsid protein (N) confirms reduction of viral protein accumulation in cells treated with specific AS-circRNAs. Vero E6 cells transfected with 2500 ng of respective circRNAs per assay were harvested, lysed, and equal amounts of protein were analyzed by Western blotting, using the nucleocapsid protein as a marker for viral protein accumulation (quantitation of protein levels relative to mock); GAPDH was used as loading control. *M*, protein markers (sizes in kDa). (**D**) AS_1–75 circRNA: dose dependence of antiviral effect, in comparison to its linear counterpart. Vero E6 cells were transfected with increasing amounts (625, 1250, 2500 and 5000 ng) of AS_1–75 circRNA (light gray), or of its linear counterpart (dark gray), followed by viral infection (MOI = 0.1 pfu/cell) after 24 h. Plaque assays were used to determine virus titers in culture supernatants collected at 24 h post-infection (mean and standard deviations of three experiments, $*P < 0.05$, ns = not significant, two-sided *t*-test). As controls, untreated (without RNA and transfection reagent) and mock-treated cells (without RNA, but with transfection reagent) were used, as well as transfections with linear or circular control RNA (CTR2). The virus titer of significantly affected samples is indicated as 'percent remaining', relative to mock treatment. (**E**) Durability of antiviral activity of AS_1–75 circRNA. Vero E6 cells were transfected with AS_1–75 circRNA or its linear counterpart (bottom panel; in red), followed by viral infection (MOI = 0.1 pfu/cell) after 24 h (mean and SEM of three experiments). Plaque assays were performed to determine virus titers in culture supernatants collected at the indicated time points (16–72 h post-infection). As controls, mock-treated cells (without RNA, but with transfection reagent) were used (top and bottom panels; in black), as well as transfections with linear or circular control RNA (CTR2; top panel; in green).

make interpretations difficult. Again, in this reverse order, the effects of linear and circular control RNA (CTR2) were not significantly different from the mock control, whereas AS_1–75 circRNA caused a significant reduction in viral titers, especially between 24 and 64 h post-transfection. The antiviral effect was also more pronounced for the circular than for the linear configuration, as observed in the usual setup (Figure 3E).

In addition to the standard Vero E6 cell culture system, we evaluated the antiviral effect of AS_1–75 circRNA in a biologically more relevant, *ex-vivo* respiratory cell culture system, based on differentiated primary normal human bronchial epithelial (NHBE) cells grown in air/liquid interface culture (Supplementary Figure S5). This mimicks the tracheobronchial region of the human respiratory tract in a physiologically relevant cellular environment (42). Differentiated NHBE cells were transfected with linear versus circular AS_1–75 RNA or CTR2, followed by viral infection with SARS-CoV-2 after 24 h and determination of virus titers in the culture supernatants at different time points (24–72 h post-infection). Comparing two independent experiments, we conclude that also in this *ex-vivo* model system AS_1–75 circRNA (as well as its linear counterpart) exhibits a strong inhibiting effect on viral replication.

To assess if an elongation of the antisense region of AS_1–75 further improves its antiviral activity, we tested two more AS-circRNAs in virus titer assays: AS_1–100 (S) and (N), both increasing the base-pairing potential of AS_1–75 circRNA by 25 positions and including a small number of nucleotides from the 5′-terminal coding regions of the S and N genes, respectively (Supplementary Figure S6). However, compared to AS_1–75 (virus titer reduced to 1%, relative to control), both elongated AS-circRNAs were slightly less active (reduction to 7 and 4%, respectively, relative to the CTR3 control circRNA of equal length). Note that the elongated AS-circRNAs were designed to specifically target the sgRNAs that are used for S- and N-protein expression, respectively, whereas AS_1–75 has a broader specificity by targeting both genomic RNA and all plus-strand subgenomic RNAs.

Finally, we assessed the effect of AS_1–75 RNA on viral RNA synthesis more directly (Figure 4). Viral genome RNA and all subgenomic mRNAs were detected in infected and transfected cells by Northern blotting with a probe specific for the 3′-terminus of the genome (Figure 4A). We compared the effects of linear and circular versions of AS_1–75 with four different controls (untreated cells, mock, linear and circular control CTR2 RNA). Only the circular configuration of AS_1–75, but not its linear version, strongly reduced viral RNA levels, both genomic RNA and all subgenomic RNAs that can be resolved, indicating a global effect of this most active AS-circRNA on viral RNA synthesis.

Since Northern blotting cannot be quantitated precisely under these conditions, and not all eight subgenomic RNA species (RNAs 2–9) could be unambiguously identified, we performed RNA-seq, using poly(A)-selected RNA from infected cells. By comparing normalized SARS-CoV-2 genome-mapped reads, which reflect total viral RNA accumulation in infected cells, we found that only the read-counts obtained for cells transfected with AS_1–75 circRNA were strongly reduced (to 12.5% of mock levels; Figure 4B).

In order to analyze individual viral RNA species, we measured the read coverage for nine segments across the SARS-CoV-2 viral genome, each of which are delimited by flanking TRS sites (Figure 4C). Due to the characteristic 3′-coterminal structure of each of the viral RNA species, only full-length viral genome RNA (g) can be assessed directly by read coverage between positions 76 and 21,562. In contrast, production of the individual subgenomic RNAs can be determined only as 'cumulative read coverage': For example, the read coverage between positions 21,562 and 25,391 combines reads for both the genome RNA (RNA 1) and the sgRNA 2 (S).

When we compared cumulative read coverage across the viral genome sequence for cells transfected with linear AS_1–75 RNA, AS_1–75 circRNA, or one of the controls, we found that only in the AS_1–75 circRNA-transfected cells viral RNA levels were strongly reduced (to between 37 and 10% relative to mock). Moreover, the extent of reduction increased with a 5′-to-3′ gradient, and most profoundly within the first three segments, proceeding from viral genome RNA to regions that include more and more sgRNAs. This characteristic behavior suggests that the AS_1–75 circRNA interferes, at least in part, with sgRNA synthesis.

AS-circRNAs exhibit robust activity against SARS-CoV-2 mutant sequences and are superior to modified ASOs

Since newly emerging mutations in the viral genome are of great concern in the current SARS-CoV-2 pandemic, we also assayed whether the activity of designer antisense-circRNA was affected by single point mutations in the target sequence. We focussed on the highly conserved 5′-leader region, where the AS_1–75 circRNA had proved most active, in combination with 5′-leader reporter constructs carrying five different single-point mutations, which naturally occur most frequently in this region (https://www.biosino.org/ViGTK/): 21C→T, 34A→T, 35A→T, 36C→T, 66C→T (Figure 5A).

The reduction of reporter activity by AS_1–75 circRNA was not significantly different for the wildtype reporter and for four different mutant versions at positions 21, 34, 35 and 36; only for the 66C→T mutation the antisense activity of AS_1–75 circRNA was reduced, from residual levels of around 25–50% of control levels (Figure 5B–D). These data suggest that the activity of AS_1–75 circRNA is in most cases surprisingly robust and resistant towards single-point mutations.

Finally we compared the activity of AS_1-75 circRNA with corresponding modified, linear antisense oligonucleotides (ASOs), using both the 5′-leader reporter construct as well as viral infection assays (Figure 5BC and EF, respectively). We assayed two different ASOs of standard length, covering positions 1–45 of the 5′-leader sequence (with stem-loop 1 skipped, as in the AS_1–75 circRNA) and positions 56–75, respectively (Figure 5C). These ASOs were modified either by 2′-*O*-methyl (2′-OMe) or 2′-*O*-methoxyethyl (2′-MOE) nucleotides, which

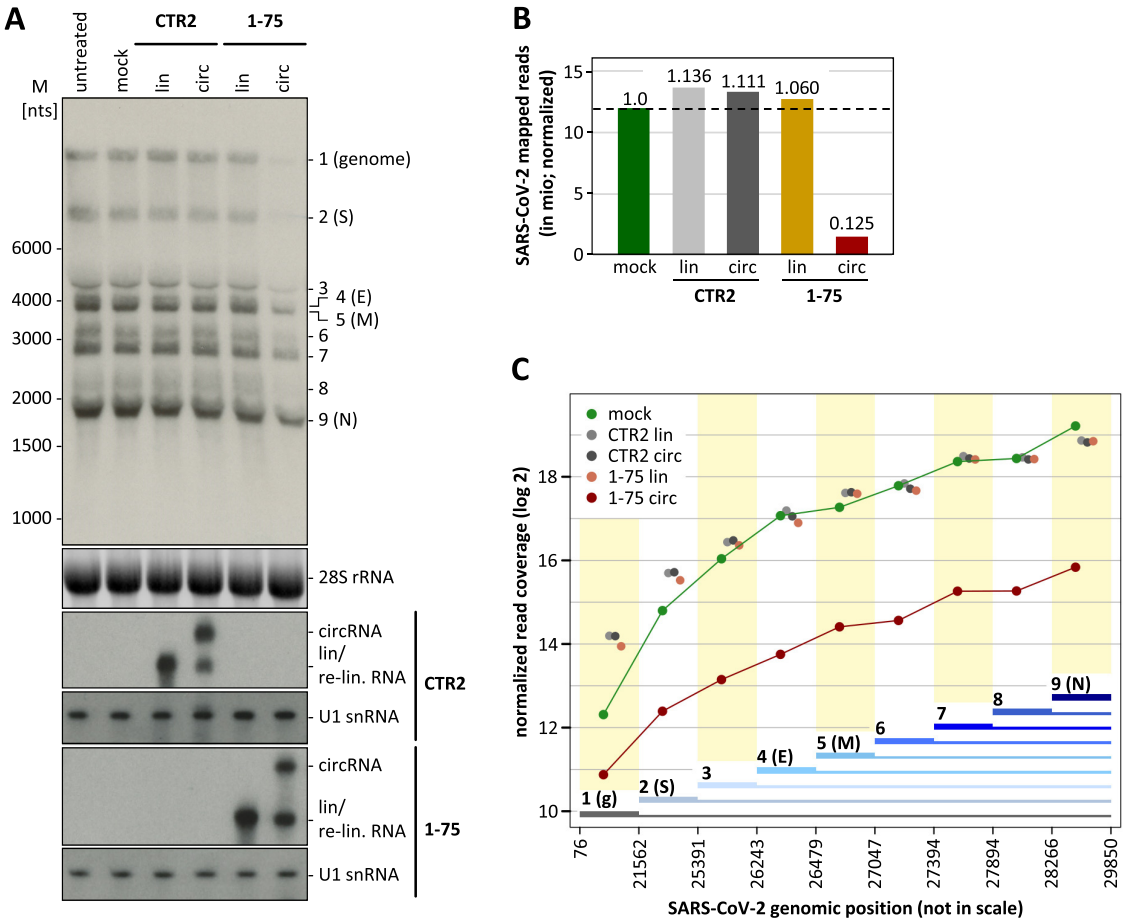

Figure 4. Inhibition of viral RNA synthesis and processing by AS_1–75 circRNA. (**A**) Northern blot analysis of genomic and subgenomic viral RNAs. Vero E6 cells were transfected with AS_1–75 circRNA or its linear counterpart; as controls, untreated (without RNA and transfection reagent) and mock-treated cells (without RNA, but with transfection reagent) were used, as well as cells transfected with linear or circular control RNA (CTR2). At 24 h post-transfection, cells were infected with SARS-CoV-2 (MOI = 0.1 pfu/cell). At 24 h post-infection, total RNA was prepared and subjected to glyoxal-Northern blot analysis, to detect genomic and all subgenomic viral RNA species. *M*, RiboRuler High Range RNA Ladder (Thermo Fisher Scientific). As input control, 28S rRNA was detected by ethidium bromide staining, and CTR2 and AS_1–75 RNAs by specific Northern probes. (**B**) RNA-seq analysis of total viral RNA synthesis. The total numbers of SARS-CoV-2-mapped reads (in mio; normalized to total read number) were compared for RNAs isolated from virus-infected Vero E6 cells that were mock-transfected or transfected with CTR2 control and AS_1–75 RNA, each in linear or circular form, with ratios of read numbers relative to mock conditions indicated. (**C**) Effect of AS_1–75 circRNA on viral genome (g) and subgenomic RNA production in infected cells. Cumulative read coverages (in $\log_2$; normalized to total read number) are plotted for mock-treated, and CTR2 control RNA (lin/circ) or AS_1–75 RNA (lin/circ)-transfected cells. The SARS-CoV-2 genome was divided in nine sections with boundaries defined by the body-TRS sites of the eight subgenomic RNAs (sections used for cumulative read numbers are marked by thick lines; genomic positions are indicated below and drawn not in scale).

should enhance both base-pairing interaction as well as cellular stability. Based on luciferase reporter assays, all four ASOs were clearly less efficient than the AS_1–75 circRNA (by a factor of 3.5–5.4; see Figure 5E). Based on viral infection and virus-titer assays, only the AS_1–75 circRNA, but none of the four ASOs exhibited significant antiviral effects (Figure 5F). We conclude that, comparing antisense-circRNA and state-of-the-art ASOs, these initial assays indicate the superiority of antisense-circRNA as novel and sequence-specific antiviral agents.

DISCUSSION

To our knowledge, this is the first study to report the design and functional evaluation of a series of AS-circRNAs as a novel tool suitable to interfere with gene expression, applied here to block SARS-CoV-2 proliferation. We focussed on the 5′-UTR region, which is not only highly conserved in sequence and structure, but also absolutely essential for the viral life cycle. Based on a series of AS-circRNAs targeting specific 5′-UTR regions of SARS-CoV-2 genome and sgRNAs, we identified a cap-proximal region (including part of the 5′-leader sequence) as the most effective target region. In particular, AS-circRNAs 1–65 and 1–75 strongly interfered with virus proliferation, resulting in at least 10-fold reduced virus titers. Note that the target sequences of these two antisense-RNAs are discontinuous, omitting the first stem–loop. These data suggest that RNA structure information (if available) should be taken into account in the design and optimization of AS-circRNAs.

When evaluating and comparing the efficiencies of AS-circRNAs in our study, one should also take into account that efficiencies are limited by the circRNA transfection efficiencies under our cell culture conditions; therefore the

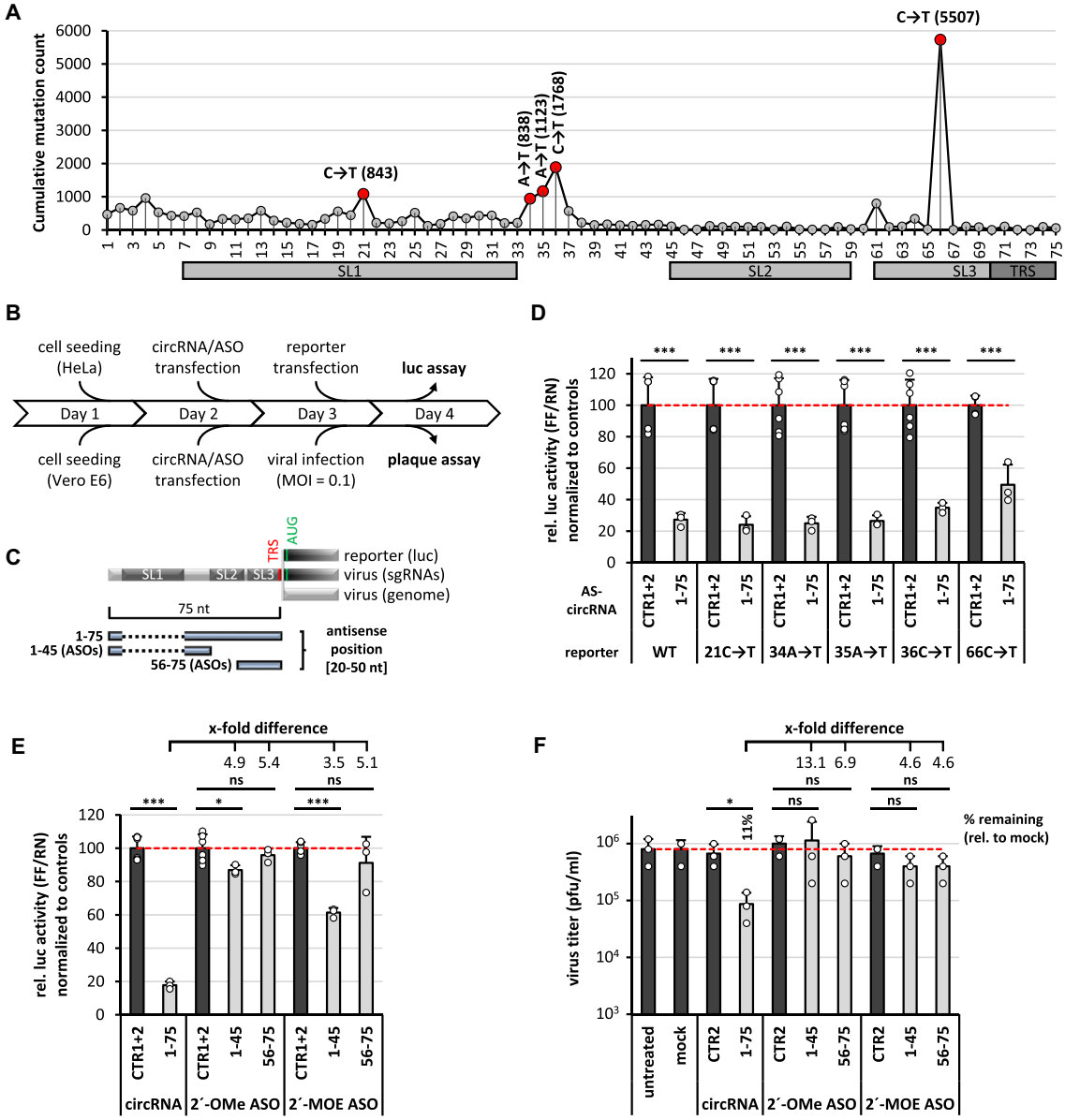

Figure 5. AS-circRNAs exhibit robust activity against SARS-CoV-2 mutant sequences and are superior to modified ASOs. (**A**) Summary of naturally occurring point mutations within the viral 5′-leader of SARS-CoV-2. All annotated mutations are indicated per nucleotide position [cumulative mutation count, as deposited in the ViGTK database (https://www.biosino.org/ViGTK/); as at 30 April 2021). The five most frequent single-point mutations in the 5′-leader region (positions 1–75) are highlighted in red (occurrences given in parentheses) and were selected for mutational analysis. Secondary structures and regulatory elements are marked (SL1–3, TRS). (**B**) Experimental workflow for luciferase reporter assays in HeLa cells, and for viral infection assays using Vero E6 cells, transfected with synthetic circRNAs or modified antisense oligonucleotides (ASOs). (**C**) Schematic representation of the 5′-leader (nts 1–75) sequence, targeted by a AS-circRNA (1–75) or two antisense oligonucleotides (ASOs, 1–45 and 56–75), either in a luciferase-reporter (luc), or in the viral SARS-CoV-2 context (sgRNAs/genome). Target regions of individual AS-circRNA or ASOs are represented as blue bars with nucleotide coordinates. Secondary structures and regulatory elements are marked (SL1–3, TRS, AUG). Note that the targeting regions of AS_1–75 circRNA and 1–45 ASO omit the first stem-loop (SL1), represented as a dashed line. (**D**) Activity of AS_1–75 circRNA in presence of single point mutations within the 5′-leader: luciferase reporter assays. HeLa cells were transfected with 1–75 AS-circRNA or with control circRNAs. After 24 h, the respective 5′-leader reporter plasmids, either without (WT) or with the indicated point mutations, were transfected, and relative luciferase activities (ratio of Firefly and Renilla expression) were measured, normalized to control circRNAs CTR1 and 2 (mean and standard deviations of three replicates, $P < 0.001$***, two-sided t-test). (**E**) Activity of 2′-OMe or 2′-MOE modified ASOs: luciferase reporter assays. HeLa cells were transfected with the AS_1–75 circRNA (1 μg) or ASOs (molar equivalents), respectively. After 24 h, the 5′-leader reporter was transfected, and relative luciferase activities (ratio of Firefly and Renilla expression) were measured, normalized to control circRNAs CTR1 and 2, or correspondingly modified control ASOs CTR1 and 2 (mean and standard deviations of three replicates, $P < 0.05$*, $P < 0.001$***, ns = not significant, two-sided t-test). Fold differences in translational repression between AS_1–75 circRNA and ASO treatments are indicated. (**F**) Antiviral activity of 2′-OMe or 2′-MOE modified ASOs: virus infection assays. Vero E6 cells were transfected with AS_1–75 circRNA (2500 ng per assay) or with ASOs (molar equivalents). After 24 h, cells were infected with SARS-CoV-2 (MOI = 0.1 pfu/cell). The antiviral effects were measured by virus plaque assays at 24 h post-infection (mean and standard deviations of three experiments, *$P < 0.05$, ns = not significant, two-sided t-test). Untreated (without RNA and transfection reagent) and mock-treated cells (without RNA, but with transfection reagent) served as controls. In addition, control circRNA CTR2 and the correspondingly modified control ASO CTR2 were used. Residual virus titers of significantly affected samples are indicated as 'percent remaining' relative to mock treatment, as well as fold differences between circRNA and ASO treatments.

'real' activities are likely higher than the apparent values determined here. In addition, the experimental conditions of circRNA lipofection, as well as the *in vivo* stabilities of circRNAs can certainly be further improved, for example by systematically optimizing circRNA delivery, evaluating backbone sequences and structure, or introducing RNA modifications or peptide conjugation.

We were able to demonstrate that the inhibitory potency of circular versions of antisense sequences consistently surpassed that of the corresponding linear versions (Figures 2 and 3); moreover, the optimal AS_1–75 circRNA proved superior to state-of-the-art modified ASOs against the same target region, as used in traditional antisense strategies (Figure 5). Most likely this is due to the relatively high metabolic stability of circular RNAs; in addition, structural peculiarities and constraints of how the antisense sequence is exposed in circular configuration may contribute to the activity of AS-circRNAs. Obviously there are more ASO varieties available, as well as combinations of modified nucleotides, that could be tested more systematically, beyond the 2′-OMe and 2′-MOE moieties assayed here. In addition, integrating modified nucleotide positions within synthetic AS-circRNAs appears an attractive and promising option for follow-up studies to further optimize the antisense-circRNA concept.

Our approach to assay the efficiency of antisense-circRNA against SARS-CoV-2 is based on circRNA transfection followed by virus infection, reflecting a prophylactic treatment. However, we have assayed also in the reverse order, viral infection followed by circRNA transfection, and we were able to confirm the efficiency of AS_1–75 circRNA and durability of the antiviral effect (Supplementary Figure S4). This demonstrates that our antisense-circRNA approach is useful not only for prophylactic strategies, but also for protecting against viral infection and for antiviral therapy.

Finally, we were able to confirm the antiviral effect of AS_1–75 circRNA also in an *ex-vivo* cell culture system (Supplementary Figure S5).

What is the mechanistic basis for the strong antiviral effects observed for these AS-circRNAs? Detailed analyses remain to be performed, but will likely reveal a complex picture, because the 5′-terminal region of SARS-CoV-2 is predicted to be involved in multiple levels of the viral replication cycle, such as translational initiation, viral genome replication, synthesis of the 5′-leader-containing subgenomic RNAs, RNA stability, and RNA packaging. Our analysis of viral RNA synthesis (Figure 4) and the data obtained in reporter assays (Figure 2) indicate that the most potent AS-circRNA, AS_1–75, interferes with both the production of subgenomic RNAs and viral protein translation. Effects on other steps are likely but remain to be corroborated by further studies. Initial direct Northern blot assays with reporters argue against the possibility that an RNAi-type cleavage mechanism induced by perfectly base-paired antisense regions is involved. These results, complemented by measuring luciferase mRNA reporter levels via qPCR, rather support a blockage-type mechanism (Supplementary Figure S7).

The extended length of our optimal, unmodified AS_1–75 circRNA confers a certain robustness towards single point mutations in the antisense target region, as we have demonstrated for several naturally occuring point mutations in the leader region (Figure 5). Obviously this represents an added benefit of an AS-circRNA based antiviral strategy, considering the continuously arising mutant SARS-CoV-2 virus forms.

The confirmed functionality of AS-circRNAs designed and characterized in this study in the context of virus infection, including the superior activity of circular over linear RNAs, suggests that circRNAs with antisense functions may exist in nature and play a role in gene regulation. Our results establish designer AS-circRNAs as a new generation of versatile and adjustable RNA therapeutics with significant potential. Finally, in the context of antiviral therapeutic applications, it is worth noting that AS-circRNAs could be easily adjusted to virus escape mutants potentially arising during viral replication and transmission, particularly during virus pandemics of newly emerging viruses.

DATA AVAILABILITY

RNA-seq data were deposited in the Sequence Read Archive (SRA-ID: PRJNA693241) of NCBI.

SUPPLEMENTARY DATA

Supplementary Data are available at NAR Online.

ACKNOWLEDGEMENTS

We thank Ramakanth Madhugiri for advice on SARS-CoV-2 sequences and subgenomic RNA annotation, Stefan Günther for RNA-seq support, Katharina Rudek for circRNA production, other lab members for discussions, and Zefeng Wang and Guoqing Zhang (PICB Shanghai) for discussions and help with the ViGTK SARS-CoV-2 mutant database.

Author contributions: C.P., T.S., C.M. and S.S. designed and carried out experiments, L.-H.H. did the bioinformatic analysis and J.Z. and A.B. wrote the manuscript.

FUNDING

Deutsche Forschungsgemeinschaft [RTG 2355; project Bi 316/18-1 and 18-2 within SPP 1935 to A.B.; project Bi 316/20-1 within Research Unit FOR 5116 to A.B.; project A01 within SFB1021 to J.Z.; project P3 within KFO309 to J.Z.; project P10 within GRK2581 to J.Z.]; Cardio-Pulmonary Institute (CPI) within the Excellence Strategy Program [Exc 2026 to T.S.]; State of Hessen, LOEWE Centre DRUID [E2 to A.B.; B2 to J.Z.]; German Federal Ministry for Education and Research (COVINET to J.Z.); German Center for Infection Research (DZIF) to J.Z. Funding for open access charge: DFG.

Conflict of interest statement. C.P., T.S., C.M., J.Z. and A.B. filed a patent application on the use of designer antisense-circRNAs (EP 20211415.3, 'Circular nucleic acids and uses thereof for interfering with genome expression and proliferation of coronaviruses'; patent pending).

REFERENCES

1. Perlman,S. and Netland,J. (2009) Coronaviruses post-SARS: update on replication and pathogenesis. *Nat. Rev. Microbiol.*, **7**, 439–450.
2. Perlman,S. and Masters,P.S. (2021) Coronaviridae: the viruses and their replication. In: Howley,P.M., Knipe,D.M. and Whelan,S. (eds). *Fields Virology*. Wolters Kluwer, Philadelphia, PA, Vol. **I**. pp. 410–448.
3. Madhugiri,R., Karl,N., Petersen,D., Lamkiewicz,K., Fricke,M., Wend,U., Scheuer,R., Marz,M. and Ziebuhr,J. (2018) Structural and functional conservation of cis-acting RNA elements in coronavirus 5′-terminal genome regions. *Virology*, **517**, 44–55.
4. Miao,Z., Tidu,A., Eriani,G. and Martin,F. (2021) Secondary structure of the SARS-CoV-2 5′-UTR. *RNA Biol.*, **18**, 447–456.
5. Sola,I., Almazán,F., Zúñiga,S. and Enjuanes,L. (2015) Continuous and discontinuous RNA synthesis in coronaviruses. *Annu. Rev. Virol.*, **2**, 265–288.
6. Kim,D., Lee,J.Y., Yang,J.S., Kim,J.W., Kim,V.N. and Chang,H. (2020) The architecture of SARS-CoV-2 transcriptome. *Cell*, **181**, 914–921.
7. Zhou,P., Yang,X.L., Wang,X.G., Hu,B., Zhang,L., Zhang,W., Si,H.R., Zhu,Y., Li,B., Huang,C.L. *et al.* (2020) A pneumonia outbreak associated with a new coronavirus of probable bat origin. *Nature*, **579**, 270–273.
8. Zhu,N., Zhang,D., Wang,W., Li,X., Yang,B., Song,J., Zhao,X., Huang,B., Shi,W., Lu,R. *et al.* (2020) A novel coronavirus from patients with pneumonia in China, 2019. *N. Engl. J. Med*, **382**, 727–733.
9. Polack,F.P., Thomas,S.J., Kitchin,N., Absalon,J., Gurtman,A., Lockhart,S., Perez,J.L., Pérez Marc,G., Moreira,E.D., Zerbini,C *et al.* (2020) Safety and efficacy of the BNT162b2 mRNA Covid-19 vaccine. *N. Engl. J. Med*, **383**, 2603–2615.
10. Bennett,C.F. and Swayze,E.E. (2010) RNA targeting therapeutics: molecular mechanisms of antisense oligonucleotides as a therapeutic platform. *Annu. Rev. Pharmacol. Toxicol.*, **50**, 259–293.
11. Crooke,S.T., Witztum,J.L., Bennett,C.F. and Baker,B.F. (2018) RNA-targeted therapeutics. *Cell Metab.*, **27**, 714–739.
12. Bennett,C.F., Krainer,A.R. and Cleveland,D.W. (2019) Antisense oligonucleotide therapies for neurodegenerative diseases. *Annu. Rev. Neurosci*, **42**, 385–406.
13. Le,T.K., Paris,C., Khan,K.S., Robson,F., Ng,W.-L. and Rocchi,P. (2021) Nucleic acid-based technologies targeting coronaviruses. *Trends Biochem. Sci.*, **46**, 351–365.
14. Roberts,T.C., Langer,R. and Wood,M.J.A. (2020) Advances in oligonucleotide drug delivery. *Nat. Rev. Drug Discov.*, **19**, 673–694.
15. Neuman,B.W., Stein,D.A., Kroeker,A.D., Churchill,M.J., Kim,A.M., Kuhn,P., Dawson,P., Moulton,H.M., Bestwick,R.K., Iversen,P.L. *et al.* (2005) Inhibition, escape, and attenuated growth of severe acute respiratory syndrome coronavirus treated with antisense morpholino oligomers. *J. Virol.*, **79**, 9665–9676.
16. Burrer,R., Neuman,B.W., Ting,J.P.C., Stein,D.A., Moulton,H.M., Iversen,P.L., Kuhn,P. and Buchmeier,M.J. (2007) Antiviral effects of antisense morpholino oligomers in murine coronavirus infection models. *J. Virol.*, **81**, 5637–5648.
17. Sänger,H.L., Klotz,G., Riesner,D., Gross,H.J. and Kleinschmidt,A.K. (1976) Viroids are single-stranded covalently closed circular RNA molecules existing as highly base-paired rod-likestructures. *Proc. Natl. Acad. Sci. U.S.A.*, **73**, 3852–3856
18. Wilusz,J.E. (2018) A 360° view of circular RNAs: From biogenesis to functions. *Wiley Interdiscip. Rev. RNA*, **9**, e1478.
19. Kristensen,L.S., Andersen,M.S., Stagsted,L.V.W., Ebbesen,K.K., Hansen,T.B. and Kjems,J. (2019) The biogenesis, biology and characterization of circular RNAs. *Nat. Rev. Genet.*, **20**, 675–691.
20. Chen,L.L. (2020) The expanding regulatory mechanisms and cellular functions of circular RNAs. *Nat. Rev. Mol. Cell Biol.*, **21**, 475–490.
21. Salzman,J., Gawad,C., Wang,P.L., Lacayo,N. and Brown,P.O. (2012) Circular RNAs are the predominant transcript isoform from hundreds of human genes in diverse cell types. *PLoS One*, **7**, e30733.
22. Jeck,W.R., Sorrentino,J.A., Wang,K., Slevin,M.K., Burd,C.E., Liu,J., Marzluff,W.F. and Sharpless,N.E. (2013) Circular RNAs are abundant, conserved, and associated with ALU repeats. *RNA*, **19**, 141–157.
23. Memczak,S., Jens,M., Elefsinioti,A., Torti,F., Krueger,J., Rybak,A., Maier,L., Mackowiak,S.D., Gregersen,L.H., Munschauer,M. *et al.* (2013) Circular RNAs are a large class of animal RNAs with regulatory potency. *Nature*, **495**, 333–338.
24. Starke,S., Jost,I., Rossbach,O., Schneider,T., Schreiner,S., Hung,L.-H. and Bindereif,A. (2015) Exon circularization requires canonical splice signals. *Cell Rep.*, **10**, 103–111.
25. Hansen,T.B., Jensen,T.I., Clausen,B.H., Bramsen,J.B., Finsen,B., Damgaard,C.K. and Kjems,J. (2013) Natural RNA circles function as efficient microRNA sponges. *Nature*, **495**, 384–388.
26. Piwecka,M., Glažar,P., Hernandez-Miranda,L.R., Memczak,S., Wolf,S.A., Rybak-Wolf,A., Filipchyk,A., Klironomos,F., Cerda Jara,C.A., Fenske,P. *et al.* (2017) Loss of a mammalian circular RNA locus causes miRNA deregulation and affects brain function. *Science*, **357**, eaam8526.
27. Kleaveland,B., Shi,C.Y., Stefano,J. and Bartel,D.P. (2018) A network of noncoding regulatory RNAs acts in the mammalian brain. *Cell*, **174**, 350–362.
28. Hentze,M.W. and Preiss,T. (2013) Circular RNAs: splicing's enigma variations. *EMBO J.*, **32**, 923–925.
29. Jost,I., Shalamova,L.A., Gerresheim,G.K., Niepmann,M., Bindereif,A. and Rossbach,O. (2018) Functional sequestration of microRNA-122 from Hepatitis C Virus by circular RNA sponges. *RNA Biol.*, **15**, 1032–1039.
30. Müller,S., Wedler,A., Breuer,J., Glaß,M., Bley,N., Lederer,M., Haase,J., Misiak,C., Fuchs,T., Ottmann,A. *et al.* (2020) Synthetic circular miR-21 RNA decoys enhance tumor suppressor expression and impair tumor growth in mice. *NAR Cancer*, **2**, zcaa014.
31. Schreiner,S., Didio,A., Hung,L.-H. and Bindereif,A. (2020) Design and application of circular RNAs with protein-sponge function. *Nucleic Acids Res.*, **48**, 12326–12335.
32. Litke,J.L. and Jaffrey,S.R. (2019) Highly efficient expression of circular RNA aptamers in cells using autocatalytic transcripts. *Nat. Biotechnol.*, **37**, 667–675.
33. Breuer,J. and Rossbach,O. (2020) Production and purification of artificial circular RNA sponges for application in molecular biology and medicine. *Methods Protoc.*, **3**, 42.
34. Medenbach,J., Seiler,M. and Hentze,M.W. (2011) Translational control via protein-regulated upstream open reading frames. *Cell*, **145**, 902–913.
35. Müller,C., Schulte,F.W., Lange-Grünweller,K., Obermann,W., Madhugiri,R., Pleschka,S., Ziebuhr,J., Hartmann,R.K. and Grünweller,A. (2018) Broad-spectrum antiviral activity of the eIF4A inhibitor silvestrol against corona- and picornaviruses. *Antivir. Res.*, **150**, 123–129.
36. Schneider,T., Schreiner,S., Preußer,C., Bindereif,A. and Rossbach,O. (2018) Northern blot analysis of circular RNAs. *Methods Mol. Biol.*, **1724**, 119–133.
37. Dobin,A., Davis,C.A., Schlesinger,F., Drenkow,J., Zaleski,C., Jha,S., Batut,P., Chaisson,M. and Gingeras,T.R. (2013) STAR: ultrafast universal RNA-seq aligner. *Bioinformatics*, **29**, 15–21.
38. Ziv,O., Price,J., Shalamova,L., Kamenova,T., Goodfellow,I., Weber,F. and Miska,E.A. (2020) The Short- and Long-Range RNA-RNA Interactome of SARS-CoV-2. *Mol. Cell*, **80**, 1067–1077.
39. Kim,D., Kim,S., Park,J., Chang,H.R., Chang,J., Ahn,J., Park,H., Park,J., Son,N., Kang,G. *et al.* (2021) A high-resolution temporal atlas of the SARS-CoV-2 translatome and transcriptome. *Nat. Commun.*, **12**, 5120.
40. Cao,C., Cai,Z., Xiao,X., Rao,J., Chen,J., Hu,N., Yang,M., Xing,X., Wang,Y., Li,M. *et al.* (2021) The architecture of the SARS-CoV-2 RNA genome inside virion. *Nat. Commun.*, **12**, 3917.
41. Boulant,S., Stanifer,M. and Lozach,P.Y. (2015) Dynamics of virus-receptor interactions in virus binding, signaling, and endocytosis. *Viruses*, **7**, 2794–2815.
42. Jonsdottir,H.R. and Dijkman,R. (2016) Coronaviruses and the human airway: a universal system for virus-host interaction studies. *Virol. J.*, **13**, 24.

nature COMMUNICATIONS

ARTICLE

https://doi.org/10.1038/s41467-021-25551-1 OPEN

Multi-level inhibition of coronavirus replication by chemical ER stress

Mohammed Samer Shaban[1,11], Christin Müller[2,11], Christin Mayr-Buro[1,11], Hendrik Weiser[1], Johanna Meier-Soelch[1], Benadict Vincent Albert[1], Axel Weber[1], Uwe Linne[3], Torsten Hain[4,5], Ilya Babayev[1], Nadja Karl[2], Nina Hofmann[6], Stephan Becker[7], Susanne Herold[8,9], M. Lienhard Schmitz[9,10], John Ziebuhr[2,5,12]✉ & Michael Kracht[1,9,12]✉

Coronaviruses (CoVs) are important human pathogens for which no specific treatment is available. Here, we provide evidence that pharmacological reprogramming of ER stress pathways can be exploited to suppress CoV replication. The ER stress inducer thapsigargin efficiently inhibits coronavirus (HCoV-229E, MERS-CoV, SARS-CoV-2) replication in different cell types including primary differentiated human bronchial epithelial cells, (partially) reverses the virus-induced translational shut-down, improves viability of infected cells and counteracts the CoV-mediated downregulation of IRE1α and the ER chaperone BiP. Proteome-wide analyses revealed specific pathways, protein networks and components that likely mediate the thapsigargin-induced antiviral state, including essential (HERPUD1) or novel (UBA6 and ZNF622) factors of ER quality control, and ER-associated protein degradation complexes. Additionally, thapsigargin blocks the CoV-induced selective autophagic flux involving p62/SQSTM1. The data show that thapsigargin hits several central mechanisms required for CoV replication, suggesting that this compound (or derivatives thereof) may be developed into broad-spectrum anti-CoV drugs.

[1] Rudolf Buchheim Institute of Pharmacology, Justus Liebig University, Giessen, Germany. [2] Institute of Medical Virology, Justus Liebig University, Giessen, Germany. [3] Mass spectrometry facility of the Department of Chemistry, Philipps University, Marburg, Germany. [4] Institute of Medical Microbiology, Justus Liebig University, Giessen, Germany. [5] German Center for Infection Research (DZIF), partner site Giessen-Marburg-Langen, Giessen, Germany. [6] Bioinformatics and Systems Biology, Justus Liebig University, Giessen, Germany. [7] Institute of Virology, Philipps University, Marburg, Germany. [8] Department of Internal Medicine II for Pulmonary and Critical Care Medicine and Infectious Diseases, Justus Liebig University, and Institute for Lung Health (ILH), Giessen, Germany. [9] German Center for Lung Research (DZL) and Universities of Giessen and Marburg Lung Center (UGMLC), Giessen, Germany. [10] Institute of Biochemistry, Justus Liebig University, Giessen, Germany. [11] These authors contributed equally: Mohammed Samer Shaban, Christin Müller, Christin Mayr-Buro. [12] These authors jointly supervised this work: John Ziebuhr, Michael Kracht. ✉email: john.ziebuhr@viro.med.uni-giessen.de; michael.kracht@pharma.med.uni-giessen.de

Coronaviruses are enveloped plus-strand RNA viruses with a broad host range, including humans[1,2]. The four seasonal human CoVs (HCoV-229E, -NL63, -HKU1, -OC43) generally cause a spectrum of (mild) symptoms that are mainly restricted to the upper respiratory tract[3–6]. In contrast, the three highly pathogenic CoVs that emerged from animal reservoirs over the past two decades are frequently associated with significant disease burden and mortality in humans. The latter include the severe acute respiratory syndrome CoV (SARS-CoV)[7–9], SARS-CoV-2[10,11], and Middle-East respiratory syndrome CoV (MERS-CoV)[12].

The current SARS-CoV-2 pandemic highlights the urgent need to identify new antiviral strategies, including drugs that target the host side[10]. CoVs impose multiple functional but also structural changes to a wide range of cellular pathways and there is increasing evidence that some of these pathways may be exploited therapeutically[13,14].

In common with other cellular stress conditions, including infections by diverse pathogens, CoVs are known to activate the NF-κB, JNK, and p38 MAPK pathways and to reprogram host cell transcriptomes[15–17]. In addition, they induce the formation of replicative organelles (ROs), an intracellular network of convoluted membranes (CMs), and double-membrane vesicles (DMV) that harbor the viral replication/transcription complexes (RTC) and shield these complexes from recognition by cellular defense mechanisms[18]. The origins of the membranes used for RO are still under debate but can be linked, at least partly, to ER- and autophagy-related processes[19]. The combination of these and other events leads to cell damage and cell death upon virus budding and release within a few days[14]. The virus-induced cellular changes are associated with an activation of the unfolded protein response (UPR), which is evident from a profound transcriptomic endoplasmic reticulum (ER) stress signature, as reported for cells infected with HCoV-229E[17].

The ER is critically involved in surveying the quality and fidelity of membrane and secreted protein synthesis, as well as the folding, assembly, transport, and degradation of these proteins[20]. The accumulation of unfolded or misfolded proteins in the ER lumen leads to ER stress and UPR activation, thereby slowing down protein synthesis and increasing the folding capacity of the ER[21]. As a result, cellular protein homeostasis can be restored and the cell survives. If this compensatory mechanism fails, ER stress pathways can also switch their functions, inducing oxidative stress and resulting in cell death[20,22].

The system relies on sensors residing in the ER membrane which include the protein kinase R (PKR)-like ER kinase (PERK), inositol-requiring protein 1α (IRE1α), and cyclic AMP-dependent transcription factor 6α (ATF6α). PERK and IRE1α are Ser/Thr kinases whose conserved N termini are oriented towards the ER lumen[23]. In non-stressed cells, the highly abundant major ER chaperone and ER stress sensor binding-immunoglobulin protein BiP (also called 78 kDa glucose-regulated protein, GPR78; heat shock protein family A member 5, HSPA5) binds to PERK and IRE1α, which keeps these two proteins in an inactive monomeric state[24,25]. Upon increased binding of BiP to misfolded ER clients, BiP is released from both PERK and IRE1α, resulting in an (indirect) activation of the two kinases by oligomerization and trans(auto)phosphorylation[26–28].

Active PERK phosphorylates the eukaryotic translation initiation factor 2 (eIF2) subunit α to shut down translation and also activates ATF4, the master transcription factor orchestrating ER stress-induced genes[29,30]. Phosphorylated IRE1α activates its own RNase domain to generate spliced (s)XBP1 protein, a multifunctional transcriptional regulator responsible for adaptive responses or cell death[31]. The specific function(s) of yet another ER stress-activated transcription factor, ATF3, is less well understood[32]. Generally, the various branches of the UPR act in concert, allowing a multitude of potential outcomes, ranging from the compensation of ER stress and restoration of proteostasis to cell death[22].

The activation of ER stress by microbial and viral infections has been widely observed. However, with few exceptions, it remains to be studied how this response is shaped in an infectious agent-specific manner and whether or not these responses are beneficial or detrimental to the host[33]. Moreover, there is a lack of knowledge on CoV-mediated (de)regulation of ER stress components at the protein level. The latter is important because CoVs, in common with many RNA viruses, are known to cause a global shutdown of host protein synthesis[34].

Here, we report that CoV infection activates ER stress signaling and induces UPR components at the mRNA level while suppressing them at the protein level. Strikingly, the well-known chemical activator of the UPR, thapsigargin, exerts a profound antiviral effect in the lower nanomolar range on three different CoVs in four different cell types, including human primary bronchial epithelial cells. A detailed proteomics analysis revealed multiple thapsigargin-regulated pathways and a network of proteins involved in ER quality control (ERQC) or ER-associated degradation (ERAD) that are suppressed by CoV but (re)activated by chemically stressed infected cells. Additionally, we discovered that thapsigargin blocks the autophagic flux in CoV-infected cells. Taken together, these data provide important new insight into central factors involved in CoV replication and open new avenues for targeted CoV antivirals.

Results

To investigate how CoVs modulate ER stress components at the mRNA compared to the protein level, we determined the expression levels of 166 components of the ER stress pathway KEGG hsa04141 “protein processing in ER” in human HuH7 liver cells, a commonly used cellular model for CoV replication, in response to infections with HCoV-229E and MERS-CoV, respectively. For untreated HuH7 cells, we obtained mRNA (by RNA-seq) and protein (by LC-MS/MS) expression data for 119 components which revealed a positive correlation between mRNA and protein abundances (Fig.1a, upper graph). However, in cell lysates obtained at 24 h post infection (p.i.), this effect was largely lost (Fig. 1a, middle and lower graph). Pearson correlation matrix confirmed a progressive loss of correlation between mRNA levels and protein levels for this pathway over a time course from 3 to 24 h p.i. (Fig. 1b). Thus, out of 39 (for HCoV-229E) or 56 (for MERS-CoV) ER stress factors that were found to be regulated at the mRNA level, only a few remained regulated at the protein level at late time points (Fig. 1c, shown as a projection on KEGG hsa04141 in Supplementary Fig. 1).

To determine the functional consequences of this opposing regulation at the mRNA and protein levels in CoV-infected cells, we focused on HCoV-229E and assessed key regulatory features of the ER stress pathway as shown in Fig. 2a. As a reference, we included samples from cells exposed to thapsigargin, a compound that has been widely used to study prototypically activated ER stress mechanistically[25,35]. This setup included experiments, in which thapsigargin and virus were added simultaneously to the cell culture medium (followed by a further incubation for 24 h) or thapsigargin was added to the cells at 8 h p.i. for 16 h (Fig. 2b).

The presence of thapsigargin in the growth medium resulted in a major drop in viral titers by more than 150-fold (from 9.18×10^6 to 5.7×10^4 pfu/ml), which was paralleled by reduced amounts of viral RNA isolated from thapsigargin-treated, HCoV-229E-infected cells at 24 h p.i. (Fig. 2c). Immunofluorescence analysis of HCoV-229E-infected cells treated with thapsigargin

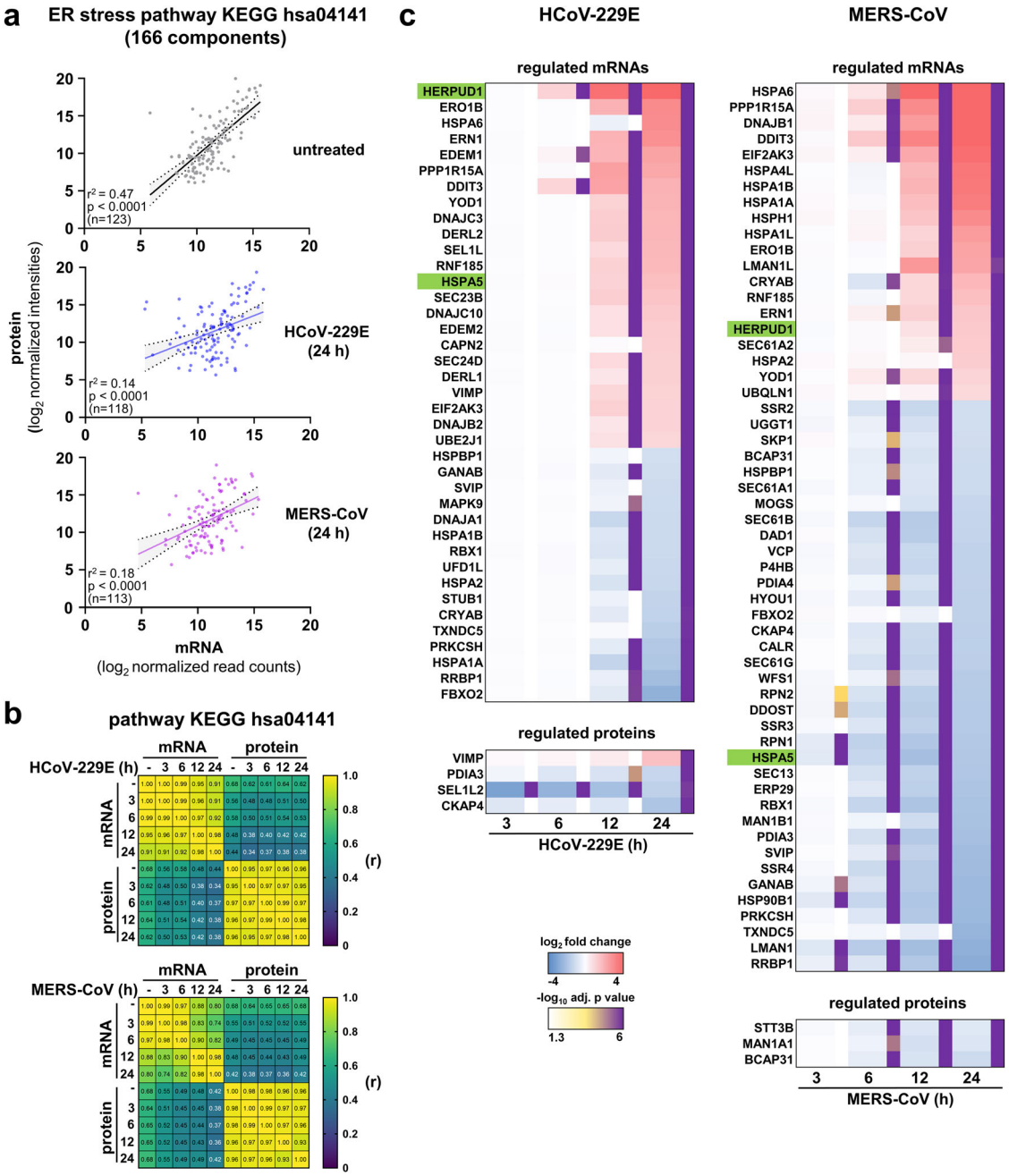

Fig. 1 CoVs uncouple mRNA and protein levels of ER stress components in infected cells. a–c HuH7 cells were left untreated or were infected with HCoV-229E or MERS-CoV (MOI = 1) for 3, 6, 12, or 24 h. Transcriptomic and proteomic data were derived from samples obtained at the indicated time points post infection (p.i.). Subsequently, mRNA and protein expression values for the KEGG pathway hsa04141 "protein processing in endoplasmic reticulum" from two biologically independent experiments were extracted and used for further analysis. **a** Scatter plots show mean normalized protein/mRNA expression values for the number (*n*) of expressed components, fitted linear regression lines, 95% confidence intervals, and coefficients of determination for non-infected HuH7 cells and HuH7 cells infected with virus for 24 h. *P* values were calculated from an F test to test the null hypothesis that the overall slope is zero. **b** Correlation matrix of Pearson's r across all conditions. All corresponding p values are provided in the Source data. **c** The heatmaps show mean ratio values of differentially expressed mRNAs or proteins based on significant differences (fold change ≥ 2, adjusted $p \leq 0.01$) calculated from the replicates by moderated t-tests. See also Supplementary Fig. 1 for pathway mappings of mRNA and protein data and Source data for complete data sets.

confirmed the impaired formation of functional viral RTCs as shown by the reduced levels of both double-stranded RNA (an intermediate of viral RNA replication) and nonstructural protein (nsp) 8 (an essential part of the viral RTC) (Fig. 2d).

A strong suppression of viral replication was also demonstrated by the reduced protein levels observed for the nucleocapsid (N) protein (a major coronavirus structural protein) as well as nsp 8 and 12, both representing essential components of the viral replication complex[36] (Fig. 2e, f). In all cases, the antiviral effect of thapsigargin remained readily detectable when the compound was added at 8 h p.i, suggesting that it does not prevent viral entry but rather suppresses intracellular pathways required for efficient viral RNA replication and virus formation and release, or, activates unknown antiviral effector systems (Fig. 2c, e, f).

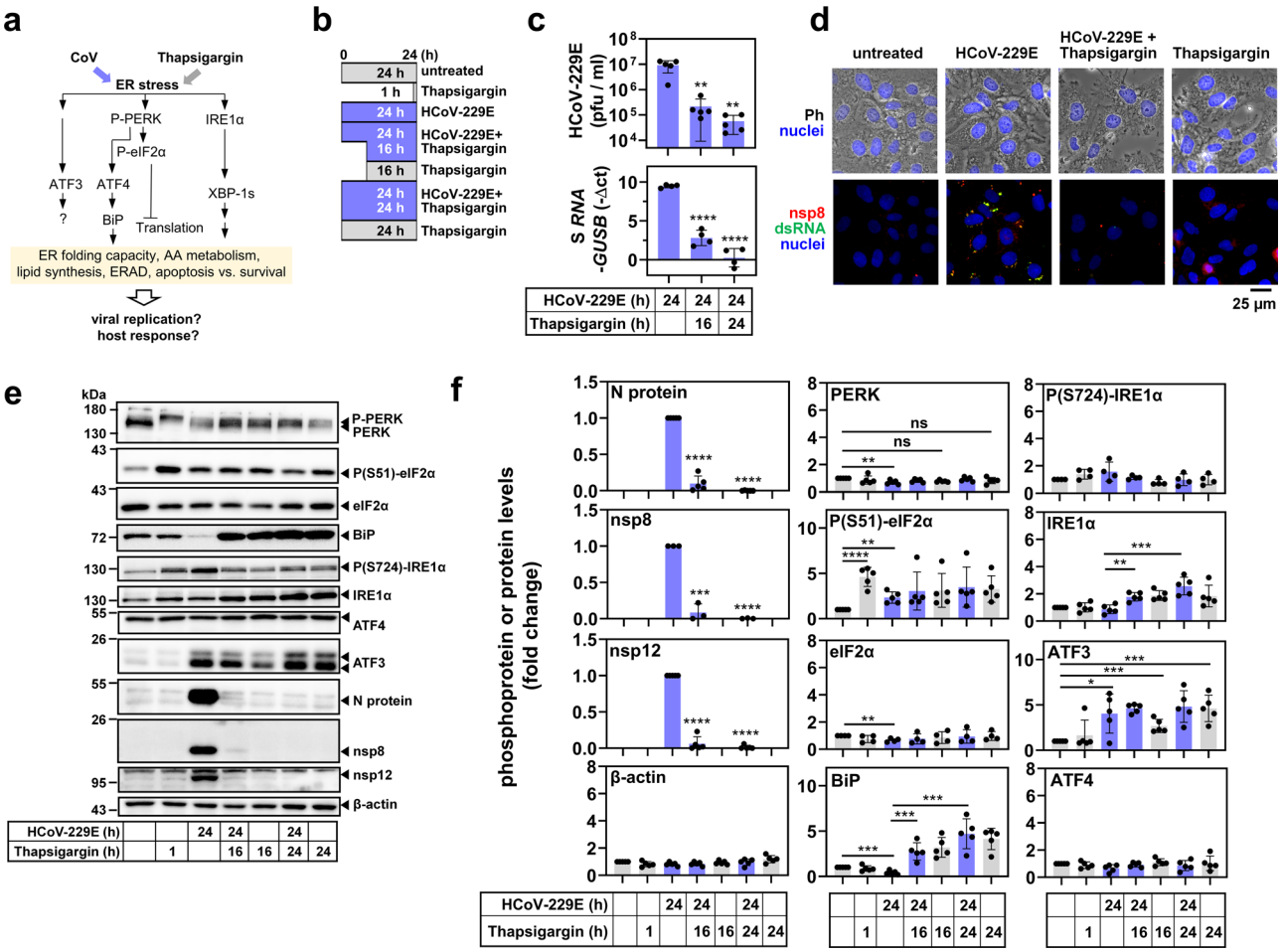

Fig. 2 Thapsigargin inhibits HCoV-229E replication and counteracts virus-mediated BiP downregulation. a Schematic overview of parameters used to monitor virus- and thapsigargin-mediated ER stress. **b** Schematic presentation of HCoV-229E infection of cells and/or treatment with thapsigargin as applied in this study. **c** HuH7 cells were left untreated or infected with HCoV-229E (MOI = 1) for 24 h and treated with thapsigargin (1 µM) according to the scheme shown in (**b**). Supernatants and RNA isolated from the cell pellets were used to determine viral titers by virus plaque assay and expression of HCoV-229E S gene-encoding RNA (five (upper graphs) or four (lower graphs) biologically independent experiments). **d** Phase-contrast (Ph) and fluorescence microscopy images showing the morphology of HuH7 cells and the subcellular HCoV-229E replication sites (at 24 h p.i.) identified by nsp8- and double-strand RNA-specific antibodies in the presence or absence of thapsigargin (1 µM for 24 h) (representative images from one out of two biologically independent experiments). Nuclei were stained with Hoechst 33342. **e** Representative immunoblots of total cell extracts from HuH7 cells infected with HCoV-229E (MOI = 1) and treated with thapsigargin (1 µM) according to (**b**) showing the expression/modification of the indicated host cell and viral proteins. **f** Quantification of immunoblot data as shown in (**e**) relative to the untreated control (three or more biologically independent experiments). All bar graphs show means ± s.d.; asterisks indicate *p* values (*$p \le 0.05$, **$p \le 0.01$, ***$p \le 0.001$, ****$p \le 0.0001$) obtained by two-tailed unpaired t-tests.

Next, we investigated ER stress signaling under these conditions. Both virus and thapsigargin were confirmed to activate the PERK branch of ER stress (Fig. 2e, f), as shown by the retarded mobility of PERK in SDS gels (indicating multisite phosphorylation) and by phosphorylation of the PERK substrate eIF2α at Ser51 (Fig. 2e, f). HCoV-229E infection led to a weak but significant decrease of PERK (mean 71 ± 15%) and eIF2α (mean 67 ± 13%) levels compared to the controls. Infection also caused an approximately twofold (mean 42 ± 22%) reduction of BiP expression (Fig. 2e, f). In contrast, long-term thapsigargin treatment (for 16 h or 24 h) caused a 3–4-fold increase of BiP expression, also in HCoV-229E-infected cells, thus reversing the suppression by viral infection (Fig. 2e, f). Similarly, thapsigargin treatment for 16 h or 24 h caused a 1.5–2-fold increase in IRE1α expression (but not phosphorylation), again also in infected cells (Fig. 2e, f). In this set of experiments, ATF3 proved to be the only protein that was induced by the virus alone (Fig. 2e, f), while the expression levels of ATF4 remained largely unchanged (Fig. 2e, f). To reveal the role of PERK in these effects, we treated cells with the protein kinase inhibitor GSK2656157. This compound suppressed PERK autophosphorylation, PERK activity (on eIF2α), and CoV replication without having a major impact on cell viability (Supplementary Fig. 2a–c). However, inhibition of viral replication by GSK2656157 was less effective than thapsigargin and, in combined treatments, it did not abolish the thapsigargin-mediated suppression of N protein expression and virus replication, placing the thapsigargin-mediated viral suppression downstream of PERK (Supplementary Fig. 2d, e).

These data show that both CoV infection and chemicals like thapsigargin activate ER stress through the same proximal PERK pathway, although they affect downstream cellular outcomes differentially. The restoration of BiP and IRE1α levels by long-term thapsigargin treatment further suggests that the CoV-induced block of inducible host factors is reversible and can be reprogrammed by a (presumably protective) thapsigargin-mediated response. Our comparative analyses of viral replication and host

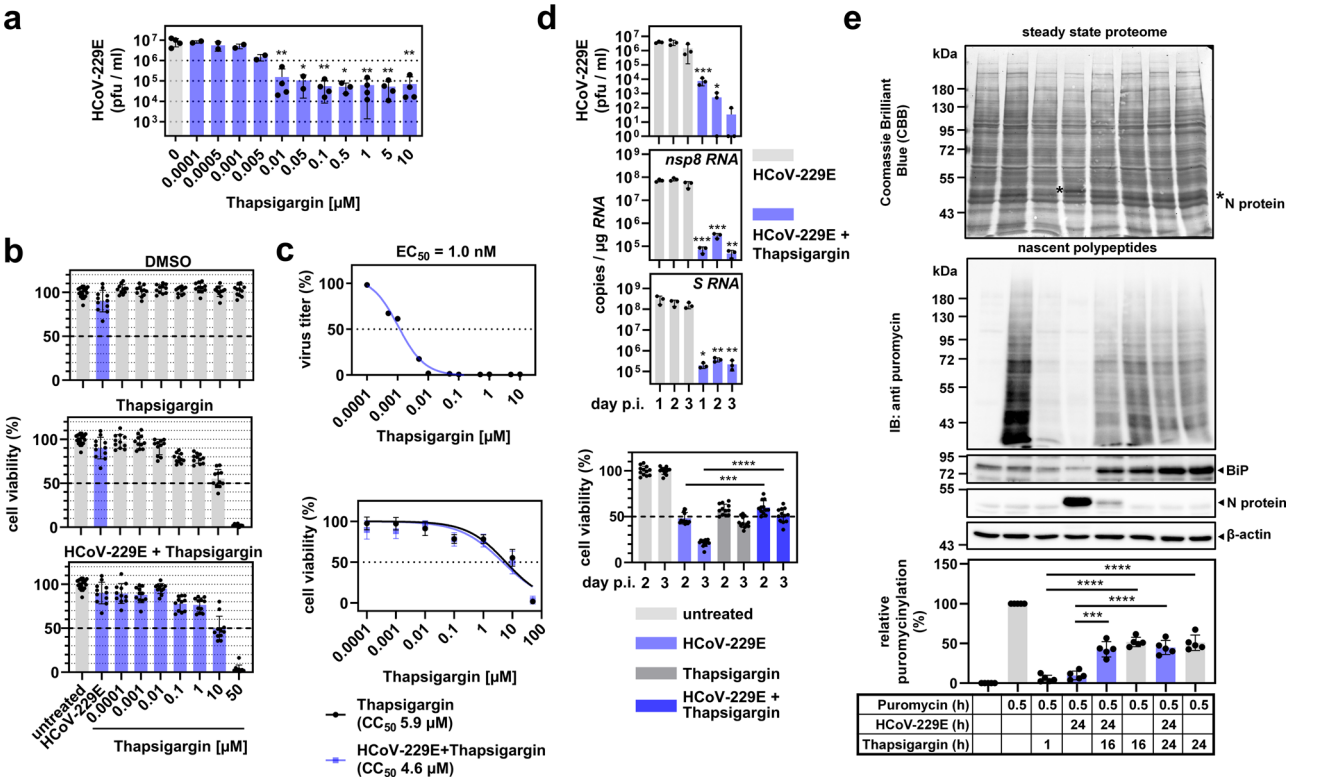

Fig. 3 Thapsigargin mediates dose-dependent, long-lasting inhibition of HCoV-229E replication and leads to partially improved survival and protein biosynthesis of infected cells. a Dose-dependent suppression of HCoV-229E replication in the absence or presence of increasing concentrations of thapsigargin. At 24 h p.i., viral titers of cell culture supernatants were determined (two or more biologically independent experiments). **b** HuH7 cells were left untreated, or were infected with HCoV-229E (MOI = 1) in the presence/absence of increasing concentrations of thapsigargin or DMSO as solvent control. After 24 h, cell viability was assessed by MTS assay (five biologically independent experiments). **c** All data from (**a**) and (**b**) were used to compute the relative estimated half-maximal effective (EC_{50}) (upper graph, means of two or more biologically independent experiments) and cytotoxic (CC_{50}) (lower graph, means ± s.d. of five biologically independent experiments) concentrations of thapsigargin in HuH7 cells infected with HCoV-229E. **d** HuH7 cells were infected with HCoV-229E (MOI = 1) and treated with a single dose of thapsigargin (1 μM) as indicated. Viral titers, copy numbers of viral RNAs (detected using *nsp8* coding sequence- and *S* gene-specific primers, respectively), and cell viabilities were determined after 1–3 days (three biologically independent experiments). **e** HuH7 cells were treated and infected according to Fig. 2b. Thirty minutes before harvesting, puromycin (3 μM) was added where indicated. Total cell extracts were analyzed by immunoblotting. The blot membrane was stained with CBB to assess the steady-state proteomes and then hybridized with anti-puromycin antibodies to detect de novo synthesized nascent polypeptides. Puromycin signals of each lane were normalized to the corresponding CBB staining and were background corrected by subtracting signals of samples in which puromycin had been omitted. The upper graphs show representative images and the lower graph shows the quantification of five biologically independent experiments. All bar graphs show means ± s.d.; asterisks indicate *p* values (*$p \leq 0.05$, **$p \leq 0.01$, ***$p \leq 0.001$, ****$p \leq 0.0001$) obtained by two-tailed unpaired t-tests. See Supplementary Fig. 2 for PERK inhibitor data.

response, along with the effects of PERK inhibition, lead us to conclude that chemically and virus-induced forms of ER stress, although proceeding through the same core PERK pathway, do not simply potentiate each other but rather (somewhat counter-intuitively) counteract each other.

To explore a potential pharmacological exploitation of this effect, we assessed the (half-maximal) effective and cytotoxic concentrations (EC_{50}, CC_{50}) of the combined thapsigargin treatment and virus infection, because both conditions are known to promote cell death. HCoV-229E replication was suppressed with an EC_{50} of 1 nM (Fig. 3a, c), as judged by virus titration of cell culture supernatants obtained from these cells. At 24 h p.i., the cell viability of HCoV-229E-infected HuH7 cells was only marginally reduced (mean 90.02 ± 12.32%) (Fig. 3b, upper graph). After 24 h of incubation, thapsigargin decreased cell viability in a dose-dependent manner with a CC_{50} of 5.9 μM in line with previous reports (Fig. 3b, middle graph, Fig. 3c)[37,38]. The combination of thapsigargin treatment and HCoV-229E infection did not cause additional cytotoxicity as shown by a nearly identical CC_{50} of 4.6 μM (Fig. 3b, lower graph, Fig. 3c). At 1 μM thapsigargin, i.e., a concentration shown to completely abolish viral protein translation and production of infectious virus progeny (see above), the cell viability of cells infected with HCoV-229E and treated with thapsigargin was 76.6 ± 7.9% (Fig. 3b, c). Furthermore, the antiviral effects of thapsigargin remained detectable for three days after a single dose, with a profound reduction of viral titers and RNA levels by several orders of magnitude (Fig. 3d). After three days, 50% of the cells infected with HCoV-229E and treated with thapsigargin were still viable, compared to only 20% of cells that survived the infection in the absence of thapsigargin (Fig. 3d). The data suggest that thapsigargin exerts long-lasting antiviral effects at concentrations well below its cytotoxic concentrations.

To further characterize the metabolic state of the cells under the conditions used in these experiments, we investigated protein de novo synthesis. Newly produced proteins were quantified by in vivo puromycinylation tagging of nascent protein chains followed by immunoblotting using anti-puromycin antibodies. HCoV-229E infection was found to shut down cellular protein biosynthesis by 90.3 ± 5.4%, while treatment with thapsigargin for

1 h led to a translational shut-down by 94.3 ± 4.3% (Fig. 3e). However, in infected cells, the simultaneous or delayed addition of thapsigargin restored (or rescued) protein biosynthesis to approximately 50% of the level observed in untreated cells (Fig. 3e). These data demonstrate that, although both viral infection and thapsigargin treatment (individually) induce ER stress and cause a translational shut-down, their combination shows no additive harmful effects on the cells. On the contrary, their combination appears to have opposing effects that result in a partial restoration of the cellular metabolic capacity while retaining a profound antiviral effect.

We next assessed if these effects were cell type or virus-specific. In line with the results described above, the antiviral effects of thapsigargin, the reconstitution of the BiP and IRE1α levels, and the lack of additional cytotoxicity in infected cells could be confirmed for diploid MRC-5 embryonic lung fibroblasts infected with HCoV-229E (Fig. 4a–d), as well as for HuH7 cells infected with MERS-CoV and Vero E6 African green monkey kidney epithelial cells infected with SARS-CoV-2 (Fig. 4e–k and Supplementary Fig. 3a, b). MERS-CoV and SARS-CoV-2 replication were suppressed by thapsigargin with an EC_{50} of 4.8 and 260 nM, respectively (Fig. 4i, j), while the CC_{50} for thapsigargin in Vero E6 cells was 18.25 µM (based on MTT assay) or 20.27 µM (based on ATPlite assay) (Fig. 4k), resulting in selectivity indices (SI, CC_{50}/EC_{50}) of 1229 for MERS-CoV and 70 (MTT) to 78 (ATPlite) for SARS-CoV-2, respectively. In contrast to thapsigargin, the inhibition of PERK by GSK2656157 required higher concentrations in the low micromolar range to attain a significant drop of MERS-CoV replication, once again supporting the exceptional efficacy of thapsigargin (Supplementary Fig. 2f).

Next, we tested potential antiviral activities of thapsigargin against other RNA viruses and used (as a reference) remdesivir, an adenosine analog that inhibits coronavirus RNA-dependent RNA polymerases[39]. We found that thapsigargin suppressed influenza A virus (IAV) but not poliovirus replication (Supplementary Fig. 4a, b). As shown in Supplementary Fig. 5a–c, remdesivir reduced the replication of HCoV-229E ($EC_{50} < 10$ nM), MERS-CoV ($EC_{50} =$ 5.3 nM), and SARS-CoV-2 ($EC_{50} = 2.38$ µM) in HuH7 and Vero E6 cells at non-toxic concentrations (Supplementary Fig. 5d, e), in line with previously published studies[40–42]. The data show that thapsigargin has potent antiviral activity against another family of enveloped RNA viruses and is at least as effective as remdesivir against HCoV-229E and MERS-CoV, while thapsigargin is approximately 10-times more effective than remdesivir against SARS-CoV-2.

To corroborate these observations in a physiologically more relevant system, we established cell cultures of differentiated normal human bronchial epithelial (NHBE) cells[43]. After the initial expansion, the cells were exposed to air-liquid interfaces allowing their differentiation into various airway cell types, which was validated by fluorescence microscopy using antibodies detecting tight junctions and marker proteins specific for the goblet, ciliated and basal cells, respectively (Fig. 5a, b). As shown in Fig. 5c, thapsigargin inhibited the replication of all three coronaviruses included in this experiment (HCoV-229E, MERS-CoV, SARS-CoV-2) in a dose-dependent manner in NHBE cells obtained from different donors. Cell viability following thapsigargin treatment (as judged by measuring the integrity of the epithelial monolayer using TEER) ranged between 70 and 80% after 72 h (Supplementary Fig. 5f). Similar to the cell lines used before, SARS-CoV-2 was found to be slightly less sensitive to thapsigargin treatment. Importantly, in the presence of 1 µM thapsigargin, no infectious virus progeny of any of the three CoVs was detectable at later time points p.i. (Fig. 5c).

To characterize the underlying molecular mechanisms responsible for the observed antiviral effects of thapsigargin, we focused on the two highly pathogenic coronaviruses, MERS-CoV and SARS-CoV-2, for which, to our knowledge, no side-by-side comparison of proteomic changes has been reported at the time of our study. The large-scale proteomic study included (i) untreated cells and cells that were (ii) infected with MERS-CoV, (iii) infected with SARS-CoV-2, (iv) treated with thapsigargin, or, (v and vi) infected with one of these viruses in the presence of thapsigargin. We used label-free quantification to determine the expression levels of >5000 protein IDs from total cell extracts.

In a systematic approach, we identified differentially expressed proteins (DEPs) based on pairwise comparisons of proteins obtained from untreated cells, virus-infected cells, or thapsigargin-treated cells using a p value of $-\log_{10}(p) \geq 1.3$ as cut-off. As visualized by Volcano plot representations, MERS-CoV infection suppressed 412 (at 12 h p.i.) and 1171 proteins (at 24 h p.i.), respectively, and increased the levels of 150 proteins (at 12 h p.i.) and 508 proteins (at 24 h p.i.), respectively (Fig. 6a, b), while SARS-CoV-2 suppressed the expression of 250 proteins at 12 h p.i. and 159 proteins at 24 h p.i. and increased the expression of 224 proteins at 12 h p.i. and 63 proteins at 24 h p.i. (Fig. 6c, d). Thapsigargin treatment alone suppressed/induced large numbers of proteins in HuH7 cells (918 down, 893 up at 12 h; 1711 down, 958 up at 24 h) and in Vero E6 cells (225 down, 191 up at 12 h; 249 down, 162 up at 24 h) (Fig. 6a–d). As expected, this analysis also identified viral proteins as the most strongly regulated DEPs. A comparison of virus-infected cells with virus-infected cells treated with thapsigargin revealed a complete suppression of all viral proteins and a large number of proteins with increased expression in thapsigargin-treated cells infected with MERS-CoV (843, 12 h p.i.; 1208, 24 h p.i.; red groups of proteins) or SARS-CoV-2 (299, 12 h; 362, 24 h; red groups of proteins) (Fig. 6a–d, right graphs). Also, similar numbers of proteins were identified with higher expression in virus-infected cells compared to virus-infected cells treated with thapsigargin (Fig. 6a–d, right graphs; blue groups of proteins). Together, these data lead us to conclude that thapsigargin causes a profound shift in protein expression in infected cells that likely contributes to the antiviral effects of this compound.

We then devised a bioinformatics strategy to identify patterns of co-regulated or unique pathways and link deregulated protein sets identified in these data to specific (known) biological functions. As shown schematically in Fig. 6e, we sorted the DEPs from each of the four groups shown in Fig. 6a–d into four multiple gene ID lists, annotated the gene IDs to biological pathways, and generated hierarchically clustered heatmaps of the top 100 differentially enriched pathway categories for the 12 h p.i. and 24 h p.i. time points of MERS-CoV- and SARS-CoV-2-infected cells, respectively, versus thapsigargin-treated cells by over-representation analysis (ORA) using Metascape software[44]. In this analysis, the groups of up- or downregulated proteins were kept separate to preserve information on whether specific DEPs belonging to particular overrepresented pathway terms were regulated in the same or opposite direction. Inspection of the four top 100 clustered heatmaps shows many similarities but also differences in pathways and their enrichment p values in response to virus infection or thapsigargin, with the combined data revealing the complexity of cellular responses to CoV infections or chemical stressors (Supplementary Figs. 6, 7). By condensing this information to the top 5 pathways for up- or downregulated DEPs, we found that many of the most highly enriched categories are related to RNA, DNA, metabolic functions and localization (Supplementary Fig. 8a). We then combined the 400 pathway categories and searched this list for identical or unique GO terms in response to MERS-CoV, SARS-CoV-2, or thapsigargin. By filtering 229 pathways (out of 400) with enrichment p values of $\log_{10}(p) \leq -3$, we found 36 pathway categories shared by both viruses and by thapsigargin, which are mostly related to RNA,

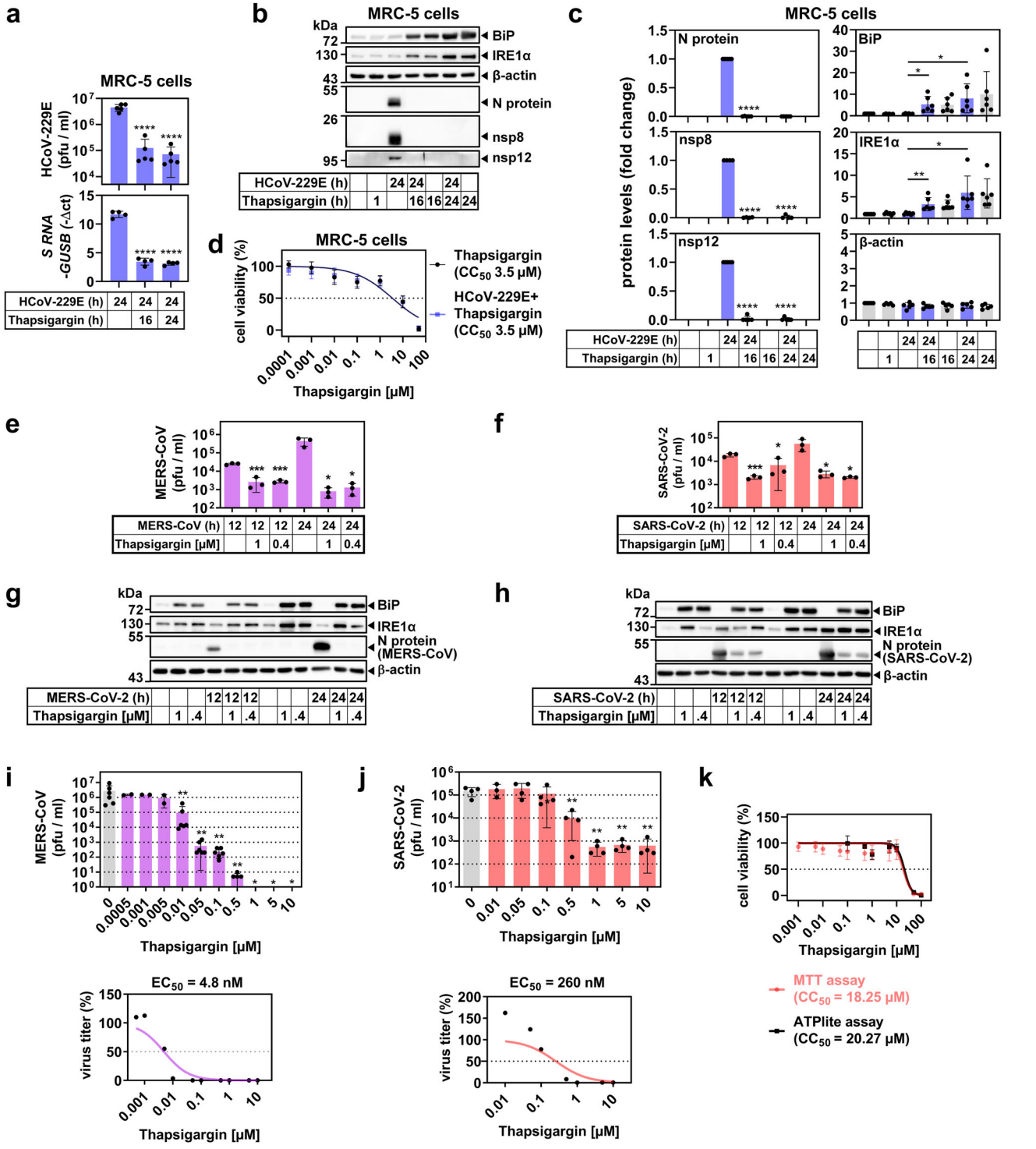

folding, stress, and localization (Fig. 6f and Supplementary Fig. 8b). Fifty-two pathway categories unique to thapsigargin almost exclusively represented metabolic and biosynthetic pathways as shown for the top 20 overrepresented pathways containing up- or downregulated DEPs, suggesting that thapsigargin on its own, unlike CoV infection, initiates a broad metabolic response (Fig. 6f and Supplementary Fig. 8b).

This raised the question of whether the thapsigargin effects were retained in infected cells or, alternatively, drug-sensitive pathway patterns were reprogrammed (or masked) by the virus infection. To address this point, we pooled all pathways enriched under virus + thapsigargin conditions and compared them to virus infection or thapsigargin treatment alone. 59% (147 out 249) pathway terms were shared by these three conditions, reflecting multiple stress-related catabolic, RNA regulatory, and vesicle or autophagy processes (Fig. 6g, h). 20 pathway terms were unique to the virus + thapsigargin situation. They primarily mapped to specific splicing, signaling (TORC, RHOA, ARF3) and transport/localization pathways (Fig. 6g, h). The 37 categories shared by virus + thapsigargin and thapsigargin conditions but not detectable in cells infected with virus (only) recapitulate the thapsigargin-regulated metabolic pathways (metabolism of

Fig. 4 Thapsigargin inhibits the replication of high- and low-pathogenic human coronaviruses in multiple cell types. a–d Human embryonic MRC-5 lung fibroblasts were infected with HCoV-229E according to the scheme shown in Fig. 2b. **a** Viral titers (upper graph, five biologically independent experiments) and expression of viral *S* gene-encoding RNAs (lower graph, four biologically independent experiments). **b**, **c** Expression of viral and host cell proteins. **b** Shows one representative immunoblot of total cell extracts and **c** shows quantification from four or more biologically independent experiments. **d** Cell viability was analyzed and quantified as described in the legend of Fig. 3 (four biologically independent experiments). **e–j** Similarly, HuH7 cells or Vero E6 African green monkey kidney epithelial cells were infected with MERS-CoV (MOI = 0.5) or SARS-CoV-2 (MOI = 0.5) for 12 h or 24 h in the presence/absence of 0.4 μM or 1 μM thapsigargin. **e**, **f** Show viral titers and **g**, **h** display representative images of the corresponding expression of MERS-CoV/SARS-CoV-2 nucleocapsid (N) and host cell proteins, respectively (three biologically independent experiments). **i** Dose-dependent suppression of MERS-CoV-2 replication by thapsigargin in HuH7 cells infected with an MOI of 0.5 (upper graph, two or more biologically independent experiments) and the estimated EC_{50} concentration calculated from the mean values (lower graph). **j** Dose-dependent suppression of SARS-CoV-2 replication by thapsigargin in Vero E6 cells infected with an MOI of 0.5 (upper graph, three or more biologically independent experiments) and the estimated EC_{50} concentration from the mean values (lower graph). **k** The CC_{50} of thapsigargin in Vero E6 cells was calculated by MTT or ATPlite assays as described in the legend of Fig. 3b, c. Data are from three or more biologically independent experiments. All bar graphs show means ± s.d.; asterisks indicate *p* values (*$p \le 0.05$, **$p \le 0.01$, ***$p \le 0.001$, ****$p \le 0.0001$) obtained by two-tailed unpaired t-tests (**a**, **c**, **e**, **f**, **j**) or ordinary one-way ANOVA (**i**). See Supplementary Figs. 3–5 for quantifications from replicates for MERS-CoV/SARS-CoV-2 immunoblot experiments and for further inhibitor data.

monosaccharide, cysteine, glutathione, methionine, fructose, mannose, pyruvate, TCA cycle, ERAD pathway) (Fig. 6g, h). For some of these pathways (e.g., ERAD, monocarboxylic acid metabolism), some DEPs were induced while others were repressed, indicating remodeling of pathway functions at the protein level (Fig. 6g, h). The 36 pathway terms that were absent in the virus + thapsigargin group of terms (groups 15, 9, 12 of the Venn diagram shown in Fig. 6g) represent a distinct set of terms, most of which being related to nucleotide and DNA-related processes, such as DNA repair, DNA unwinding, chromatin silencing (Fig. 6g, h). In summary, the functional analysis of DEPs at the level of differentially enriched pathway categories shows that the antiviral effects of thapsigargin strongly correlate with the activation/suppression of a range of metabolic programs.

The enriched pathway terms provided important overarching information on shared and unique biological processes but not necessarily encompassed identical sets of DEPs as exemplified by the twelve pathways shown in Fig. 6i. We, therefore, refined our analysis to the individual component level to identify proteins with similar regulation between both viruses across both cell types. The proteomes of HuH7 and Vero E6 cells overlap by 57% (Fig. 7a). In this group, only 43 identical proteins were found to be deregulated by both MERS-CoV and SARS-CoV-2 (Fig. 7b, left Venn diagrams). However, under thapsigargin + virus conditions, 120 proteins were upregulated and 63 proteins were downregulated (Fig. 7b, right Venn diagrams). Using the top 50 DEPs as an example, it becomes apparent that the majority of proteins are regulated into the same direction by thapsigargin alone; demonstrating that thapsigargin largely overrides any virus-induced modulation of host processes (Fig. 7c).

In the absence of thapsigargin, the virus infection generally has little or opposite effects on the levels of the 120 proteins, as exemplified by the suppression observed for BiP (HSPA5) or HERPUD1 (Fig. 7c, highlighted in green). The 120 induced factors map to pathways involving Golgi vesicle transport, ER stress, fiber organization, and apoptosis (Fig. 7d). Across their pathway annotations, 71 out of the 120 proteins were reported to strongly interact, thus probably being involved in protein:protein networks that coordinate activities of the enriched pathways (Fig. 7e, left graph). Likewise, the 63 repressed proteins map to specific (though different) pathways, such as monocarboxylic acid metabolism or viral life cycle (Fig. 7d). 26 components can be allocated to a few small protein interaction networks (Fig. 7e, right graph).

In our proteomic/bioinformatics analysis, HERPUD1 and p62/SQSTM1 were revealed to be among the most prominent thapsigargin-regulated factors in MERS-CoV- and SARS-CoV-2-infected cells (Fig. 7c, highlighted in green, orange). Both proteins are key regulators of two major and highly interconnected intracellular degradation pathways, ERAD and autophagy[45,46], leading us to focus our further analyses of the antiviral effects of thapsigargin on these processes.

The protein HERPUD1 has an essential scaffolding function for the organization of components of the core ERAD complex[47,48]. ERQC and ERAD pathways are critically involved in the qualitative and quantitative control of misfolded or excessively abundant proteins in the ER. If protein folding in the ER fails, the proteins are retro-translocated through a HERPUD1-dependent ER membrane complex to the cytosol for proteasomal degradation[49]. By searching our proteomics data for further ERAD factors, we were able to retrieve a total of 33 (for MERS-CoV) and 20 (for SARS-CoV-2) proteins of the canonical ERQC and ERAD pathways for which a differential expression was observed in virus-infected cells treated with thapsigargin (Fig. 7f). Mapping of these data on the KEGG hsa04141 pathway suggests that thapsigargin enhances or restores these mechanisms at key nodes of ERQC and ERAD in coronavirus-infected cells (Supplementary Fig. 9).

We also intersected the 120 + 63 proteins jointly regulated by thapsigargin in MERS-CoV- and SARS-CoV-2-infected cells with data from a recent genome-wide sgRNA screen that reported new ERAD factors required for protein degradation[50]. This analysis identified 30 additional thapsigargin-regulated factors that may further support antiviral ERAD, including the E1 ubiquitin ligase UBA6 and the zinc finger protein ZNF622 (also called ZPR9), which were recently described either as negative regulators of autophagy or of some DNA virus infections (Fig. 7g)[51,52].

The protein p62/SQSTM1 is a multifunctional signaling protein and cargo receptor that targets clients for destruction by selective autophagy[53]. This raised the question of whether the elevated p62/SQSTM1 levels observed in thapsigargin-treated cells affected autophagy pathways during CoV infection. We, therefore, assessed, under these conditions, viral replication and the autophagic flux by determining the levels of p62/SQSTM1 and the non-lipidated/lipidated forms of the ATG8 ortholog LC3B, a protein that is central to autophagosome formation, in the presence/absence of lysosomal inhibition. Pre-treatment of HuH7 cells with the lysosomal V-ATPase inhibitor bafilomycin A_1 for 4 h suppressed HCoV-229E infection to a similar extent as thapsigargin (by about 100-fold) (Fig. 8a, lanes 3 and 4), while the addition of bafilomycin A_1 at 8 h p.i. reduced viral replication only 10-fold (Fig. 8a, lanes 5 and 6). Under these conditions, bafilomycin A_1 showed no negative effects on cell viability (Supplementary Fig. 10). Bafilomycin A_1 alone did not suppress MERS-CoV replication but inhibited SARS-CoV-2 (Fig. 8b).

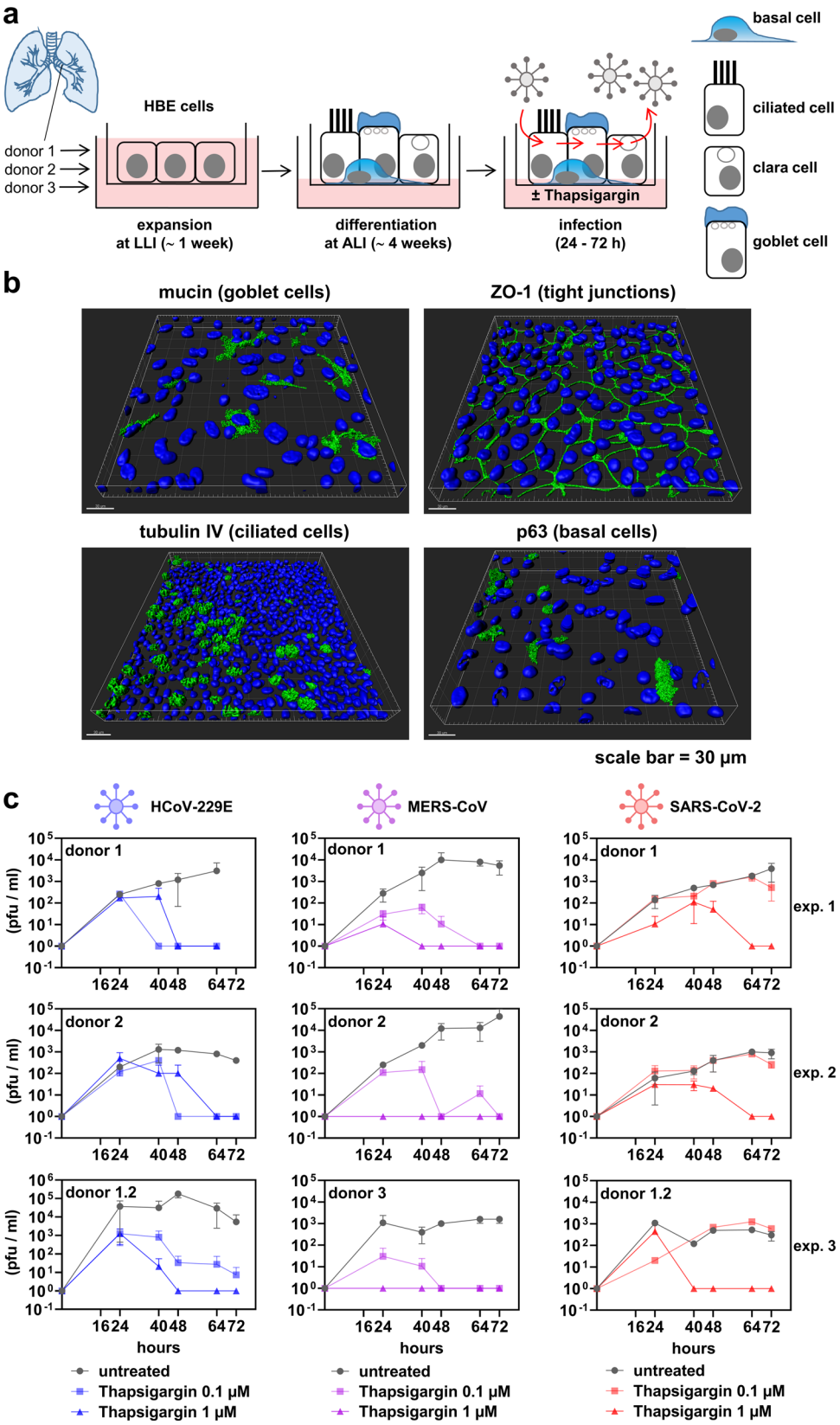

These (variable) antiviral effects of bafilomycin A_1 are in line with other alkylating agents that suppress lysosomal pathways[54].

Bafilomycin A_1 and thapsigargin strongly increased the appearance of p62/SQSTM1-positive foci representing autophagosomes in untreated but also in infected cells, suggesting that HCoV-229E infection but also thapsigargin treatment stimulate early events in autophagosome biogenesis (Fig. 8c).

With respect to viral protein synthesis, pretreatment of cells with bafilomycin A_1 partially reduced HCoV-229E N protein levels but had no effect on viral N protein accumulation when

Fig. 5 Thapsigargin suppresses CoV replication in differentiated primary human bronchial epithelial cells. a Scheme showing the expansion in a liquid −liquid interphase (LLI) followed by the differentiation at an air-liquid interphase (ALI) of normal human bronchial epithelial cells (NHBE). **b** Three-dimensional immunofluorescence analysis (z-stacks) of representative NHBE cells stained with antibodies specific for the indicated differentiation markers. Shown is one representative out of two biologically independent experiments. **c** NHBE cells were left untreated or infected with the indicated CoV (MOI = 3) and treated for up to three days with thapsigargin (0.1 or 1 μM). Supernatants were collected at five time points p.i. and virus titers determined by plaque assay. Data represent three biologically independent experiments using NHBE cells derived from two or three independent donors. Shown are means ± s.d. of technical duplicates. For HCoV-229E and MERS-CoV, cells from donor 1 were plated and differentiated a second time to generate an additional independent experiment (labeled donor 1.2). See Supplementary Fig. 5f for cell viability experiments.

added 8 h p.i. This was in clear contrast to thapsigargin, which (similar to the experiments presented above) suppressed N protein accumulation completely (Fig. 8d, e). HCoV-229E infection reduced p62/SQSTM1 levels by approximately 70% (mean 26 ± 8%) (Fig. 8d, e, lane 1 compared with lanes 5 or 14), whereas there was no such effect on total LC3B (mean 105 ± 27%) or lipidated LC3B-II (mean 120 ± 23%) (Fig. 8d, e). Thapsigargin upregulated p62/SQSTM1 (mean 294 ± 30%), total LC3B (mean 196 ± 28%), and LC3B-II (mean 218 ± 27%) (Fig. 8d, e). Blocking lysosome acidification by bafilomycin A_1 strongly induced p62 levels in HCoV-229E-infected cells by six-fold (to a mean of 179 ± 21%) (Fig. 8d, e, lanes 5 and 6) and increased LC3B-II levels by three-fold (mean 321 ± 145%) (Fig. 8d, e, lanes 5 and 6). Under all conditions used, there was no bafilomycin A_1-mediated effect on p62/SQSTM1 or LC3B levels upon addition of thapsigargin (Fig. 8d, e). These changes were used to calculate the turnover of LC3B-II and p62/SQSTM1 as a measure of basal and selective autophagic flux, respectively (Fig. 8f), which were determined according to the procedures described in ref. [55]. Compared to untreated cells, HCoV-229E-infected cells displayed a weakly reduced basal autophagy by about 25%, with selective autophagy being stimulated by around three-fold early upon infection (Fig. 8f). Under all conditions tested, thapsigargin strongly suppressed the autophagic flux (Fig. 8f). These data suggest that the increased levels of p62/SQSTM1 and LC3B-II, respectively, observed in thapsigargin-exposed cells result from a suppression of their lysosomal degradation and lead us to conclude that the blockade of CoV-induced selective autophagic flux represents an additional antiviral mechanism of thapsigargin.

Finally, we sought to validate the protein changes observed by mass spectrometry and by the detailed analysis of the autophagic flux for HCoV-229E, MERS-CoV, and SARS-CoV-2 including also cystathionine-γ-lyase (CTH), an additional hit belonging to the enriched pathways GO:0006520 (cellular amino acid metabolic process) and GO:0034976 (response to ER stress, as shown in Fig. 6g–i). CTH is a regulator of glutathione homeostasis and cell survival[56]. As shown by immunoblotting, we confirmed the upregulation of proteins representative for the UPR (IRE1α, BiP, CTH), for ERQC/ERAD (HERPUD1, UBA6, ZNF622), and for autophagy (p62/SQSTM1, LC3B-I/LC3B-II) in thapsigargin-treated cells infected with one of the three CoVs (Fig. 9a, b).

In conclusion, these data show that thapsigargin forces the (re) expression of a dedicated network of proteins with roles in ER stress, a range of metabolic pathways, ERQC, ERAD, and the regulation of autophagy. Noteworthy, it is the combination of these changes at the protein level that confers a sustained "antiviral state" and profoundly suppresses CoV replication as summarized schematically in Fig. 9c.

Discussion

In this study, we report a potent inhibitory effect of the chemical thapsigargin on the replication of three human CoVs in four different cell types. Following up on observations that CoV globally suppresses UPR/ER stress factors, we find that thapsigargin counteracts the CoV-induced downregulation of BiP, HERPUD1 (and CTH) and increases IRE1α levels. In this context, thapsigargin also plays a role in overcoming the coronavirus-induced block of global protein biosynthesis. Proteome-wide data revealed a thapsigargin-mediated reprogramming of metabolic pathways and helped to identify a network of specific thapsigargin-regulated factors, including candidates from the ERQC/ERAD pathways that, most likely, are involved in the destruction of viral proteins. The positive effects of prolonged thapsigargin treatment on the expression of cellular BiP and HERPUD1 are well documented[57–60]. Thus, one key finding of our study is that the thapsigargin-mediated induction of ER factors overrides suppressive effects of CoVs on ER functions, as illustrated here for BiP, IRE1α and HERPUD1, but also at the global proteomic scale.

BiP is one of the most abundant cellular proteins (also in our mass spectrometry data) and plays an essential role in development and disease[61,62]. In yeast, the inducible expression of the BiP homolog Karp2 was shown to be essential for disposing of toxic proteins and reducing cellular stress[63]. Hence, a reduction of BiP levels (as seen during CoV infection) and the contrary effect of thapsigargin-mediated upregulation are likely to have opposing consequences for the host cell following viral infection. Similarly, IRE1α is suggested to mediate protective and adaptive responses suitable to alleviate ER stress, e.g., by balancing lipid bilayer stress, an aberrant perturbation of ER membrane structures, which may be expected to occur upon DMV formation in CoV-infected cells[18,31,64]. Accordingly, high levels of BiP, HERPUD1, and IRE1α may increase in general the resilience of cells when infected by diverse pathogens. In line with this, our data show that, in cells infected with representative coronaviruses, a protective ER/UPR response is initially elicited at the mRNA level (Fig. 1c and ref. [17]). However, the global suppression at the protein level (or the lack of induction) indicates that CoVs have evolved strategies at the posttranscriptional or translational level to escape the protective antiviral activities of BiP, IRE1α, and HERPUD1.

Together with PERK, all three proteins are key regulators of ERQC/ERAD pathways and there is ample evidence to suggest that their expression, regulation, and activities are intimately linked[21,22]. A recent study reported that PERK activation induces the RPAP2 phosphatase, inactivates IRE1α kinase activity, and aborts IRE1α-mediated adaptive functions in response to the chemical stressor Brefeldin A[65]. In another report, high BiP levels exerted negative control of IRE1α by directly binding the kinase or by promoting IRE1α degradation[66]. Here, we show a different scenario, in which high BiP and IRE1α protein levels coincide with an antiviral state, as well as with improved metabolic functions, suggesting unique modes of cross-regulation of PERK, BiP, and IRE1α in CoV-infected cells exposed to chemical stress.

The (up)regulation of HERPUD1 and several ERAD factors by thapsigargin provides an additional layer of control contributing to the rapid suppression of CoV proteins. While ERAD is generally needed to dispose of unwanted proteins in the ER[67,68], a process called "ERAD tuning" that has been suggested to dampen or balance ERAD activity by

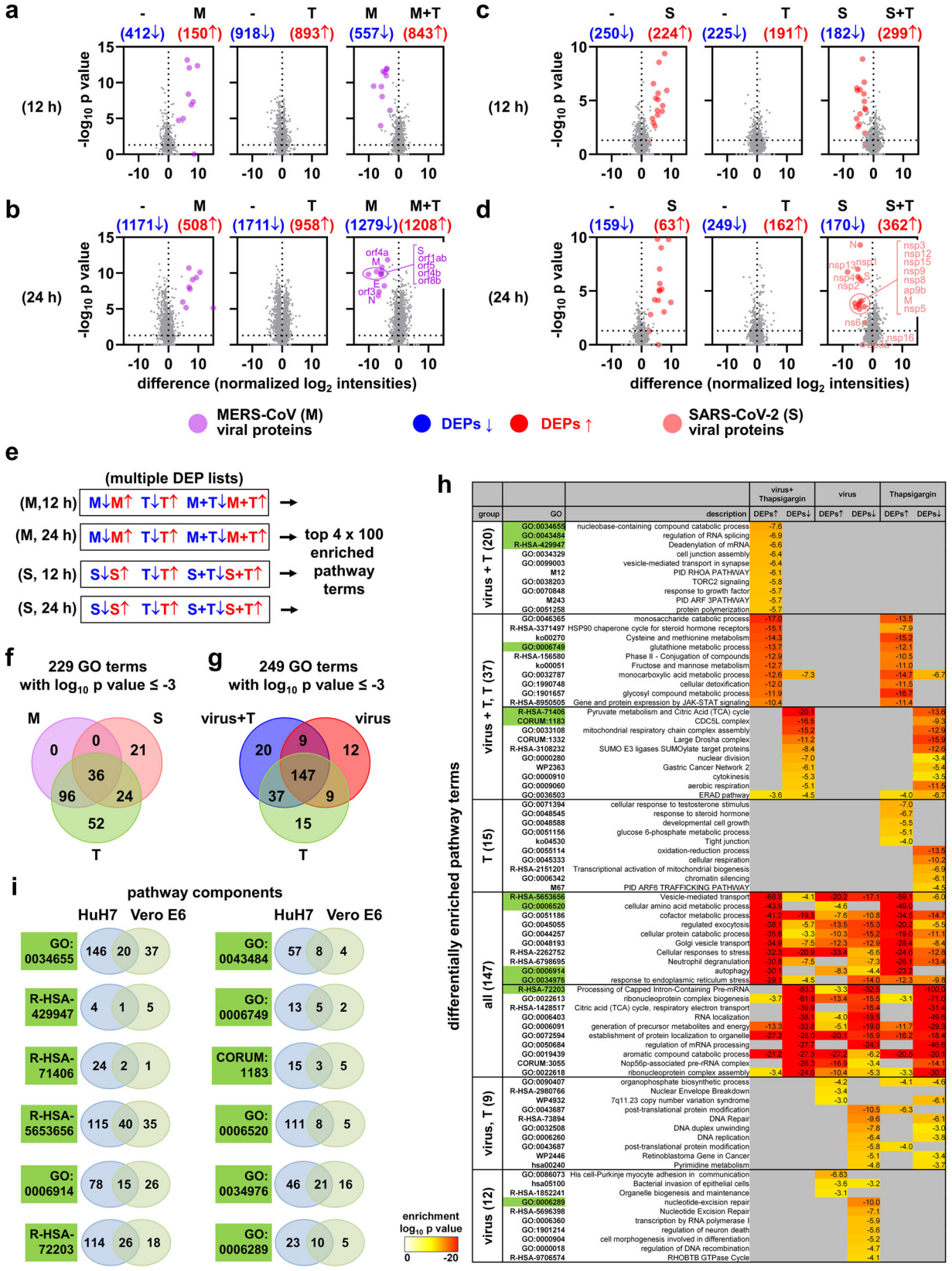

segregating ERAD components into specific ER-derived vesicles called EDEMosomes. During CoV infection, ERAD tuning may prevent the destruction of CoV proteins[69–71]. Our data are compatible with a model in which a modulation of ERAD components by small molecules may antagonize "ERAD tuning" promoted by CoVs, thereby preserving normal ERAD topology, as well as high ERAD activity.

High HERPUD1 levels were also reported to impair autophagy and, conversely, its depletion increased autophagic flux upon glucose stress[72], suggesting that HERPUD1 may contribute to the

Fig. 6 Proteome-wide identification of thapsigargin action on MERS-CoV- or SARS-CoV-2-infected cells reveals virus- and thapsigargin-specific protein and pathway patterns. Total cell extracts from uninfected cells (−), HuH7 cells infected with MERS-CoV (M, MOI = 3) for 12 h (**a**) or 24 h (**b**), or Vero E6 cells infected with SARS-CoV-2 (S, MOI = 3) for 12 h (**c**) or 24 h (**d**), in the presence or absence of thapsigargin (T, 1 μM) were subjected to LC-MS/MS analysis. 5,367 (from HuH7) or 5,066 (from Vero E6 cells) majority protein IDs were identified and their intensities were normalized between samples. Volcano plots show pairwise ratio comparisons and corresponding *p* values obtained from Student's t-tests, which were derived from the means of two independent experiments for each condition and three technical replicates per sample. Blue and red colors indicate differentially expressed proteins (DEPs, ratio > 0, *p* value of $-\log_{10}(p) \geq 1.3$). Purple and light red colors indicate individual viral proteins. **e** Majority IDs (for HuH7 cells) or NCBI gene IDs (for Vero E6 cells) corresponding to the DEPs shown in (**a**)−(**d**)) were used for overrepresentation analyses to identify the top 100 enriched pathway categories per virus and time point using Metascape software[44]. Complete lists of pathways are shown in Supplementary Figs. 6 and 7 as clustered heatmaps. The top five enriched pathway categories for up- or downregulated DEPs are shown in Supplementary Fig. 8a. (**f**, **g**) The 400 enriched pathway categories were pooled and filtered for common and distinct pathways considering only terms with enrichment *p* values of $\log_{10}(p) \leq -3$. **f** Venn diagram showing pathway terms specific to MERS-CoV (M), SARS-CoV-2 (S), or thapsigargin (T). The top 20 enriched pathway categories are shown in Supplementary Fig. 8b. **g** Venn diagram showing pathway terms specific for the virus, thapsigargin, or infection plus thapsigargin (virus + T) conditions. **h** The heatmap shows the top differentially enriched pathways corresponding to the Venn diagram shown in (**g**). Green colors refer to the pathways highlighted in (**i**). **i** Twelve examples of differential and joint gene ID compositions of pathways enriched in HuH7 or Vero E6 cells.

antiviral effects of thapsigargin by a dual-mode, through ERAD and as a repressor of autophagy. The contribution of (macro) autophagy to CoV replication is still controversial with evidence for both pro- and antiviral roles, depending on the virus strains and model systems used (reviewed in refs. [71,73]). Here, we provide evidence to suggest that human CoVs induce (and require) p62/SQSTM1-mediated selective autophagy early in their replication cycle because N protein translation and replication are repressed to some extent by inhibitors of lysosomal acidification. Recently, p62/SQSTM1 was shown to act as an adaptor to mediate a selective form of autophagy, called ER-phagy, that normally serves to remove larger parts of damaged ER or bulky protein aggregates that cannot readily be disposed of by ERAD[74–76]. Based on our findings, we speculate that CoV may leverage ER-phagy, in addition to "ERAD tuning", to generate membrane sources for their specific CM/DMV environment. Compared to lysosomal inhibition, the thapsigargin effects on blocking CoV-mediated autophagic flux were much more sustained and durable. This observation is in line with the work from Ganley et al. who showed that thapsigargin blocks the fusion of autophagosomes with lysosomes, a late step in the autophagy pathway, by an unknown mechanism[77]. Genetic experiments in *Drosophila* revealed a role of the SERCA Ca^{2+} pump in membrane fusion events of lysosomes[78]. Because thapsigargin inhibits SERCA[79], it, therefore, remains a possibility that thapsigargin is particularly efficient in blocking autophagy and CoV-replication because it prevents the Ca^{2+} gradients required for multiple vesicle fusion events known to occur during the CoV replication cycle.

Clearly, the precise mechanistic basis for these effects remains to be identified in additional studies. One approach will be to identify direct interactions between CoV proteins and ER stress or autophagy pathway components. A number of affinity purification- or proximity labeling-based mass spectrometry data sets are now available for host cell proteins interacting with individually expressed SARS-CoV-2 proteins (reviewed in ref. [80]). These data reveal a large number of host interactors from a broad range of pathways, several of which including regulators of ER stress or autophagy[81]. However, it remains to be seen which of the reported protein:protein interactions can be confirmed in CoV-infected cells with their unique subcellular compartmentalization.

In line with the interaction studies, our proteomic and functional data show that thapsigargin affects multiple pathways beyond the core ER stress response. Overall, the available evidence indicates that it will not be trivial to identify the essential targets that mediate thapsigargin's multimodal antiviral effects.

Our data provide a rich resource for further drug target analysis, also in conjunction with the few deep protein sequencing studies available for SARS-CoV-2 (but not MERS-CoV)[82–85]. Thus, our study fills an important knowledge gap by providing a direct side-by-side comparison of pharmacologically targeted cells infected with two highly pathogenic human coronaviruses.

In the absence of specific and effective therapeutic strategies to combat coronaviruses, and in view of the current SARS-CoV-2 pandemic, we hope that our observations will stimulate a broader investigation of this potential therapeutic avenue. This will also include more detailed studies on the antiviral effects and specificity of thapsigargin for other RNA viruses, such as influenza A virus. Given that thapsigargin concentrations in the lower nanomolar range were shown to abolish CoV replication in cultured cells (including primary bronchial epithelial cells) for up to three days after a single application, this work identifies thapsigargin as an interesting drug candidate. The Ca^{2+} mobilizing and cytotoxic features of plant-derived thapsigargin have been studied for 40 years[86,87]. Several analogs have already been designed and efficient and scalable purification or synthesis is now available for application in humans[88–90]. Recently, a protease-cleavable prodrug of thapsigargin, mipsagargin, has been evaluated in phase I and II clinical trials for prostate cancer[86,91–93]. It is not uncommon to adapt anti-proliferative cytostatic drugs (e.g., azathioprine, cylophosphamide, methotrexate) for the treatment of autoimmune and inflammatory disorders by applying lower doses than those needed for treating cancer[94]. Similarly, low doses of thapsigargin combined with short-term systemic or topical application in the airways might reduce viral load early on or in critically ill patients with a favorable therapeutic index with respect to antiviral versus cytotoxic effects. CoVs also activate inflammatory, NF-κB-dependent cytokine and chemokines at the mRNA level[17], some of which (CXCL2, CCL20) escaping translational shut-down and being secreted in a cell-type-specific manner (Supplementary Fig. 11). Some of these cytokines may contribute to the cytokine storm observed in some COVID-19 patients[95]. While thapsigargin had no effect on IL-8, IL-6, CXCL2, and CCL20 in cell culture (Supplementary Fig. 11), a single bolus of the compound was shown to efficiently reduce the translation of pro-inflammatory cytokines in preclinical models of sepsis[96]. Thus, an additional benefit of thapsigargin treatment may arise from dampening overshooting tissue inflammation in COVID-19 patients. In summary, the study provides several lines of evidence that thapsigargin hits a unique combination of central mechanisms required for CoV replication, which may be exploited to develop novel therapeutic strategies. This compound or derivatives thereof with improved specificity, pharmacokinetics, and safety profiles may also turn out to be suitable

77

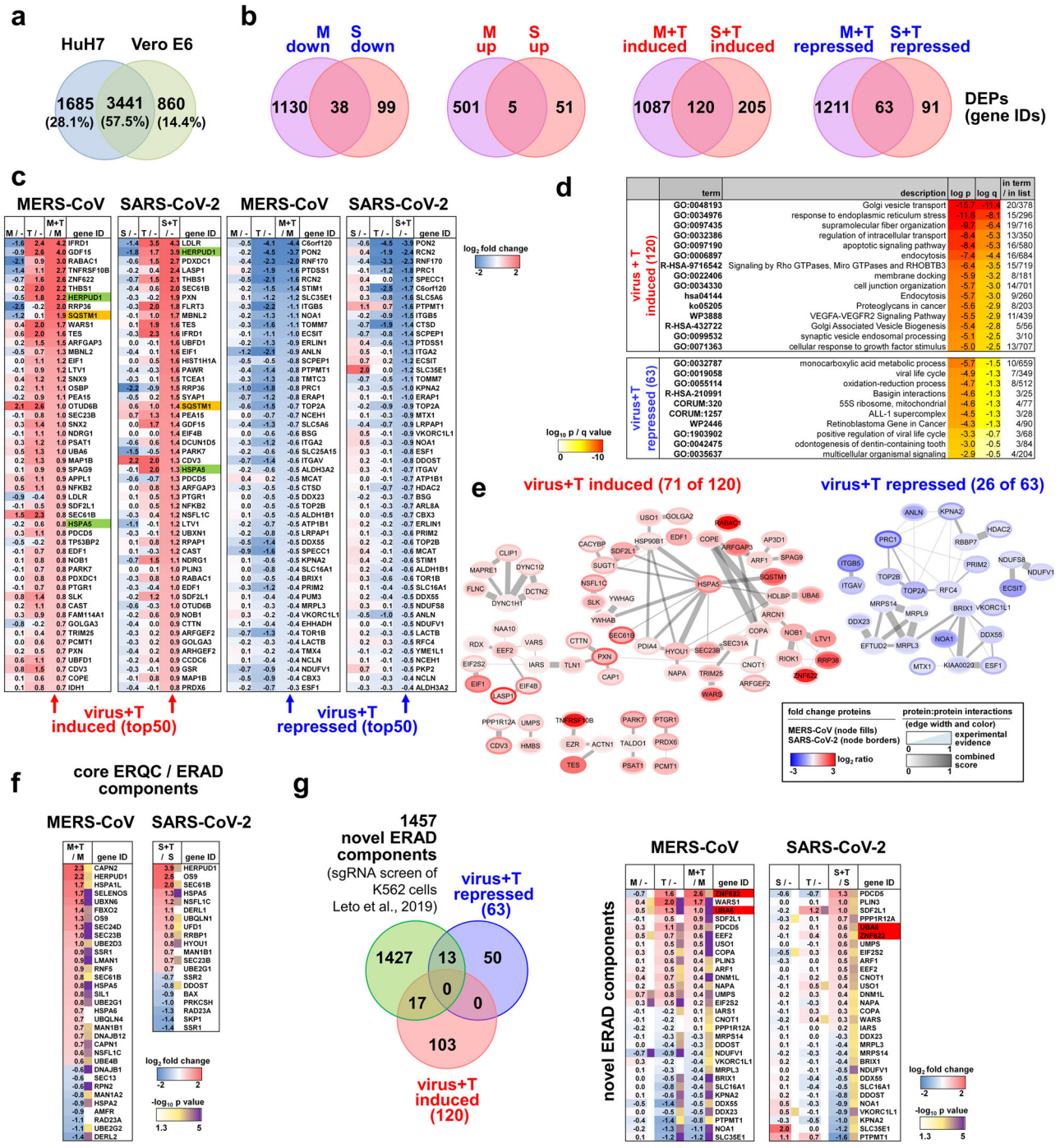

Fig. 7 Thapsigargin regulates a specific network of proteins involved in transport, ERQC/ERAD, and ER stress in MERS-CoV or SARS-CoV-2-infected cells. a Overlap of orthologous proteins expressed in HuH7 and Vero cells. **b** Overlap of virus- and thapsigargin-regulated proteins common to HuH7 and Vero E6 cells showing 120 proteins with higher and 63 proteins with lower expression in thapsigargin-treated infected cells compared to virus infection alone (ratio > 0, *p* value of $-\log_{10}(p) \geq 1.3$). **c** Heatmaps showing individual mean ratio values of normalized protein intensities for the top 50 up- or downregulated proteins in virus-infected and thapsigargin-treated cells. Ratio values of infected or thapsigargin-treated conditions compared to untreated cells (−) are shown for comparison and are sorted according to the virus plus thapsigargin conditions. Green colors highlight HERPUD1 and BiP (HSPA5), while orange colors highlight p62/SQSTM1. **d** Top pathways mapping to gene IDs with increased (120 proteins, red) or decreased (63 proteins, blue) expression levels in thapsigargin-treated and infected cells compared to virus infection alone as revealed by overrepresentation analysis using Metascape software[44]. **e** Protein:protein interactions (PPI) amongst the 120 up- and 63 downregulated thapsigargin-sensitive proteins based on experimental evidence, co-occurrence, co-expression, and confidence scores from the STRING database[108]. According to experimental evidence and combined STRING score criteria, 71 and 26 coregulated proteins are engaged in defined PPI networks; the remaining proteins are not known to interact. **f** Heatmap showing thapsigargin-reprogrammed proteins of KEGG hsa04141 (mean ratio ≥ 1.5 fold). See also Supplementary Fig. 9 for projection of thapsigargin-mediated protein changes on the KEGG pathway map. **g** Venn diagram showing the intersection of thapsigargin-/virus-regulated proteins with all novel ERAD components (FDR of 1%) identified by ref. [50]. The regulation of 30 overlapping components is shown as a heatmap displaying mean ratio values in thapsigargin-treated or infected cells. Red colors highlight UBA6 and ZNF622 as discussed in the text. (**b**, **c**, **f**, **g**) Mean ratio and *p* values were determined as described in the legend of Fig. 6a–d. Abbreviations: *M* MERS-CoV; *S* SARS-CoV-2; *T* thapsigargin.

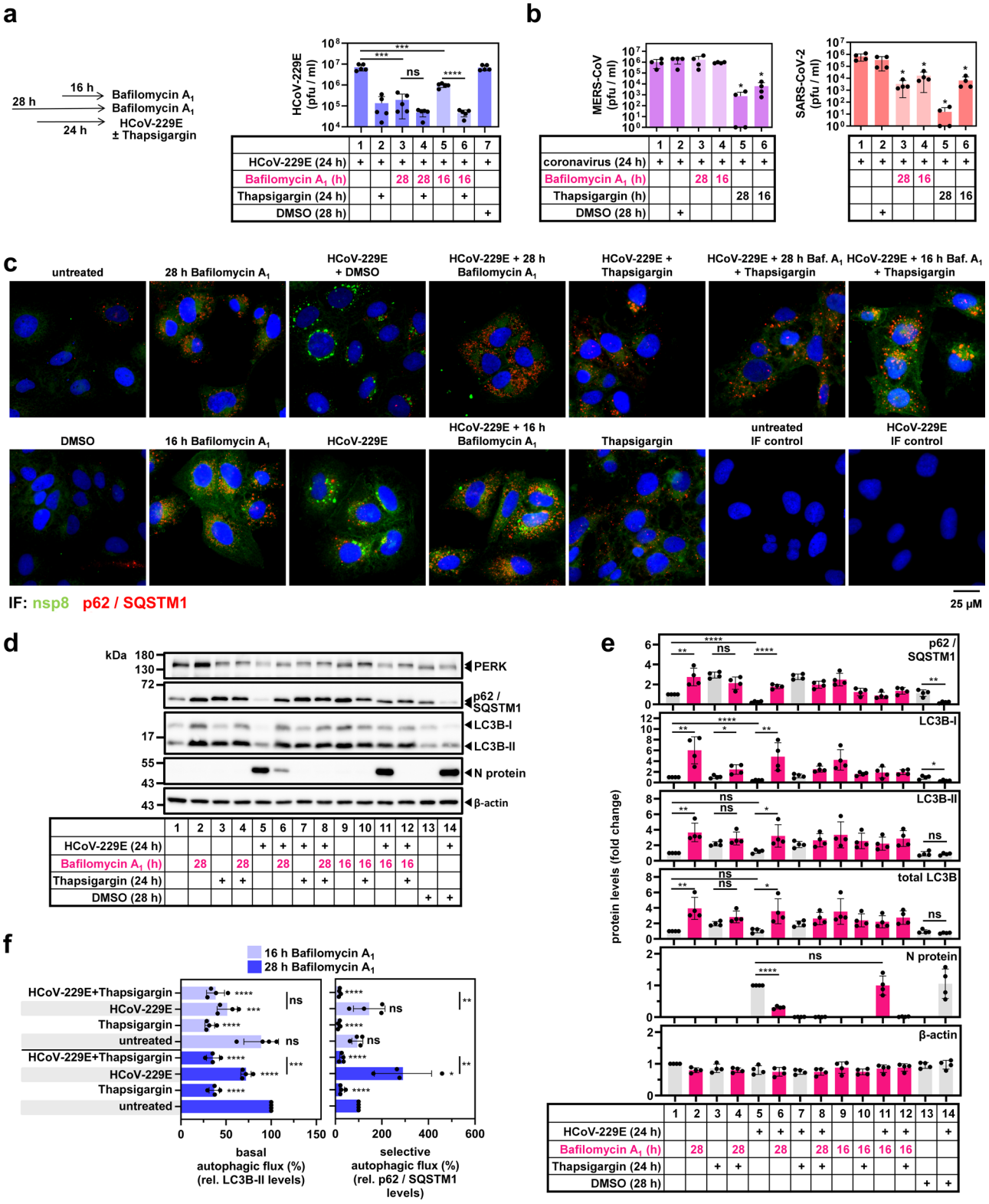

for mitigating the consequences of potential future CoV epidemics more effectively.

Methods

Cells and viruses. HuH7 human hepatoma cells (Japanese Collection of Research Bioresources (JCRB) cell bank;[97]) were maintained in Dulbecco's modified Eagle's medium (DMEM, including 3.7 g/l $NaHCO_3$; PAN Biotech Cat No P04-03550) complemented with 10% filtrated bovine serum (FBS Good Forte; PAN Biotech, Cat No. P40-47500), 2 mM L-glutamine (Gibco, 21935-028), 100 U/ml penicillin and 100 µg /ml streptomycin. MRC-5 human embryonic lung fibroblasts (ATCC, CCL-171) were maintained in DMEM containing 1.5 g/l (w/v) $NaHCO_3$ and complemented with 10% fetal calf serum (FCS; PAN Biotech Cat No. 1502-P110704), 2 mM L-glutamine, 100 U/ml penicillin, and 100 µg/ml streptomycin, 1% minimum essential medium non-essential amino acids (100x MEM NEAA; Gibco Cat No 11140-035) and 1 mM sodium pyruvate (100 mM; Gibco 11360-039). Vero E6 African green monkey kidney epithelial cells (ATCC CRL-1586), A549 cells (ATCC CCL-185), and MDCK-II (ATCC CRL-2936) cells were grown

Fig. 8 Thapsigargin suppresses CoV-induced autophagic flux. a HuH7 cells were treated with bafilomycin A_1 4 h before (28 h) or 8 h after (16 h) infection with HCoV-229E (MOI = 1). Thapsigargin was added as indicated. Samples from DMSO-treated cells served as solvent controls. After 24 h, supernatants were used to determine viral titers (five biologically independent experiments). **b** Effects of pre- or post-infection treatments with bafilomycin A_1 as shown in the scheme of (**a**) on viral titers in supernatants collected from HuH7 or Vero E6 cells infected with MERS-CoV (MOI = 0.5, left graphs) or with SARS-CoV-2 (MOI = 0.5, right graphs) for 24 h (four biologically independent experiments). **c** Fluorescence microscopy images representative for one out of two biologically independent experiments showing the distribution and subcellular localization of p62/SQSTM1-positive foci in untreated cells or cells infected with HCoV-229E in the presence/absence of bafilomycin A_1 and thapsigargin. Viral replication sites were stained with antibodies specific for nsp8. **d**, **e** HuH7 cells were treated or infected with HCoV-229E as described in (**a**). Total cell extracts were analyzed by immunoblotting for PERK, the non-lipidated (LC3B-I) or lipidated (LC3B-II) forms of LC3B, p62/SQSTM1, and N protein as indicated. Antibodies against β-actin were used to validate equal loading. **d** Shows a representative experiment and **e** shows the quantification of immunoblot data from four independent experiments relative to the untreated control. **f** Data from (**d**, **e**) were used to calculate the autophagic flux relative to untreated and non-infected conditions. All bar graphs show means ± s.d.; asterisks indicate *p* values (*$p \le 0.05$, **$p \le 0.01$, ***$p \le 0.001$, ****$p \le 0.0001$) obtained by two-tailed unpaired t-tests. See Supplementary Fig. 10 for cell viability assays under bafilomycin A_1 treatment conditions.

in DMEM, 10% FBS, 100 U/ml penicillin, and 100 µg/ml streptomycin. HuH7 and MRC-5 cells were confirmed to be free of mycoplasma using the Venor® GeM Classic kit (Minerva Biolabs).

Cryopreserved normal human bronchial epithelial (NHBE) cells were obtained from Lonza. All donors (donor 1: TAN 24717, Lot No. 000312626; donor 2: TAN 36585, Batch: 18TL269120; donor 3: TAN 28968, Lot No. 00004859609) were non-smoking and lacking respiratory pathology. Undifferentiated cells were seeded on transwell plates (Corning Costar, CLS3470-48EA) coated with collagen IV (Invitrogen) and grown in a mixture of DMEM (Invitrogen) and BEGM (Lonza, CC-3170) supplemented with retinoic acid (75 nM). Fresh medium was added regularly after 2 days. After reaching confluence, the cells were cultivated under air-liquid conditions for four additional weeks until full differentiation into pseudostratified human airway epithelia was observed. Medium from the basolateral compartment was renewed every 2–3 days and the apical surface was washed every week with PBS (Invitrogen).

Genome sequences of coronavirus strains used in this study are as follows: HCoV-229E (NCBI accession number AF304460.1, NCBI reference sequence NC_002645.1), MERS-CoV (NCBI accession number JX869059, NCBI reference sequence NC_01984 3.3). SARS-CoV-2 genome sequencing data have been submitted to the NCBI Short Read Archive repository under bioproject PRJNA658242 (SRA accession number SRX9907172 and SRX8975039). MERS-CoV and SARS-CoV-2 were kindly provided by Christian Drosten. For infection with other RNA viruses, influenza A virus (A/Thailand/1(KAN-1)/2004(H5N1); IAV; NCBI:txid266827) and human poliovirus type 1 (strain Mahoney, NCBI:txid12081) were used.

Virus infections and assessments of antiviral activity. To analyze the antiviral activity of thapsigargin, HuH7 cells (for HCoV-229E, MERS-CoV), MRC-5 cells (for HCoV-229E), Vero E6 cells (for SARS-CoV-2, poliovirus), and A549 cells (for IAV), respectively, were infected at the indicated multiplicities of infection (MOI) and incubated at 33 °C (for HCoV-229E and SARS-CoV-2) or 37 °C (for MERS-CoV, IAV, poliovirus) in the presence or absence of thapsigargin, or with the appropriate volume of solvent control (DMSO) as indicated. At 24 h p.i., supernatants were collected and stored at −80 °C. Virus titers in the supernatants were determined by plaque assay. HCoV-229E was titrated on HuH7 cells seeded on 12-well plates. MERS-CoV was titrated on HuH7 cells seeded on 24-well plates, SARS-CoV-2 and poliovirus were titrated on Vero E6 cells seeded on 24-well plates and IAV was titrated on MDCK-II cells seeded on 24-well plates using standard procedures. Briefly, confluent monolayers of the appropriate cells were incubated with serial dilutions of virus-containing supernatants (diluted 10^1 to 10^7) and incubated at 33 °C (HCoV-229E, SARS-CoV-2) or 37 °C (MERS-CoV, poliovirus, IAV). After 1 h, the virus inoculum was replaced with fresh medium (MEM, Gibco) containing 1.25% Avicel® (FMC Biopolymer, #RC591), 100 U/ml penicillin, 100 µg/ml streptomycin, and 10% FBS. For IAV infection, FBS was replaced with 0.2% bovine albumin (Sigma, A7979) and 1 µg/ml TPCK-treated trypsin). For poliovirus infection, 40 mM of $MgCl_2$ was added to the titration medium. At 48 h p.i. (for MERS-CoV, IAV, PV) or 72 h p.i. (for SARS-CoV-2 and HCoV-229E), cell culture supernatants were removed. Cells were washed with PBS and fixed in freshly prepared 3.7% PFA in PBS overnight. Next, the fixing solution was removed, the cell layer was washed with PBS and stained with 0.15% (w/v) crystal violet (diluted in 20% Ethanol) and plaques were counted. For EC_{50} calculation, virus titers determined for virus-infected cells treated with DMSO only (no inhibitor) were used for normalization. EC_{50} values were calculated by non-linear regression analysis using GraphPad Prism 5.0 or 8.4.3 (GraphPad Software). All virus work was performed in biosafety level 2 (BSL-2; HCoV-229E) or biosafety level 3 (BSL-3; MERS-CoV, SARS-CoV-2, IAV, poliovirus) containment laboratories approved for such use by the local authorities (RP Giessen, Germany).

For the infection of the NHBE cells, the apical surface was washed three times with PBS, and cells were infected with the indicated virus (MOI = 3). After 1 h, the inoculum was removed and the medium in the basal compartment was replaced with a medium containing 1, 0.1, or 0 µM thapsigargin. At the indicated time points, the apical surface of the cells was incubated with 150 µl/well PBS for 15 min and virus titers in the supernatants were determined by plaque assay.

Materials. Thapsigargin (Cay10522-1), GSK2656157 (Cay17372), and remdesivir (Cay30354) were obtained from Cayman Chemicals and were dissolved in DMSO as a 10 mM stock solution. Thapsigargin was used at 1 µM concentration unless stated otherwise. Bafilomycin A_1 (Cay11038) was dissolved as 1 mM stock in DMSO and used at 1 µM in all assays. Appropriate DMSO concentrations served as vehicle controls in some experiments. The following inhibitors were used: leupeptin hemisulfate (Carl Roth, #CN33.2), microcystin (Enzo Life Sciences, #ALX-350012-M001), pepstatin A (Applichem, #A2205), PMSF (SigmaAldrich, #P-7626). Pepstatin A, PMSF, and microcystin were dissolved in ethanol and leupeptin in water. Other reagents were from Sigma-Aldrich or Thermo Fisher Scientific, Santa Cruz Biotechnology, Jackson ImmunoResearch, or InvivoGen and were of analytical grade or better.

Primary antibodies against the following proteins or peptides were used: anti β-actin (Santa Cruz, #sc-47778, 1:1000), anti PERK (Santa Cruz, #sc-377400, 1:1000), anti PERK (Abcam, #ab65142, 1:1000), anti BiP (Cell Signaling, #3177, 1:1000), anti eIF2α (Cell Signaling #9722, 1:1000), anti P(S51)-eIF2α (Cell Signaling #9721, 1:1000), anti P(S724)-IRE1α (Novus Biologicals, #NB100-2323, 1:1000), anti IRE1α (Santa Cruz, #sc-390960, 1:1000), anti ATF4 (Santa Cruz, #sc-390063, 1:1000), anti ATF3 (Santa Cruz, #sc-188, 1:500), anti HERPUD1 (Abnova, #H00009709-A01, 1:1000), anti CTH (Cruz, #sc-374249, 1:1000), anti HCoV-229E N protein (Ingenasa, Batch 250609, 1:500), rabbit anti HCoV-229E nsp12 (Eurogentec; directed against full-length nsp12 produced in *E. coli* and purified by the Ziebuhr laboratory, 1:500), rabbit anti HCoV-229E nsp8 ([98] 1:500, IF 1:100), anti MERS-CoV N protein (Sinobiological, #100213-RP02, 1:1000), rabbit anti SARS-CoV N protein cross-reacting with SARS-CoV-2 N protein (gift from Friedemann Weber,[99], 1:2000), anti SARS-CoV-2 N protein (Rockland, #200-401-A50, 1:2000), anti puromycin (Kerafast Inc., 3RH11, #EQ 0001, 1:1000), anti ds-RNA J2 (SCICONS, English & Scientific Consulting Kft, #10010200, IF 1:100), anti p62/SQSTM1 (Santa Cruz, #sc-28359, 1:500, IF 1:100), anti ZNF622 (ZPR9) (Bethyl Laboratories, #A304-076A, 1:1000), anti LC3B XP® (Cell signaling, #3868, 1:1000), anti UBA6 (Cell signaling, #13386, 1:1000), anti ZO-1 (Invitrogen, #40-2200, IF 1:100), anti p63 (abcam, #ab124762, IF 1:100), anti mucin 5AC (abcam, #ab198294, IF 1:100), anti tubulin IV (abcam, #ab179509, 1:100).

The following secondary antibodies were used: polyclonal goat anti mouse immunoglobulins/HRP (Dako P0447, 1:2000), polyclonal goat anti rabbit immunoglobulins/HRP (Dako, P0448, 1:2000), Cy3-coupled anti rabbit (rb) IgG (dk, Merck Millipore, #AP182C, IF 1:200), Dylight 488-coupled anti mouse (ms) IgG (dk, ImmunoReagent, #DkxMu-003D488NHSX, IF 1:200), Alexa Flour594-coupled goat anti mouse IgG (H + L) (Invitrogen, #A11005, IF 1:100), Alexa Fluor 488-coupled F(ab')2 goat anti rabbit IgG (H + L) (Invitrogen, #A-11070, IF 1:100).

Cell lysis, in vivo puromycinylation, and immunoblotting. For whole-cell extracts, samples derived from experiments performed with HCoV-229E were lysed in Triton cell lysis buffer (10 mM Tris, pH 7.05, 30 mM NaPPi, 50 mM NaCl, 1% Triton X-100, 2 mM Na_3VO_4, 50 mM NaF, 20 mM ß-glycerophosphate and freshly added 0.5 mM PMSF, 2.5 µg/ml leupeptin, 1.0 µg/ml pepstatin, 1 µM microcystin). After 10−15 min on ice, lysates were cleared by centrifugation at 15,000 × *g* for 15 min at 4 °C. Protein concentrations of supernatants were determined by Bradford assay and samples stored at −80 °C.

To label nascent polypeptides in intact cells[100], HuH7 cells were seeded in 6 cm cell culture dishes (3×10^5 cells) and treated as described in the figure legends. Thirty minutes prior to harvest, the medium was supplemented with 3 µM puromycin (InvivoGen, #ant-pr-1). Then, cells were lysed as described above. After immunoblotting (see below), membranes were stained with Coomassie brilliant blue and then hybridized with an anti puromycin antibody (Kerafast, #EQ0001) to detect puromycinylated polypeptides.

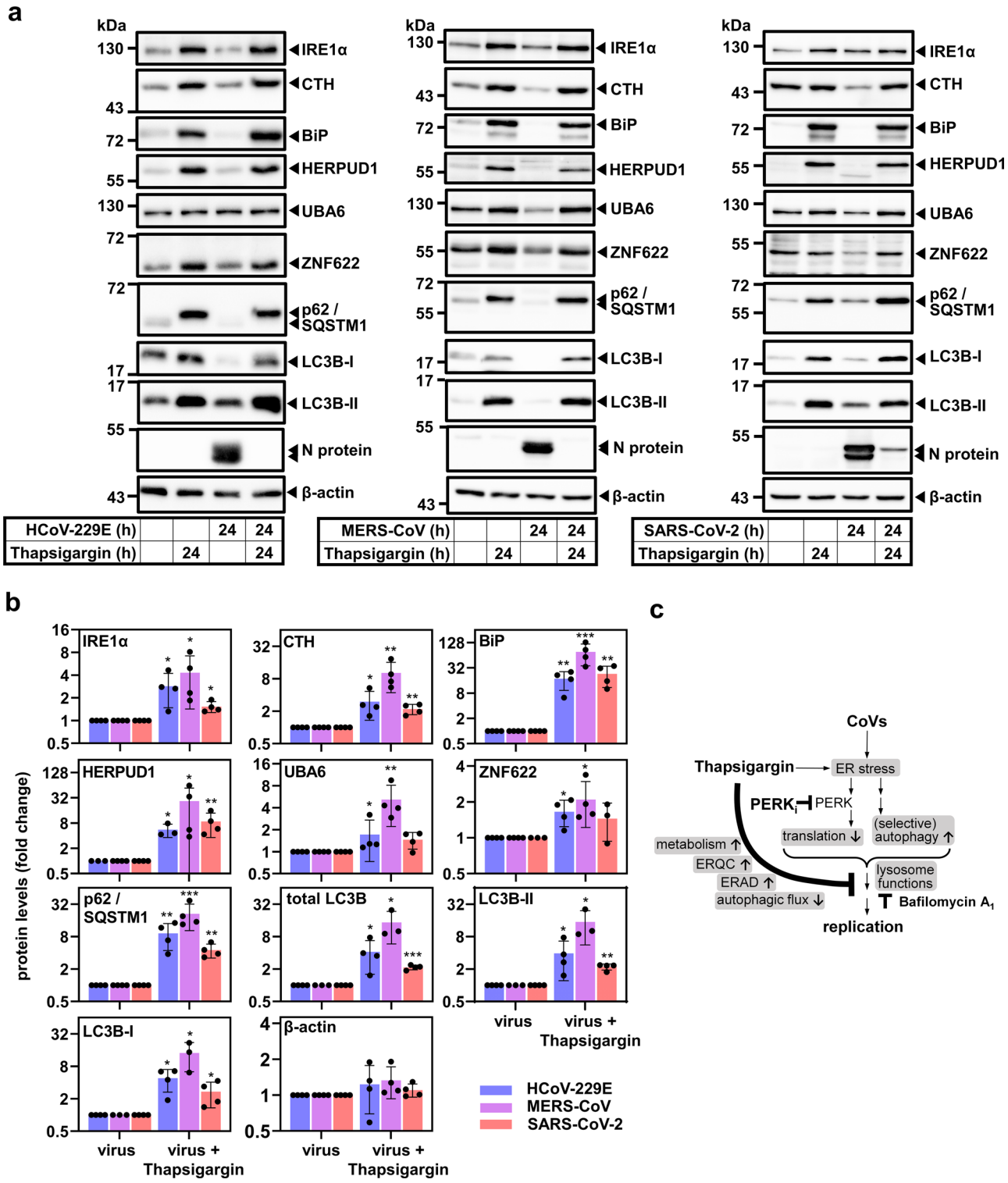

Fig. 9 Thapsigargin induces key regulators of UPR, ERQC, ERAD, and autophagy in HCoV-229E, MERS-CoV- and SARS-CoV-2-infected cells. **a**, **b** Validation of thapsigargin-induced proteins in CoV-infected HuH7 or Vero E6 cells by immunoblotting of whole-cell extracts from cells treated as indicated. BiP and IRE1α levels are shown for comparison. **a** Depicts representative images and **b** shows quantification of four biologically independent experiments, except for HERPUD1 (HCoV-229E samples) or LC3B, LC3B-I, and LC3B-II levels from MERS-CoV-infected cells which were quantified from three experiments. Bar graphs show means ± s.d.; asterisks indicate *p* values (*$p \le 0.05$, **$p \le 0.01$, ***$p \le 0.001$, ****$p \le 0.0001$) obtained by two-tailed ratio-paired or Mann−Whitney t-tests. Note that LC3B-I and LC3B-II images represent different exposures of the same blot membrane (see source files). **c** Summary of the main findings of our study.

Total cell lysates of MERS-CoV- and SARS-CoV-2-infected cells used for immunoblotting or mass spectrometry were prepared as follows. Cells were scraped in ice-cold PBS and pelleted at 500 × *g* for 5 min at 4 °C. Cell pellets were washed in ice-cold PBS and stored in liquid N_2 (or lysed and processed immediately). After thawing, cell pellets (corresponding to ≈300.000 cells seeded in 60 mm dishes at the start of the experiment) were resuspended in 90 µl of ice-cold Ca^{2+}/Mg^{2+}-free PBS and transferred to fresh tubes. After the addition of 10 µl of 10% SDS, samples were heated at 100 °C for 10 min and centrifuged at 600 × *g* for 1 min at room temperature. Supernatants were transferred to a fresh tube and heated again at 100 °C for 10 min and centrifuged at 600 × *g* for 1 min at room temperature. Protein concentrations were determined with the detergent compatible Bradford assay kit (Pierce™, #23246) using a 150-fold dilution. Aliquots corresponding to 20−25 µg protein (per lane) were mixed with 4 × SDS sample buffer (ROTI®Load, Roth, #K929) and stored at −20 °C prior to SDS-PAGE, or loaded immediately. Cell lysates were subjected to SDS-PAGE on 8−12.5% gels. The PageRuler™ prestained protein ladder (Thermo Scientific, #26616) was used as a molecular weight marker.

For immunoblotting, proteins were separated on SDS-PAGE and electrophoretically transferred to PVDF membranes (Roti-PVDF, #T830 Roth). Membranes were stained with 0.1% (w/v) Ponceau S (Sigma) dissolved in 5% acetic acid or Coomassie brilliant blue to confirm the transfer and equal loading of proteins. After blocking with 5% dried milk in Tris-HCl-buffered saline/0.05% Tween (TBST) for 1 h, membranes were incubated for 12−24 h with primary antibodies, washed in TBST, and incubated for 1−2 h with the peroxidase-coupled secondary antibody. Proteins were detected by using enhanced chemiluminescence (ECL) systems from Millipore or GE Healthcare. Images were acquired with the ChemiDoc TouchImaging System (BioRad) and quantified using the software ImageLab (versions V_5.2.1 or V_6.0.1, Bio-Rad).

mRNA expression analysis by RT-qPCR. 0.25−1 µg of total RNA was prepared by column purification (Macherey-Nagel) and transcribed into cDNA using Moloney murine leukemia virus reverse transcriptase (RevertAid Reverse Transcriptase, Thermo Fisher Scientific, #EP0441) in a total volume of 20 µl. 1 or 2 µl of this reaction mixture was used to amplify cDNAs using Taqman assays on demand (0.25 or 0.5 µl) (Applied Biosystems/Thermo Fisher Scientific) for *GUSB* (81 bp, Hs99999908_m1), *IL6* (95 bp, Hs00174131_m1), *IL8* (101 bp, Hs00174103_m1), *CXCL2* (68 bp, Hs00236966_m1), and *CCL20* (81 bp, Hs00171125_m1), as well as TaqMan Fast Universal PCR Master Mix (Applied Biosystems/ Thermo Fisher Scientific). Alternatively, primer pairs were designed and used with 2 µl of cDNA and Fast SYBR Green PCR Master Mix (Applied Biosystems/Thermo Fisher Scientific) to detect the mRNA of *EIF2AK3* (encoding PERK) (fw5′-AGAGATTGAGACTGCGTGGC-3′, re 5′-TCCCAAATACCTCTGGTTTGCT-3′), *nsp8* RNA (fw 5′-GCTGTTGCAAATGGTTCCTCAC-3′, re 5′-GATGCACATTCTTACCATCATTATCC-3′) and of HCoV-229E *S* RNA (fw5′-TTTCAGGTGATGCTCACATACC-3′, re 5′-ACAAACTCACGAACTGTCTTAGG-3′). All PCRs were performed in duplicate on an ABI 7500 real-time PCR instrument. The cycle threshold value (ct) for each individual PCR product was calculated by the instrument's software, and the ct values obtained for inflammatory/target mRNAs were normalized by subtracting the ct values obtained for GUSB. The resulting Δct values were also used to calculate relative changes of mRNA expression as the ratio (*R*) of mRNA expression of treated/untreated cells according to the following equation: $R = 2^{-((\Delta ct\ treated) - (\Delta ct\ untreated))}$. Alternatively, *S RNA* and *nsp8 RNA* copy numbers were determined using absolute quantification against a standard curve derived from gel-purified RT-PCR products of *nsp8* and *S RNA*.

A list of oligonucleotides is provided in Supplementary Table 1.

Immunofluorescence. Cells were seeded in µ-slides VI (Ibidi) and pre-cultured at 37 °C, 6% CO_2. Virus infection as well as simultaneous thapsigargin treatment (1 µM) was performed for 24 h at 33 °C, 6% CO_2. After 2× washing, cells were fixed with 4% paraformaldehyde in PBS (Santa Cruz, #281692) for 5 min, washed 3 × 10 min with Hank's BSS (PAN, #P04-32505), blocked with 10% normal donkey serum (Jackson ImmunoResearch, #017-000-121) for 20 min and incubated with primary and secondary antibodies diluted in Hank's BSS containing 0.005% saponin (Sigma-Aldrich, #S4521-10G) for 2 h at room temperature. Following three washing steps with Hank's BSS containing 0.005% saponin, Cy3-conjugated (Millipore, #AP182C, 1:100), Dylight488-conjugated (ImmunoReagents #DkxMu-003D488NHSX, 1:100) secondary antibodies or Alexa Fluor 594 goat anti-mouse IgG (Invitrogen, A11005) and Alexa Fluor 488 F(ab)2-goat anti-rabbit IgG (Invitrogen, A11070) were used. For controls, primary antibodies were omitted. Nuclei were stained with Hoechst 33342 (Invitrogen). Immunofluorescence images were analyzed using Leica DMi8, Leica SP05, and the Leica LASX software. For double immunofluorescence analyses appropriate filter cubes were used (Dylight488: excitation 480/40 and emission 527/30, Cy3: excitation 560/40 and emission 630/75, as well as counterstaining with Hoechst 33342: excitation 405/60 and emission 470/50). For three-dimensional reconstructions, z-stacks were analyzed using Imaris software (Bitplane, version 8.4).

Cell viability assays. MTS assays of HCoV-229E experiments were performed using the The CellTiter 96® AQueous One Solution Cell Proliferation Assay kit (Promega, #G3582). In brief, 1.2 × 10^4 HuH7 or 1 × 10^4 MRC-5 cells were seeded in 96-well plates for 24 h and thereafter treated with DMSO, thapsigargin, remdesivir, GSK2656157, bafilomycin A_1, virus alone or virus plus chemical for 16, 24, or 28 h as indicated in the figure legends. Then, the medium was replaced by 100 µl complete cell culture medium including 4 µl or 20 µl CellTiter 96® AQueous one solution reagent according to the manufacturer's recommendations. Cells were further incubated for 1 h at 33 °C. Then, absorbance values were measured at 490 nm. Control wells containing only medium and reagent were used to correct for background absorbance. Relative values for cell viability were calculated in relation to the mean of all untreated controls (set to 100%).

For MTT and ATPlite assay (Perkin Elmer), Vero E6 cells seeded at near confluency were incubated with a serial dilution of thapsigargin in a 96-well format. After 24 h, either 200 µl MTT mix (DMEM supplemented with 10% FCS containing 250 µg/ml tetrazolium bromide, Sigma) or 100 µl ATPlite assay buffer was added to each well. For ATPlite assay, cells were incubated for 10 min and luminescence was measured using Spark 10 M (Tecan). For MTT assay, cells were incubated for 90−120 min at 37 °C and fixed using 3.7% PFA in PBS. The tetrazolium crystals were dissolved by adding 200 µl/well isopropanol and the absorbance at 490 nm was measured using an ELISA reader (BioTek). To determine CC_{50} values, the MTT/ATPlite values were calculated in relation to the untreated control (which was set to 100%). CC_{50} values were then calculated by non-linear regression using GraphPadPrism 5.0 (GraphPad Software).

For analyzing cytotoxicity in NHBE cells after 72 h treatment, the transepithelial electrical resistance (TEER) was measured using Epithelial Volt/Ohm Meter 3 (EVOM3, WPI). The obtained TEER values were compared to those obtained for untreated cells.

ELISA. Sandwich ELISAs from R&D Systems (DuoSet ELISA for human IL-8 (DY208), IL-6 (DY206), CXCL2 (DY276-05), CCL20 (DY360)) were used to measure secreted human cytokine /chemokine protein concentrations in cell culture supernatants of HuH7 or MRC-5 cells treated as described in the figure legends. The cell culture supernatants were harvested, centrifuged at 15,000 × *g* at 4 °C for 15 s, and stored at −80 °C. 100 µl of the supernatants were either used undiluted or were diluted in cell culture medium as follows (HuH7: IL-8 (1:10), CXCL2 (1:3), CCL20 (1:8), MRC-5: IL-8 (1:10), IL-6 (1:20), CXCL2 (1:1.5)) and ELISAs were performed according to the manufacturer's instructions using serial dilutions of recombinant proteins as standards. All measurements were within the linear range of the standard curve. In some experiments, an IL-1α (10 ng/ml) stimulation for 16 h was used as a positive control.

RNA-seq and bioinformatics. For the data shown in Fig. 1, total RNA was isolated from uninfected and infected cells obtained at 3, 6, 12, 24 h p.i. (or mock infection) using two biological replicates resulting in 32 RNA-seq data sets. RNA was sequenced (with rRNA depletion) using Illumina reagents and an Illumina HiSeq 4000 instrument (single read, 150 bases). Quality control of RNA-seq reads was performed using the FastQC (https://www.bioinformatics.babraham.ac.uk/projects/fastqc/) command line tool version 0.11.7.

After adapter trimming using fastp version 0.19.7[101], the reads were aligned to an index based on human genome hg38 using STAR version 2.7.0d[102].

Gene-specific read counts based on hg38 UCSC gene annotations were extracted using FeatureCounts from the R Subread package version 1.6.3[103] and were imported into R, versions 3.4.4 to 3.6.2 (R Core Team, 2018, https://www.R-project.org/).

Detection of differentially expressed genes was done using DESeq2 version 1.22.1[104]. For significance testing, DESeq2 utilizes the Wald test with adjustments for multiple testing by the Benjamini and Hochberg procedure[104]. From the entire data set, only normalized read counts and ratio values for 166 gene IDs assigned to KEGG hsa04141 were extracted and further analyzed.

Mass spectrometry and bioinformatics. Protein extracts were lysed in SDS lysis buffer as described above. Prior to digestion, the SDS-containing solution was exchanged to 8 M urea applying the filter-aided sample preparation (FASP) for proteome analysis protocol using Microcon YM-30 filter devices (Millipore, Cat. MRCF0R030)[105]. Cysteines were alkylated with Iodoacetamide and 8 M urea buffer was exchanged to 50 mM ammonium-bicarbonate buffer with a pH of 8.0. Samples were digested within the filter devices by the addition of sequencing grade modified trypsin (Serva) and incubated at 37 °C over-night. Thereafter, the filter-units were transferred to fresh tubes. Peptides were eluted by the addition of 50 µL 0.5 M NaCl solution and centrifugation (14.000 × *g* for 10 min). After drying the filtrates in a vacuum concentrator (Speed Vac), pellets were resuspended in 25 µL of 0.1% formic acid.

Peptides were desalted and concentrated using Chromabond C18WP spin columns (Macherey-Nagel, Part No. 730522). Finally, peptides were dissolved in 25 µl water with 5% acetonitrile and 0.1% formic acid. The mass spectrometric analysis of the samples was performed using a timsTOF Pro mass spectrometer (Bruker Daltonic). A nanoElute HPLC system (Bruker Daltonics), equipped with an Aurora C18 RP column (25 cm × 75 µm) filled with 1.7 µm beads (IonOpticks), was connected online to the mass spectrometer. A portion of approximately 200 ng of peptides corresponding to 2 µl was injected directly on the separation column.

Sample loading was performed at a constant pressure of 800 bar. Separation of the tryptic peptides was achieved at 50 °C column temperature with the following gradient of water/0.1% formic acid (solvent A) and acetonitrile/0.1% formic acid (solvent B) at a flow rate of 400 nl/min: Linear increase from 2%B to 17%B within 60 min, followed by a linear gradient to 25%B within 30 min and linear increase to 37% solvent B in additional 10 min. Finally, B was increased to 95% within 10 min and hold for an additional 10 min. The built-in "DDA PASEF-standard_1.1sec_cycletime" method developed by Bruker Daltonics was used for mass spectrometric measurement. Data analysis was performed using MaxQuant with the Andromeda search engine and Uniprot databases were used for annotating and assigning protein identifiers[106]. Perseus software (versions 1.6.10.50 for HuH7 and 1.6.14.0 for VeroE6 proteomes) was used for further analyses[107].

For the data shown in Fig. 1, raw data from 47 LC-MS/MS runs (representing two independent experiments and three technical replicates per sample for the 3, 6, 12, 24 h infection time points with the exception of the MERS-CoV 24 h time point which has only five replicates, were mapped to the manually annotated and reviewed *Homo sapiens* proteome (UniProtKB/Swiss-Prot Release 2019_06 of 03-Jul-2019), $\log_2$-transformed and normalized using the width adjustment function of Perseus. The expression values assigned to uninfected HuH7 cells were derived from a total of 59 mock samples representing multiple technical repeats of two biological samples generated at each of the 3, 6, 12, 24 h time points in order to generate a common reference sample for the mean protein expression found in uninfected/untreated HuH7 cells. This mean reference was used to calculate all pairwise ratio values. The significance of changes was tested by the Student's t-test with a FDR of 5% (250 permutations) using Perseus functions. From the entire data set, only protein intensity values for 166 uniprot IDs assigned to KEGG hsa04141 were extracted and further analyzed using the software tools described below.

For the data shown in Figs. 6 and 7, raw data from 96 LC-MS/MS runs (representing two independent experiments per time point and three technical replicates per sample) were mapped to *Homo sapiens* (uniprot ID UP000005640 for HuH7 cells), *Chlorocebus sabaeus* (Green monkey, *Cercopithecus sabaeus*, uniprot ID UP000029965 for Vero E6 cells), MERS-CoV (uniprot IDs UP000139997 and UP000171868) or SARS-CoV-2 (uniprot ID UP000464024) peptide sequences. All data sets were processed by MaxQuant version 1.6.10.43 (raw data submission was done with version 1.6.17.0)[106] including the match between runs option enabled resulting in the identification of 5,376 (HuH7 cells) or 5,066 (Vero E6 cells) majority protein IDs. For further quantifications, $\log_2$-transformed protein intensities were width normalized with Perseus[107] and IDs assigned to contaminants, and reverse sequences were omitted resulting in data sets of 5,172 protein IDs (assigned to 5,130 gene IDs) for HuH7 or 4,873 protein IDs (assigned to 4,305 gene IDs) for Vero E6 cells. For calculation of ratio values between conditions, the 2×3 replicates from each condition were assigned to one analysis group. DEPs were identified from $\log_2$ transformed normalized protein intensity values by Student's t-test analysis using Perseus functions. Subsequent filtering steps and heatmap representations were performed in Excel 2016 according to the criteria described in the figure legends. Venn diagrams were created with tools provided at http://bioinformatics.psb.ugent.be/webtools/Venn/. Overrepresentation analyses of gene sets were done using the majority protein IDs (for HuH7 cells) or gene IDs (for Vero E6 cells) of differentially enriched proteins and Metascape software with the express settings[44]. Coregulated proteins in HuH7 and Vero E6 cells were identified based on NCBI gene ID annotation corresponding to the majority protein IDs. Protein network data of filtered gene ID lists were extracted from STRING (version 10, https://string-db.org/,[108]) and networks were visualized with Cytoscape 3.8.0[109]. Mapping of ratio values on KEEG pathway hsa04141 was done with Pathview Web software or the Pathview R-package 1.18.2 and R 3.4.4 (https://pathview.uncc.edu/,[110]).

Statistics, quantification, and reproducibility. Quantification of data and statistical parameters (means, t-tests, standard variations, confidence intervals, Pearson correlations, linear regressions, non-linear fittings for EC_{50} and CC_{50} values) were calculated using SigmaPlot 11, DESeq2 (version 1.22.1), GraphPad Prism 5.0 or 8.4.3, Perseus (versions 1.6.10.50 (MERS-CoV) or 1.6.14 (SARS-CoV-2)), ImageLab (versions 5.2.1 or 6.0.1), or Microsoft Excel 2016.

Dot plots of cell viability assay results (Figs. 3b, d, 4d and Supplementary Figs. 2c, 5d, e, 10) show technical replicates according to the numbers of independent experiments indicated in the legends.

All statistical tests for pathway enrichment analyses (Figs. 6e–i, 7d and Supplementary Figs. 6–8) were calculated online by Metascape software (https://metascape.org/) using the ontology sources KEGG Pathway, GO Biological Processes, Reactome Gene Sets, Canonical Pathways, CORUM, TRRUST, DisGeNET, PaGenBase, Transcription Factor Targets, WikiPathways, PANTHER Pathway, and COVID and all genes in the genome as the enrichment background. *P*-values were based on the accumulative hypergeometric distribution and *q*-values were calculated using the Benjamini–Hochberg procedure to account for multiple testings. Terms with a *p*-value < 0.01, a minimum count of 3, and an enrichment factor > 1.5 were collected. Kappa scores were used as the similarity metric for hierarchical clustering on the enriched terms, and sub-trees with a similarity of > 0.3 were considered a cluster. The most statistically significant terms within a cluster were chosen to represent the cluster.

Reporting summary. Further information on research design is available in the Nature Research Reporting Summary linked to this article.

Data availability

The mass spectrometry proteomics data in this study shown in Fig. 6a–d have been deposited to the ProteomeXchange Consortium[111] via the PRIDE partner repository[112] with the dataset identifier PXD021222 (https://doi.org/10.6019/PXD021222). The remaining data generated in this study are provided in the Supplementary Information/Source Data files. Source data are provided with this paper.

Received: 7 September 2020; Accepted: 2 August 2021;
Published online: 20 September 2021

References

1. de Wit, E., van Doremalen, N., Falzarano, D. & Munster, V. J. S. A. R. S. and MERS: recent insights into emerging coronaviruses. *Nat. Rev. Microbiol.* **14**, 523–534 (2016).
2. Gorbalenya, A. E. et al. The species Severe acute respiratory syndrome-related coronavirus: classifying 2019-nCoV and naming it SARS-CoV-2. *Nat. Microbiol.* **5**, 536–544 (2020).
3. Gerna, G. et al. Genetic variability of human coronavirus OC43-, 229E-, and NL63-like strains and their association with lower respiratory tract infections of hospitalized infants and immunocompromised patients. *J. Med. Virol.* **78**, 938–949 (2006).
4. Greenberg, S. B. Update on rhinovirus and coronavirus infections. *Semin. Respir. Crit. Care Med.* **32**, 433–446 (2011).
5. Nicholson, K. G., Kent, J., Hammersley, V. & Cancio, E. Acute viral infections of upper respiratory tract in elderly people living in the community: comparative, prospective, population based study of disease burden. *BMJ* **315**, 1060–1064 (1997).
6. Jevsnik, M. et al. Coronavirus infections in hospitalized pediatric patients with acute respiratory tract disease. *BMC Infect. Dis.* **12**, 365 (2012).
7. Drosten, C. et al. Identification of a novel coronavirus in patients with severe acute respiratory syndrome. *N. Engl. J. Med.* **348**, 1967–1976 (2003).
8. Rota, P. A. et al. Characterization of a novel coronavirus associated with severe acute respiratory syndrome. *Science* **300**, 1394–1399 (2003).
9. Guan, Y. et al. Molecular epidemiology of the novel coronavirus that causes severe acute respiratory syndrome. *Lancet* **363**, 99–104 (2004).
10. Zhu N. et al. A novel coronavirus from patients with pneumonia in China, 2019. *N. Engl. J. Med.* **382**, 727−733 (2020).
11. Zhou, P. et al. A pneumonia outbreak associated with a new coronavirus of probable bat origin. *Nature* **579**, 270–273 (2020).
12. Zaki, A. M., van Boheemen, S., Bestebroer, T. M., Osterhaus, A. D. & Fouchier, R. A. Isolation of a novel coronavirus from a man with pneumonia in Saudi Arabia. *N. Engl. J. Med.* **367**, 1814–1820 (2012).
13. Fung, T. S. & Liu, D. X. Human coronavirus: host-pathogen interaction. *Annu Rev. Microbiol.* **73**, 529–557 (2019).
14. de Wilde, A. H., Snijder, E. J., Kikkert, M. & van Hemert, M. J. Host factors in coronavirus replication. *Curr. Top. Microbiol. Immunol.* **419**, 1–42 (2018).
15. Liao, Y., Wang, X., Huang, M., Tam, J. P. & Liu, D. X. Regulation of the p38 mitogen-activated protein kinase and dual-specificity phosphatase 1 feedback loop modulates the induction of interleukin 6 and 8 in cells infected with coronavirus infectious bronchitis virus. *Virology* **420**, 106–116 (2011).
16. Mizutani, T., Fukushi, S., Saijo, M., Kurane, I. & Morikawa, S. JNK and PI3k/Akt signaling pathways are required for establishing persistent SARS-CoV infection in Vero E6 cells. *Biochim. Biophys. Acta* **1741**, 4–10 (2005).
17. Poppe, M. et al. The NF-kappaB-dependent and -independent transcriptome and chromatin landscapes of human coronavirus 229E-infected cells. *PLoS Pathog.* **13**, e1006286 (2017).
18. Snijder, E. J. et al. A unifying structural and functional model of the coronavirus replication organelle: tracking down RNA synthesis. *PLoS Biol.* **18**, e3000715 (2020).
19. Romero-Brey, I. & Bartenschlager, R. Endoplasmic reticulum: the favorite intracellular niche for viral replication and assembly. *Viruses* **8**, 160 (2016).
20. Wang, M. & Kaufman, R. J. Protein misfolding in the endoplasmic reticulum as a conduit to human disease. *Nature* **529**, 326–335 (2016).
21. Karagoz, G. E., Acosta-Alvear, D. & Walter, P. The unfolded protein response: detecting and responding to fluctuations in the protein-folding capacity of the endoplasmic reticulum. *Cold Spring Harb. Perspect. Biol.* **11**, a033886 (2019).
22. Hetz, C. & Papa, F. R. The unfolded protein response and cell fate control. *Mol. Cell* **69**, 169–181 (2018).
23. Wu, H., Ng, B. S. & Thibault, G. Endoplasmic reticulum stress response in yeast and humans. *Biosci. Rep.* **34**, e00118 (2014).

24. Pobre, K. F. R., Poet, G. J. & Hendershot, L. M. The endoplasmic reticulum (ER) chaperone BiP is a master regulator of ER functions: getting by with a little help from ERdj friends. *J. Biol. Chem.* **294**, 2098–2108 (2019).
25. Bertolotti, A., Zhang, Y., Hendershot, L. M., Harding, H. P. & Ron, D. Dynamic interaction of BiP and ER stress transducers in the unfolded-protein response. *Nat. Cell Biol.* **2**, 326–332 (2000).
26. Cui, W., Li, J., Ron, D. & Sha, B. The structure of the PERK kinase domain suggests the mechanism for its activation. *Acta Crystallogr D. Biol. Crystallogr.* **67**, 423–428 (2011).
27. Carrara, M., Prischi, F., Nowak, P. R. & Ali, M. M. Crystal structures reveal transient PERK luminal domain tetramerization in endoplasmic reticulum stress signaling. *EMBO J.* **34**, 1589–1600 (2015).
28. Kopp, M. C., Larburu, N., Durairaj, V., Adams, C. J. & Ali, M. M. U. UPR proteins IRE1 and PERK switch BiP from chaperone to ER stress sensor. *Nat. Struct. Mol. Biol.* **26**, 1053–1062 (2019).
29. Han, J. et al. ER-stress-induced transcriptional regulation increases protein synthesis leading to cell death. *Nat. Cell Biol.* **15**, 481–490 (2013).
30. Urra, H. & Hetz, C. Fine-tuning PERK signaling to control cell fate under stress. *Nat. Struct. Mol. Biol.* **24**, 789–790 (2017).
31. Chen, Y. & Brandizzi, F. IRE1: ER stress sensor and cell fate executor. *Trends Cell Biol.* **23**, 547–555 (2013).
32. Mungrue, I. N., Pagnon, J., Kohannim, O., Gargalovic, P. S. & Lusis, A. J. CHAC1/MGC4504 is a novel proapoptotic component of the unfolded protein response, downstream of the ATF4-ATF3-CHOP cascade. *J. Immunol.* **182**, 466–476 (2009).
33. Grootjans, J., Kaser, A., Kaufman, R. J. & Blumberg, R. S. The unfolded protein response in immunity and inflammation. *Nat. Rev. Immunol.* **16**, 469–484 (2016).
34. Hilton, A., Mizzen, L., MacIntyre, G., Cheley, S. & Anderson, R. Translational control in murine hepatitis virus infection. *J. Gen. Virol.* **67**, 923–932 (1986).
35. Oslowski, C. M., Urano, F. & Measuring, E. R. stress and the unfolded protein response using mammalian tissue culture system. *Methods Enzymol.* **490**, 71–92 (2011).
36. Snijder, E. J., Decroly, E. & Ziebuhr, J. The nonstructural proteins directing coronavirus RNA synthesis and processing. *Adv. Virus Res.* **96**, 59–126 (2016).
37. Tombal, B., Weeraratna, A. T., Denmeade, S. R. & Isaacs, J. T. Thapsigargin induces a calmodulin/calcineurin-dependent apoptotic cascade responsible for the death of prostatic cancer cells. *Prostate* **43**, 303–317 (2000).
38. Sehgal, P. et al. Inhibition of the sarco/endoplasmic reticulum (ER) Ca(2+)-ATPase by thapsigargin analogs induces cell death via ER Ca(2+) depletion and the unfolded protein response. *J. Biol. Chem.* **292**, 19656–19673 (2017).
39. Kokic, G. et al. Mechanism of SARS-CoV-2 polymerase stalling by remdesivir. *Nat. Commun.* **12**, 279 (2021).
40. Sheahan, T. P. et al. Comparative therapeutic efficacy of remdesivir and combination lopinavir, ritonavir, and interferon beta against MERS-CoV. *Nat. Commun.* **11**, 222 (2020).
41. Ogando, N. S. et al. SARS-coronavirus-2 replication in Vero E6 cells: replication kinetics, rapid adaptation and cytopathology. *J. Gen. Virol.* **101**, 925–940 (2020).
42. Brown, A. J. et al. Broad spectrum antiviral remdesivir inhibits human endemic and zoonotic deltacoronaviruses with a highly divergent RNA dependent RNA polymerase. *Antivir. Res.* **169**, 104541 (2019).
43. Jonsdottir, H. R. & Dijkman, R. Coronaviruses and the human airway: a universal system for virus-host interaction studies. *Virol. J.* **13**, 24 (2016).
44. Zhou, Y. et al. Metascape provides a biologist-oriented resource for the analysis of systems-level datasets. *Nat. Commun.* **10**, 1523 (2019).
45. Oikonomou, C. & Hendershot, L. M. Disposing of misfolded ER proteins: A troubled substrate's way out of the ER. *Mol. Cell Endocrinol.* **500**, 110630 (2020).
46. Mizushima, N. A brief history of autophagy from cell biology to physiology and disease. *Nat. Cell Biol.* **20**, 521–527 (2018).
47. Leitman, J. et al. Herp coordinates compartmentalization and recruitment of HRD1 and misfolded proteins for ERAD. *Mol. Biol. Cell* **25**, 1050–1060 (2014).
48. Okuda-Shimizu, Y. & Hendershot, L. M. Characterization of an ERAD pathway for nonglycosylated BiP substrates, which require Herp. *Mol. Cell* **28**, 544–554 (2007).
49. Behnke, J., Feige, M. J. & Hendershot, L. M. BiP and its nucleotide exchange factors Grp170 and Sil1: mechanisms of action and biological functions. *J. Mol. Biol.* **427**, 1589–1608 (2015).
50. Leto, D. E. et al. Genome-wide CRISPR analysis identifies substrate-specific conjugation modules in ER-associated degradation. *Mol. Cell* **73**, 377–389 e311 (2019).
51. Mun, K. & Punga, T. Cellular zinc finger protein 622 hinders human adenovirus lytic growth and limits binding of the viral pVII protein to virus DNA. *J Virol.* **93**, e01628−18 (2019).
52. Jia, R. & Bonifacino, J. S. Regulation of LC3B levels by ubiquitination and proteasomal degradation. *Autophagy* **16**, 382–384 (2020).
53. Katsuragi, Y., Ichimura, Y. & Komatsu, M. p62/SQSTM1 functions as a signaling hub and an autophagy adaptor. *Febs J.* **282**, 4672–4678 (2015).
54. Gorshkov, K. et al. The SARS-CoV-2 cytopathic effect is blocked by lysosome alkalizing small molecules. *ACS Infect. Dis.* **7**, 1389−1408 (2020).
55. Yoshii, S. R. & Mizushima, N. Monitoring and measuring autophagy. *Int. J. Mol. Sci.* **18**, 1865 (2017).
56. Lee, Z. W., Low, Y. L., Huang, S., Wang, T. & Deng, L. W. The cystathionine gamma-lyase/hydrogen sulfide system maintains cellular glutathione status. *Biochem J.* **460**, 425–435 (2014).
57. Kokame, K., Agarwala, K. L. & Kato, H. Miyata T. Herp, a new ubiquitin-like membrane protein induced by endoplasmic reticulum stress. *J. Biol. Chem.* **275**, 32846–32853 (2000).
58. Li, W. W., Alexandre, S., Cao, X. & Lee, A. S. Transactivation of the grp78 promoter by Ca2+ depletion. A comparative analysis with A23187 and the endoplasmic reticulum Ca(2+)-ATPase inhibitor thapsigargin. *J. Biol. Chem.* **268**, 12003–12009 (1993).
59. Ma, Y. J. & Hendershot, L. M. Herp is dually regulated by both the endoplasmic reticulum stress-specific branch of the unfolded protein response and a branch that is shared with other cellular stress pathways. *J. Biol. Chem.* **279**, 13792–13799 (2004).
60. Sun, S. et al. IRE1alpha is an endogenous substrate of endoplasmic-reticulum-associated degradation. *Nat. Cell Biol.* **17**, 1546–1555 (2015).
61. Wang, J., Lee, J., Liem, D. & Ping, P. HSPA5 Gene encoding Hsp70 chaperone BiP in the endoplasmic reticulum. *Gene* **618**, 14–23 (2017).
62. Zhu, G. Y. & Lee, A. S. Role of the unfolded protein response, GRP78 and GRP94 in organ homeostasis. *J. Cell Physiol.* **230**, 1413–1420 (2015).
63. Hsu, C. L., Prasad, R., Blackman, C. & Ng, D. T. Endoplasmic reticulum stress regulation of the Kar2p/BiP chaperone alleviates proteotoxicity via dual degradation pathways. *Mol. Biol. Cell* **23**, 630–641 (2012).
64. Halbleib, K. et al. Activation of the unfolded protein response by lipid bilayer stress. *Mol. Cell* **67**, 673–684 e678 (2017).
65. Chang, T. K. et al. Coordination between two branches of the unfolded protein response determines apoptotic cell fate. *Mol. Cell* **71**, 629–636 e625 (2018).
66. Sepulveda, D. et al. Interactome screening identifies the ER luminal chaperone Hsp47 as a regulator of the unfolded protein response transducer IRE1alpha. *Mol. Cell* **69**, 238–252 e237 (2018).
67. Brodsky, J. L. Cleaning Up: ER-associated degradation to the rescue. *Cell* **151**, 1163–1167 (2012).
68. Christianson, J. C. et al. Defining human ERAD networks through an integrative mapping strategy. *Nat. Cell Biol.* **14**, 93–U176 (2012).
69. Noack, J., Bernasconi, R. & Molinari, M. How viruses hijack the ERAD tuning machinery. *J. Virol.* **88**, 10272–10275 (2014).
70. Byun, H., Gou, Y. Q., Zook, A., Lozano, M. M. & Dudley, J. P. ERAD and how viruses exploit it. *Front. Microbiol.* **5**, 330 (2014).
71. Miller K. et al. Coronavirus interactions with the cellular autophagy machinery. *Autophagy* **16**, 1−9 (2020).
72. Quiroga, C. et al. Herp depletion protects from protein aggregation by up-regulating autophagy. *Biochim. Biophys. Acta* **1833**, 3295–3305 (2013).
73. Fecchi, K. et al. Coronavirus interplay with lipid rafts and autophagy unveils promising therapeutic targets. *Front. Microbiol.* **11**, 1821 (2020).
74. Ji, C. H. et al. The N-degron pathway mediates ER-phagy. *Mol. Cell* **75**, 1058–1072 e1059 (2019).
75. Chino, H. & Mizushima, N. ER-Phagy: quality control and turnover of endoplasmic reticulum. *Trends Cell Biol.* **30**, 384–398 (2020).
76. Wilkinson, S. ER-phagy: shaping up and destressing the endoplasmic reticulum. *Febs J.* **286**, 2645–2663 (2019).
77. Ganley, I. G., Wong, P. M. & Jiang, X. Thapsigargin distinguishes membrane fusion in the late stages of endocytosis and autophagy. *Autophagy* **7**, 1397–1399 (2011).
78. Mauvezin, C., Nagy, P., Juhasz, G. & Neufeld, T. P. Autophagosome-lysosome fusion is independent of V-ATPase-mediated acidification. *Nat. Commun.* **6**, 7007 (2015).
79. Toyoshima, C., Nakasako, M., Nomura, H. & Ogawa, H. Crystal structure of the calcium pump of sarcoplasmic reticulum at 2.6 A resolution. *Nature* **405**, 647–655 (2000).
80. Terracciano, R. et al Mapping the SARS-CoV-2-host protein-protein interactome by affinity purification mass spectrometry and proximity-dependent biotin labeling: a rational and straightforward route to discover host-directed anti-SARS-CoV-2 therapeutics. *Int. J. Mol. Sci.* **22**, 532 (2021).
81. Samavarchi-Tehrani, P. et al. A SARS-C`oV-2-host proximity interactome. Preprint at *bioRxiv* https://doi.org/10.1101/2020.09.03.282103 (2020).
82. Stukalov, A. et al. Multi-level proteomics reveals host-perturbation strategies of SARS-CoV-2 and SARS-CoV. *Nature* **594**, 246–252 (2021)
83. Bojkova, D. et al. Proteomics of SARS-CoV-2-infected host cells reveals therapy targets. *Nature* **583**, 469–472 (2020).
84. Grenga, L. et al. Shotgun proteomics analysis of SARS-CoV-2-infected cells and how it can optimize whole viral particle antigen production for vaccines. *Emerg. Microbes Infect.* **9**, 1712–1721 (2020).

85. Bouhaddou, M. et al. The global phosphorylation landscape of SARS-CoV-2 infection. *Cell* **182**, 685–712 e619 (2020).
86. Patkar, S. A., Rasmussen, U. & Diamant, B. On the mechanism of histamine release induced by thapsigargin from Thapsia garganica L. *Agents Actions* **9**, 53–57 (1979).
87. Andersen, T. B., Lopez, C. Q., Manczak, T., Martinez, K. & Simonsen, H. T. Thapsigargin–from Thapsia L. to mipsagargin. *Molecules* **20**, 6113–6127 (2015).
88. Chu, H., Dunstl, G., Felding, J. & Baran, P. S. Divergent synthesis of thapsigargin analogs. *Bioorg. Med. Chem. Lett.* **28**, 2705–2707 (2018).
89. Chu, H., Smith, J. M., Felding, J. & Baran, P. S. Scalable synthesis of (-)-thapsigargin. *ACS Cent. Sci.* **3**, 47–51 (2017).
90. Lopez, C. Q. et al. Use of a temporary immersion bioreactor system for the sustainable production of thapsigargin in shoot cultures of Thapsia garganica. *Plant Methods* **14**, 79 (2018).
91. Doan, N. T. et al. Targeting thapsigargin towards tumors. *Steroids* **97**, 2–7 (2015).
92. Mahalingam, D. et al. A phase II, multicenter, single-arm study of mipsagargin (G-202) as a second-line therapy following sorafenib for adult patients with progressive advanced hepatocellular carcinoma. *Cancers* **11**, 833 (2019).
93. Mahalingam, D. et al. Mipsagargin, a novel thapsigargin-based PSMA-activated prodrug: results of a first-in-man phase I clinical trial in patients with refractory, advanced or metastatic solid tumours. *Br. J. Cancer* **114**, 986–994 (2016).
94. Marder, W. & McCune, W. J. Advances in immunosuppressive therapy. *Semin. Respir. Crit. Care Med.* **28**, 398–417 (2007).
95. Mehta, P. et al. COVID-19: consider cytokine storm syndromes and immunosuppression. *Lancet* **395**, 1033–1034 (2020).
96. Wei, Y. et al. Pharmacological preconditioning with the cellular stress inducer thapsigargin protects against experimental sepsis. *Pharm. Res.* **141**, 114–122 (2019).
97. Nakabayashi, H., Taketa, K., Miyano, K., Yamane, T. & Sato, J. Growth of human hepatoma cells lines with differentiated functions in chemically defined medium. *Cancer Res.* **42**, 3858–3863 (1982).
98. Ziebuhr, J. & Siddell, S. G. Processing of the human coronavirus 229E replicase polyproteins by the virus-encoded 3C-like proteinase: identification of proteolytic products and cleavage sites common to pp1a and pp1ab. *J. Virol.* **73**, 177–185 (1999).
99. Spiegel, M. et al. Inhibition of beta interferon induction by severe acute respiratory syndrome coronavirus suggests a two-step model for activation of interferon regulatory factor 3. *J. Virol.* **79**, 2079–2086 (2005).
100. Iwasaki, S. & Ingolia, N. T. The growing toolbox for protein synthesis studies. *Trends Biochem. Sci.* **42**, 612–624 (2017).
101. Chen, S., Zhou, Y., Chen, Y. & Gu, J. fastp: an ultra-fast all-in-one FASTQ preprocessor. *Bioinformatics* **34**, i884–i890 (2018).
102. Dobin, A. et al. STAR: ultrafast universal RNA-seq aligner. *Bioinformatics* **29**, 15–21 (2013).
103. Liao, Y., Smyth, G. K. & Shi, W. featureCounts: an efficient general purpose program for assigning sequence reads to genomic features. *Bioinformatics* **30**, 923–930 (2014).
104. Love, M. I., Huber, W. & Anders, S. Moderated estimation of fold change and dispersion for RNA-seq data with DESeq2. *Genome Biol.* **15**, 550 (2014).
105. Wisniewski, J. R. Filter-aided sample preparation for proteome analysis. *Methods Mol. Biol.* **1841**, 3–10 (2018).
106. Tyanova, S., Temu, T. & Cox, J. The MaxQuant computational platform for mass spectrometry-based shotgun proteomics. *Nat. Protoc.* **11**, 2301–2319 (2016).
107. Tyanova, S. et al. The Perseus computational platform for comprehensive analysis of (prote)omics data. *Nat. Methods* **13**, 731–740 (2016).
108. Szklarczyk, D. et al. STRING v11: protein−protein association networks with increased coverage, supporting functional discovery in genome-wide experimental datasets. *Nucleic Acids Res.* **47**, D607–D613 (2019).
109. Cline, M. S. et al. Integration of biological networks and gene expression data using Cytoscape. *Nat. Protoc.* **2**, 2366–2382 (2007).
110. Luo, W., Pant, G., Bhavnasi, Y. K., Blanchard, S. G. Jr. & Brouwer, C. Pathview Web: user friendly pathway visualization and data integration. *Nucleic Acids Res.* **45**, W501–W508 (2017).
111. Deutsch, E. W. et al. The ProteomeXchange consortium in 2020: enabling 'big data' approaches in proteomics. *Nucleic Acids Res.* **48**, D1145–D1152 (2020).
112. Perez-Riverol, Y. et al. The PRIDE database and related tools and resources in 2019: improving support for quantification data. *Nucleic Acids Res.* **47**, D442–D450 (2019).

Acknowledgements

This work was supported by the following grants from the Deutsche Forschungsgemeinschaft (DFG, German Research Foundation): KR1143/9-2 and ZI618/6-2 (KFO309, P3 (to M.K. and J.Z.), Z1 (to T.H.) P2 (to S.H. and S.B.), project 284237345); TRR81/3 (A07 (to M.L.S.), B02 (to M.K.), project 109546710); SFB1213/2 (B03 (to M.K., M.L.S.), project 268555672); SFB1021/2 (A01 (to J.Z.), A05 (to S.B.), C01 (to M.L.S.), C02 (to M.K.), Z02 (to T.H.), Z03 (to M.K., U.L.), C05 (to S.H.), project 197785619); SFB-TR84 (B02 and B09 to S.H.), GRK 2573 (RP4 (to M.L.S), RP5 (to M.K.), project 416910386) and INST 160/708-1 FUGB (to U.L.). The work was also supported by the German Ministry for Education and Research (RAPID, COVINET, and DZIF TTU 01.806, to J. Z.) and the LOEWE program of the state of Hesse (DRUID, B02 to J.Z. and A01 to S.B.). Work in the laboratories of M.K., S.H. and M.L.S. is also supported by the IMPRS program of the Max Planck Society and the Excellence Cluster Cardio-Pulmonary Institute (EXC 2026: Cardio-Pulmonary Institute (CPI), project 390649896) and the DZL/UGMLC/ILH program. Work of J.Z., M.K., S.H. and S.B. is further supported by the Von-Behring-Roentgen-Stiftung and the Pandemics Network Hesse. We thank Andrea Nist and Thorsten Stiewe of the Genomics Core Facility, Philipps University Marburg, Marburg, Germany, and Philipp Mengel, Institute of Medical Microbiology, Justus Liebig University, Giessen, Germany, for RNA sequencing and Christian Drosten for providing SARS-CoV-2 and MERS-CoV.

Author contributions

M.S.S., C.M., C.M-B., H.W., B.V.A., N.K. and J.M-S. performed experiments, analyzed, and visualized data. U.L. performed mass spectrometry measurements and together with A.W., M.K. and I.B. analyzed proteomics data sets. N.H. analyzed RNA-seq data. T.H. sequenced SARS-CoV-2. M.K. conceived and supervised the study and analyzed and visualized data. M.K. wrote the initial paper draft. J.Z. supervised and analyzed MERS-CoV and SARS-CoV-2 experiments. J.Z., S.B., S.H., M.L.S., (and all other authors) helped to finalize the paper. All authors approved the submitted version of the paper.

Funding

Open Access funding enabled and organized by Projekt DEAL.

Competing interests

The authors declare no competing interests.

Additional information

Supplementary information The online version contains supplementary material available at https://doi.org/10.1038/s41467-021-25551-1.

Correspondence and requests for materials should be addressed to John Ziebuhr or Michael Kracht.

Peer review information *Nature Communications* thanks Saeid Ghavami and the other, anonymous, reviewer(s) for their contribution to the peer review of this work. Peer reviewer reports are available.

Reprints and permission information is available at http://www.nature.com/reprints

Publisher's note Springer Nature remains neutral with regard to jurisdictional claims in published maps and institutional affiliations.

Antiviral Research 150 (2018) 123–129

Contents lists available at ScienceDirect

Antiviral Research

journal homepage: www.elsevier.com/locate/antiviral

Broad-spectrum antiviral activity of the eIF4A inhibitor silvestrol against corona- and picornaviruses

Christin Müller[a,c,1], Falk W. Schulte[b,1], Kerstin Lange-Grünweller[b], Wiebke Obermann[b], Ramakanth Madhugiri[a], Stephan Pleschka[a,c], John Ziebuhr[a,c], Roland K. Hartmann[b], Arnold Grünweller[b,*]

[a] Institut für Medizinische Virologie, Justus-Liebig-Universität Gießen, Schubertstraße 81, 35392 Gießen, Germany
[b] Institut für Pharmazeutische Chemie, Philipps-Universität Marburg, Marbacher Weg 6, 35037 Marburg, Germany
[c] Deutsches Zentrum für Infektionsforschung (DZIF) at the partner site Gießen-Marburg-Langen, Germany

ARTICLE INFO

Keywords:
Silvestrol
Coronavirus
Picornavirus
eIF4A
Cap-dependent translation
IRES

ABSTRACT

Coronaviruses (CoV) and picornaviruses are plus-strand RNA viruses that use 5′ cap-dependent and cap-independent strategies, respectively, for viral mRNA translation initiation. Here, we analyzed the effects of the plant compound silvestrol, a specific inhibitor of the DEAD-box RNA helicase eIF4A, on viral translation using a dual luciferase assay and virus-infected primary cells. Silvestrol was recently shown to have potent antiviral activity in Ebola virus-infected human macrophages. We found that silvestrol is also a potent inhibitor of cap-dependent viral mRNA translation in CoV-infected human embryonic lung fibroblast (MRC-5) cells. EC_{50} values of 1.3 nM and 3 nM silvestrol were determined for MERS-CoV and HCoV-229E, respectively. For the highly pathogenic MERS-CoV, the potent antiviral activities of silvestrol were also confirmed using peripheral blood mononuclear cells (PBMCs) as a second type of human primary cells. Silvestrol strongly inhibits the expression of CoV structural and nonstructural proteins (N, nsp8) and the formation of viral replication/transcription complexes. Furthermore, potential antiviral effects against human rhinovirus (HRV) A1 and poliovirus type 1 (PV), representing different species in the genus *Enterovirus* (family *Picornaviridae*), were investigated. The two viruses employ an internal ribosomal entry site (IRES)-mediated translation initiation mechanism. For PV, which is known to require the activity of eIF4A, an EC_{50} value of 20 nM silvestrol was determined in MRC-5 cells. The higher EC_{50} value of 100 nM measured for HRV A1 indicates a less critical role of eIF4A activity in HRV A1 IRES-mediated translation initiation. Taken together, the data reveal a broad-spectrum antiviral activity of silvestrol in infected primary cells by inhibiting eIF4A-dependent viral mRNA translation.

1. Introduction

We have recently identified the natural compound silvestrol as a potent antiviral molecule to inhibit Ebola virus (EBOV) replication (Biedenkopf et al., 2017). Silvestrol can be isolated from plants of the genus *Aglaia*. It belongs to the flavaglines, which have a cyclopenta[*b*] benzofuran skeleton in common (Pan et al., 2014). Recently, a CRISPR/Cas-based genetic proof of silvestrol's target specificity for the DEAD-box RNA helicase eIF4A was provided (Chu et al., 2016). This enzyme is required to unwind stable RNA secondary structures in 5′ UTRs of capped mRNAs to create a binding platform for the 43S preinitiation complex which then scans the 5′ UTR for the start codon to initiate protein synthesis (Hinnebusch et al., 2016). Binding of silvestrol to eIF4A increases its affinity to the mRNA, thereby stalling the helicase to its substrate (Sadlish et al., 2013). This might lead to depletion of eIF4A from the translation initiation complex eIF4F that recognizes the m7GpppN cap structure of mRNAs (Pelletier et al., 2015). Silvestrol is cytotoxic at low nanomolar concentrations to a large number of cancer cell lines and was also shown to exert strong antitumorigenic effects in several tumor mouse models (Cencic et al., 2009; Kogure et al., 2013; Patton et al., 2015). Importantly, in non-cancer cells and primary cells, silvestrol seems to be well tolerated up to low micromolar concentrations (Su et al., 2006; Zhu et al., 2007; Biedenkopf et al., 2017). The reasons are so far not well understood, however several proto-oncogenes that are sensitive to silvestrol harbor extended 5′UTRs with extensive RNA secondary structure elements. Therefore, it has been

* Corresponding author.
E-mail address: gruenwel@staff.uni-marburg.de (A. Grünweller).
[1] Both authors contributed equally to this work.

https://doi.org/10.1016/j.antiviral.2017.12.010
Received 5 October 2017; Received in revised form 12 December 2017; Accepted 14 December 2017
Available online 16 December 2017
0166-3542/

proposed that targeting eIF4A by silvestrol might lead to mRNA discrimination during translation (Cencic et al., 2009; Rubio et al., 2014). Long and structured 5′ UTRs are also often found in capped viral mRNAs like those from EBOV (Weik et al., 2002; Schlereth et al., 2016). In line with this, we have found that low nanomolar concentrations of silvestrol strongly reduce EBOV titers in primary human macrophages by efficiently decreasing viral protein expression without having cytotoxic side effects at concentrations of effective antiviral activity (Biedenkopf et al., 2017). Also many plus-strand (+) RNA viruses, such as corona- and picornaviruses, carry long and highly structured 5′ UTRs with important functions in viral replication and/or translation initiation (reviewed in Madhugiri et al., 2016). We therefore asked the question whether these viruses are also sensitive to silvestrol treatment and if this sensitivity differs among viruses using alternative mechanisms of translation initiation.

Here we established a cellular dual luciferase reporter assay which allows us to rapidly screen for inhibition of eIF4A-dependent translation initiation on viral 5′ UTRs by silvestrol and related compounds. Subsequently, we analyzed potential antiviral effects of silvestrol in human primary cells (human embryonic lung fibroblasts (MRC-5) or peripheral blood mononuclear cells (PBMCs)) that were infected with the Middle East Respiratory Syndrome coronavirus (MERS-CoV) or human coronavirus 229E (HCoV-229E). Both (+) ssRNA viruses use a 5′ cap-dependent mechanism of translation initiation and carry highly structured 5′ UTRs. We also analyzed the effects of silvestrol on replication of two (+) ssRNA viruses of the *Picornaviridae* family, human rhinovirus A1 (HRV A1) and poliovirus type 1 (PV), because it is known that picornaviruses, although utilizing an IRES-dependent mechanism for viral mRNA translation, still require the action of host factors such as eIF4A (Bordeleau et al., 2006).

2. Material and methods

2.1. Cells and viruses

Huh-7 cells, African green monkey kidney cells (Vero cells), HeLa cells and primary human lung fibroblasts (MRC-5 cells) were grown in Dulbecco's modified eagle medium (DMEM) supplemented with 10% fetal calf serum (FCS) and antibiotics (100 U/ml penicillin and 100 µg/ml streptomycin) at 37 °C and 5% CO_2. HepG2 cells were cultured in Iscove's Modified Dulbecco's Medium (IMDM) supplemented with 10% FCS at 37 °C and 5% CO_2. HCoV-229E, MERS-CoV (EMC/2012), HRV A1 and PV (strain Mahoney) were obtained from the virus collection of the Institute of Medical Virology, Justus Liebig University Gießen.

2.2. Reagent

Silvestrol was obtained from Medchemexpress (LLC, Princeton, USA; purity > 98%). A stock solution of 6 mM was prepared in DMSO (sterile-filtered; Carl Roth, Germany) and diluted working solutions were prepared in DMEM or IMDM. Control cells were treated with corresponding DMSO dilutions lacking silvestrol.

2.3. Cloning of the dual luciferase constructs

All 5′ UTRs were cloned into the plasmid pFR_HCV_xb containing an HSV-TK promoter, the firefly luciferase gene, an HCV IRES and the renilla luciferase gene. The different 5′ UTRs (NP: 414 bp, 38% GC; VP35: 97 bp, 35% GC; VP40: 89 bp, 33% GC; GP: 139 bp, 41% GC; VP30: 212 bp, 33% GC; VP24: 460 bp, 40% GC; L: 80 bp, 34% GC; ß-Globin: 50 bp, 44% GC; ß-Actin: 84 bp, 76% GC; PIM1: 157 bp, 75% GC; HCoV-229E: 292 bp, 41% GC; MERS-CoV: 278 bp, 44% GC) were cloned downstream to the HSV-TK promoter and directly followed by the firefly luciferase AUG start codon. All primers were designed by the software *SnapGene® 3.3.3* (GSL Biotech LLC) and their sequences can be provided upon request.

2.4. Dual-luciferase reporter assay

The day before transfection, 2×10^4 HepG2 cells per well were seeded in a 96-well plate (Greiner Bio One International GmbH) in 200 µL IMDM (Lonza) supplemented with 10% FCS (Biochrom AG) and incubated at 37 °C, 5% CO_2. The transfection was performed using 100 µL Opti-MEM (Thermo Fisher Scientific). For transfection of five wells, 0.5 µg of the reporter construct DNA were diluted in 25 µL of Opti-MEM. In parallel, 0.5 µL of Lipofectamine® 2000 Transfection Reagent (Thermo Fisher Scientific) were mixed with 24.5 µL of Opti-MEM. Both samples were preincubated for 5 min at room temperature, then combined and incubated for another 15 min at room temperature. Then, 10 µL of the solution were added to each well containing the cells in 100 µL Opti-MEM medium. The plates were incubated at 37 °C and 5% CO_2. 4–6 h post transfection, the medium was aspirated and substituted with 200 µL fresh medium (IMDM + 10% FCS) containing the appropriate silvestrol concentration. As control, the added amount of microliters of silvestrol solution was replaced with the same volume of a solution containing the same DMSO concentration but lacking silvestrol. Following incubation of the cells for 48 h at 37 °C at 5% CO_2, a Dual-Luciferase® Reporter Assay (Promega) was performed according to the manufacturer's instructions. Measurements were done using a Tecan Safire 2 Multimode Reader.

2.5. Cell toxicity

The cytotoxic concentration 50% (CC_{50}) of silvestrol was determined by incubating cells, which were seeded near confluency in FCS-free medium, with serial dilutions of silvestrol in a 96-well format. After incubation for 24 h, 200 µL of MTT-mix (DMEM supplemented with 10% FCS containing 250 µg/ml tetrazolium bromide, Sigma) was added to each well. Cells were further incubated for 90–120 min at 37 °C and subsequently fixed with 3.7% paraformaldehyde in PBS. Tetrazolium crystals were dissolved by adding 200 µL isopropanol to each well and absorbance at 490 nm was determined using an ELISA reader (BioTek). To determine the CC_{50}, the MTT values were calculated in percentage with the respective DMSO control set as 100% (see section 2.4). CC_{50} values were calculated by non-linear regression analysis using GraphPad Prism 5.0 (GraphPad Software).

2.6. Antiviral activity

To determine the effective concentration 50% (EC_{50}) of silvestrol, cell cultures were infected with the respective virus at an MOI of 0.1 for 1 h in PBS/BA/P/S (PBS containing 0.2% BSA, 1 mM $MgCl_2$, 0.9 mM $CaCl_2$, 100 U/ml penicillin and 100 mg/ml streptomycin) at 33 °C (for HCoV-229E and HRV A1) or 37 °C (for MERS-CoV and PV). After removing the inoculum, cells were incubated with FCS-free DMEM containing different inhibitor concentrations. Supernatants were collected at 24 h post infection (p.i.) and virus titers were analyzed by plaque assay. Briefly, cells were seeded in 24-well plates and inoculated for 1 h with 10-fold virus dilutions in PBS/BA/P/S. Next, the virus inoculum was replaced with Avicel-containing medium (1xMEM [Gibco], 1.25% Avicel [FMC Biopolymer]). At 24 h p.i., the plates were washed with PBS, fixed with 3.7% PFA in PBS and the cell layer was stained with 0.15% crystal violet. To calculate EC_{50} values, the virus titer determined for virus-infected cells treated with DMSO only (see section 2.4) was set to 100% and titers obtained for silvestrol-treated cells were calculated in relation to it. EC_{50} values were calculated by non-linear regression analysis using GraphPad Prism 5.0 (GraphPad Software).

2.7. Western blot analysis

Viral protein accumulation was analyzed by Western blot analysis. MRC-5 or Huh-7 cells were infected with HCoV-229E at an MOI of 3. At 1 h p.i., the indicated concentrations of silvestrol in DMEM

supplemented with antibiotics were added to the cells for 12 h and 48 h, respectively. The cells were lysed with NP40-containing buffer (150 mM NaCl, 50 mM Tris-HCl, pH 7.5, 1% NP40, 1x protease inhibitor cocktail [Sigma-Aldrich]). Proteins were separated by 10% SDS-PAGE and blotted onto a nitrocellulose membrane (Amersham). Membranes were incubated with mouse anti-nucleocapsid protein mAb (Ingenasa), rabbit antiserum specific for HCoV-229E nonstructural protein 8 (nsp8) (Ziebuhr and Siddell, 1999) and rabbit anti-actin antibody (Abcam), respectively, each diluted 1:1000 in PBS containing 1% bovine serum albumin (BSA). Following incubation for 60 min, the membranes were extensively washed with PBS and incubated with appropriate secondary antibodies (IRDye-conjugated anti-mouse and anti-rabbit mAb [Li-Cor], respectively) diluted 1:10,000 in PBS containing 1% BSA. After 1 h, membranes were washed and analyzed using the LI-COR Odyssey imaging system.

2.8. Immunofluorescence

Immunofluorescence was performed as described previously (Müller et al., 2016). Briefly, MRC-5 cells were infected with HCoV-229E (MOI of 3) and treated with the indicated concentrations of silvestrol for 12 h p.i. or left untreated. Then, the cells were fixed with ice-cold methanol and stained with mouse anti-dsRNA mAb (J2, SCICONS English & Scientific Consulting Kft.) and polyclonal rabbit anti-HCoV-229E nsp8 serum (Ziebuhr and Siddell, 1999). As secondary antibodies, Alexa Fluor 594 goat anti-mouse IgG and Alexa Fluor 488 F(ab')2 fragment of goat anti-rabbit IgG (Thermo Fisher Scientific) were used. Confocal microscopy was done using a Leica SP05 CLSM and LAS-AF software (Leica).

3. Results and discussion

3.1. Effects of silvestrol on translation of a luciferase reporter mRNA fused to viral 5' UTRs

In our previous study we identified silvestrol as an efficient inhibitor of translation of several EBOV mRNAs and EBOV replication. To understand the effects of silvestrol on cap-dependent viral protein synthesis in more detail, we fused the 5′ UTRs of all seven EBOV mRNAs to the firefly luciferase coding sequence in a dual luciferase reporter plasmid (Fig. 1A). Expression of the fusion genes was driven by the HSV-TK promoter, and the corresponding mRNA transcripts underwent co-transcriptional 5′-terminal capping by the respective host factors. The bicistronic reporter transcripts harbor a hepatitis C virus (HCV) IRES element downstream of the firefly luciferase ORF. This type III IRES directs Renilla luciferase gene translation by a 5′-cap- and eIF4A-independent mechanism (Bordeleau et al., 2006; Lee et al., 2017) and was used to normalize transfection efficiencies (Fig. 1A). The 5′ UTR of the mRNA encoding the oncogenic kinase PIM1, known to be highly sensitive to inhibition of eIF4A by silvestrol (Schatz et al., 2011), served as a positive control, while the unstructured and short 5′ UTRs of the ß-globin and ß-actin mRNAs were used as negative controls. Concentrations of 5 or 10 nM silvestrol inhibited firefly luciferase expression of the ß-globin construct not at all, and that of the ß-actin construct by not more than 10%, whereas the same silvestrol concentrations resulted in ~40% inhibition for the PIM1 construct (Fig. 1B). As a further control we analyzed the 5′ UTR of the classical swine fever virus (CSFV) which contains an eIF4A-independent type III IRES element. As expected, no sensitivity towards silvestrol could be observed in the dual luciferase assay (Suppl. Fig. S1). For all seven EBOV 5′ UTR constructs, the inhibitory effects of 10 nM silvestrol clearly exceeded the effects of the negative controls, with firefly luciferase activities decreasing by 23% (VP40 matrix protein) and up to 33% (L, RNA-directed RNA polymerase L). This is consistent with our previous results obtained for EBOV-infected macrophages (Biedenkopf et al., 2017), where we observed efficient inhibition of viral mRNA translation at 10 nM silvestrol, although the effects of the same silvestrol concentration on reporter gene expression were generally less pronounced than on EBOV replication. In summary, we conclude that the dual luciferase assay is a suitable and reliable system to analyze the eIF4A dependence of 5′-capped viral mRNAs as an initial screen before infecting cells with pathogenic viruses.

We next applied the reporter assay to the study of silvestrol effects on the translation of mRNAs harboring 5′ UTRs derived from (+) ssRNA viruses. We cloned the 5′ UTRs of the human coronavirus HCoV-229E (which causes mild common cold-like symptoms) and of the highly pathogenic MERS-CoV into our reporter plasmid. In both cases, a relatively strong decrease of luciferase activity in the same range as for the PIM1 positive control (~40%) was measured at a silvestrol concentration of 10 nM (Fig. 1C), indicating that also polycistronic mRNAs of (+) ssRNA viruses depend on eIF4A and may thus be suitable targets for silvestrol treatment.

Coronaviruses utilize cap-dependent translation initiation mechanisms and contain structured 5′ UTRs in their genome- and subgenome-length mRNAs. Other viruses, such as the picornaviruses HRV A1 or PV translate their mRNAs in a 5' cap-independent mechanism via IRES elements within their 5′ UTRs (Thompson, 2012). Nevertheless, picornaviruses require the action of translation initiation factors, including eIF4A, for initiating IRES-dependent translation (Bordeleau et al., 2006). Therefore we decided to include HRV A1 and PV in the following experiments.

3.2. Effects of silvestrol on viruses with 5′-capped or IRES-containing mRNAs

Next, we analyzed the effects of silvestrol on viral titers in Vero cells (derived from the kidney of a normal healthy African green monkey with loss of the type I IFN cluster) and the cancer cell lines Huh-7 and HeLa. EC_{50} and EC_{90} values (see Table 1) were determined using cell lines infected with HCoV-229E, HRV A1 and PV, respectively, at an MOI of 0.1. Following inoculation of the infected cells with the appropriate virus, silvestrol was added in increasing concentrations ranging from 0.01 nM to 10 µM and viral titers in cell culture supernatants collected at 24 h p.i. were determined. For HCoV-229E-infected Huh-7 cells, we measured an EC_{50} value of 40 nM. The EC_{50} values for HRV A1-infected HeLa cells and PV-infected Vero cells were 400 nM and 100 nM, respectively (Fig. 2 and Table 1). To assess the cytotoxicity of silvestrol in these cell lines, CC_{50} values were determined in MTT assays. CC_{50} values of 30 nM for Huh-7 cells, 160 nM for Vero cells and 5 nM for HeLa cells were obtained (Suppl. Fig. S2), suggesting that the metabolic activities of these cell lines are very sensitive towards silvestrol treatment. Our findings are in line with the strong inhibitory effects of silvestrol reported previously for a range of cancer cell lines (Schatz et al., 2011). The data result in very low selectivity indices for this compound if permanent rather than primary cells were used for infections with the respective viruses (SI ≤ 1.6, Table 1). Taken together, the data obtained here and in our previous study (Biedenkopf et al., 2017) led us to conclude that permanent cell lines are not suitable for studying antiviral activities of silvestrol and prompted us to use primary cells in subsequent experiments.

In our previous study, specific and potent antiviral activity of silvestrol was observed in EBOV-infected primary human macrophages (Biedenkopf et al., 2017). We therefore decided to assess potential antiviral activities in human primary cells susceptible to the human corona- and picornaviruses used in this study. Human embryonic lung fibroblasts (MRC-5 cells) were infected with HCoV-229E, MERS-CoV, HRV A1 or PV at an MOI of 0.1 and silvestrol was added to the cell culture medium at concentrations ranging from 0.1 nM to 1 µM. Again, viral titers were determined 24 h p.i.. For HCoV-229E and MERS-CoV, EC_{50} values of 3 nM and 1.3 nM, respectively, were obtained (Fig. 3A, B, Suppl. Fig. S3A, B and Table 1). The cytotoxicity of silvestrol was measured using MRC-5 cells that were grown in the presence of varying

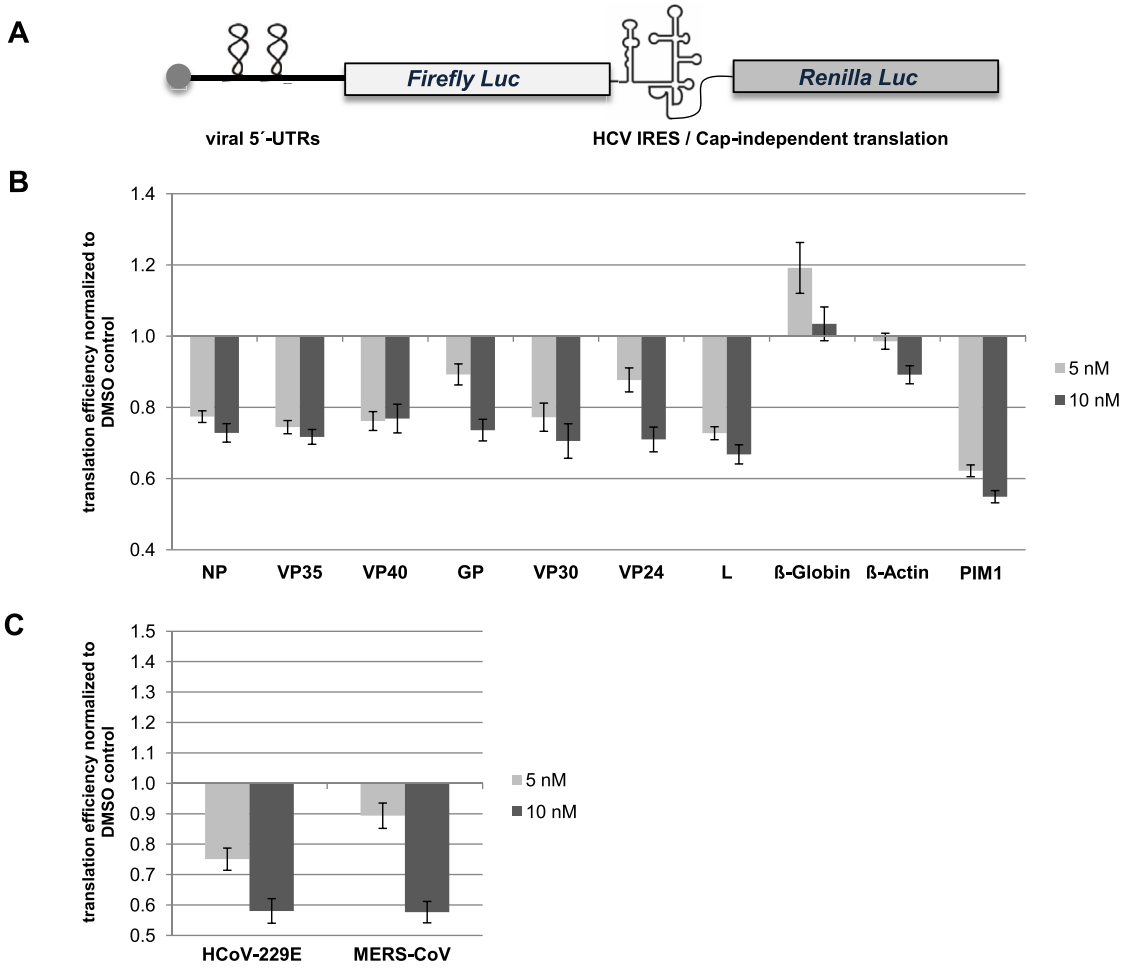

Fig. 1. Analysis of silvestrol effects on reporter gene activity mediated by viral 5′ UTRs. (**A**) Schematic presentation of the dual luciferase reporter vector. The HCV IRES-driven expression of the Renilla luciferase is eIF4A-independent and was used to normalize transfection efficiencies. (**B**) Effects of 5 and 10 nM silvestrol on Firefly luciferase activity. The seven 5′ UTRs of EBOV were cloned upstream of the reporter gene. As negative controls the 5′ UTRs of the ß-globin and the ß-actin mRNAs were analyzed. The 5′ UTR of *PIM1* served as a positive control. (**C**) Effects of silvestrol on reporter gene expression in the context of 5′ UTRs from coronaviruses HCoV-229E and MERS-CoV. All measured values were normalized to corresponding DMSO controls. Standard errors of the mean of at least 8 independent experiments are shown.

Table 1
CC_{50}, EC_{50} and EC_{90} values determined for silvestrol-treated cells that were mock infected (CC_{50}) or infected with the indicated viruses (EC_{50}/EC_{90}). MTT assays were performed at 37°C except for cells used for HCoV-229E and HRV A1 infections, which were performed at 33°C (indicated by asterisks). SI, selectivity index. Experiments were done in biological triplicate.

Cells	Virus	CC_{50} [μM]	EC_{50}/EC_{90} [nM]	SI
MRC-5	HCoV-229E	> 10*	3/27	> 3330
MRC-5	MERS-CoV	> 10	1.3/12	> 7690
MRC-5	HRV A1	> 10*	100/900	> 100
MRC-5	PV	> 10	20/180	> 500
PBMCs	HCoV-229E	> 1*	2.8/25	> 350
Huh-7	HCoV-229E	0.03*	40/360	0.75
HeLa	HRV A1	0.005*	400/3600	0.012
Vero	PV	0.16	100/900	1.6

concentrations of silvestrol for 24 h at 33 °C (corresponding to the temperature used for HCoV-229E and HRV A1 infections) or 37 °C (corresponding to the temperature used for MERS-CoV and PV infections). CC_{50} values of > 10 μM were measured at both temperatures (Fig. 4, see also Table 1). The resulting selectivity indiceswere > 3330 for HCoV-229E and > 7690 for MERS-CoV, demonstrating low cytotoxicity and extremely efficient antiviral activity of silvestrol in primary cells (Table 1). The EC_{50} values determined for HRV A1- and PV-infected MRC-5 cells were approximately 100 nM and 20 nM (Fig. 3C, D, Suppl. Fig. S3C, D and Table 1), respectively, suggesting that silvestrol also displays antiviral activities if the respective virus utilizes eIF4A-dependent IRES-driven translation mechanisms. However, HRV A1 was ~30- to 80-fold and PV ~7- to 15-fold less sensitive to silvestrol treatment compared with the two coronaviruses included in this study (Fig. 3A–D), indicating a less prominent role of eIF4A in translation initiation of the picornaviral mRNAs. In summary, the data obtained in this and our previous study (Biedenkopf et al., 2017) demonstrate that silvestrol is a potent antiviral inhibitor in primary cells infected with coronaviruses and EBOV. Importantly, the type I IRES-containing PV and, to a lesser extent, HRV A1 also proved to be sensitive to silvestrol treatment in primary cells. Altogether, these findings reveal a broad-spectrum antiviral activity of silvestrol, including viruses with 5′-capped and structured 5′ UTRs as well as those containing IRES elements that require eIF4A helicase activity for efficient translation initiation.

Anticoronaviral effects of silvestrol were further corroborated using peripheral blood mononuclear cells (PBMCs) isolated from human donors and infected with HCoV-229E. For PBMCs, a CC_{50} value of > 1 μM was determined (Fig. 4C), and EC_{50} values of 2.8 nM and 3.5 nM, respectively, were obtained using cells from two independent donors (Fig. 3E, Suppl. Fig. S3E, Table 1 and data not shown), confirming the potent antiviral activities of silvestrol in coronavirus-infected primary cells.

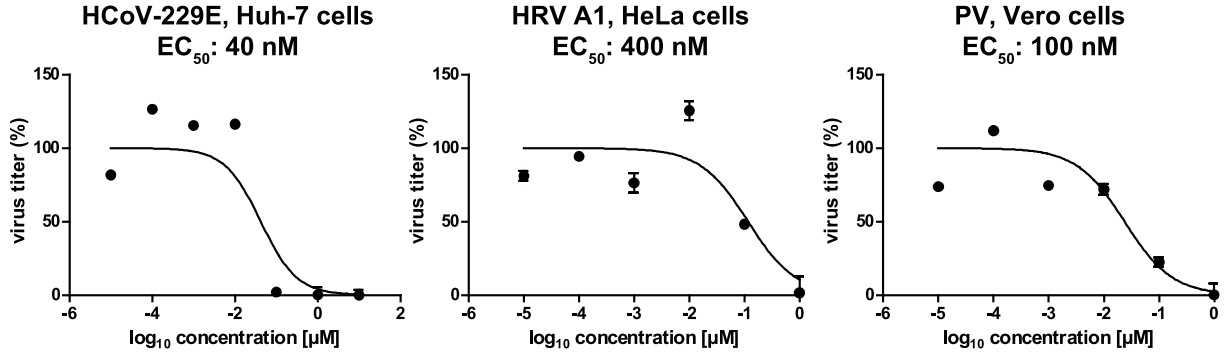

Fig. 2. Effects of silvestrol in cancer cell lines and Vero cells infected with HCoV-229E, HRV A1 and PV, respectively. Cells were infected with an MOI of 0.1 and grown in cell culture medium containing different concentrations of silvestrol. 24 h p.i., cell culture supernatants were collected and virus titers were analyzed via plaque assay. Virus titers (in percent) were calculated in relation to infected controls without silvestrol treatment, and EC_{50} values were calculated using non-linear regression analysis. Experiments were done in biological triplicate.

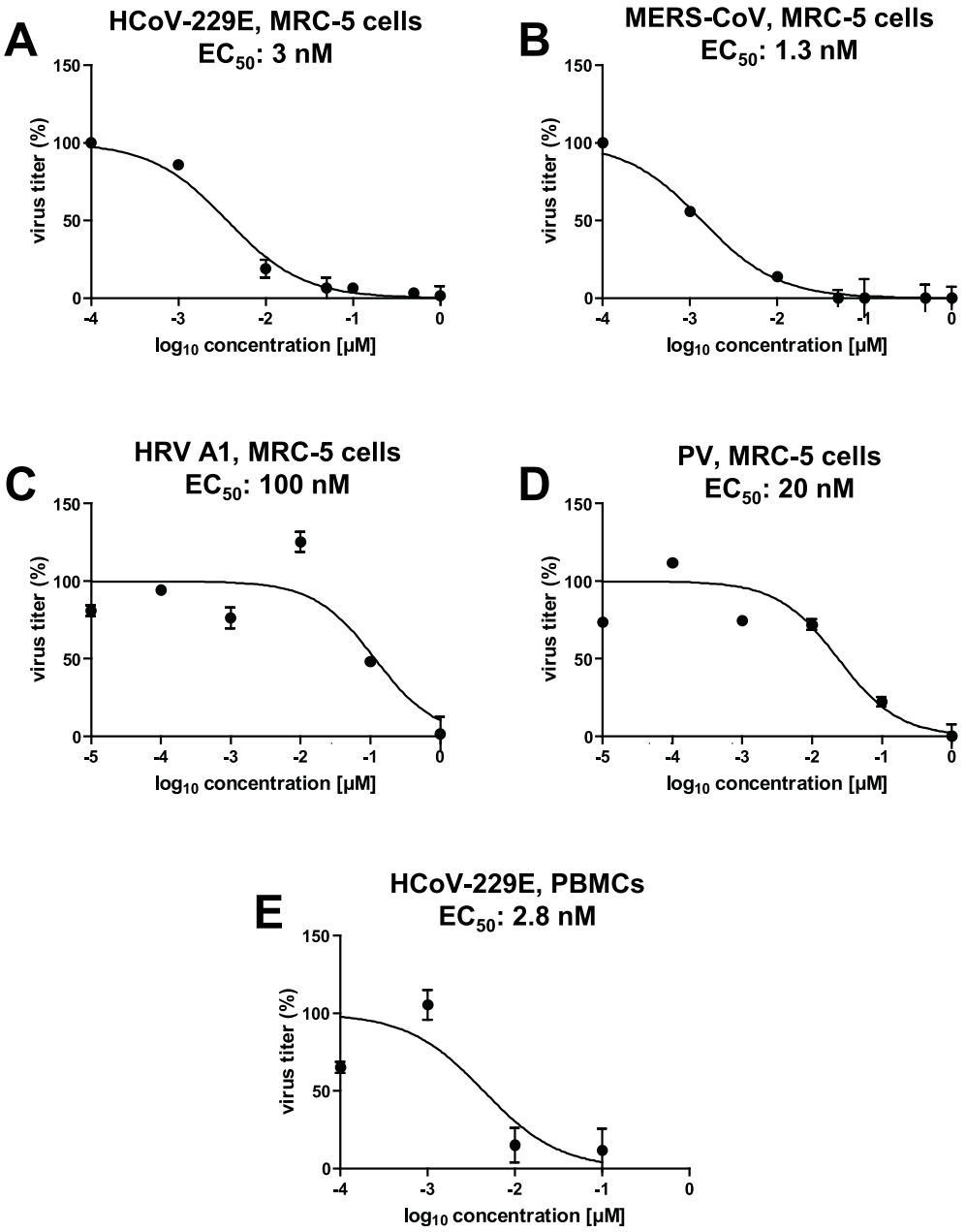

Fig. 3. Antiviral activity of silvestrol against (+) ssRNA viruses that utilize canonical (cap-dependent) translation initiation (coronaviruses) or IRES-driven translation initiation mechanisms (members of the genus *Enterovirus*). Cells were infected with the indicated viruses at an MOI of 0.1 and grown in the presence of different concentrations of silvestrol. Supernatants collected at 24 h p.i. were used to determine viral titers. **A**, HCoV-229E, MRC-5 cells; **B**, MERS-CoV, MRC-5 cells; **C**, HRV A1, MRC-5 cells; **D**, PV, MRC-5 cells; **E**, HCoV-229E, PBMCs. Virus titers (in percent) were calculated in relation to infected controls without silvestrol treatment, and EC_{50} values were calculated using non-linear regression analysis. Experiments were done in biological triplicate.

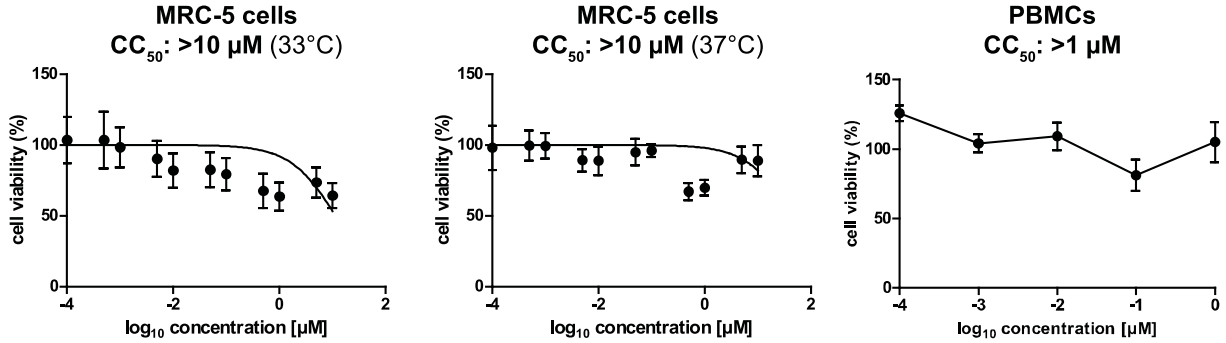

Fig. 4. Analyses of cell cytotoxicity of silvestrol. Effects of silvestrol on cell proliferation were measured by an MTT assay. MRC-5 cells or PBMCs were incubated with the indicated silvestrol concentrations and MTT assays were performed after 24 h. Results were based on three independent experiments (biological triplicates).

3.3. Silvestrol inhibits the formation of replication/transcription complexes, viral RNA synthesis and the translation of HCoV-229E proteins

In an additional set of experiments, we investigated potential effects of silvestrol on replication/transcription complex (RTC) formation and viral protein accumulation in coronavirus-infected cells. MRC-5 cells were infected with HCoV-229E at an MOI of 3 and treated with the indicated concentrations of silvestrol or left untreated. At 12 h p.i., the cells were harvested for further analyses. Immunofluorescence demonstrated a dose-dependent antiviral effect of silvestrol (Fig. 5). In the presence of 10 nM silvestrol, we observed a significant decrease of both viral double-stranded RNA (dsRNA) and the HCoV-229E nsp8 protein, which were used as markers for viral genome expression and RTC formation (Lundin et al., 2014; Müller et al., 2016). At 100 nM silvestrol, nearly no viral dsRNA and nsp8 could be detected (Fig. 5). The data suggest impaired RTC formation in HCoV-229E-infected MRC-5 cells treated with ≥ 10 nM silvestrol.

In Western blot experiments, N and nsp8 protein accumulation in HCoV-229E-infected Huh-7 cells appeared to be unaffected by silvestrol concentrations of up to 10 nM, whereas both proteins became essentially undetectable at 100 nM silvestrol (Fig. 6A). In contrast to Huh-7 cells, silvestrol severely decreased viral protein synthesis in primary cells already at much lower concentrations, with very low amounts of N and nsp8 proteins being produced in the presence of 10 nM silvestrol in HCoV-229E-infected MRC-5 cells (at 12 h as well as 48 h p.i.; Fig. 6B). The data correspond very well to the virus titration EC_{50} data shown in Figs. 2 and 3 for permanent cell lines versus primary cells and support our conclusion that specific antiviral effects of silvestrol against HCoV-229E are largely confined to primary cells.

Taken together, the data lead us to conclude that the natural compound silvestrol is a potent antiviral molecule with broad-spectrum activity, now demonstrated for mechanistically diverse (−) and (+) ssRNA viruses. Importantly, silvestrol had no major cytotoxic side effects in the primary cell systems analyzed in this study. This is in line with several studies that explored the effect of silvestrol in different cancer model systems. For example, no general toxicity of silvestrol could be detected *in vivo* in the liver, spleen or on blood cells; likewise, no general disease symptoms, loss of body weight or immune suppressive effects were observed (Lucas et al., 2009; Cencic et al., 2009; Patton et al., 2015). Moreover, silvestrol showed favorable pharmacokinetics in terms of bioavailability and biostability (Saradhi et al., 2011). In our opinion, silvestrol-mediated eIF4A inhibition is a promising new strategy for combating pathogenic RNA viruses. For therapeutic intervention, the short-term application of low doses of

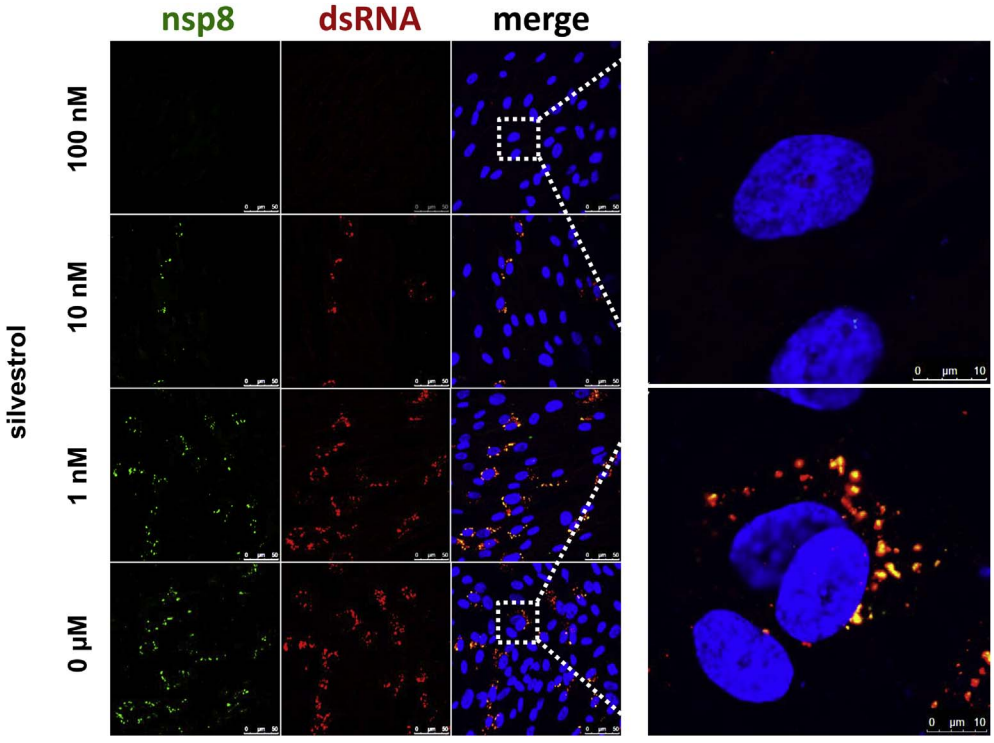

Fig. 5. Immunofluorescence analysis to visualize the effects of silvestrol on viral dsRNA and nsp8 accumulation in HCoV-229E-infected MRC-5 cells. Cells were infected with an MOI of 3 and incubated with the indicated silvestrol concentrations. Cells were fixed at 12 h p.i. and analyzed by confocal microscopy using specific antibodies for dsRNA (red) and nonstructural protein 8 (nsp8, green). The scale bar in the overview pictures represents 50 µm. (For interpretation of the references to colour in this figure legend, the reader is referred to the Web version of this article.)

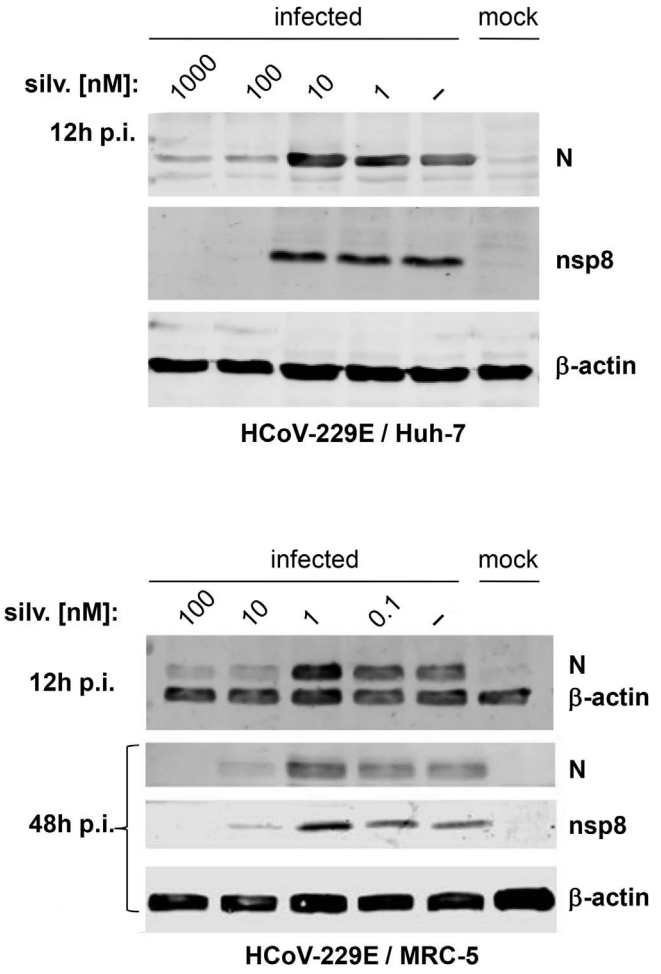

Fig. 6. Western blot analysis of HCoV-229E protein accumulation in the presence of silvestrol. (**A**) Huh-7 and (**B**) MRC-5 cells, respectively, were infected with HCoV-229E at an MOI of 3 and treated with the indicated concentrations of silvestrol. Cell lysates were prepared at 12 h p.i. and 48 h p.i. as indicated and the accumulation of viral N and nsp8 proteins was determined by Western blot analysis using appropriate antibodies (see Materials and Methods). β-actin was used as a loading control. Experiments were done in biological duplicates. Panels A and B show representative experiments.

silvestrol to reduce viral titers in the patient should be an acceptable safety risk. Specific inhibition of cellular factors, such as eIF4A, that promote the translation of structured viral transcripts should limit viral replication to low levels and thus help the immune system in establishing effective antiviral responses. Clearly, the observed antiviral effects of silvestrol need to be characterized in suitable *in vivo* infection models to validate its promising therapeutic potential.

Disclosure statement

The authors declare no conflict of interest.

Funding

The work was supported by the German Center for Infection Research (DZIF), partner site Giessen, Germany (TTU Emerging Infections, to S.P. and J.Z.), German Research Foundation (DFG) grant CRC 1021 (to J.Z. and R.K.H., respectively), LOEWE Research Center DRUID (to A.G. and J.Z.) and the LOEWE Research Cluster “Medical RNomics” grant 519/03/00.001-(0003) (to A.G. and R.K.H.).

Acknowledgments

We would like to thank Nadja Karl for excellent technical assistance.

Appendix A. Supplementary data

Supplementary data related to this article can be found at http://dx.doi.org/10.1016/j.antiviral.2017.12.010.

References

Biedenkopf, N., Lange-Grünweller, K., Schulte, F.W., et al., 2017. The natural compound silvestrol is a potent inhibitor of Ebola virus replication. Antivir. Res. 137, 76–81. http://dx.doi.org/10.1016/j.antiviral.2016.11.011.

Bordeleau, M.E., Mori, A., Oberer, M., et al., 2006. Functional characterization of IRESes by an inhibitor of the RNA helicase eIF4A. Nat. Chem. Biol. 2, 213–220.

Cencic, R., Carrier, M., Galicia-Vázquez, G., et al., 2009. Antitumor activity and mechanism of action of the cyclopenta[b]benzofuran, silvestrol. PLos One 4, e5223.

Chu, J., Galicia-Vázquez, G., Cencic, R., et al., 2016. CRISPR-mediated drug-target validation reveals selective pharmacological inhibition of the RNA helicase, eIF4A. Cell Rep 15, 2340–2347.

Hinnebusch, A.G., Ivanov, I.P., Sonenberg, N., 2016. Translational control by 5'-untranslated regions of eukaryotic mRNAs. Science 352, 1413–1416.

Kogure, T., Kinghorn, A.D., Yan, I., et al., 2013. Therapeutic potential of the translation inhibitor silvestrol in hepatocellular cancer. PLos One 8, e76136.

Lee, K.M., Chen, C.J., Shih, S.R., 2017. Regulation mechanisms of viral IRES-driven translation. Trends Microbiol. 25, 546–561 (Review).

Lucas, D.M., Edwards, R.B., Lozanski, G., et al., 2009. The novel plant-derived agent silvestrol has B-cell selective activity in chronic lymphocytic leukemia and acute lymphoblastic leukemia in vitro and in vivo. Blood 113, 4656–4666.

Lundin, A., Dijkman, R., Bergström, T., Kann, N., Adamiak, B., Hannoun, C., Kindler, E., Jónsdóttir, H.R., Muth, D., Kint, J., Forlenza, M., Müller, M.A., Drosten, C., Thiel, V., Trybala, E., 2014. Targeting membrane-bound viral RNA synthesis reveals potent inhibition of diverse coronaviruses including the middle East respiratory syndrome virus. PLoS Pathog. 10, e1004166.

Madhugiri, R., Fricke, M., Marz, M., Ziebuhr, J., 2016. Coronavirus cis-acting RNA elements. Adv. Virus Res. 96, 127–163. http://dx.doi.org/10.1016/bs.aivir.2016.08.007. Review.

Müller, C., Karl, N., Ziebuhr, J., Pleschka, S., 2016. D, L-lysine acetylsalicylate and glycine impairs Coronavirus Replication. J Antivir Antiretrovir 8, 142–150.

Pan, L., Woodard, J.L., Lucas, D.M., et al., 2014. Rocaglamide, silvestrol and structurally related bioactive compounds from Aglaia species. Nat. Prod. Rep. 31, 924–939. http://dx.doi.org/10.1039/c4np00006d. Review.

Patton, J.T., Lustberg, M.E., Lozanski, G., et al., 2015. The translation inhibitor silvestrol exhibits direct anti-tumor activity while preserving innate and adaptive immunity against EBV-driven lymphoproliferative disease. Oncotarget 6, 2693–2708.

Pelletier, J., Graff, J., Ruggero, D., Sonenberg, N., 2015. Targeting the eIF4F translation initiation complex: a critical nexus for cancer development. Cancer Res. 75, 250–263.

Rubio, C.A., Weisburd, B., Holderfield, M., et al., 2014. Transcriptome-wide characterization of the eIF4A signature highlights plasticity in translation regulation. Genome Biol. 15 (10), 476.

Sadlish, H., Galicia-Vazquez, G., Paris, C.G., et al., 2013. Evidence for a functionally relevant rocaglamide binding site on the eIF4A-RNA complex. ACS Chem. Biol. 8, 1519–1527.

Saradhi, U.V., Gupta, S.V., Chiu, M., et al., 2011. Characterization of silvestrol pharmacokinetics in mice using liquid chromatography-tandem mass spectrometry. AAPS J. 13, 347–356.

Schatz, J.H., Oricchio, E., Wolfe, A.L., et al., 2011. Targeting cap-dependent translation blocks converging survival signals by AKT and PIM kinases in lymphoma. J. Exp. Med. 208, 1799–1807.

Schlereth, J., Grünweller, A., Biedenkopf, N., et al., 2016. RNA binding specificity of Ebola virus transcription factor VP30. RNA Biol. 17, 1–16 ([Epub ahead of print]).

Su, B.N., Chai, H., Mi, Q., et al., 2006. Activity-guided isolation of cytotoxic constituents from the bark of Aglaia crassinervia collected in Indonesia. Bioorg. Med. Chem. 14, 960–972.

Thompson, S.R., 2012. Trends Microbiol. 20, 558–566. http://dx.doi.org/10.1016/j.tim.2012.08.002. (Review).

Weik, M., Modrof, J., Klenk, H.D., et al., 2002. Ebola virus VP30-mediated transcription is regulated by RNA secondary structure formation. J. Virol. 76, 8532–8539.

Zhu, J.Y., Lavrik, I.N., Mahlknecht, U., et al., 2007. The traditional Chinese herbal compound rocaglamide preferentially induces apoptosis in leukemia cells by modulation of mitogen-activated protein kinase activities. Int. J. Canc. 121, 839–846.

Ziebuhr, J., Siddell, S.G., 1999. Processing of the human coronavirus 229E replicase polyproteins by the virus-encoded 3C-like proteinase: identification of proteolytic products and cleavage sites common to pp1a and pp1ab. J. Virol. 73, 177–185.

Antiviral Research 175 (2020) 104706

Contents lists available at ScienceDirect

Antiviral Research

journal homepage: www.elsevier.com/locate/antiviral

Comparison of broad-spectrum antiviral activities of the synthetic rocaglate CR-31-B (−) and the eIF4A-inhibitor Silvestrol

Christin Müller[a,c,1], Wiebke Obermann[b,1], Falk W. Schulte[b], Kerstin Lange-Grünweller[b], Lisa Oestereich[d,e], Fabian Elgner[f], Mirco Glitscher[f], Eberhard Hildt[f], Kamini Singh[g], Hans-Guido Wendel[g], Roland K. Hartmann[b], John Ziebuhr[a,c], Arnold Grünweller[b,*]

[a] Institut für Medizinische Virologie, Justus-Liebig-Universität Gießen, Schubertstraße 81, 35392, Gießen, Germany
[b] Institut für Pharmazeutische Chemie, Philipps-Universität Marburg, Marbacher Weg 6, 35032, Marburg, Germany
[c] Deutsches Zentrum für Infektionsforschung (DZIF) at the Partner Site Gießen-Marburg-Langen, Germany
[d] Bernhard-Nocht-Institut für Tropenmedizin, Abteilung Virologie, Hamburg, Germany
[e] Deutsches Zentrum für Infektionsforschung (DZIF) at the Partner Site Hamburg, Germany
[f] Paul-Ehrlich-Institut, Bundesinstitut für Impfstoffe und Biomedizinische Arzneimittel, Abteilung Virologie, Paul-Ehrlich-Straße 51-59, 63225, Langen, Germany
[g] Cancer Biology and Genetics Program, Memorial Sloan Kettering Cancer Center, New York, NY, 10023, USA

ARTICLE INFO

Keywords:
Silvestrol
CR-31-B
Antiviral activity
eIF4A
Translation initiation
Rocaglates

ABSTRACT

Rocaglates, a class of natural compounds isolated from plants of the genus *Aglaia*, are potent inhibitors of translation initiation. They are proposed to form stacking interactions with polypurine sequences in the 5′-untranslated region (UTR) of selected mRNAs, thereby clamping the RNA substrate onto eIF4A and causing inhibition of the translation initiation complex. Since virus replication relies on the host translation machinery, it is not surprising that the rocaglate Silvestrol has broad-spectrum antiviral activity. Unfortunately, synthesis of Silvestrol is sophisticated and time-consuming, thus hampering the prospects for further antiviral drug development. Here, we present the less complex structured synthetic rocaglate CR-31-B (−) as a novel compound with potent broad-spectrum antiviral activity in primary cells and in an *ex vivo* bronchial epithelial cell system. CR-31-B (−) inhibited the replication of corona-, Zika-, Lassa-, Crimean Congo hemorrhagic fever viruses and, to a lesser extent, hepatitis E virus (HEV) at non-cytotoxic low nanomolar concentrations. Since HEV has a polypurine-free 5′-UTR that folds into a stable hairpin structure, we hypothesized that RNA clamping by Silvestrol and its derivatives may also occur in a polypurine-independent but structure-dependent manner. Interestingly, the HEV 5′-UTR conferred sensitivity towards Silvestrol but not to CR-31-B (−). However, if an exposed polypurine stretch was introduced into the HEV 5′-UTR, CR-31-B (−) became an active inhibitor comparable to Silvestrol. Moreover, thermodynamic destabilization of the HEV 5′-UTR led to reduced translational inhibition by Silvestrol, suggesting differences between rocaglates in their mode of action, most probably by engaging Silvestrol's additional dioxane moiety.

1. Introduction

The DEAD-box RNA helicase eIF4A, which is part of the heterotrimeric translation initiation complex eIF4F, unwinds RNA secondary structures in 5′-UTRs of selected mRNAs to enable binding of the 43S preinitiation complex (PIC) (Bhat et al., 2015; Wolfe et al., 2014). In cells, eIF4A has a critical role in the translation of protooncogenic mRNAs with complex-structured 5′-UTRs (Wolfe et al., 2014; Rubio et al., 2014). Viral mRNAs also contain structured 5′-UTRs (Madhugiri et al., 2015; Schlereth et al., 2016), suggesting that viral protein synthesis may also be eIF4A-dependent. Indeed, we have shown that the specific eIF4A inhibitor Silvestrol, a plant-derived rocaglate, has broad-spectrum antiviral activity at non-cytotoxic concentrations in a low nanomolar range (Müller et al., 2018a). Silvestrol inhibits the replication of RNA viruses representing different virus families, such as Ebola- (EBOV), corona- (CoV), Zika- (ZIKV), Chikungunya- (CHIKV) and hepatitis E (HEV) viruses (Müller et al., 2018a; Biedenkopf et al., 2017; Elgner et al., 2018; Glitscher et al., 2018; Henss et al., 2018). Notably, Silvestrol showed good bioavailability (Sarahdi et al., 2011), *in vivo* antiviral activity (Todt et al., 2018) and remarkably low

* Corresponding author. Philipps-Universität Marburg, Institut für Pharmazeutische Chemie, Marbacher Weg 6, 35032, Marburg, Germany.
E-mail address: arnold.gruenweller@staff.uni-marburg.de (A. Grünweller).
[1] Both authors contributed equally to this work.

https://doi.org/10.1016/j.antiviral.2020.104706
Received 26 September 2019; Received in revised form 4 January 2020; Accepted 8 January 2020
Available online 10 January 2020
0166-3542/

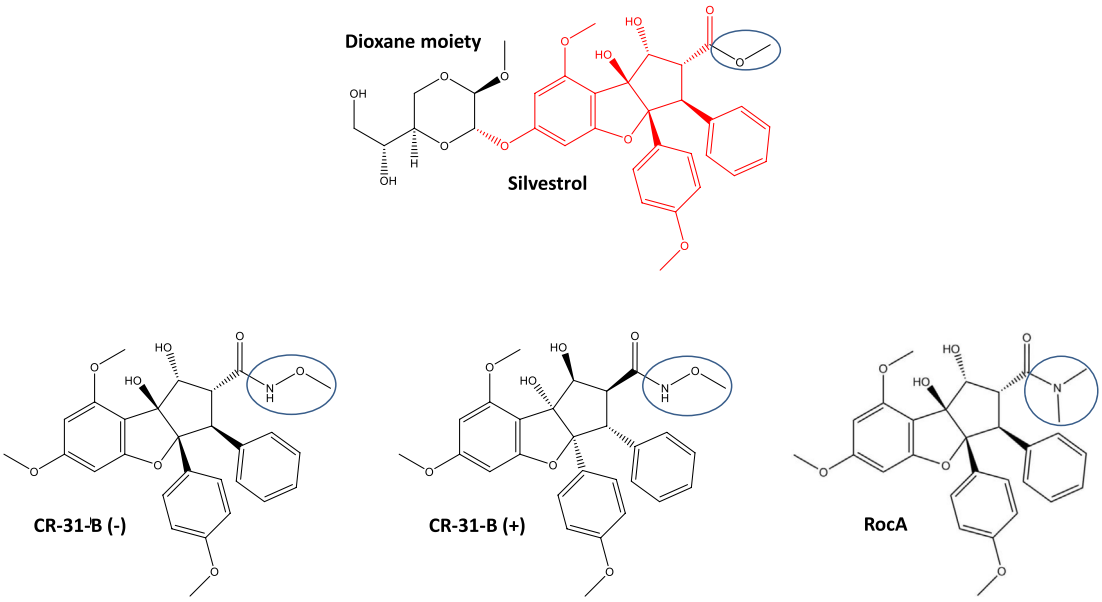

Fig. 1. Structures of the rocaglates Silvestrol, CR-31-B (−), CR-31-B (+) and RocA. The characteristic cyclopenta[b]benzofurane structure found in all rocaglates is indicated in red in the Silvestrol structure. The dioxane moiety that is only found in Silvestrol is shown on the left side in black. Blue ring: variable region in rocaglates.

cytotoxicity in primary cells, thus opening a broad therapeutic window for future applications. To date, however, chemical synthesis of Silvestrol remains difficult and alternative strategies are highly desirable. An example of a structurally less complex natural rocaglate with antiviral activity is RocA (Too et al., 2018), lacking the dioxane moiety of Silvestrol (Pan et al., 2014).

Here, we investigated the antiviral activity of the synthetic RocA analog CR-31-B (−) (Wolfe et al., 2014, Fig. 1) and compared its activity with that of Silvestrol. CR-31-B (−) showed similar antiviral activity against HCoV-229E, MERS-CoV, ZIKV, LASV, CCHFV and, to a lesser extent, HEV, thus identifying CR-31-B (−) as another rocaglate with potent broad-spectrum antiviral activity. However, we also found differential activities for these two compounds, depending on the viral 5′-UTR used for the translation inhibition assays. As shown for RocA, clamping of RNA substrates onto eIF4A by CR-31-B (−) requires polypurine sequences (Iwasaki et al., 2019), whereas Silvestrol can also clamp polypurine-free viral RNA substrates, provided that a stable hairpin structure is present. The recently published crystal structure of human eIF4A in complex with a polypurine RNA substrate and RocA (Iwasaki et al., 2019) explains the observed polypurine dependency of RocA because only purines can efficient stack on the phenyl rings of RocA. Although, further structure-based information is missing, we suggest that the dioxane moiety of Silvestrol can mediate polypurine-free RNA clamping onto eIF4A.

2. Material and methods

2.1. Cell culture

Human fetal lung fibroblasts (MRC-5), human lung carcinoma cells (A549) and murine hepatocytes (Hepa1-6 cells) were grown in Dulbecco's modified Eagle's medium (DMEM) supplemented with 10% or 5% fetal bovine serum (FBS), 100 U/ml penicillin, and 100 µg/ml streptomycin at 37 °C in an atmosphere containing 5% CO_2.

2.2. Reagents

Silvestrol was obtained from the Sarawak Biodiversity Centre (Kuching; North-Borneo, Malaysia; purity > 99%). A 6 mM stock solution was prepared in DMSO (sterile-filtered; Roth) and diluted in DMEM. Control cells were treated with corresponding DMSO dilutions lacking Silvestrol. CR-31-B (−) and CR-31-B (+) (Wolfe et al., 2014) were dissolved in DMSO at a concentration of 10 mM and stored at −20 °C.

2.3. Cell toxicity

Cell growth and viability of murine hepatocytes and MRC-5 cells in the presence of the respective compounds was determined by ATPlite assay (PerkinElmer) or the 3-(4,5-dimethylthiazol-2-yl)-2,5-diphenyl-2H-tetrazoliumbromide (MTT) method as described previously (Günther et al., 2004; Müller et al., 2018a). Cell viability of A549 cells persistently infected with HEV was determined using the PrestoBlue Cell viability reagent (Thermo Fisher Scientific) after treatment with the substances in the respective concentrations for 72 h.

2.4. Human airway epithelial cells

Cryopreserved normal human bronchial epithelial (NHBE) cells were obtained from Lonza. Undifferentiated cells were seeded on transwell plates (Corning Costar) coated with collagen IV (Invitrogen) and grown in a mixture of DMEM (Invitrogen) and BEGM (Lonza) supplemented with retinoic acid (75 nM). Fresh medium was added regularly after 2 days. After reaching confluence, the cells were cultivated under air-liquid conditions for 4 additional weeks for full differentiation into pseudostratified human airway epithelia. Medium from the basolateral compartment was renewed every 2–3 days and the apical surface was washed every week with PBS (Invitrogen).

2.5. Viruses

High-titer stocks of HCoV-229E (NCBI accession number NC_002645) and MERS-CoV (EMC/2012; NC_019843) were produced using Huh-7 cells. High-titer stocks of CCHFV strain Afg-09 2990 (Ölschläger et al., 2011) and LASV strain Ba366 (Lecompte et al., 2006) were produced in Vero E6 cells. The ZIKV strain 976 Uganda (U) was kindly provided by the European Virus Archive. Persistently HEV-infected cells (gt3c strain 47832c; GenBank ID KC618403.1) were

previously generated (Johne et al., 2014).

2.6. Antiviral activity

To determine the antiviral activity of CR-31-B and Silvestrol, MRC-5 cells or murine hepatocytes were inoculated with the respective virus at a multiplicity of infection (MOI) of 0.1 or 0.01 at 33 °C (HCoV-229E) or 37 °C (MERS-CoV, LASV, CCHFV). After 1 h, the inoculum was removed and cells were incubated with fresh medium containing the inhibitor at increasing concentrations. Supernatants were collected at 24 h post infection (hpi; HCoV-229E, MERS-CoV) or 3 dpi (LASV, CCHF) and virus titers were analyzed by virus plaque assay (Müller et al., 2018b) or immunofocus assay as described before (Günther et al., 2004). To calculate EC_{50} values, the virus titer determined for virus-infected cells treated with DMSO only was set to 100% and titers obtained for treated cells were normalized to this value. EC_{50} values were calculated by non-linear regression analysis using GraphPad Prism 6.0 (GraphPad Software).

For the infection of the primary human airway epithelial cells, the apical surface was washed 3 times with PBS and cells were infected with HCoV-229E (MOI = 3). After 1 h the inoculum was removed and the medium in the basal compartment was replaced with medium containing the indicated inhibitor concentrations. At the indicated time points, the apical surface of the cells was incubated with PBS for 15 min and virus titers in the supernatants were determined by virus plaque assay. Effects on HEV were analyzed using persistently HEV-infected A549 cells. Treatments with the compounds were started 24 h post seeding and cell culture supernatants were analyzed after 72 h via qRT-PCR.

2.7. Western blot analysis

To analyze viral protein accumulation, MRC-5 cells were infected with HCoV-229E at an MOI of 1. After inoculation, the supernatant was replaced with DMEM supplemented with antibiotics and the indicated concentrations of CR-31-B enantiomers. At 24 hpi, cell lysates were prepared and viral proteins were analyzed by Western blotting as described previously (Müller et al., 2018a).

2.8. qRT-PCR of HCoV-229E RNA or extracellular HEV RNA

MRC-5 cells were infected at an MOI of 1 and incubated for 24 h with the indicated inhibitor concentrations. Then, total cellular RNA was isolated using the RNeasy kit (Qiagen) and qRT-PCR was performed using 5 ng RNA and the Luna Universal Probe One-Step RT-qPCR Kit (NEB). Sequences of primers used to amplify genomic and total viral RNA, respectively, and GAPDH mRNA are available upon request. For the analysis of relative fold viral RNA expression in regard to inhibitor treatment the delta-delta Ct method (using GAPDH as reference) was used (Livak and Schmittgen et al., 2001). Isolation and quantification of extracellular HEV RNA was performed as described before (Glitscher et al., 2018).

2.9. Dual luciferase constructs

All constructs are based on the commercially available plasmid pFR_HCV_xb (Addgene) and were produced using PCR-based site-directed mutagenesis. Primers were designed using SnapGene 4.1.9 (GSL Biotech LLC). Primer sequences are available upon request. The respective 5′-UTRs were cloned downstream of the HSV-TK promotor directly followed by the firefly luciferase gene, an HCV IRES and the Renilla luciferase gene. The total length of the analyzed 5′-UTRs, including single-stranded and double-stranded regions, ranges from 25 bp to 292 bp ($(AG)_{15}$/$(AC)_{15}$: 30 bp; HEVgt3c: 25 bp; HEVgt3c-G4C: 25 bp; HEVgt3c-G4CC6A: 25 bp; HEVgt3c-Purine: 25 bp; HCoV-229E: 292 bp; VP30: 221 bp; VP35: 97 bp; VP35-HP only: 22 bp; VP35-HP + $(AG)_5$: 32 bp).

2.10. Dual luciferase reporter assay

The dual luciferase reporter assay was done as described previously (Müller et al., 2018a). All experiments were performed in at least three independent replicates.

3. Results

3.1. Antiviral activity of CR-31-B (−) against coronaviruses in vitro

We have recently shown that Silvestrol can efficiently inhibit viral protein synthesis in MERS-CoV- and HCoV-229E-infected MRC-5 cells (Müller et al., 2018a). Here, we investigated the antiviral potential of CR-31-B, a synthetic rocaglate lacking the dioxane moiety of Silvestrol (Fig. 1). MRC-5 cells were infected with HCoV-229E at an MOI of 1 and the effects of the CR-31-B (−)- and (+)-enantiomers on viral protein synthesis were analyzed at 24 hpi. Coronavirus nucleoprotein (N) levels were found to be strongly reduced in the presence of the (−)-enantiomer at concentrations ≥ 10 nM, while CR-31-B (+) had no detectable effect (Fig. 2A). Similarly, the genomic and subgenomic RNA levels of HCoV-229E were reduced in the presence of subnanomolar concentrations of CR-31-B (−) (Fig. 2B). In line with this, the formation of viral replication/transcription complexes was reduced in the presence of CR-31-B (−) as shown by immunofluorescence analysis using antibodies directed against nonstructural protein 8 (nsp8) and double-stranded RNA (dsRNA; Fig. S1).

Next, we analyzed the effects of CR-31-B (−) on the production of coronavirus progeny using HCoV-229E- and MERS-CoV-infected MRC-5 cells. For both viruses, CR-31-B (−) was revealed to reduce viral titers efficiently, with EC_{50} values of 2.88 nM for HCoV-229E and 1.87 nM for MERS-CoV (Fig. 2C). At a concentration of 100 nM CR-31-B (−), the MERS-CoV titer was reduced by about 5 log levels (Suppl. Fig. S2A). Cytotoxicity tests using MRC-5 cells revealed that CR-31-B (−) and CR-31-B (+) caused a slight reduction of cell viability by 10–25% and 10%, respectively, if the cells were incubated for 24 h with concentrations of up to 5 μM of the respective compound (Suppl. Fig. S2B), indicating low cytotoxicities for both compounds with selectivity indices of > 1000 (see Table 1). Even if the cells were treated for extended periods of time (48 and 72 h) using concentrations of up to 1 μM, no major cytotoxic effects were observed for CR-31-B (Fig. S2C). We further determined the CC_{50} values of a racemic mixture of CR-31-B using a range of human liver and skin carcinoma cell lines as well as primary human dermal fibroblasts (HDF). As expected, CC_{50} values in all analyzed cancer cell lines (7 liver and 3 skin carcinoma cell lines) were found to be in the low nanomolar range whereas the CC_{50} in primary HDF was calculated at ~ 500 nM (Fig. S3). Taken together, our data demonstrate low cytotoxicity of CR-31-B (−) in primary cells compared to the known cytotoxic effects in fast growing cancer cell lines.

3.2. Antiviral activity of Silvestrol and CR-31-B (−) in a human bronchial epithelial cell system

For further evaluation of the antiviral potential of Silvestrol and CR-31-B (−) in a relevant *ex vivo* system for respiratory viruses, we used 3D primary human airway epithelial cell cultures. Normal human bronchial epithelial (NHBE) cells were differentiated under air/liquid conditions to pseudostratified (columnar) epithelia. The epithelium was then infected with HCoV-229E to mimic viral infection of the different cell types in human airways in the presence of inhibitor or solvent control (Fig. 3A). At a concentration of 10 nM, CR-31-B (−) reduced the virus titer in the supernatant by about 1.5 orders of magnitude using cells from two different donors, which was similar to the antiviral effect observed for 10 nM Silvestrol in this *ex vivo* model. At 100 nM, both compounds reduced infectious virus production to undetectable

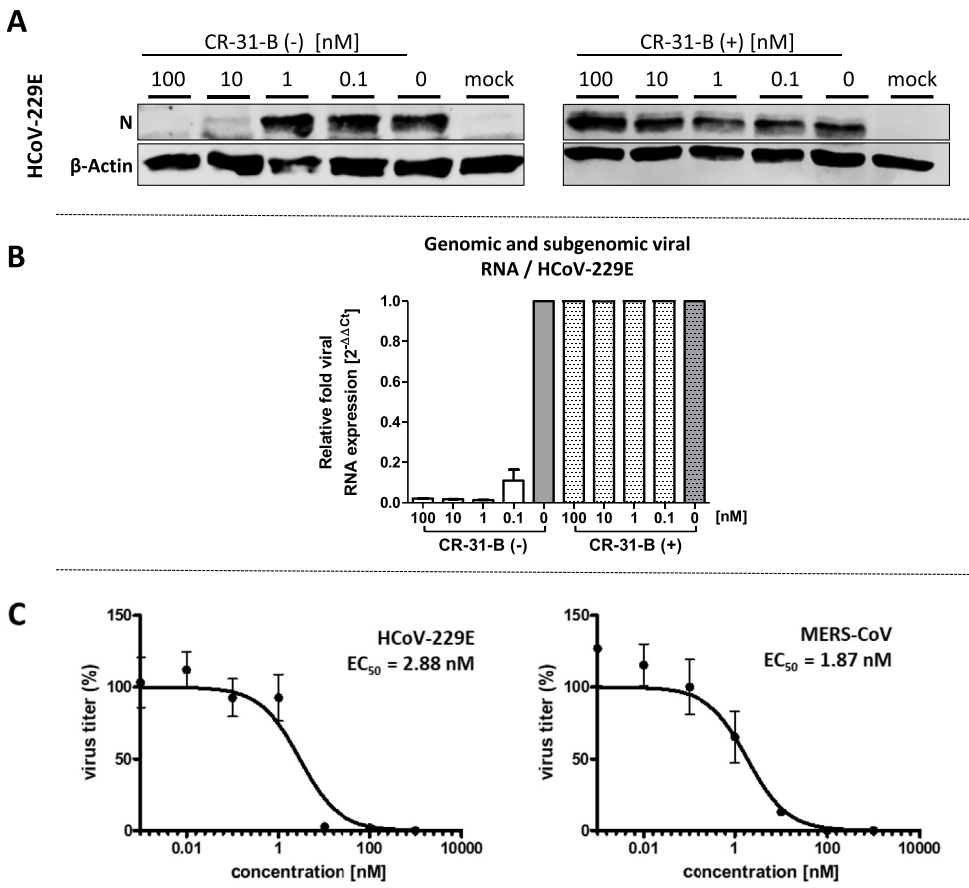

Fig. 2. Antiviral activities of the synthetic rocaglate CR-31-B (−) against HCoV-229E and MERS-CoV. **(A)** Western blot analysis of HCoV-229E N protein accumulation (top panel) in cells treated with different enantiomers of CR-31-B. β-Actin (lower panel) was used as a loading control. **(B)** Total (genomic and subgenomic) viral RNA produced in HCoV-229E-infected MRC-5 cells treated with the two enantiomers of CR-31-B. Relative changes in viral RNA levels were determined by RT-qPCR. The data were normalized to infected but untreated cells as well as GAPDH mRNA using the comparative ΔΔCt method. **(C)** HCoV-229E and MERS-CoV titers in supernatants collected from infected MRC-5 cells (MOI = 0,1) at 24 hpi. Cells were treated with CR-31-B (−/+) as indicated. Data from three independent experiments were used to calculate EC_{50} values (2.88 nM for HCoV-229E- and 1.87 nM for MERS-CoV).

levels (Fig. 3B + C), whereas 100 nM CR-31-B (+) did not significantly reduce viral replication.

3.3. Comparison of broad-spectrum antiviral activities of Silvestrol and CR-31-B (−)

We have recently shown that Silvestrol inhibits ZIKV replication in the human lung epithelial cell line A549 and in primary human hepatocytes (Elgner et al., 2018). In the present study, we found that also CR-31-B (−) causes a strong reduction of ZIKV RNA levels with a calculated EC_{50} value of 1.13 nM (Table 1; Suppl. Fig. S4). To assess potential broad-spectrum antiviral activities of CR-31-B (−) and Silvestrol against other highly pathogenic emerging viruses, we analyzed their effects in primary murine hepatocytes infected with LASV or CCHFV (Fig. 4). The data revealed that CR-31-B (−) and Silvestrol have potent antiviral activities with EC_{50} values between ~20 and 50 nM with no detectable cytotoxicity at concentrations of up to 10 μM (Fig. 4A–C). Virus titers showed a ~4-log drop for LASV- and a 3-log drop for CCHFV-infected cells (Fig. 4A,C). Furthermore, we analyzed if CR-31-B (−) inhibits HEV replication (Fig. 5). Persistently HEV-infected A549 cells were treated with different concentrations of Silvestrol and the two CR-31-B enantiomers. At 72 hpi the extracellular viral RNA levels, which correlate with released viral particles, were analyzed using quantitative RT-PCR. In line with our previous results (Glitscher et al., 2018), we confirmed the antiviral activity of Silvestrol, while the antiviral effect of CR-31-B (−) against HEV was found to be slightly weaker at the low nanomolar concentrations used in this assay (Fig. 5). However, some cytotoxicity of Silvestrol was already observed at a concentration of 2 nM whereas CR-31-B was not cytotoxic at this concentration, yet at 10 nM some cytotoxicity of CR-31-B (−) could be observed (~35% reduced viability) in persistently HEV-infected A549 cells (Fig. S5).

Table 1
CC_{50} and EC_{50} values determined for Silvestrol and CR-31-B (−)-treated cells that were mock infected (CC_{50}) or infected with the indicated viruses (EC_{50}). SI = Selectivity Index. Experiments were done in biological triplicates.

cell type	virus	compound	CC_{50} [nM]	EC_{50} [nM]	SI
MRC-5	HCoV-229E	Silvestrol	> 10000	3	> 3300
		CR-31-B (−)	> 5000	2.88	> 1736
	MERS-CoV	Silvestrol	> 10000	1.3	> 7690
		CR-31-B (−)	> 5000	1.87	> 2674
murine hepatocytes	LASV	Silvestrol	> 5000	50.73	> 99
		CR-31-B (−)	> 5000	36.11	> 139
	CCHFV	Silvestrol	> 5000	28.53	> 175
		CR-31-B (−)	> 5000	20.04	> 250
A549	ZIKV	Silvestrol	9.42	1.08	8.8
		CR-31-B (−)	19.34	1.13	17.1

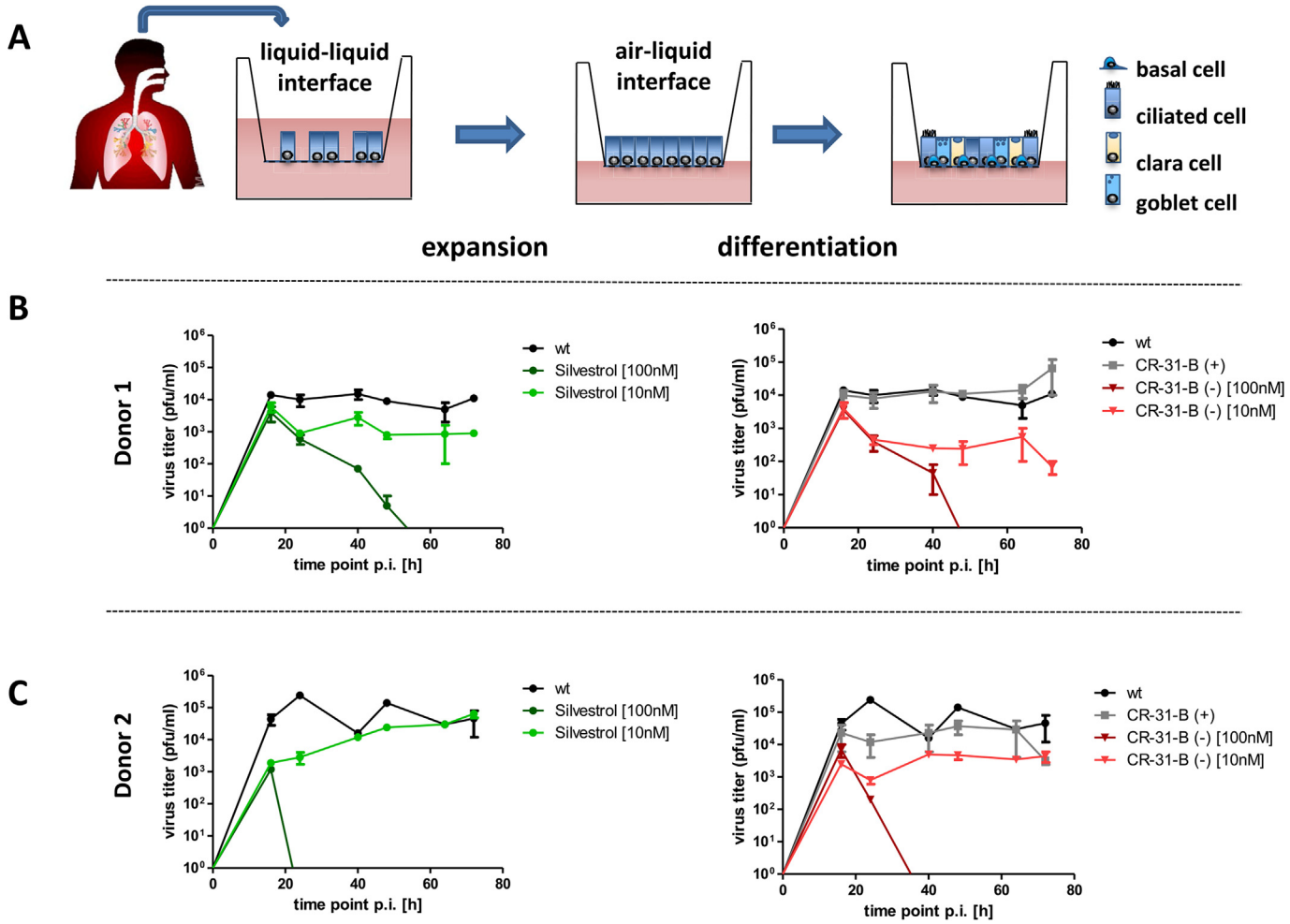

Fig. 3. Comparison of antiviral effects of CR-31-B (−) and Silvestrol using human bronchial epithelial cells infected with HCoV-229E. **(A)** Human bronchial epithelial cells were cultivated and differentiated at an air-liquid interface into different airway epithelial cell types (basal, ciliated, clara and goblet cells) und used to assess antiviral effects of the respective compounds. **(B + C)** HCoV-229E titers in cell culture supernatants collected at the indicated time points p.i. Cells obtained from two different donors were infected and treated with CR-31-B (−), Silvestrol (100/10 nM) or Cr-31-B (+) (100 nM), respectively.

3.4. Analyses of the 5′-UTR-mediated inhibitory activities of Silvestrol and CR-31-B (−)

To gain more mechanistic insights into the effects of Silvestrol and CR-31-B (−) on translation initiation and RNA clamping, we compared the inhibitory effects of the two rocaglates on different viral 5′-UTRs in a dual luciferase reporter assay (Fig. S6; Müller et al., 2018a). The 5′-UTRs of HCoV-229E, MERS-CoV and EBOV VP30 mRNA were found to be similarly sensitive to translation inhibition by Silvestrol and CR-31-B (−) (Fig. 6A). In contrast, the 5′-UTR of EBOV VP35 was insensitive to CR-31-B (−) but sensitive to Silvestrol. Interestingly, the VP30 and VP35 mRNAs both carry a likely inaccessible pentapurine stretch in their 5′-terminal stem structures (Fig. 6A). However, in the VP30 5′-UTR, this pentapurine stretch is followed by a decapurine stretch that seems to be unstructured and thus predicted to enable RNA clamping (Iwasaki et al., 2019). Such a second purine stretch is absent in the VP35 5′-UTR. The 5′-terminal hairpin of VP35 alone was sufficient to mediate translation inhibition by Silvestrol. Surprisingly, this hairpin increased the reporter activity about twofold in the presence of CR-31-B (−) (Fig. 6A, VP35-HP only). This increase was reduced back to baseline levels if an additional $(AG)_5$-polypurine stretch was inserted at the 3′-end of the VP35 hairpin. Also, this insertion resulted in a slightly increased translation inhibition by Silvestrol, indicating that polypurine sequences strengthen the inhibitory effects of rocaglates on eIF4A (Fig. 6A, VP35-HP + $(AG)_5$).

To confirm the idea of polypurines being required for stable stacking interactions with rocaglates, we constructed 5′-UTRs consisting of a 30-nt long $(AG)_{15}$ or an unstructured $(AC)_{15}$ sequence as negative control. As presumed, Silvestrol inhibited translation of the $(AG)_{15}$ construct by ~55% and CR-31-B (−) even by ~80% at concentrations of 10 nM (Fig. 6B). Remarkably, the presence of the $(AC)_{15}$ sequence caused a 1.5-fold induction of luciferase activity with both compounds (Fig. 6B), indicating that the helicase activity of eIF4A was dispensable in this case.

Interestingly, the 5′-UTR of HEV (HEVgt3c) lacks any polypurine sequence element, but it is predicted to form a stable RNA hairpin structure which, most likely, requires unwinding during translation initiation. As shown before, HEV replication can be inhibited by Silvestrol (Glitscher et al., 2018) and, to a slightly lesser extent, by CR-31-B (−) (Fig. 5). Therefore, we asked if the polypurine-free 5′-UTR of HEV is also sensitive to Silvestrol or CR-31-B (−) treatment. At a concentration of 10 nM Silvestrol, the 5′-UTR of HEV mediated reduced luciferase activity, demonstrating that Silvestrol can indeed clamp this viral RNA onto eIF4A. Importantly, this was not the case for CR-31-B (−) treatment (Fig. 6B, HEVgt3c). Moreover, this indicated that the dioxane moiety of Silvestrol may play a critical role in clamping structured RNAs onto eIF4A in a polypurine-independent manner. To test this assumption, the HEV 5′-UTR hairpin structure was thermodynamically destabilized by disrupting one or two base pairs in the stem (Fig. 6B, HEVgt3c-G4C and HEVgt3c-G4CC6A). These changes led

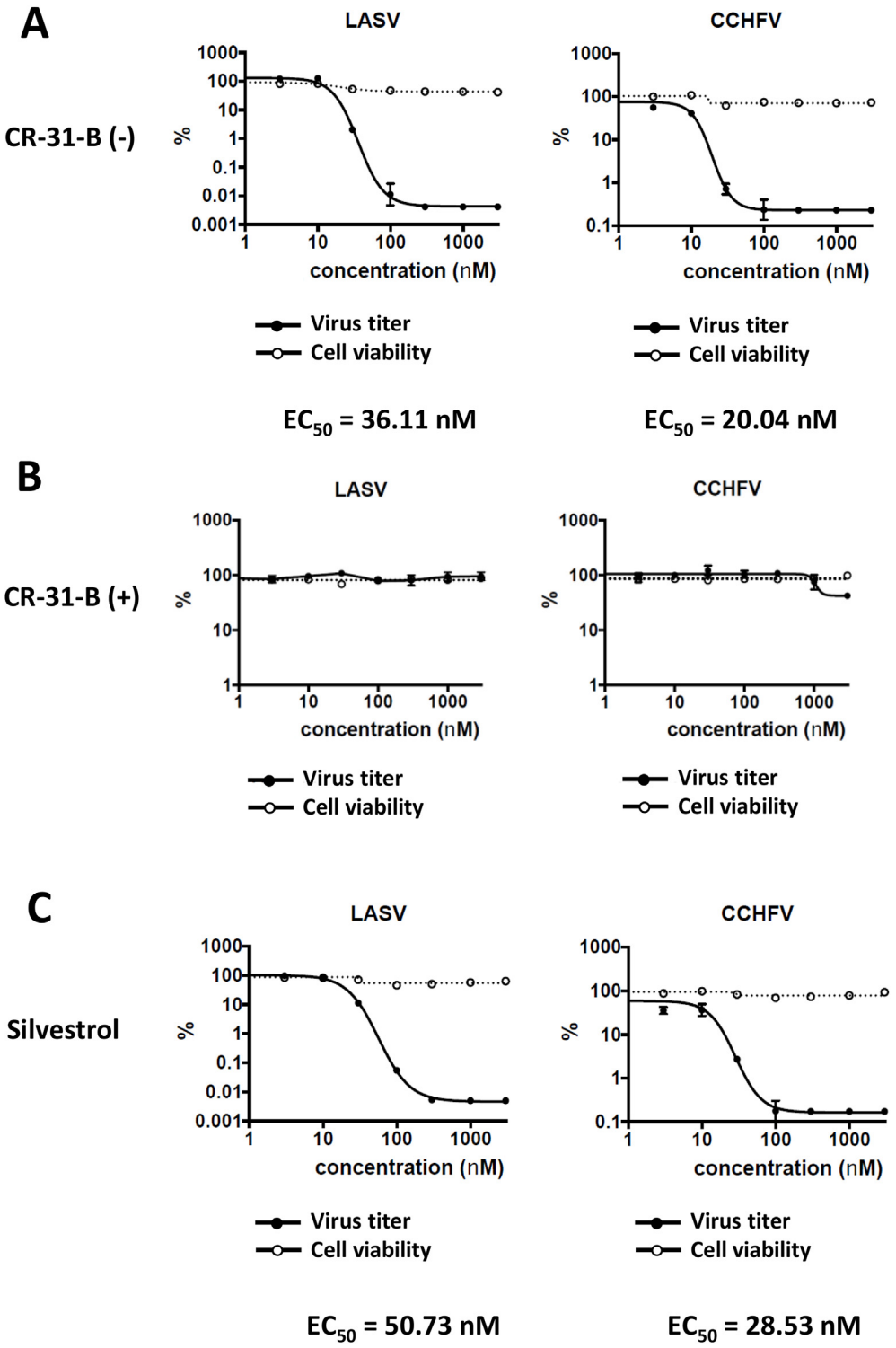

Fig. 4. CR-31-B (−) and Silvestrol inhibit LASV and CCHFV replication in primary murine hepatocytes with comparable efficiencies in a concentration range between 20 and 50 nM. **(A)** Potent antiviral activity of CR-31-B (−) against LASV and CCHFV without cytotoxicity in murine hepatocytes. **(B)** No antiviral effects of CR-31-B (+) up to a concentration of 5 μM. **(C)** Potent antiviral activity of Silvestrol against LASV and CCHFV without cytotoxicity in murine hepatocytes.

to a gradual loss of the inhibitory effect of Silvestrol. To further analyze the relevance of polypurine stretches in viral 5′-UTRs, the sequence in the HEV 5′-UTR was changed at the 5′-end from 5′-GCAGACCA… into 5′-GGAGAGGA… (Fig. 6B, HEVgt3c-Purine), thereby introducing a stretch of 8 consecutive purines. Although the thermodynamic stability of the hairpin structure was reduced by these sequence changes, the HEVgt3c-Purine 5′-UTR became now sensitive to CR-31-B (−) and Silvestrol treatment (Fig. 6B, HEVgt3c-Purine).

3.5. Modelling of Silvestrol onto the surface structure of the human eIF4A-polypurine RNA complex

Our reporter assay results indicated differences in the mode of action between Silvestrol and rocaglates lacking the dioxane moiety.

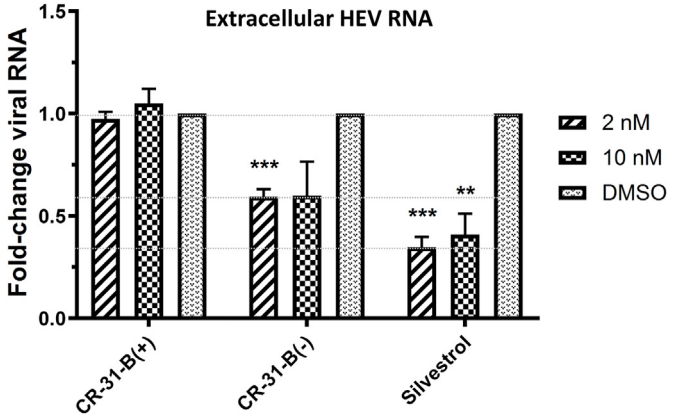

Fig. 5. CR-31-B (−) and Silvestrol reduce the levels of extracellular HEV RNA at low nanomolar concentrations. qRT-PCR measurement of extracellular HEV RNA of CR-31-B (+), CR-31-B (−) and Silvestrol treated, persistently HEV-infected cells. All data are referred to the DMSO control.

Since no structural data from co-crystallization of Silvestrol, RNA and eIF4A are available, we modeled the structure of Silvestrol into the published eIF4A-polyAG structure surface (Iwasaki et al., 2019). By comparing the localization of RocA and Silvestrol, we found that the dioxane moiety of Silvestrol can completely cross the surface of the bound RNA substrate, thus enabling Silvestrol to make additional contacts e.g. via H-bonds to arginines in eIF4A which cannot be formed in the absence of the dioxane moiety (Fig. 7). This suggests that Silvestrol is able to clamp RNA without an absolute requirement for stacking interactions with purine bases because stabilizing interactions with eIF4A at the proximal side of the bound RNA may be sufficient for locking the RNA on the helicase.

4. Discussion

We have identified the synthetic rocaglate CR-31-B (−) as a novel potent antiviral compound with broad-spectrum activity against HCoV-229E, MERS-CoV, LASV, CCHFV, HEV and ZIKV. Moreover the antiviral potential of Silvestrol and CR-31-B (−) was compared in an *ex vivo* human airway epithelial cell system under air/liquid conditions. These differentiated airway epithelial cells were used as a model for the primary airway defense barrier against inhaled pathogens, mimicking the natural situation in the infected host. This system provides a pseudostratified organization of basal, ciliated, goblet and other less common types of cells and plays a crucial role in maintaining airway homeostasis by regulating innate and acquired immunity through the production of a wide range of cytokines as well as chemokines (Davies, 2014). In this relevant *ex vivo* system, we could confirm the antiviral effect of CR-31-B (−) as well as Silvestrol against HCoV-229E replication.

CR-31-B (−) has a potent antiviral activity similar to that of the more complex-structured Silvestrol. It is active at low nanomolar concentrations with low cytotoxicity in primary human cells while it has a higher cytotoxicity in cancer cell lines (see Fig. S3). Thus, CR-31-B (−) opens a broad therapeutic window for the treatment of viral infections and qualifies as an interesting synthetic rocaglate for further *in vivo* evaluations. Even though the antiviral potential of CR-31-B (−) is similar to Silvestrol, we identified substantial mechanistic differences between the two compounds as detailed below.

RNAs generally bind to eIF4A in a sequence- and structure-independent manner via their phosphate backbone. Thus, if no RNA clamping by rocaglates occurs, active eIF4A retains its ability to unwind secondary structures in the bound substrate RNA. In our reporter assays, Silvestrol was able to clamp polypurine-free stable hairpin structures onto eIF4A, whereas CR-31-B (−) required an accessible polypurine-sequence in close proximity to the 5′-terminal hairpin. This conclusion is supported by data showing that translation of the reporter construct containing the EBOV VP35 5′-UTR is insensitive to CR-31-B (−) while it is sensitive to Silvestrol. Reduced hairpin stability correlated with a loss in Silvestrol sensitivity, suggesting that thermodynamic stability of hairpin structures is of critical importance. This is also supported by our observation that introduction of an unstructured $(AC)_{15}$ sequence rendered the reporter construct insensitive to both Silvestrol and CR-31-B (−), whereas an $(AG)_{15}$ polypurine sequence, which might be able to form a stable hairpin structure by making non-Watson-Crick G-A basepair contacts, strongly require the helicase activity of eIF4A. Remodeling the structure of Silvestrol onto the surface of the published eIF4A-RNA structure revealed that Silvestrol is in principle capable to contact eIF4A via phenylalanine (Phe163) at the lateral (Iwasaki et al., 2019) and via arginines at the proximal site of the bound substrate RNA (Fig. 7). This leads us to suggest that Silvestrol may be able to clamp any RNA sequence onto eIF4A. Our results (Fig. 6B) indicate that an unstructured sequence of sufficient length, e.g. the $(AC)_{15}$ sequence does not require the helicase activity of eIF4A to allow 43S PIC binding as a prerequisite for translation initiation, whereas a stable hairpin structure likely prevents 43S PIC binding and thus needs to be unwound.

The published crystal structure of human eIF4A in complex with a polypurine RNA substrate and RocA (Iwasaki et al., 2019) helps to explain why polypurine sequences are required to clamp RNA onto eIF4A by RocA. Stacking interactions between two phenyl rings of RocA and two consecutive purines in the substrate RNA are stable enough for RNA clamping onto eIF4A, whereas less stable interactions with pyrimidines are insufficient (Iwasaki et al., 2019). As a consequence, a stable hairpin structure without a polypurine stretch may not be bound efficiently by RocA or CR-31-B (−) due to the lack of the dioxane moiety. To date, there is no structural information on the exact binding mode of Silvestrol onto eIF4A. We therefore initiated co-crystallization studies with human eIF4A, poly-AG RNA and Silvestrol to identify the exact position of the dioxane moiety.

Surprisingly, we observed some antiviral activity of CR-31-B (−) in HEV-producing A549 cells at a non-cytotoxic concentration of 2 nM even though the compound did not inhibit reporter translation in the presence of a polypurine-free HEVgt3c 5′-UTR. We propose an indirect antiviral effect of CR-31-B (−) that could be caused by inhibition of eIF4A-dependent cellular mRNAs of unknown identity.

Importantly, the effects of CR-31-B *in vivo* are comparable to Silvestrol. In a xenograft mouse model, both compounds reduced tumor growth efficiently (Wolfe et al., 2014). CR-31-B treatment did not change body weight or the number of blood cells and no toxicity could be observed in the gastrointestinal tract of mice. Moreover, serum levels of aminotransferases (ALT and AST), albumin, total bilirubin as well as creatinine were not significantly changed two weeks after cessation of treatment, indicating that CR-31-B has a favorable toxicity profile *in vivo* (Wolfe et al., 2014). So far, no published data on the pharmacokinetic properties of CR-31-B (−) are available. It was already shown that daily intraperitoneal injection of CR-31-B (−) works well in mice (Wolfe et al., 2014; Chan et al., 2019) while the systemic availability of rocaglates following oral application seems to be limited (Saradhi et al., 2011). Based on this and our own data, we conclude that CR-31-B (−) may represent an interesting alternative to the broad-spectrum antiviral Silvestrol, which remains to be confirmed in appropriate *in vivo* studies to evaluate and compare the antiviral potential, toxicity and pharmacokinetics profiles of the two compounds.

In conclusion, our results confirm that CR-31-B (−) has potent broad-spectrum antiviral activity similar to that of Silvestrol (Table 1). Moreover, polypurine sequences in the 5′-UTR were found to be required for rocaglate-dependent clamping onto eIF4A if the dioxane moiety of Silvestrol is missing as shown for the synthetic CR-31-B (−) compound. Our data also suggest that Silvestrol retains its ability to clamp RNA substrates containing a stable hairpin structure in cases where polypurine sequences are not accessible (see the VP35 5′-UTR) or

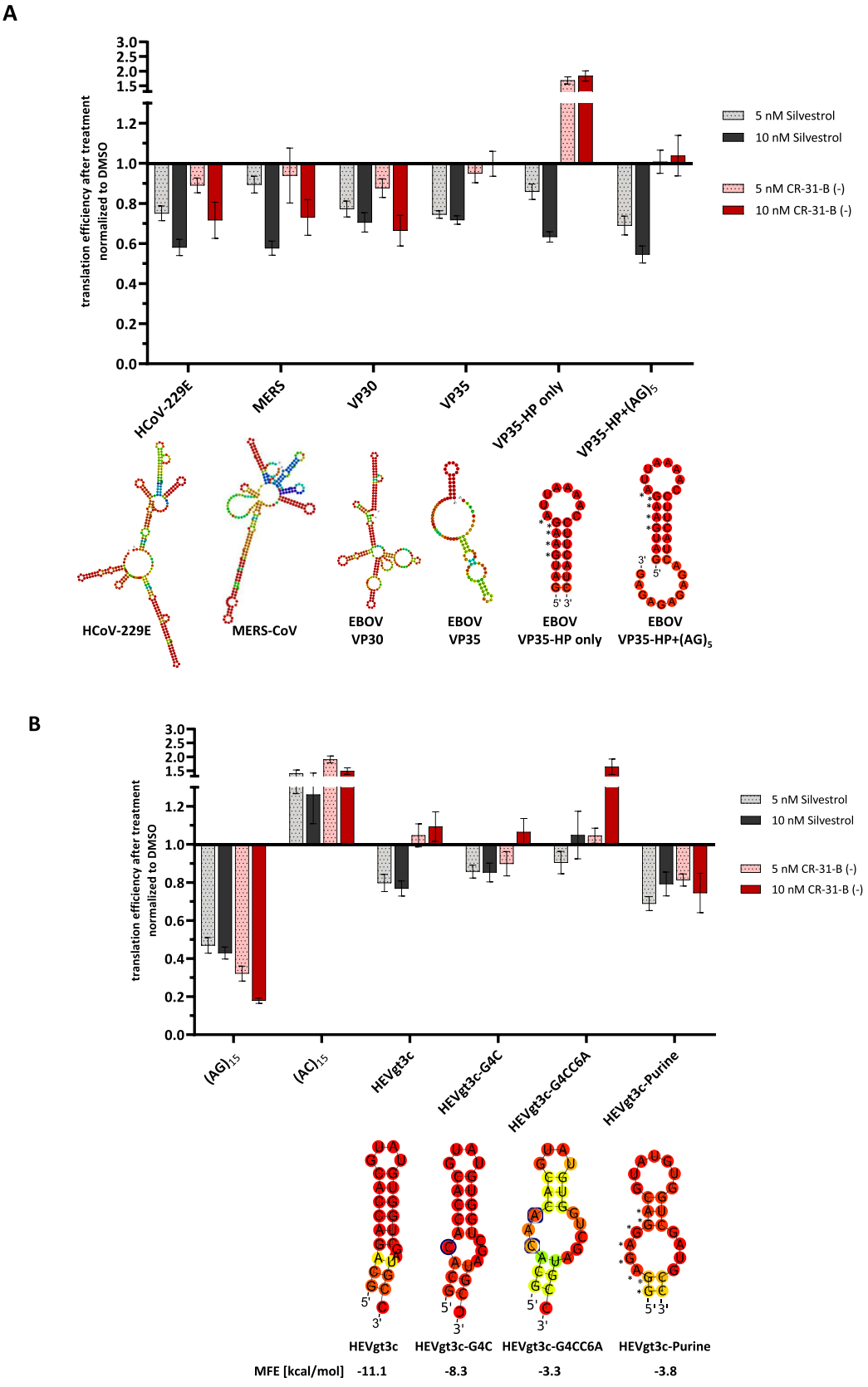

(caption on next page)

Fig. 6. Comparison of the inhibitory effects of CR-31-B (−) and Silvestrol on reporter gene expression constructs containing different viral 5′-UTRs. **(A)** Effects of 5 and 10 nM Silvestrol or CR-31-B (−) on reporter gene expression in the context of 5′-UTRs from coronaviruses HCoV-229E and MERS-CoV as well as EBOV VP30 and VP35. The VP35 5′-terminal hairpin and the VP35 hairpin with $(AG)_5$ extensions were also analyzed. The predicted RNA secondary structures of the indicated 5′-UTRs are shown. Asterisks mark the positions of purines as part of the polypurine stretch in the VP35 hairpin. **(B)** The 5′-UTR of HEV and derivatives thereof were analyzed towards their sensitivity against 5 and 10 nM Silvestrol and CR-31-B (−) treatment in a dual luciferase assay. $(AG)_{15}$ and $(AC)_{15}$ sequences were used as positive and negative controls, respectively. Predicted RNA secondary structures of the HEV 5′-UTRs are shown. The reporter gene expression data were normalized to the transfection efficiencies and the corresponding DMSO controls. Blue circles indicate the mutated nucleotides in HEVgt3c-G4C and HEVgt3c-G4CC6A. Asterisks mark the positions of purines as part of the polypurine stretch in HEVgt3c-Purine. Standard errors of the mean of at least three independent experiments are shown. MFE = minimal free energy (kcal/mol).

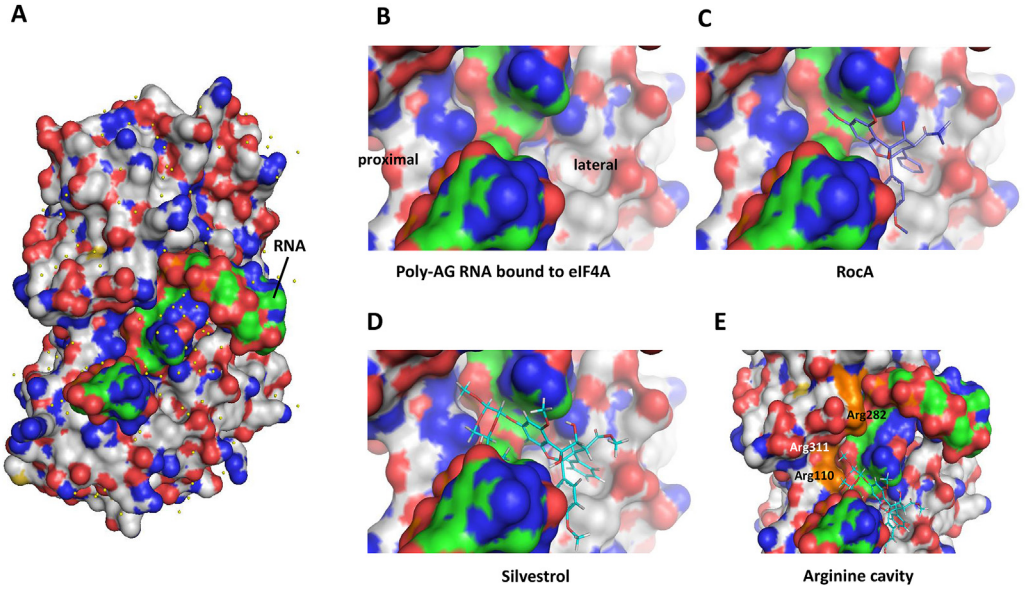

Fig. 7. Possible binding mode of Silvestrol and RNA clamping using structure-based comparative modeling of RocA or Silvestrol onto a 10-mer polyAG RNA bound to the surface of human eIF4A. **(A)** Surface of human eIF4A with a bound polyAG 10mer (adapted from Iwasaki et al., 2019). **(B-E)** Zoom in to show the binding region of RocA and Silvestrol. The dioxane moiety of Silvestrol is able to cross the RNA stretch to make additional contacts with proximal positioned arginine residues in eIF4A. Pymol was used for graphical illustration. eIF4A: grey; RNA: green; RocA: purple; Silvestrol; cyan.

absent (see the HEV 5′-UTR).

Acknowledgements

We like to thank Nadja Karl for technical assistance and Dr. Janis Müller and Dr. Serghei Glinca for their assistance in structural modeling of the human eIF4A-RNA-Silvestrol complex.

Appendix A. Supplementary data

Supplementary data to this article can be found online at https://doi.org/10.1016/j.antiviral.2020.104706.

Disclosure statement

The authors declare no conflict of interest.

Funding

The work was supported by the LOEWE Center DRUID (projects A2, B2 and D3 to A.G., J.Z. and E.H.), the German Center for Infection Research (DZIF), partner sites Giessen and Hamburg, Germany (TTU Emerging Infections, to J.Z. and L.O.), Deutsche Forschungsgemeinschaft (SFB 1021 'RNA viruses: RNA metabolism, pathogenesis and host response'; projects A01 and A02, to J.Z. and R.K.H., respectively; CRU KFO309, project P3 to J.Z.), and the Leibniz Gesellschaft (Leibniz Best Minds, to L.O.)

References

Bhat, M., Robichaud, N., Hulea, L., et al., 2015. Targeting the translation machinery in cancer. Nat. Rev. Drug Discov. 14, 261–278 (submitted for publication).
Biedenkopf, N., Lange-Grünweller, K., Schulte, F.W., et al., 2017. The natural compound silvestrol is a potent inhibitor of Ebola virus replication. Antivir. Res. 137, 76–81.
Chan, K., Robert, F., Oertlin, C., et al., 2019. eIF4A supports an oncogenic translation program in pancreatic ductal adenocarcinoma. Nat. Commun. 10, 5151.
Davies, D.E., 2014. Epithelial barrier function and immunity in asthma. Ann. Am. Thorac. Soc. 11 (Suppl. 5), S244–S251 (submitted for publication).
Elgner, F., Sabino, C., Basic, M., et al., 2018. Inhibition of Zika virus replication by silvestrol. pii. Viruses 10, E149.
Glitscher, M., Himmelsbach, K., Woytinek, K., et al., 2018. Inhibition of hepatitis E virus spread by the natural compound silvestrol. pii. Viruses 10, E301.
Günther, S., Asper, M., Röser, C., et al., 2004. Application of real-time PCR for testing antiviral compounds against Lassa virus, SARS coronavirus and Ebola virus in vitro. Antivir. Res. 63, 209–215.
Henss, L., Scholz, T., Grünweller, A., Schnierle, B.S., 2018. Silvestrol inhibits Chikungunya virus replication. pii. Viruses 10, E592.
Iwasaki, S., Iwasaki, W., Takahashi, M., et al., 2019. The translation inhibitor rocaglamide targets a bimolecular cavity between eIF4A and polypurine RNA. Mol. Cell 73, 738–748 e9.
Johne, R., Reetz, J., Ulrich, R.G., et al., 2014. An ORF1-rearranged hepatitis E virus derived from a chronically infected patient efficiently replicates in cell culture. J. Viral Hepat. 21, 447–456.
Lecompte, E., Fichet-Calvet, E., Daffis, S., et al., 2006. Mastomys natalensis and Lassa fever, west Africa. Emerg. Infect. Dis. 12, 1971–1974.
Livak, K.J., Schmittgen, T.D., 2001. Analysis of relative gene expression data using real-time quantitative PCR and the 2(-Delta Delta C(T)) Method. Methods 25, 402–408.
Madhugiri, R., Fricke, M., Marz, M., Ziebuhr, J., 2016. Coronavirus cis-acting RNA elements. Adv. Virus Res. 96, 127–163 (submitted for publication).
Müller, C., Schulte, F.W., Lange-Grünweller, K., et al., 2018a. Broad-spectrum antiviral activity of the eIF4A inhibitor silvestrol against corona- and picornaviruses. Antivir. Res. 150, 123–129.
Müller, C., Hardt, M., Schwudke, D., et al., 2018b. Inhibition of cytosolic phospholipase A2α impairs an early step of coronavirus replication in cell culture. J. Virol. 92 pii: e01463-17.
Ölschläger, S., Gabriel, M., Schmidt-Chanasit, J., et al., 2011. Complete sequence and phylogenetic characterisation of Crimean-Congo hemorrhagic fever virus from Afghanistan. J. Clin. Virol. 50, 90–92.
Pan, L., Woodard, J.L., Lucas, D.M., et al., 2014. Rocaglamide, silvestrol and structurally related bioactive compounds from Aglaia species. Nat. Prod. Rep. 31, 924–939 (submitted for publication).
Rubio, C.A., Weisburd, B., Holderfield, M., et al., 2014. Transcriptome-wide characterization of the eIF4A signature highlights plasticity in translation regulation. Genome Biol. 15 (10), 476.
Saradhi, U.V., Gupta, S.V., Chiu, M., et al., 2011. Characterization of silvestrol pharmacokinetics in mice using liquid chromatography-tandem mass spectrometry. AAPS J. 13, 347–356.

Schlereth, J., Grünweller, A., Biedenkopf, N., et al., 2016. RNA binding specificity of Ebola virus transcription factor VP30. RNA Biol. 13, 783–798.
Todt, D., Moeller, N., Praditya, D., et al., 2018. The natural compound silvestrol inhibits hepatitis E virus (HEV) replication in vitro and in vivo. Antivir. Res. 157, 151–158.
Too, I.H.K., Bonne, I., Tan, E.L., et al., 2018. Prohibitin plays a critical role in Enterovirus 71 neuropathogenesis. PLoS Pathog. 14 e1006778.
Wolfe, A.L., Singh, K., Zhong, Y., et al., 2014. RNA G-quadruplexes cause eIF4A-dependent oncogene translation in cancer. Nature 513, 65–70.

Antiviral Research 186 (2021) 105012

Contents lists available at ScienceDirect

Antiviral Research

journal homepage: www.elsevier.com/locate/antiviral

The rocaglate CR-31-B (−) inhibits SARS-CoV-2 replication at non-cytotoxic, low nanomolar concentrations *in vitro* and *ex vivo*

Christin Müller [a,c], Wiebke Obermann [b], Nadja Karl [a], Hans-Guido Wendel [d], Gaspar Taroncher-Oldenburg [e], Stephan Pleschka [a,c], Roland K. Hartmann [b], Arnold Grünweller [b,*], John Ziebuhr [a,c]

[a] Institute of Medical Virology, Justus Liebig University Giessen, Schubertstrasse 81, 35392, Giessen, Germany
[b] Institute of Pharmaceutical Chemistry, Philipps University Marburg, Marbacher Weg 6, 35032, Marburg, Germany
[c] German Center for Infection Research (DZIF) at the Partner Site Giessen-Marburg-Langen, Germany
[d] Cancer Biology and Genetics Program, Memorial Sloan Kettering Cancer Center, New York, NY, 10023, USA
[e] Gaspar Taroncher Consulting, Philadelphia, PA, 19119, USA

ARTICLE INFO

Keywords:
Rocaglate
SARS-CoV-2
COVID-19
Antiviral activity
eIF4A
Translation initiation

ABSTRACT

Severe acute respiratory syndrome coronavirus 2 (SARS-CoV-2) is the causative agent of COVID-19, a severe respiratory disease with varying clinical presentations and outcomes, and responsible for a major pandemic that started in early 2020. With no vaccines or effective antiviral treatments available, the quest for novel therapeutic solutions remains an urgent priority. Rocaglates, a class of plant-derived cyclopenta[*b*]benzofurans, exhibit broad-spectrum antiviral activity against multiple RNA viruses including coronaviruses. Specifically, rocaglates inhibit eukaryotic initiation factor 4A (eIF4A)-dependent mRNA translation initiation, resulting in strongly reduced viral RNA translation. Here, we assessed the antiviral activity of the synthetic rocaglate CR-31-B (−) against SARS-CoV-2 using both *in vitro* and *ex vivo* cell culture models. In Vero E6 cells, CR-31-B (−) inhibited SARS-CoV-2 replication with an EC_{50} of ~1.8 nM. In primary human airway epithelial cells, CR-31-B (−) reduced viral titers to undetectable levels at a concentration of 100 nM. Reduced virus reproduction was accompanied by substantially reduced viral protein accumulation and replication/transcription complex formation. The data reveal a potent anti-SARS-CoV-2 activity by CR-31-B (−), corroborating previous results obtained for other coronaviruses and supporting the idea that rocaglates may be used in first-line antiviral intervention strategies against novel and emerging RNA virus outbreaks.

Severe acute respiratory syndrome coronavirus 2 (SARS-CoV-2), a member of the genus *Betacoronavirus* (Gorbalenya et al., 2020), causes a potentially severe respiratory illness, coronavirus disease 2019 (COVID-19), with case fatality rates ranging from 0.5% to 1% according to recent estimates (Rajgor et al., 2020; Meyerowitz-Katz and Merone, 2020). Following its rapid global spread, the World Health Organization declared COVID-19 a pandemic in March 2020 (WHO, 2020). To date, no approved therapeutic is available against any human coronavirus but a number of investigational antiviral compounds that target viral functions have entered clinical trials (Brown et al., 2019; de Wit et al., 2020; Sheahan et al., 2017; de Wilde et al., 2014; Choy et al., 2020; Sanders et al., 2020). Moreover, compounds that modulate the human immune system and/or have an anti-inflammatory effect are also being tested for their potential to reduce the severity of COVID-19 progression (Oldenburg and Doan, 2020; Guaraldi et al., 2020; Jalkanen et al., 2020; Lucas et al., 2009). Finally, antivirals that target host mechanisms critical to viral replication are being developed, including inhibitors targeting host proteases required to activate the fusogenic activity of the SARS-CoV-2 spike protein (Bestle et al., 2020; Hoffmann et al., 2020).

We and others have focused on approaches that inhibit viral protein synthesis, another host function critical to viral proliferation. Incidentally, a recently published SARS-CoV-2 protein interaction map identified the host translational machinery as a top target for repurposing drugs to block SARS-CoV-2 (Gordon et al., 2020). In particular, two eukaryotic factors involved in the initiation phase of translation, eukaryotic initiation factor-1A (eIF1A) and eukaryotic initiation factor-4A (eIF4A), have been singled out for further development. eIF1A is a small protein that binds to the 40S ribosome subunit-mRNA complex

* Corresponding author.
E-mail address: gruenwel@staff.uni-marburg.de (A. Grünweller).

https://doi.org/10.1016/j.antiviral.2021.105012
Received 5 October 2020; Received in revised form 28 December 2020; Accepted 4 January 2021
Available online 8 January 2021

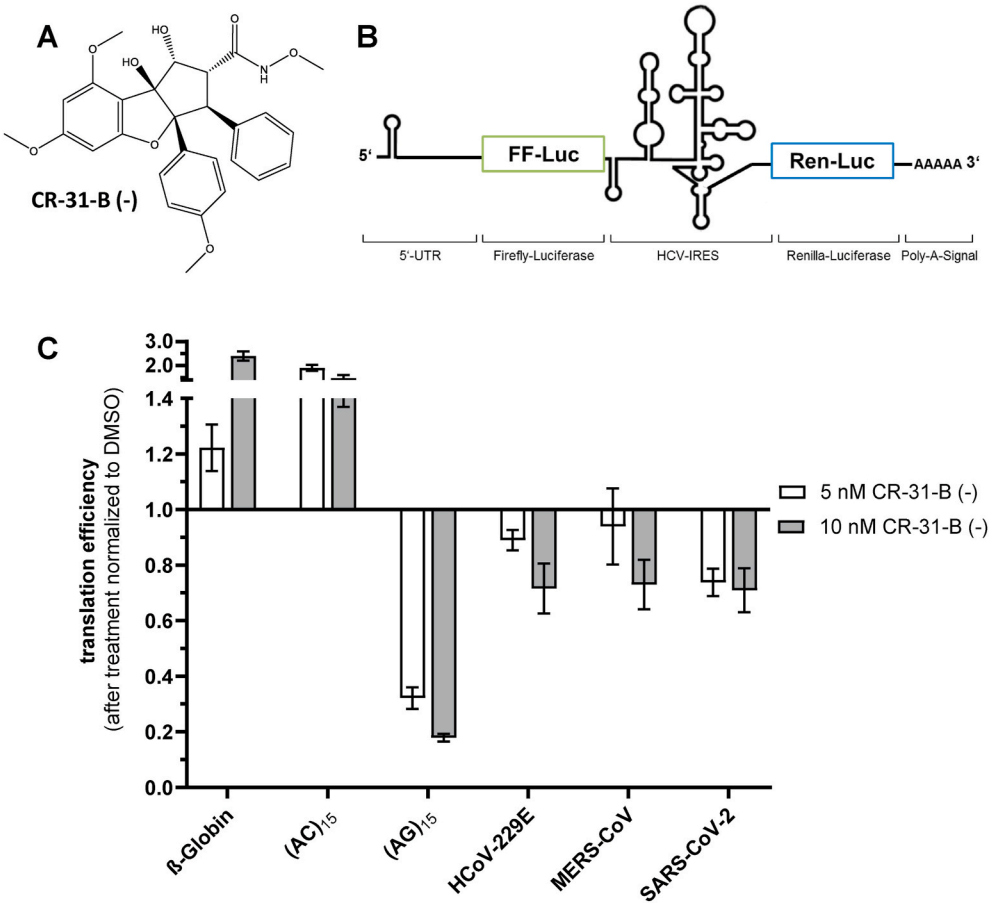

Fig. 1. Effect of CR-31-B (−) on dual reporter gene expression from constructs containing different 5′-UTRs. **(A)** Structure of the synthetic rocaglate CR-31-B (−). **(B)** Schematic illustration of the dual luciferase reporter construct used to determine eIF4A-dependent translation of coronavirus 5′-UTRs. **(C)** Effects of 5 and 10 nM CR-31-B (−) on reporter gene expression in the context of 5′-UTRs from three human coronaviruses, HCoV-229E, MERS-CoV and SARS-CoV-2. The 5′-UTR of the human β-globin mRNA and the unstructured $(AC)_{15}$ sequence served as negative controls, while the $(AG)_{15}$ polypurine sequence served as a positive control. Experiments were performed using previously described protocols (Müller et al., 2018a, 2020) with at least three independent biological replicates.

(Passmore et al., 2007), and eIF4A is a DEAD-box RNA helicase central to the activity of the eukaryotic translation initiation complex eIF4F (Chu and Pelletier, 2015). As of this writing, the eIF1A inhibitor aplidin (PharmaMar) has entered a Phase 2 clinical trial for the treatment of COVID-19, and the eIF4A inhibitor zotatifin (eFFECTOR Therapeutics) is undergoing evaluation for potential COVID-19 clinical development (Harrison, 2020; Bronstrup and Sasse, 2020).

We recently demonstrated the antiviral potency of rocaglates, a class of natural and synthetic compounds, against MERS-CoV and the common cold human coronavirus HCoV-229E *in vitro* and *ex vivo* (Müller et al., 2018a, 2020). Natural (e.g. rocaglamide A, silvestrol) and synthetic rocaglates (CR-31-B (−), zotatifin) are highly specific nanomolar eIF4A inhibitors. Rocaglates form stacking interactions with polypurine sequences in the 5′-untranslated regions (UTRs) of capped mRNAs, clamping the mRNAs onto eIF4A and stalling mRNA unwinding, which results in a dissociation of the mRNA-eIF4A complex from eIF4E and eIF4G. Because eIF4A-mediated translation is key to the activation of a majority of oncogenes, several of these selective rocaglates are in preclinical cancer studies and at least one compound, zotatifin, has been advanced into early stage clinical studies (Bordeleau et al., 2008; Lucas et al., 2009; Kogure et al., 2013; Patton et al., 2015; Ernst et al., 2020).

Many viral RNAs contain 5′-UTRs with stable RNA structures (Madhugiri et al., 2016; Schlereth et al., 2016) and are thus dependent on eIF4A for translation. Silvestrol exhibits broad-spectrum antiviral activity against a range of RNA viruses such as Ebola virus, Zika virus, Chikungunya virus, Crimean Congo hemorrhagic fever virus, Lassa virus, hepatitis E and several coronaviruses (Biedenkopf et al., 2017; Elgner et al., 2018; Henss et al., 2018; Müller et al., 2018a, 2020; Glitscher et al., 2018; Todt et al., 2018). While silvestrol and other natural rocaglates represent promising therapeutic leads due to their activities in the low nanomolar range and high selectivity indices (≥100) in primary cells, their natural availability is limited (Pannell, 1998) and their chemical synthesis is challenging due to their complex structures (Adams et al., 2009; Pan et al., 2014). As an alternative, a variety of synthetic rocaglate analogs have been generated that exhibit similar or enhanced eIF4A-targeting characteristics and can be produced to high purity and in large quantities.

Recently, we compared the antiviral activity of silvestrol with that of CR-31-B (−), which lacks the dioxane moiety of silvestrol and makes it structurally less complex and more straightforward to synthesize (Wolfe et al., 2014). We were able to show that, similar to silvestrol, CR-31-B (−) inhibits the replication of a range of RNA viruses both *in vitro* and *ex vivo* (Müller et al., 2020). Here, we evaluated the potential activity of the synthetic rocaglate CR-31-B (−) against SARS-CoV-2 using both *in vitro* and human *ex vivo* cell culture systems.

In a first set of experiments, we analyzed potential inhibitory effects of CR-31-B (−) (Fig. 1A) on 5′-UTRs of different coronaviruses including SARS-CoV-2 in a dual luciferase reporter assay (Fig. 1B) to assess whether translation of mRNAs containing these viral 5′-UTRs depends on eIF4A. Cap-dependent translation of the firefly luciferase gene was measured and transfection efficiencies were normalized to renilla luciferase expression, which is under control of an eIF4A-independent IRES element from HCV. The short and unstructured 5′-UTR of the beta-globin gene and an unstructured $(AC)_{15}$ sequence served as negative controls, since these 5′-UTR sequences were shown to be not repressible upon inhibition of eIF4A (Müller et al., 2018a, 2020). The polypurine sequence $(AG)_{15}$ was used as a positive control since this sequence can be efficiently clamped onto the surface of eIF4A by different rocaglates due to π-π stacking interactions (Iwasaki et al., 2019; Müller et al., 2020). Using this experimental setup, eIF4A-dependency can be inferred from sensitivity of firefly luciferase mRNA translation to the presence of a specific eIF4A inhibitor. The data revealed that the

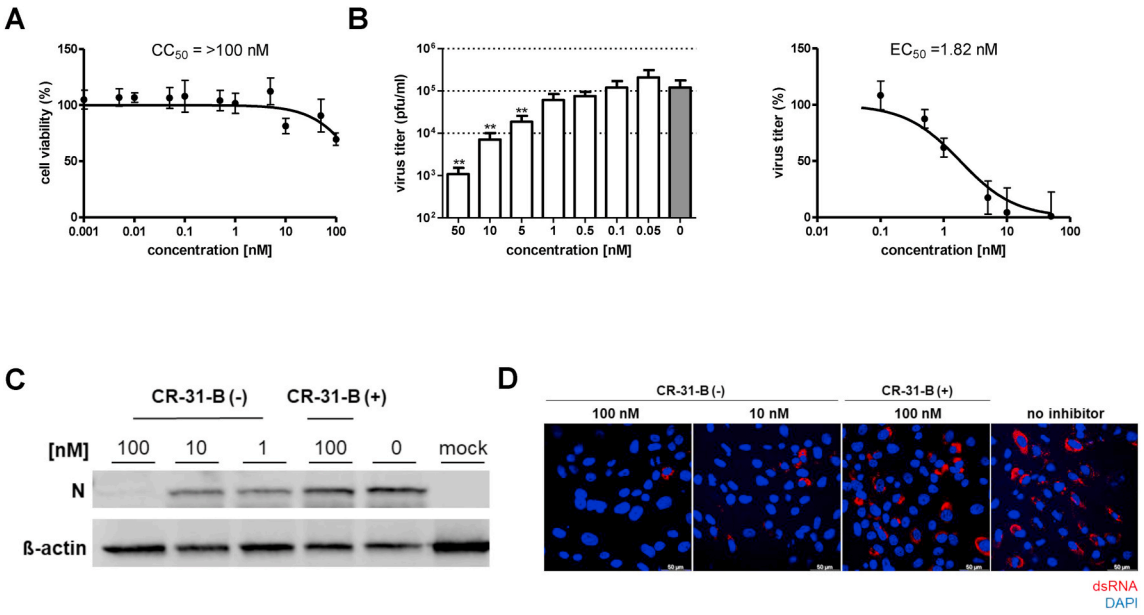

Fig. 2. Dose-dependent antiviral activity of the synthetic rocaglate CR-31-B (−) in SARS-CoV-2 infected Vero E6 cells. **(A)** Vero E6 cells were treated for 24 h with the indicated CR-31-B (−) concentrations. Cell viability (compared to that of untreated cells) was determined by MTT assay (n = 8) as described previously (Müller et al., 2018a). **(B)** SARS-CoV-2 titers in supernatants collected from infected Vero E6 cells (MOI = 0.1) treated with the indicated CR-31-B (−) concentrations were collected at 24 h p.i. (n = 6) and virus titers were determined by plaque assay. Significance levels compared to the results for untreated cells were determined by the two-tailed Mann Whitney *U* test and are indicated as follows: *, $P < 0.05$; **, $P < 0.005$. Data from six independent experiments were used to calculate the EC_{50} value by non-linear regression analysis. **(C)** Representative Western blot analysis of SARS-CoV-2 N protein accumulation (top panel) after treatment with CR-31-B (−) and CR-31-B (+). Vero E6 cells were infected with SARS-CoV-2 (MOI = 1) or left uninfected and treated with the indicated CR-31-B concentrations for 24 h p.i. Protein accumulation was analyzed by Western blotting using polyclonal rabbit anti-SARS nucleocapsid protein antibody (Rockland) and mouse-anti actin antibody (abcam), respectively, each diluted 1:500 in PBS containing 1% bovine serum albumin (BSA). Beta-actin (lower panel) was used as a loading control (n = 3). **(D)** Representative immunofluorescence analysis to determine the effects of CR-31-B (+) and CR-31-B (−) on viral dsRNA accumulation in SARS-CoV-2-infected Vero E6 cells. Cells were infected (MOI = 1) and cultivated in medium containing the indicated CR-31-B concentrations. Cells were fixed at 24 h p.i. and analyzed by confocal microscopy using a mouse anti-dsRNA mAb (J2, SCICONS English & Scientific Consulting Kft, red) that detects a viral RNA replication intermediate (red) (Müller et al., 2018b). Cell nuclei were stained with DAPI (blue) (n = 2). (For interpretation of the references to colour in this figure legend, the reader is referred to the web version of this article.)

5′-UTRs of SARS-CoV-2, HCoV-229E and MERS-CoV were similarly sensitive to eIF4A-dependent translation inhibition by CR-31-B (−) in the dual luciferase reporter assay, when 10 nM CR-31-B (−) was used (Fig. 1C), indicating that CR-31-B (−) may have also antiviral activity against SARS-CoV-2.

To analyze possible antiviral effects of CR-31-B (−) in cell culture, African green monkey Vero E6 cells were used (Ogando et al., 2020). No major cytotoxicity was detected for concentrations of up to 100 nM, with cell viability being reduced by about 10–25% at this highest concentration tested (Fig. 2A). Moreover, the production of infectious SARS-CoV-2 progeny was found to be reduced in a dose-dependent manner with an EC_{50} of ~1.8 nM (Fig. 2B), which is in a similar range as the CR-31-B (−) EC_{50} values reported previously for other coronaviruses (~2.9 nM for HCoV-229E; ~1.9 nM for MERS-CoV) (Müller et al., 2020). The selectivity index (CC_{50}/EC_{50}) for SARS-CoV-2-infected Vero E6 cells was determined to be > 50. Next, we analyzed the effect of

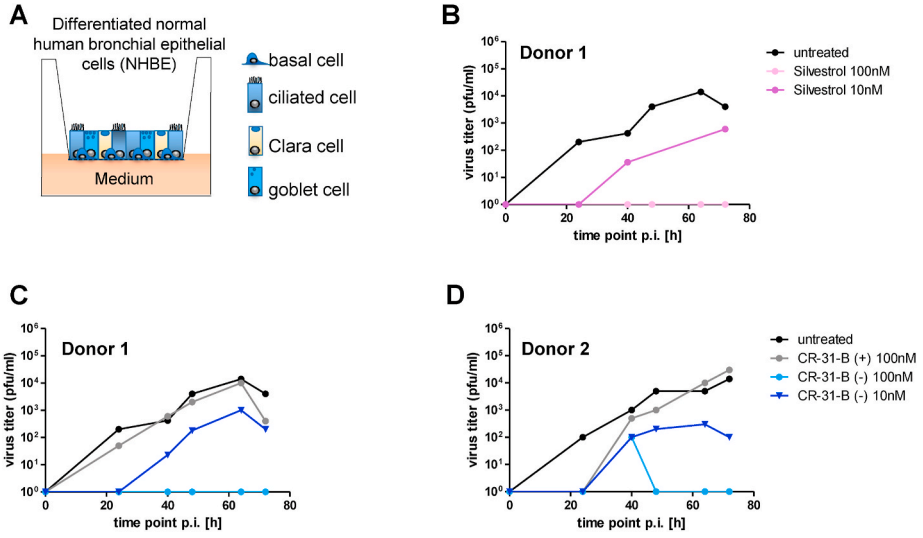

Fig. 3. Comparison of antiviral effects of CR-31-B (−) and silvestrol using differentiated NHBE cells infected with SARS-CoV-2. **(A)** NHBE cells (Lonza, CC-2540) obtained from a 13-year-old Caucasian boy (Donor 1) and a 36-year-old Caucasian man (Donor 2), which both were non-smoking and lacking respiratory pathology, were seeded on collagen IV-coated transwell plates (Corning Costar, CLS3470-48 EA) and grown in a mixture of DMEM (Invitrogen) and BEGM (Lonza; CC-4175) supplemented with retinoic acid (75 nM). After reaching confluence, the cells were cultivated under air-liquid conditions for at least four additional weeks to allow differentiation into pseudostratified human airway epithelia. **(B and C)** Differentiated NHBE cells were infected with SARS-CoV-2 (MOI = 3) and treated with silvestrol **(B)**, CR-31-B (−) or CR-31-B (+) **(C)** at the indicated concentrations. At the indicated time points p.i., the apical surface of the cells was incubated with 100 µl PBS for 15 min and SARS-CoV-2 titers in the cell culture supernatants were determined by virus plaque assay.

CR-31-B (−) on SARS-CoV-2 protein accumulation and the formation of viral replication/transcription complexes in Vero E6 cells. Viral nucleocapsid (N) protein levels were found to be drastically reduced in the presence of 100 nM CR-31-B (−), and moderately reduced at concentrations of 10 or 1 nM (Fig. 2C). As expected, viral protein accumulation was not affected in the presence of 100 nM of the inactive (+)-enantiomer CR-31-B (+) nor was it affected in cells treated with solvent only. In line with this, the formation of SARS-CoV-2 replication/transcription complexes was impaired in infected cells treated with CR-31-B (−) (Fig. 2D).

To further evaluate the antiviral potential of CR-31-B (−) in a biologically relevant *ex vivo* respiratory cell culture system, we analyzed air/liquid interface (ALI) cultures of differentiated primary normal human bronchial epithelial (NHBE) cells obtained from two different donors. ALI cultures are increasingly recognized as an excellent culture model mimicking the tracheobronchial region of the human respiratory tract and thus enabling respiratory infection research in a physiologically relevant cellular environment (Jonsdottir and Dijkman, 2016). Differentiated NHBE cells (Fig. 3A) were infected with SARS-CoV-2 in the presence of inhibitor, CR-31-B (−) or silvestrol (obtained from the Sarawak Biodiversity Center, Kuching; North-Borneo, Malaysia; purity > 99%), the inactive enantiomer CR-31-B (+) or solvent control (untreated). Silvestrol was included as a reference in this experiment because this rocaglate has previously been tested extensively against a broad range of viruses. Silvestrol treatment reduced SARS-CoV-2 titers at different time points p.i. about 10 to 100-fold when used at a concentration of 10 nM, while virus replication in NHBE cells was completely abolished at a concentration of 100 nM (Fig. 3B). Next, we analyzed the effects of CR-31-B on viral replication in NHBE cells. CR-31-B (−) reduced the production of infectious virus progeny by ~1.5 log steps at a concentration of 10 nM in differentiated NHBE cells obtained from two different donors. At 100 nM, CR-31-B (−) reduced SARS-CoV-2 titers to undetectable levels, whereas the enantiomer CR-31-B (+) did not affect viral replication compared to the solvent control (Fig. 3C and D). No obvious cytotoxicity could be observed at this concentration using light microscopy.

The discovery and development of antivirals that target host mechanisms critical to viral proliferation is of growing importance. The rationale behind this approach is twofold: first, host mechanisms are not virus-specific, but are used by a broad range of viruses, and second, targeting a host mechanism preempts the risk for developing resistance typically associated with targeting viral structures or mechanisms. Several host-targeting approaches against SARS-CoV-2 are currently under investigation. Most of these represent efforts to repurpose approved drugs with known safety profiles.

Here, we added to the antiviral toolbox against SARS-CoV-2 the synthetic rocaglate CR-31-B (−), a specific inhibitor of eIF4A-dependent mRNA translation. We identified CR-31-B (−) as a potent and non-cytotoxic inhibitor of SARS-CoV-2 replication *in vitro* and *ex vivo*. The observed antiviral activities are directly comparable to those that we reported previously for other coronaviruses, namely HCoV-229E and MERS-CoV, and a range of highly pathogenic positive- and negative-sense RNA viruses. To our knowledge, this is the first report of a rocaglate inhibiting SARS-CoV-2 proliferation in a relevant *ex vivo* human bronchial cell system.

Against the backdrop of a number of reports we and others have published over the past three years documenting the broad-spectrum antiviral activity of CR-31-B (−) and related rocaglates, the data we report here strengthen the case for the potential use of rocaglates as first-line, broad-spectrum 'pan-antivirals'. The necessary next step is the *in vivo* evaluation of CR-31-B (−) and other rocaglates to confirm safety and determine appropriate dosing regimens. Extensive preclinical work with CR-31-B (−), zotatifin, and other rocaglates as cancer therapeutics is *a priori* highly encouraging for the potential antiviral application of rocaglates in humans. Minimal or no toxicities were reported for long-term dosing regimens in animal models, along with favorable safety, ADME- and bioavailability profiles (Wolfe et al., 2014; Chan et al., 2019; Rodrigo et al., 2012). In addition, the advancement of zotatifin into the clinic supports the potential of this class of molecules to be used as antivirals in humans.

In summary, the path to clinical implementation is still long and will most likely require further optimization of CR-31-B (−) or other lead rocaglates currently under investigation. Nevertheless, the antiviral efficacy against viruses from diverse families, the low toxicity of this class of compounds both *in vitro* and *ex vivo*, and the ongoing advanced efforts to harness their activity as cancer therapeutics lead us to suggest that rocaglates represent a potentially powerful addition to the toolbox of therapeutic options for mitigating the consequences of global outbreaks by newly emerging RNA viruses.

Funding

The work was supported by the LOEWE Center DRUID (projects A2 and B2 to A.G. and J.Z.), the German Center for Infection Research (DZIF), partner site Giessen-Marburg-Langen (TTU Emerging Infections, to J.Z. and S.P.), Deutsche Forschungsgemeinschaft (SFB 1021 'RNA viruses: RNA metabolism, pathogenesis and host response'; projects A01 and A02, to J.Z. and R.K.H., respectively and project C01 to S.P.; CRU KFO309, project P3 to J.Z.), and the BMBF project HELIATAR (A.G. and J.Z). Further support to H.G.W. were from the NCI Cancer Center Support Grant to MSKCC (CCSG, P30 CA08748), the Starr Cancer Consortium (GC230724) and from NIH grants RO1CA183876-05, RO1CA207217–03, R35 CA252982-01, P50 CA192937-03, P50 CA217694), LLS 7014-17, LLS 1318-15.

Declaration of competing interest

The authors declare that they have no known competing financial interests or personal relationships that could have appeared to influence the work reported in this paper.

Acknowledgements

We thank Ulrike Wend for her excellent technical assistance.

References

Adams, T.E., El Sous, M., Hawkins, B.C., et al., 2009. Total synthesis of the potent anticancer Aglaia metabolites (-)-silvestrol and (-)-episilvestrol and the actice analogue (-)-4'-desmethoxyepisilvestrol. J. Am. Chem. Soc. 131, 1607–1616.

Bestle, D., Heindl, M.R., Limburg, H., et al., 2020. TMPRSS2 and furin are both essential for proteolytic activation of SARS-CoV-2 in human airway cells. Life Sci Alliance 3, e202000786.

Biedenkopf, N., Lange-Grünweller, K., Schulte, F.W., et al., 2017. The natural compound silvestrol is a potent inhibitor of Ebola virus replication. Antivir. Res. 137, 76–81.

Bordeleau, M.E., Robert, F., Gerard, B., et al., 2008. Therapeutic suppression of translation initiation modulates chemosensitivity in a mouse lymphoma model. J. Clin. Invest. 118 (7), 2651–2660. https://doi.org/10.1172/JCI34753. PMID: 18551192; PMCID: PMC2423864.

Bronstrup, M., Sasse, F., 2020. Natural products targeting the elongation phase of eukaryotic protein biosynthesis. Nat. Prod. Rep. 37, 752–762.

Brown, A.J., Won, J.J., Graham, R.L., et al., 2019. Broad spectrum antiviral remdesivir inhibits human endemic and zoonotic deltacoronaviruses with a highly divergent RNA dependent RNA polymerase. Antiviral Res 169, 104541.

Chan, K., Robert, F., Oertlin, C., et al., 2019. eIF4A supports an oncogenic translation program in pancreatic ductal adenocarcinoma. Nat. Commun. 10, 5151.

Choy, K.T., Wong, A.Y., Kaewpreedee, P., et al., 2020. Remdesivir, Iopinavir, emetine, and homoharringtonine inhibit SARS-CoV-2 replication in vitro. Antivir. Res. 178, 104786.

Chu, J., Pelletier, J., 2015. Targeting the eIF4A RNA helicase as an anti-neoplastic approach. Biochim. Biophys. Acta 1849, 781–791.

de Wilde, A.H., Jochmans, D., Posthuma, C.C., et al., 2014. Screening of an FDA-approved compound library identifies four small-molecule inhibitors of Middle East respiratory syndrome coronavirus replication in cell culture. Antimicrob. Agents Chemother. 58, 4875–4884.

de Wit, E., Feldmann, F., Cronin, J., et al., 2020. Prophylactic and therapeutic remdesivir (GS-5734) treatment in the rhesus macaque model of MERS-CoV infection. Proc. Natl. Acad. Sci. U. S. A. 117, 67771-6776.

Elgner, F., Sabino, C., Basic, M., et al., 2018. Inhibition of Zika virus replication by silvestrol. Viruses 10, 149.
Ernst, J.T., Thompson, P.A., Nilewski, C., et al., 2020. Design of development candidate eFT226, a first in class inhibitor of eukaryotic initiation factor 4A RNA helicase. J. Med. Chem. 11, 5879–5955. https://doi.org/10.1021/acs.jmedchem.0c00182.
Glitscher, M., Himmelsbach, K., Woytinek, K., et al., 2018. Inhibition of hepatitis E virus spread by the natural compound silvestrol. Viruses 10, 301.
Gorbalenya, A.E., Baker, S.C., Baric, R.S., et al., 2020. The species Severe acute respiratory syndrome-related coronavirus: classifying 2019-nCoV and naming it SARS-CoV-2. Nat Microbiol 5, 536–544.
Gordon, E.G., Jang, G.M., Bouhaddou, M., et al., 2020. A SARS-CoV-2 protein interaction map reveals targets for drug repurposing. Nature 583, 459–468. https://doi.org/10.1038/s41586-020-2286-9.
Guaraldi, G., Meschiari, M., Cozzi-Lepri, A., et al., 2020. Tocilizumab in patients with severe COVID-19: a retrospective cohort study. Lancet Rheumatol 2, e474–e484.
Harrison, C., 2020. Drug researchers pursue new lines of attack against COVID-19. Nat. Biotechnol. 38, 659–662.
Henss, L., Scholz, T., Grünweller, A., Schnierle, B.S., 2018. Silvestrol inhibits Chikungunya virus replication. Viruses 10, 592.
Hoffman, M., Kleine-Weber, H., Schroeder, S., et al., 2020. SARS-CoV-2 cell entry depends on ACE2 and TMPRSS2 and is blocked by a clinically proven protease inhibitor. Cell 181, 271–280.
Iwasaki, S., Iwasaki, W., Takahashi, M., et al., 2019. The translation inhibitor rocaglamide targets a bimolecular cavity between eIF4A and polypurine RNA. Mol. Cell 73, 738–748.
Jalkanen, J., Hollmén, M., Jalkanen, S., 2020. Interferon beta-1a for COVID-19: critical importance of the administration route. Crit. Care 24, 335.
Jonsdottir, H.R., Dijkman, R., 2016. Coronaviruses and the human airway: a universal system for virus-host interaction studies. Virol. J. 13, 24.
Kogure, T., Kinghorn, A.D., Yan, I., et al., 2013. Therapeutic potential of the translation inhibitor silvestrol in hepatocellular cancer. PLoS One 8, e76136.
Lucas, D.M., Edwards, R.B., Lozanski, G., et al., 2009. The novel plant-derived agent silvestrol has B-cell selective activity in chronic lymphocytic leukemia and acute lymphoblastic leukemia in vitro and in vivo. Blood 113, 4656–4666.
Madhugiri, R., Fricke, M., Marz, M., Ziebuhr, J., 2016. Coronavirus cis-acting RNA elements. Adv. Virus Res. 96, 127–163.
Meyerowitz-Katz, G., Merone, L., 2020. A systematic review and meta-analysis of published research data on COVID-19 infection fatality rates. Int. J. Infect. Dis. 101, 138–148.
Müller, C., Schulte, F.W., Lange-Grünweller, K., et al., 2018a. Broad-spectrum antiviral activity of the eIF4A inhibitor silvestrol against corona- and picornaviruses. Antivir. Res. 150, 123–129.
Müller, C., Hardt, M., Schwudke, D., et al., 2018b. Inhibition of cytosolic phospholipase A2alpha impairs an early step of coronavirus replication in cell culture. J. Virol. 92 e01463-17.
Müller, C., Obermann, W., Schulte, F.W., et al., 2020. Comparison of broad-spectrum antiviral activities of the synthetic rocaglate CR-31-B (-) and the eIF4A-inhibitor Silvestrol. Antivir. Res. 175, 104706.
Ogando, N.S., Dalebout, T.J., Zevenhoven-Dobbe, J.C., et al., 2020. SARS-coronavirus-2 replication in Vero E6 cells: replication kinetics, rapid adaptation and cytopathology. J. Gen. Virol. 101, 925–940.
Oldenburg, C.E., Doan, T., 2020. Azithromycin for severe COVID-19. Lancet 6736, 31863–31868.
Pan, L., Wooard, J.L., Lucas, D.M., et al., 2014. Rocaglamide, silvestrol and structurally related bioactive compounds from Aglaia species. Nat. Prod. Rep. 31, 924–939.
Pannell, C.M., 1998. Aglaia Foveolate. The IUCN Red List of Threatened Species. https://doi.org/10.2305/IUCN.UK.1998.RLTS.T34910A9896555.en.
Passmore, L.A., Schmeing, T.M., Maag, D., 2007. The eukaryotic translation initiation factors eIF1 and eIF1A induce an open conformation of the 40S ribosome. Mol. Cell 26, 41–50.
Patton, J.T., Lustberg, M.E., Lozanski, G., et al., 2015. The translation inhibitor silvestrol exhibits direct anti-tumor activity while preserving innate and adaptive immunity against EBV-driven lymphoproliferative disease. Oncotarget 6, 2693–2708.
Rajgor, D.D., Lee, M.H., Archuleta, S., et al., 2020. The many estimates of the COVID-19 case fatality rate. Lancet Infect. Dis. 20, 776–777.
Rodrigo, C.M., Cencic, R., Roche, S.P., et al., 2012. Synthesis of rocaglamide hydroxamates and related compounds as eukaryotic translation inhibitors: synthetic and biological studies. J. Med. Chem. 55, 558–562.
Sanders, J.M., Monogue, M.L., Jodlowski, T.Z., Cutrell, J.B., 2020. Pharmacologic treatments for coronavirus disease 2019 (COVID-19): a review. J. Am. Med. Assoc. 323, 1824–1836.
Schlereth, J., Grünweller, A., Biedenkopf, N., et al., 2016. RNA binding specificity of Ebola virus transcription factor VP30. RNA Biol. 13, 783–798.
Sheahan, T.P., Sims, A.C., Graham, R.L., et al., 2017. Broad-spectrum antiviral GS-5734 inhibits both epidemic and zoonotic coronaviruses. Sci. Transl. Med. 9, 396.
Todt, D., Moeller, N., Praditya, D., et al., 2018. The natural compound silvestrol inhibits hepatitis E virus (HEV) replication in vitro and in vivo. Antivir. Res. 157, 151–158.
WHO, 2020. In: World Health Organization. Coronavirus Sease 2019 (COVID-19) Situation Report- 51.
Wolfe, A.L., Singh, K., Zhong, Y., et al., 2014. RNA G-quadruplexes cause eIF4A-dependent oncogene translation in cancer. Nature 513, 65–70.

viruses

MDPI

Article

Rocaglates as Antivirals: Comparing the Effects on Viral Resistance, Anti-Coronaviral Activity, RNA-Clamping on eIF4A and Immune Cell Toxicity

Wiebke Obermann [1], Alexandra Friedrich [2], Ramakanth Madhugiri [2], Paul Klemm [1], Jan Philipp Mengel [3], Torsten Hain [3,4], Stephan Pleschka [2,4], Hans-Guido Wendel [5], Roland K. Hartmann [1], Susanne Schiffmann [6], John Ziebuhr [2,4], Christin Müller [2,4,*] and Arnold Grünweller [1,*]

1 Institute of Pharmaceutical Chemistry, Philipps University Marburg, 35032 Marburg, Germany; wiebkeobermann@staff.uni-marburg.de (W.O.); klemmp@staff.uni-marburg.de (P.K.); roland.hartmann@staff.uni-marburg.de (R.K.H.)
2 Institute of Medical Virology, Justus Liebig University Giessen, 35392 Giessen, Germany; alexandra.friedrich@viro.med.uni-giessen.de (A.F.); ramakanth.madhugiri@viro.med.uni-giessen.de (R.M.); stephan.pleschka@viro.med.uni-giessen.de (S.P.); john.ziebuhr@viro.med.uni-giessen.de (J.Z.)
3 Institute of Medical Microbiology, Justus Liebig University Giessen, 35392 Giessen, Germany; jan.p.mengel@mikrobio.med.uni-giessen.de (J.P.M.); torsten.hain@mikrobio.med.uni-giessen.de (T.H.)
4 German Center for Infection Research, Partner Site Giessen-Marburg-Langen, 35392 Giessen, Germany
5 Cancer Biology and Genetics Program, Memorial Sloan Kettering Cancer Center, New York, NY 10023, USA; wendelh@mskcc.org
6 Fraunhofer Institute for Translational Medicine and Pharmacology, 60596 Frankfurt am Main, Germany; susanne.schiffmann@itmp.fraunhofer.de
* Correspondence: christin.mueller@viro.med.uni-giessen.de (C.M.); gruenwel@staff.uni-marburg.de (A.G.)

check for updates

Citation: Obermann, W.; Friedrich, A.; Madhugiri, R.; Klemm, P.; Mengel, J.P.; Hain, T.; Pleschka, S.; Wendel, H.-G.; Hartmann, R.K.; Schiffmann, S.; et al. Rocaglates as Antivirals: Comparing the Effects on Viral Resistance, Anti-Coronaviral Activity, RNA-Clamping on eIF4A and Immune Cell Toxicity. *Viruses* **2022**, *14*, 519. https://doi.org/10.3390/v14030519

Academic Editor: Gilda Tachedjian

Received: 2 February 2022
Accepted: 28 February 2022
Published: 3 March 2022

Publisher's Note: MDPI stays neutral with regard to jurisdictional claims in published maps and institutional affiliations.

Abstract: Rocaglates are potent broad-spectrum antiviral compounds with a promising safety profile. They inhibit viral protein synthesis for different RNA viruses by clamping the 5′-UTRs of mRNAs onto the surface of the RNA helicase eIF4A. Apart from the natural rocaglate silvestrol, synthetic rocaglates like zotatifin or CR-1-31-B have been developed. Here, we compared the effects of rocaglates on viral 5′-UTR-mediated reporter gene expression and binding to an eIF4A-polypurine complex. Furthermore, we analyzed the cytotoxicity of rocaglates on several human immune cells and compared their antiviral activities in coronavirus-infected cells. Finally, the potential for developing viral resistance was evaluated by passaging human coronavirus 229E (HCoV-229E) in the presence of increasing concentrations of rocaglates in MRC-5 cells. Importantly, no decrease in rocaglate-sensitivity was observed, suggesting that virus escape mutants are unlikely to emerge if the host factor eIF4A is targeted. In summary, all three rocaglates are promising antivirals with differences in cytotoxicity against human immune cells, RNA-clamping efficiency, and antiviral activity. In detail, zotatifin showed reduced RNA-clamping efficiency and antiviral activity compared to silvestrol and CR-1-31-B, but was less cytotoxic for immune cells. Our results underline the potential of rocaglates as broad-spectrum antivirals with no indications for the emergence of escape mutations in HCoV-229E.

Keywords: rocaglates; coronavirus; eIF4A; silvestrol; CR-1-31-B; zotatifin; escape mutations; broad-spectrum antivirals

1. Introduction

RNA viruses, like coronaviruses and influenza viruses, are important human pathogens and have significant zoonotic potential, facilitating the transmission of newly emerging viruses from animal reservoirs to humans. As a result, they represent a formidable challenge for global disease control, which is highlighted by the ongoing SARS-CoV-2 pandemic [1]. RNA viruses have a high genetic variability and use a plethora of mechanisms to increase their fitness, including short replication times, high yields and fast mutation rates [2]. The

rapid accumulation of beneficial mutations facilitates adaptation to new environmental conditions, including the evolution of resistant variants that escape from, e.g., antiviral treatments [3]. Specifically, influenza A viruses (IAVs) were reported to acquire drug-resistance against adamantanes (e.g., rimantadine, targeting the M2 ion channel) or neuraminidase (NA) inhibitors (e.g., oseltamivir). Consequently, these inhibitors have become partially obsolete as a treatment option for IAV due to the appearance of drug-resistance mutations in M2 (and NA) [4].

Compared to IAV and other RNA viruses, the mutation rate during coronavirus genome replication is slightly lower because these viruses employ in their replication-transcription complex a 3′-to-5′ exoribonuclease that acts in conjunction with the viral RNA-dependent RNA polymerase to remove misincorporated nucleotides (proof-reading activity) [5,6]. Despite their increased replication fidelity, coronaviruses retained their capability of readily acquiring mutations under specific selection pressures, often resulting in changes in replication efficiency, disease severity, transmissibility and antigenicity. For example, genetic variants (of concern) with altered phenotypes continue to emerge in the current SARS-CoV-2 pandemic, preferentially with mutations in the spike protein gene that improve replication efficiency, transmissibility or lead to immune escape [7,8].

Thus far, very few anti-coronaviral drugs are available [9], highlighting the urgent need to develop broad-spectrum antiviral drugs against this group of RNA viruses [10]. Historically, drug development efforts mainly focused on direct-acting antivirals (DAAs) targeting viral proteins. DAAs have, in general, the advantage of shorter treatment times and fewer side effects, but can give rise to rapidly emerging drug-resistant variants, as highlighted above for IAVs. However, viruses as obligate intracellular parasites exploit numerous host proteins for their replication. There is increasing evidence that these essential proteins can be targeted in therapeutic approaches using a second class of antivirals called host-directed antivirals (HDAs). HDAs are potentially active against many (if not all) members of a given virus family or virus genus and, thus, may potentially be used as broad-spectrum antivirals [11,12]. However, HDAs may also increase the risk of side effects and less favorable safety profiles owing to interference with essential cellular processes.

A host function essential for viral replication is the protein synthesis carried out by the cellular translation machinery. In this context, the cellular DEAD-box RNA helicase eIF4A, which unwinds RNA secondary structures in 5′-untranslated regions (5′-UTRs) as part of the translation initiation complex eIF4F, has been identified as an essential factor for viral protein synthesis (reviewed in [13]). Since a large number of RNA viruses harbor highly structured 5′-UTRs, they require the unwinding activity of eIF4A to allow binding of the 43S-preinitiation complex (43S-PIC) during translation initiation [14]. Therefore, it is not surprising that pharmacological inhibition of eIF4A has been shown to efficiently prevent replication of a large set of RNA viruses, including corona-, picorna-, flavi-, filo-, hepe-, toga-, arena-, nairo-, orthomyxo- and bunyaviruses [15–23].

A very promising class of eIF4A inhibitors (and therefore HDAs) are rocaglates, a group of flavaglines that can clamp the 5′-UTRs of viral and selected cellular mRNAs onto the eIF4A surface. This RNA-clamping prevents the unwinding of mRNA secondary structures by eIF4A and, consequently, translation initiation [24]. Since the translation of many proto-oncogenes is eIF4A-dependent, some of these selective rocaglates are in pre-clinical and early-stage clinical cancer studies [25–28]. One prominent example is zotatifin, a synthetic rocaglate that successfully reached clinical trials aimed to establish therapeutics against advanced solid tumor malignancies (phases 1–2), and also entered an efficacy and dose-escalating study in patients with mild or moderate COVID-19 (phase 1b) [25], which laid the foundations for the further development of rocaglates as potential pan-antivirals.

In the study presented here, the potential to develop rocaglate-resistant mutations was evaluated by multiple passages of human coronavirus 229E (HCoV-229E) in cells grown in a culture medium containing increasing concentrations of two different rocaglates. In our experimental setup, we found no reduction in the sensitivity of passaged HCoV-229E to rocaglate treatment, providing evidence that the emergence of coronaviral escape mutants

is unlikely when targeting the host factor eIF4A. Moreover, we compared the effects of zotatifin as well as silvestrol and CR-1-31-B on (i) viral 5′-UTR-mediated reporter gene expression in HepG2 cells, (ii) binding to a purified human eIF4A-polypurine complex, (iii) cytotoxicity in a diverse set of primary human immune cells, and (iv) on antiviral activity in MRC-5 and in primary human bronchial epithelial cells as a relevant ex vivo cell model system.

In summary, all three rocaglates are suitable potent antiviral compounds that differ in their cell type-specific cytotoxicity, RNA-clamping efficiency and antiviral activity. In detail, zotatifin showed slightly reduced RNA-clamping and antiviral activity compared to silvestrol and CR-1-31-B but was less cytotoxic for immune cells and normal bronchial epithelial cells. Our results underline the potential of rocaglates as broad-spectrum antiviral compounds, especially for the treatment of coronaviruses, but also reveal differences between rocaglate variants regarding their antiviral activity and cytotoxicity in cells of the human immune system.

2. Materials and Methods

2.1. Cell Culture and Viruses

Human fetal lung fibroblasts (MRC-5; ATCC CCL-171), Huh-7 (Japanese Collection of Research Bioresources (JCRB) cell bank, Osaka, Japan [29]) and Vero E6 (ATCC CRL-1586) cells were grown in Dulbecco's modified Eagle's medium (DMEM, Invitrogen, Carlsbad, CA, USA) supplemented with 10% fetal calf serum (FCS), 100 U/mL of penicillin and 100 µg/mL of streptomycin. HepG2 cells were cultured in Iscove's Modified Dulbecco's Medium (IMDM) supplemented with 10% FCS. Primary human monocytes, macrophages, T cells and dendritic cells were cultured in RPMI1640 GlutaMAX medium supplemented with 10% FCS, 100 U/mL of penicillin and 100 µg/mL of streptomycin. All cells were cultured at 37 °C in a 5% CO_2 atmosphere.

Genome sequences of coronavirus strains used in this study are as follows: HCoV-229E (NCBI accession number AF304460.1, NCBI reference sequence NC_002645.1), MERS-CoV (NCBI accession number JX869059, NCBI reference sequence NC_019843.3). The SARS-CoV-2 isolate Munich 929 [30] was kindly provided by Christian Drosten (Institute of Virology, Charité-Universitätsmedizin, Berlin, Germany).

2.2. Human Airway Epithelial Cells

Cryopreserved normal human bronchial epithelial (NHBE; CC-2540, donor 1: TAN 24717, Lot No. 000312626; donor 2: TAN 36585, Batch: 18TL269120) cells were obtained from Lonza, and undifferentiated cells were seeded on collagen-coated transwell plates (Corning Costar, Corning, NY, USA). Cells were grown in a mixture of DMEM and bronchial epithelial cell growth medium (BEGM, Lonza, Basel, Switzerland) supplemented with retinoic acid (75 nM, Sigma Aldrich, St. Louis, MO, USA) at 37 °C in a 5% CO_2 atmosphere. Fresh medium was added regularly after 2 days. After reaching confluence, the cells were cultivated under air-liquid interface conditions for 4 additional weeks for full differentiation into pseudostratified human airway epithelia. Medium from the basolateral compartment was replaced with fresh medium every 2–3 days, and the apical surface was washed every week with PBS (Invitrogen, Carlsbad, CA, USA).

2.3. Reagents

Silvestrol was obtained from the Sarawak Biodiversity Centre (Kuching; North-Borneo, Malaysia; purity > 99%). A 6 mM stock solution was prepared in DMSO (sterile-filtered; Roth). Zotatifin (MedChemExpress, Monmounth Junction, NJ, USA; purity: 98%), CR-1-31-B (also known as CR-31-B (−)) and the inactive enantiomer CR-1-30-B (also known as CR-31-B (+), for further details see [20,31–33]) were dissolved in DMSO at a concentration of 10 mM. All stock solutions were stored at −20 °C and diluted in the corresponding growth media (DMEM or IMDM).

2.4. Cell Toxicity

Cell growth and viability of MRC-5 cells in the presence of the respective compounds were determined by the 3-(4,5-dimethylthiazol-2-yl)-2,5-diphenyl-2H-tetrazoliumbromide (MTT) method, as described previously [19]. For analyzing cytotoxicity in NHBE cells after 72 h treatment, the trans-epithelial electrical resistance (TEER) was measured using an epithelial Volt/Ohm meter 3 (EVOM3, WPI, Sarasota, FL, USA). The obtained TEER values were then compared to those obtained from untreated cells.

The OranguTM assay (Cell Guidance Systems Ltd., Cambridge, UK) was used to determine the cell viability of human monocytes, M1 and M2 macrophages, monocyte-derived dendritic cells (MdDCs) and T cells. CD14+ and CD4+ cells were isolated using the human CD14 or CD4 microbeads (Miltenyi Biotec, Bergisch Gladbach, Germany) as recommended by the supplier. CD14+ monocytes were differentiated to monocyte-derived dendritic cells, M1 macrophages or M2 macrophages, as described previously [34]. Then, 1×10^5 cells were seeded in 96-well plates. Different concentrations of silvestrol, zotatifin, CR-1-31-B and CR-1-30-B (0.5–100 nM) or vehicle (DMSO) were added, and cells were incubated at 37 °C and 5% CO_2. After 20 h (T cells) or 24 h (monocytes, MdDCs, M1 and M2 macrophages) of incubation, 10 µL of Orangu^{TM} cell counting solution was added, followed by incubation for 4 h (T cells) or 1 h (monocytes, MdDCs, M1 and M2 macrophages) at 37 °C and 5% CO_2. After incubation, the absorbance was measured at a wavelength of 450 nm with a reference at 650 nm using an EnSpire® 2300 Multimode Plate Reader (Perkin Elmer, Waltham, MA, USA). To calculate cell viability in the Orangu^{TM} assay, the absorbance of vehicle-treated cells was set to 100%, and the rocaglate-treated samples were normalized to this value correlated to them.

2.5. Serial Passaging of Virus

Serial passaging of virus-containing cell culture supernatants until passage (p) 15 was performed in the presence of increasing concentrations of silvestrol and CR-1-31-B (5–10 nM). As a control, the virus was passaged in the presence of the inactive enantiomer CR-1-30-B or in the absence of any inhibitor. More precisely, MRC-5 cells were infected in triplicate with HCoV-229E at a defined multiplicity of infection (MOI) of 0.1/0.01 and incubated at 33 °C for 48/72 h post-infection (hpi) in the presence of silvestrol, CR-1-31-B, CR-1-30-B or solvent control. Viral titers of the collected supernatants were determined by plaque assay on Huh-7 cells (as described in [19]). At p15, each virus stock and the original stock from p0 were used to obtain individual isolates by two rounds of end-point dilution assay. Virus stocks prepared for each of these isolates were subsequently used to infect Huh-7 cells. At 24 h hpi, total RNA was isolated from infected cells using the RNeasyKit (Qiagen, Venlo, Netherlands). Libraries for sequencing were prepared using NEB Ultra II RNA directional reagents according to the manufacturer's instructions. Library fragments for each sample were then molecular barcoded and amplified with unique dual index primers (NEB E6440) to avoid barcode noise in sequencing. Finally, the sequencing of pooled libraries was performed on an Illumina MiSeq system using v2 chemistry and 2×251 bp reads. The supernatants collected from these cells at 24 hpi were used in subsequent challenge experiments with the respective rocaglates.

2.6. Antiviral Activity

To determine and compare the antiviral activities of CR-1-31-B, silvestrol and zotatifin, MRC-5 or Vero E6 cells were inoculated with the respective virus at a MOI of 0.1 at 33 °C (HCoV-229E; SARS-CoV-2) or 37 °C (Middle East respiratory syndrome coronavirus (MERS-CoV)). After 1 h, the inoculum was removed, and cells were incubated with fresh medium containing the inhibitor at increasing concentrations. Supernatants were collected at 24 hpi and virus titers were analyzed by virus plaque assay [19]. To calculate the EC_{50} values, the virus titer determined for virus-infected cells treated with DMSO only was set to 100%, and titers obtained for treated cells were normalized to this value. EC_{50} values were calculated by non-linear regression analysis using GraphPad Prism 6.0 (GraphPad Software). For

the infection of primary human airway epithelial cells, the apical surface was washed three times with PBS and cells were infected with MERS-CoV (MOI = 3). The inoculum was removed after 1 h and the medium in the basal compartment was replaced with a medium containing the indicated inhibitor concentrations. At the indicated time points, the apical surface of the cells was incubated with 100 µL/well PBS for 15 min and virus titers in the supernatants were determined by virus plaque assay. Challenge experiments were performed to assess potentially existing differences between non-passaged (p0) and serially passaged (p15) viruses in their viral replication efficiency in cells grown in rocaglate-containing culture medium. To this end, MRC-5 cells were infected with individual p15 and p0 virus isolates, respectively, at an MOI of 0.1 and kept in a medium containing the indicated concentrations of silvestrol, CR-1-31-B or in a medium without these compounds. Viral titers at 24 hpi were determined by plaque assay.

2.7. Dual-Luciferase Reporter Assay

The dual-luciferase reporter assay was done as described previously [19–21]. For rocaglate treatment, the highest non-cytotoxic concentration (previously determined as 10 nM in a WST-1 assay [19–21]) was used. A second concentration of 5 nM was additionally used to substantiate the observed effects. All experiments were performed in at least three independent replicates.

2.8. Thermal Shift Assay

Thermal shift assays were performed by incubating 5 µM of recombinant human eIF4AI (19–406) with 50 µM of poly $(AG)_5$ RNA, 1 mM AMP-PNP (Roche, Basel, Switzerland), 100 µM of the indicated compound and 75 SYPRO Orange (S6650, Invitrogen, Carlsbad, CA, USA) in the presence of buffer containing 20 mM HEPES-KOH pH 7.5, 300 mM KCl, 5 mM $MgCl_2$, 1 mM DTT, 0.1 mM EDTA and 10% glycerol for 10 min at room temperature. Measurements were performed from 10 °C to 95 °C at a 1.6 °C/min ramp rate using the QuantStudio3™ Real-Time PCR system (Applied Biosystems, Waltham, MA, USA) in a MicroAmp™ Fast Optical 96-well plate (0.1 mL, Applied Biosystems, Waltham, MA, USA).

2.9. Docking Analysis

Molecular docking was performed using AutoDock, v4.2 [35]. The protein molecules were processed by adding all hydrogen atoms and the merging non-polar hydrogen atoms using AutoDock Tools 1.5.7. Charges were assigned using the Gasteiger method and torsions were fixed for the ligand. The grid box of 60 × 60 × 60 with 3.75 Å was set around the active sites with the x, y and z-dimensions of 46.355, 9.919, 47.473, respectively. The rigid grid box was attained using Autogrid 4, followed by AutoDock with the Lamarckian genetic algorithm to obtain the best docking poses [36]. The docking was performed in two trials, and the average binding energy was calculated. The pose with the best binding affinity was visualized using UCSF Chimera (University of California).

3. Results

3.1. Serial Passaging of HCoV-229E in the Presence of Rocaglates Does Not Decrease Sensitivity to the Corresponding Rocaglates

To examine the ability of coronaviruses to develop resistance against rocaglates by acquiring mutations in the viral genome, we passaged HCoV-229E in three independent experiments 15 times in the presence of increasing concentrations (from 5 to 10 nM) of rocaglate derivatives, silvestrol or CR-1-31-B (Figure 1A). Corresponding concentrations of the inactive enantiomer CR-1-30-B or a solvent-only sample served as negative controls.

As shown exemplarily in Figure 1B, there was no increase of virus replication as a result of serial passaging of the virus in cells propagated in the rocaglate-containing medium. After 15 passages in cell culture, virus-containing supernatants were collected and used to obtain individual isolates by two consecutive end-point dilutions. The individual isolates

were subsequently used in a challenge experiment to determine potential differences in drug sensitivity between non-passaged (p0) and serially passaged viruses (p15). As illustrated in Figure 1C, none of the passaged isolates displayed a reduced sensitivity to rocaglate treatment. All p15 isolates replicated with similar efficiency (e.g., CR-1-31-B p15 #2 and #3) or even less efficiently (e.g., CR-1-31-B p15 #1) compared to non-passaged (p0) virus (Figure 1C, black line). Moreover, the genomes of p0 and p15 viruses were sequenced to identify and compare potential mutations that were acquired during in vitro passaging (Figure 2). Most of the mutations were found to be randomly distributed over the virus genome, with very few single-nucleotide polymorphisms (SNPs) in each of the isolates. Besides synonymous mutations (Figure 2, light brown), several non-synonymous mutations (Figure 2, black and red) were identified, including conservative and non-conservative substitutions (by residues with similar or different physico-chemical properties; indicated in red or black, respectively, in Figure 2). Compared to the p0 non-passaged virus, all p15 virus isolates (including the controls) had acquired three non-synonymous mutations in the nsp4, nsp14 and M protein-coding regions, respectively, most likely resulting from a general cell culture adaptation process.

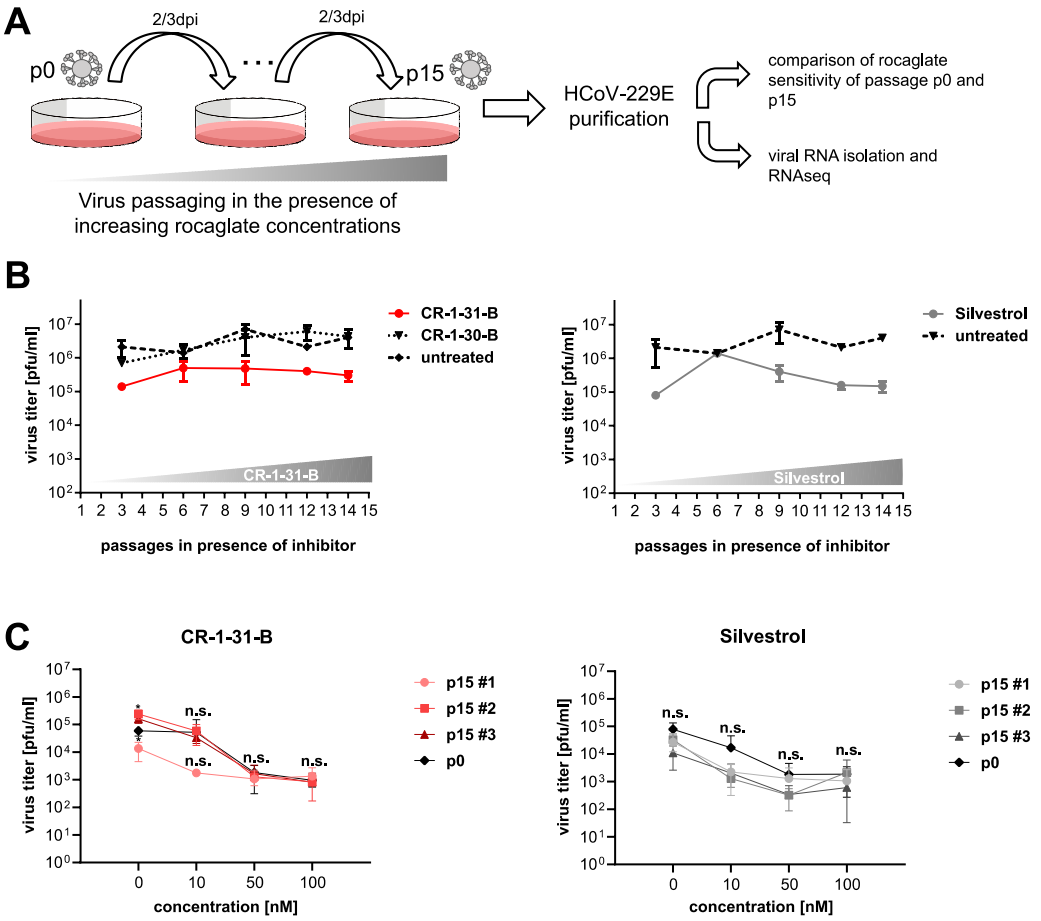

Figure 1. Passaging of HCoV-229E in the presence of increasing concentrations of rocaglates. (**A**) Schematic illustration of workflow. (**B**) MRC-5 cells were infected and treated as shown in (**A**) and titers were determined ($n = 3$). Here, one representative passaging experiment out of three is shown. (**C**) MRC-5 cells were infected with plaque-purified HCoV-229E from p0 (non-passaged) to p15 (serially passaged, obtained as shown in panel (**B**) at an MOI of 0.1 and treated for 24 h either at the indicated concentrations of CR-1-31-B or silvestrol or left untreated for the same time period. Viral titers were then determined using plaque assay ($n = 3$). Significance levels compared to p0 were obtained using the unpaired *t*-test and are indicated as follows: *: $p < 0.05$; n.s.: not significant. Error bars show SD.

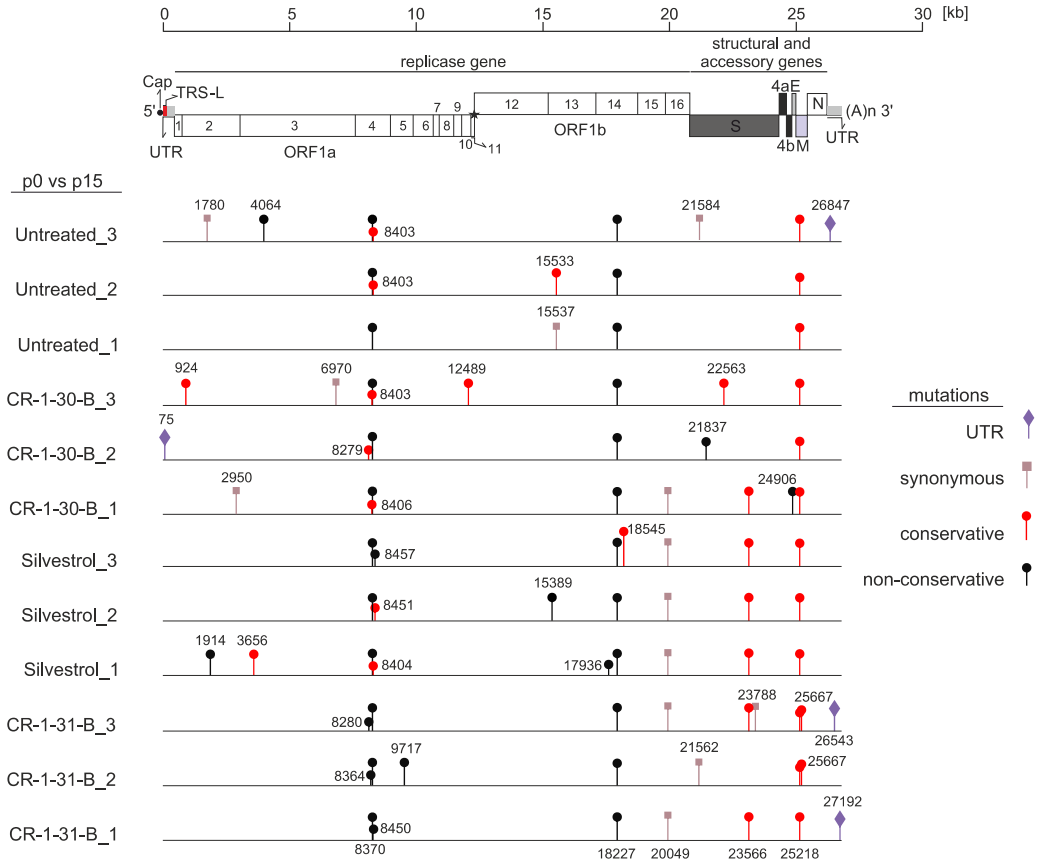

Figure 2. Genetic comparison of input HCoV-229E virus genomes (p0) to obtained p15 virus isolates treated with different rocaglates. CR-1-30-B, the inactive enantiomer of CR-1-31-B, served as a control. MRC-5 cells were infected with the input virus (p0) or the 15 times passaged virus isolates obtained in Figure 1. (MOI = 3). Viral RNA was isolated 24 hpi and sequenced. Single-nucleotide changes are indicated at their location in the virus genome (synonymous: light brown; conservative missense: red; non-conservative missense: black).

Moreover, one synonymous mutation in nsp15 and one non-synonymous mutation in the spike protein-coding region (position 23566 in the genome), leading to a Glu-to-Asp replacement, could be found in all silvestrol-treated samples and in 2 out of 3 virus isolates passaged in the presence of CR-1-31-B. Considering that (i) this non-synonymous mutation is associated with the connector domain of the spike protein and (ii) generally no reduced drug sensitivity was observed (Figure 1C), it appears unlikely that this represents a rocaglate-specific mutation.

Overall, these findings suggest that HCoV-229E, passaged 15 times in the presence of increasing concentrations of rocaglates, did not acquire mutations that could potentially cause rocaglate resistance in infected cells.

3.2. Silvestrol, CR-1-31-B and Zotatifin Show Dose-Dependent Inhibition of In Vitro Translation

Besides resistance analysis, we compared the effects of natural and synthetic rocaglates on in vitro translation efficiency using a dual-luciferase reporter assay [19]. In the presence of the coronavirus 5′-UTRs of HCoV-229E, MERS-CoV and SARS-CoV-2, translation efficiency was sensitive towards silvestrol, CR-1-31-B and zotatifin treatment (Figure 3A). However, the translation inhibition with 10 nM of zotatifin in the presence of the SARS-CoV-2 and the MERS-CoV 5′-UTR appeared to be slightly weaker than with 10 nM of silvestrol or CR-1-31-B. This is not the case for the HCoV-229E reporter construct. The reasons for these differences can so far not be explained and require further investigation.

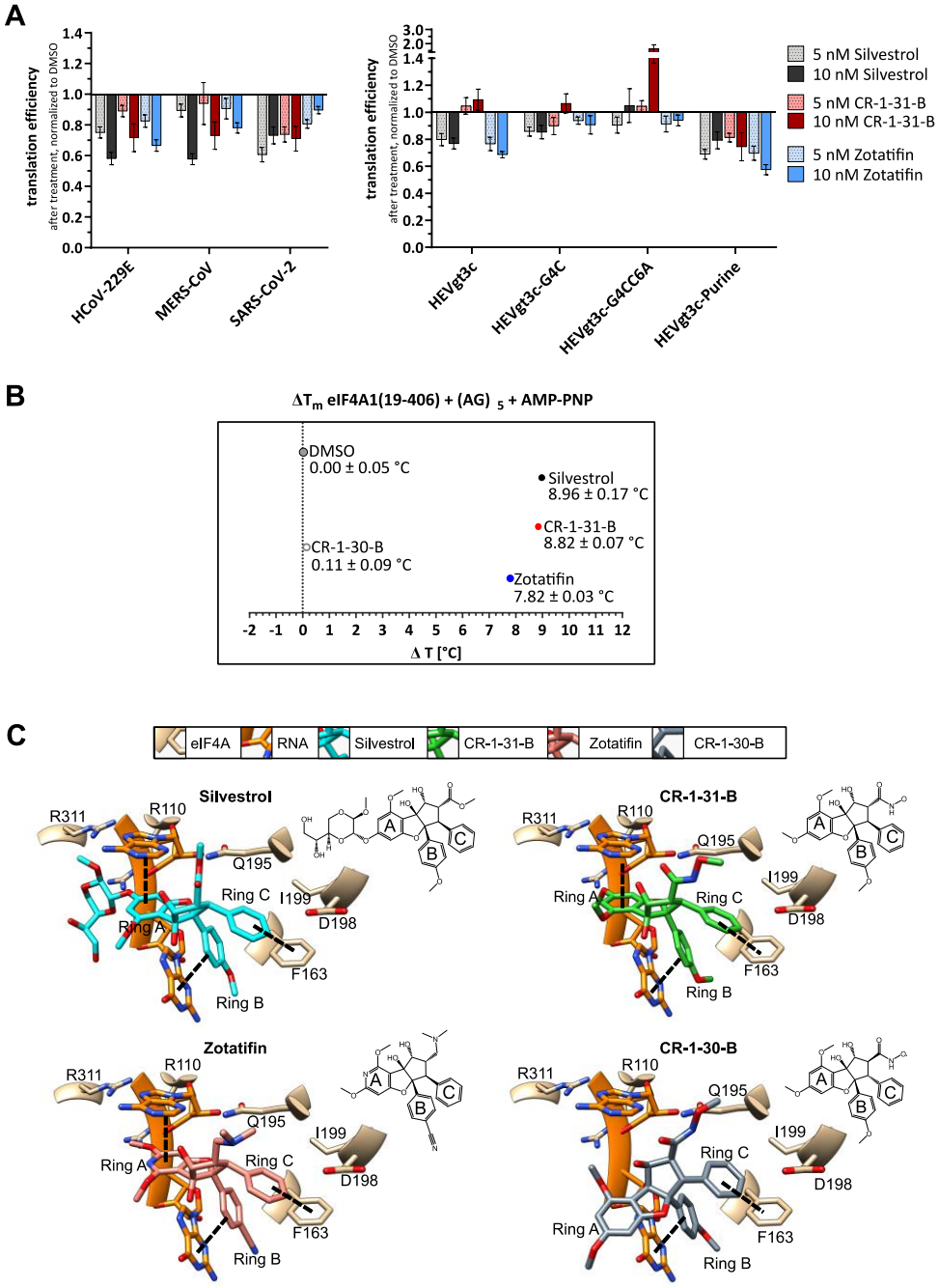

Figure 3. Translation inhibition, thermal shift assay and docking of silvestrol, CR-1-31-B and zotatifin. (**A**) Comparison of the inhibitory effects of silvestrol, CR-1-31-B and zotatifin on reporter gene expression constructs containing 5′-UTRs from coronaviruses HCoV-229E, MERS-CoV and SARS-CoV-2 and analyses of the 5′-UTRs of hepatitis E virus genotype 3c (HEVgt3c) and derivatives thereof with regard to their sensitivity towards silvestrol, CR-1-31-B and zotatifin treatment. Reporter gene expressions were normalized to transfection efficiencies and DMSO controls ($n \geq 3$). Error bars show SEM. For predicted RNA secondary structures of HEVgt3c 5′-UTR and the respective variants, see Supplementary Figure S1 (**B**) Melting temperature of the eIF4A-polypurine RNA $(AG)_5$-AMP-PNP complex in the presence of silvestrol, CR-1-31-B, zotatifin or the inactive enantiomer CR-1-30-B or DMSO to compare the binding affinities of rocaglates to eIF4A-RNA complexes. Numbers indicate the temperature shift compared to DMSO control ± SEM for $n \geq 3$. (**C**) Predicted binding modes of silvestrol, CR-1-31-B, zotatifin and CR-1-30-B (inactive enantiomer of CR-1-31-B) to the human eIF4A-polypurine RNA $(AG)_5$ complex (PDB: 5ZC9) using AutoDock Vina.

Since it is known that different rocaglates have different abilities to bind purine-rich sequences [37], we aimed to gain more mechanistic insight into eIF4A inhibition by the rocaglates via investigation of RNA-clamping. For this purpose, we also analyzed the 5′-UTR of HEV (HEVgt3c) that lacks any polypurine stretches but is predicted to form a stable RNA hairpin structure (Figure 3A and Figure S1). Previous studies hypothesized that silvestrol could clamp this HEVgt3c 5′-UTR onto eIF4A with its dioxane moiety, which is excluded from CR-1-31-B that lacks this part of the molecule [20]. Interestingly, we observed translation inhibition of HEVgt3c with zotatifin, suggesting that purine-independent clamping of RNAs onto eIF4A can also be achieved in the absence of a dioxane moiety. By mutating the stem of the HEVgt3c-5′-UTR, we created thermodynamically destabilized variants of HEVgt3c (HEVgt3c-G4C and HEVgt3c-G4CC6A). These weakened RNA structures led to a loss of the inhibitory effects of silvestrol and zotatifin. To further test the relevance of purines, a purine stretch with a length of eight nucleotides was introduced into the 5′-UTR of HEVgt3c (HEVgt3c-Purine, for further details, see Supplementary Figure S1 and [20]). Similar to our previous results, we regain translation inhibition of HEVgt3c-Purine with silvestrol, CR-1-31-B and zotatifin. This demonstrates that with silvestrol and zotatifin either a stable hairpin substrate or a polypurine stretch is sufficient to clamp the RNA onto eIF4A. In contrast, CR-1-31-B shows translation inhibition only in the presence of a polypurine stretch. This is in line with in vitro translation experiments in the presence of CR-1-31-B that indicated the requirement for a stretch of at least 5 purines to elicit inhibition of translation [37].

To further compare the inhibition mechanism, we performed a thermal shift assay to monitor the thermal stability of an eIF4A-$(AG)_5$ RNA-rocaglate complex (Figure 3B). The highest thermal shifts were observed in the presence of silvestrol (8.96 ± 0.17 °C) or CR-1-31-B (8.82 ± 0.07 °C). In the presence of zotatifin, the thermal stability of the eIF4A-RNA complex increased by 7.82 ± 0.03 °C, indicating that the complex is somewhat less stable than the complex formed with CR-1-31-B or silvestrol. As expected, the inactive enantiomer CR-1-30-B only showed a thermal shift of 0.11 ± 0.09 °C, confirming that the RNA substrate cannot be efficiently clamped with the (+)-enantiomer.

With regard to the mode of action, we performed docking experiments with silvestrol, zotatifin, CR-1-31-B and CR-1-30-B using the crystal structure of the eIF4A1-AMPPNP-RocA-polypurine RNA complex (PDB: 5ZC9, [38] (Figure 3C)). The three crucial π-π-stacking interactions with the phenylalanine at position 163 of eIF4A, the adenine base of A7, and the guanine base of G8 of the RNA substrate can be formed with all active rocaglates. The inactive enantiomer CR-1-30-B lacks the interaction with A7 of the RNA, explaining the absence of inhibitory activity. In line with the predicted docking poses, only the dioxane moiety of silvestrol can cross the bound RNA substrate and might form additional H-bonds with arginine residues. Therefore, differences in the mode of action of rocaglates might arise from very individual structure-activity relationships (SAR) based on their deviating chemical structures.

3.3. Effects on Viability of Silvestrol, CR-1-31-B and Zotatifin in Primary Human Immune Cells

Next, the effects of the three rocaglates on the viability of primary human immune cells (monocytes, M1 macrophages, M2 macrophages, monocyte-derived dendritic cells (MdDCs) and T cells) were analyzed (Figure 4). The cytotoxic concentration of silvestrol that reduced the viability of monocytes and M1 macrophages by 50% (CC_{50}) was 29 nM and 45.6 nM, respectively. For the treatment with CR-1-31-B, the obtained CC_{50} values for monocytes and M1 macrophages were 2.6 and 8.8 nM, respectively. No significant cytotoxicity could be observed for any of the rocaglates on M2 macrophages, MdDCs and T cells (see Figure 4). However, a concentration of 100 nM silvestrol or 100 nM CR-1-31-B reduced the viability of M2 macrophages and MdDCs by approximately 50%, whereas T cells were not affected (Figure 4, Table 1). Interestingly, 100 nM of zotatifin only reduced the viability of monocytes to approximately 75%. CR-1-30-B, the inactive (+)-enantiomer,

had essentially no impact on cell viability at all. These data indicate that the cytotoxic effects of natural and synthetic rocaglates are cell type-dependent and compound-specific.

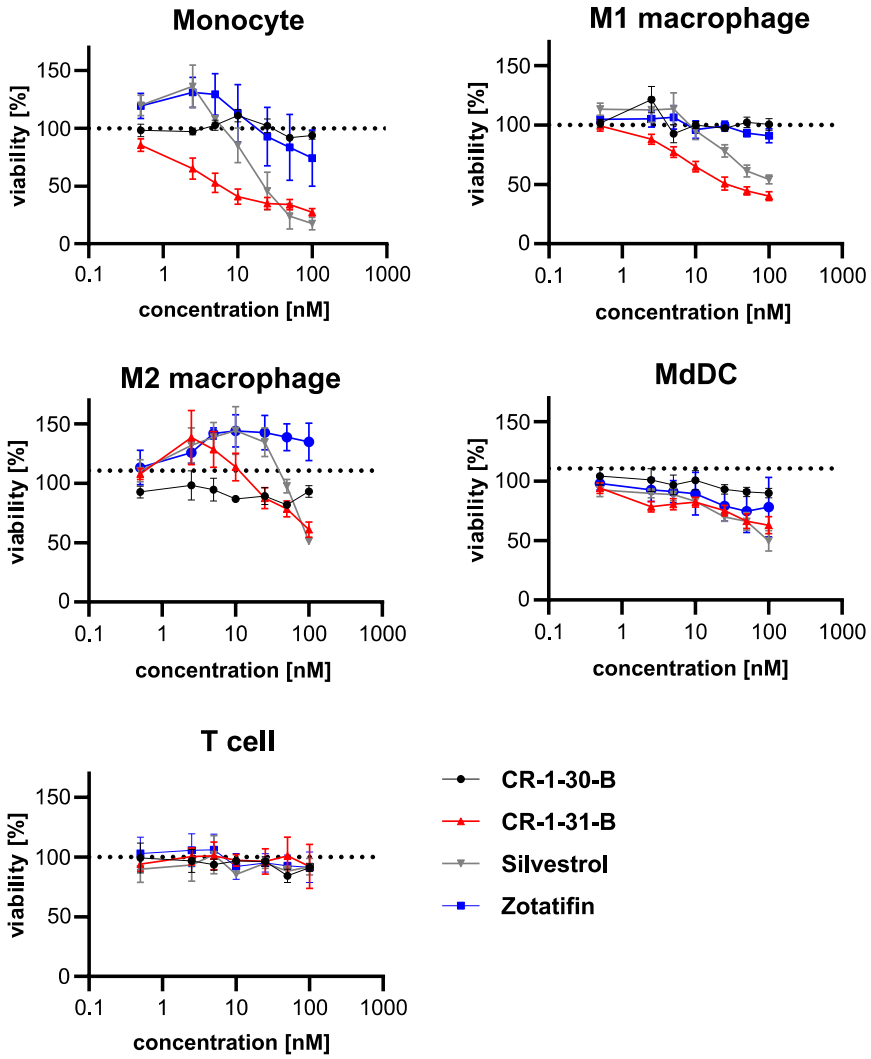

Figure 4. Effects of rocaglates on immune cell viability. Percentage of viable human monocytes, M1/M2 macrophages, MdDCs and T cells in the presence or absence of different concentrations of silvestrol, CR-1-31-B, zotatifin, the inactive enantiomer CR-1-30-B or DMSO control determined by Orangu assay in triplicates. Error bars show SEM with $n \geq 3$.

Table 1. Overview of cytotoxic concentration 50 (CC_{50}) of the indicated compounds in corresponding cell systems.

Cell Type	CC_{50} (nM)			
	Silvestrol	CR-1-31-B	CR-1-30-B	Zotatifin
monocytes	29.0	2.6	>100	78.1
M1 macrophages	45.6	8.8	>100	>100
M2 macrophages	>100	>100	>100	>100
dendritic cells	>100	>100	>100	>100
T cells	>100	>100	>100	>100

3.4. Zotatifin Reduces Coronavirus Replication In Vitro

We have recently shown that the natural rocaglate silvestrol and the synthetic rocaglate CR-1-31-B efficiently reduce the replication of different coronaviruses in infected cells [19–21].

Here, we analyzed the antiviral activity of zotatifin in human fetal lung fibroblasts (MRC-5 cells) infected with HCoV-229E and MERS-CoV, respectively, and Vero E6 cells infected with SARS-CoV-2 (MOI = 0.1). A dose-dependent reduction in virus titers was observed for all three coronaviruses, resulting in EC_{50} values of 3.9 nM for HCoV-229E, 4.3 nM for MERS-CoV and 41.6 nM for SARS-CoV-2 (Figure 5A). Under the conditions used in these experiments, no significant cytotoxicity was observed for up to 10 µM zotatifin (Figure 5B). Taken together, the data demonstrate a similar antiviral potency of zotatifin in comparison to silvestrol and CR-1-31-B (Figure 5C). However, compared to CR-1-31-B, zotatifin was around 20-fold less efficient against SARS-CoV-2, potentially indicating a Vero E6 cell-specific effect (SARS-CoV-2 does not replicate in MRC-5 cells [30]).

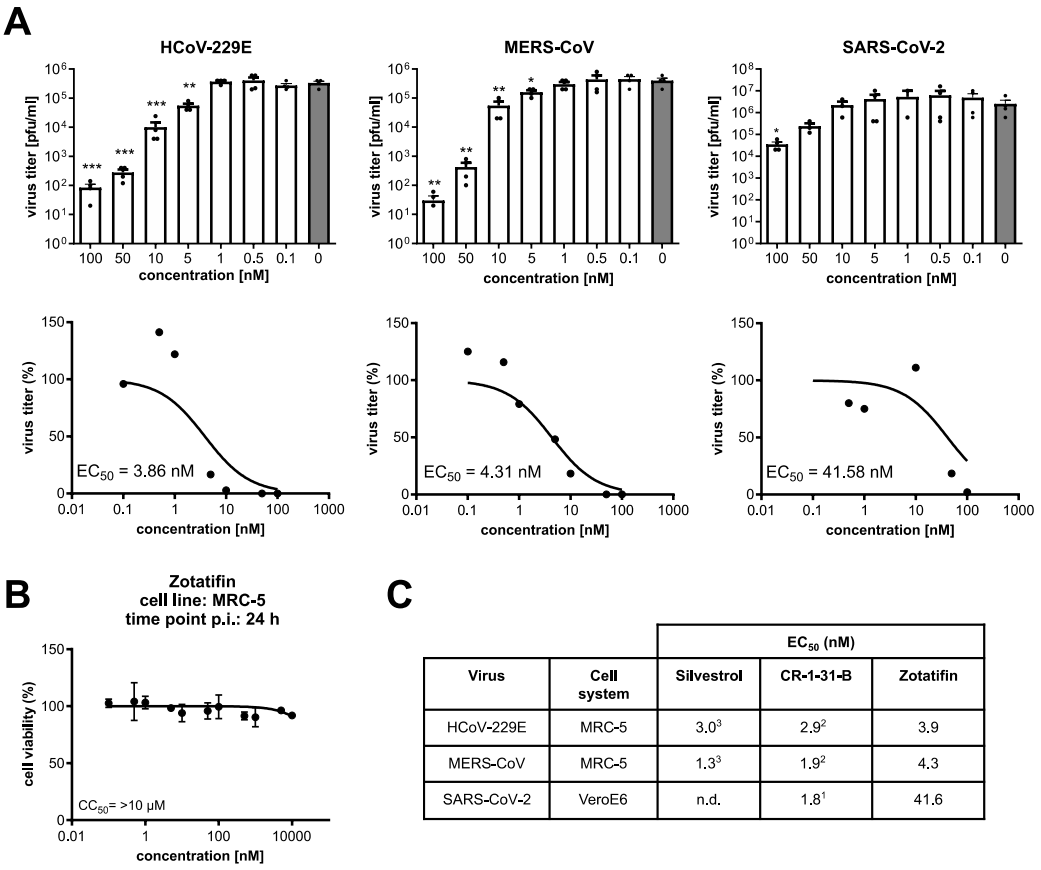

Figure 5. Antiviral activity of zotatifin against different CoVs and comparison with silvestrol and CR-1-31-B. (**A**) MRC-5 or Vero E6 cells were infected with an MOI of 0.1 with HCoV-229E (MRC-5 cells), MERS-CoV (MRC-5 cells) or SARS-CoV-2 (Vero E6 cells) for 24 h in the presence of indicated concentrations of zotatifin or solvent control. Significance levels compared to the results for untreated cells are indicated as follows: *, $p < 0.05$; **, $p < 0.005$; ***, $p < 0.0005$. Error bars show SEM. ($n \geq 3$). (**B**) Viability assay (MTT assay) of MRC-5 cells treated for 24 h with the indicated concentrations of zotatifin. (**C**) Overview of EC_{50} values against CoVs measured in the present study or reported previously (as described in [1] = [21]; [2] = [20]; [3] = [19]); n.d.: not determined.

3.5. Synthetic Rocaglates Zotatifin and CR-1-31-B Efficiently Reduce Mers-Cov Replication in a Human Airway Epithelial Cell Model

To evaluate and compare the antiviral potency of zotatifin in a more relevant setting, we used primary normal human bronchial epithelial (NHBE) cells. These cells, cultured and differentiated under air–liquid interface conditions, serve as a universal model system to study the replication of respiratory viruses, including coronaviruses. Differentiated NHBE cells (Figure 6A), produced from cells obtained from two healthy donors, were infected with MERS-CoV in the presence of the indicated rocaglates or solvent control.

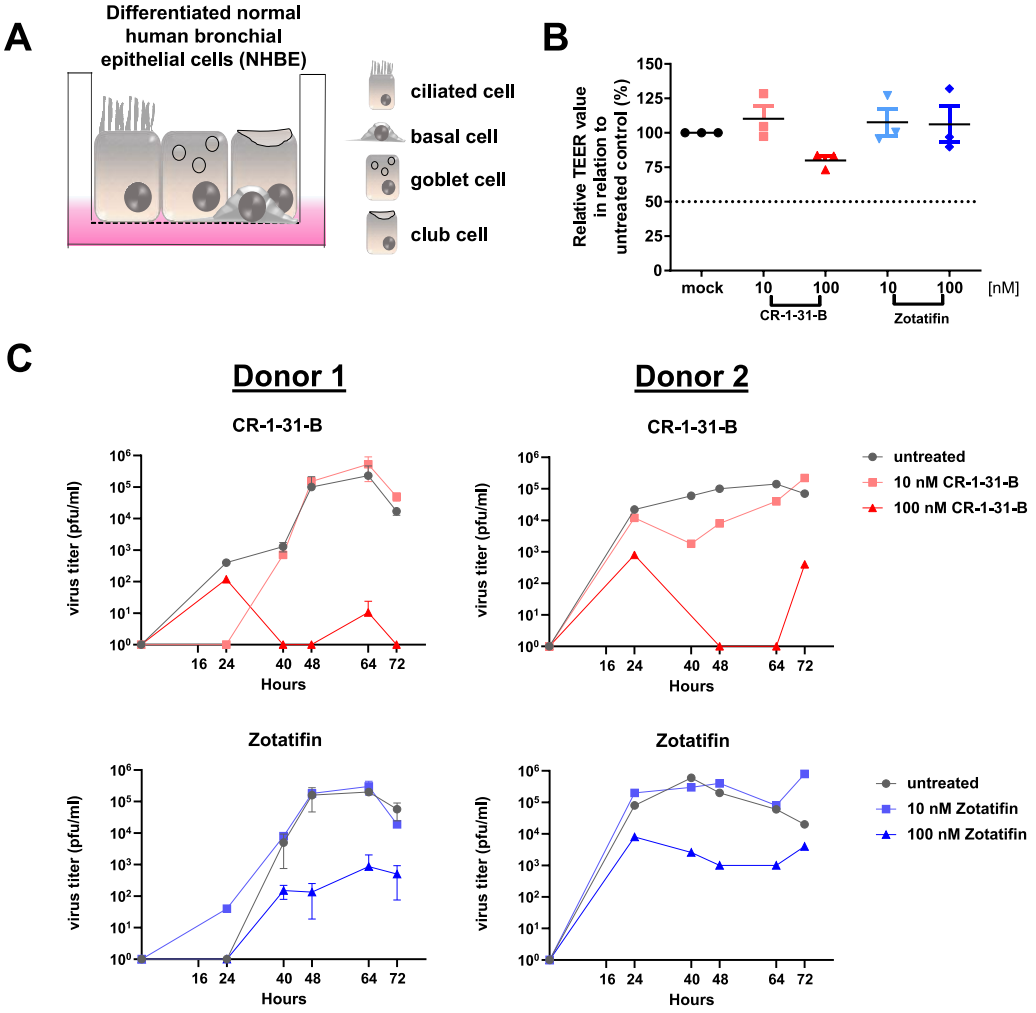

Figure 6. Comparison of antiviral effects of CR-1-31-B and zotatifin using human bronchial epithelial cells infected with MERS-CoV. (**A**) Human bronchial epithelial cells were cultivated and differentiated under the air–liquid interface into different airway epithelial cell types (basal, ciliated, club and goblet cells) and used to assess antiviral effects of the respective compounds. (**B**) Trans-epithelial electrical resistance (TEER) measurement of NHBE cells treated for 72 h with the indicated compounds. (**C**) MERS-CoV titers of infected NHBE cells from two different donors collected at the indicated time points p.i. and treated with CR-1-31-B or zotatifin (each at 10 and 100 nM) in comparison with the solvent control.

The degree of cell layer integrity as an indication of cytotoxic effects of the used compounds was analyzed 72 h post-treatment by measuring the trans-epithelial electrical resistance (TEER; [39]). Except for 100 nM of CR-1-31-B treatment (~25% signal reduction), no significant cytotoxicity was detectable in the treated NHBE cells compared to the untreated control (Figure 6B). Whereas 10 nM of CR-1-31-B or 10 nM of zotatifin had no significant effect on the replication of MERS-CoV in infected NHBE cells from both donors (Figure 6C), 100 nM of CR-1-31-B reduced viral replication to nearly undetectable levels and 100 nM of zotatifin reduced viral replication by about two orders of magnitude.

4. Discussion

Here, we evaluated the ability of coronaviruses to evolve drug-resistant mutations against rocaglates targeting the host factor eIF4A. Interestingly, rocaglate resistance has been reported in cancer cell lines, treated for a prolonged period with rocaglates. As an example, the acute lymphoblastic leukemia cell line 697, treated for 40 weeks with increasing concentrations of silvestrol, obtained drug-resistance by overexpressing the

multidrug-resistance protein 1 (MDR1), which is a major cellular efflux transporter [40]. Since in our study only the virus was constantly passaged in the presence of rocaglates, resistances linked to host metabolism were not expected and therefore not followed up.

Viruses passaged 15 times in MRC-5 cells in the presence or absence of increasing concentrations of silvestrol or CR-1-31-B remained sensitive to rocaglates in vitro, thus providing no evidence for the emergence of viral escape mutants in the applied settings upon rocaglate treatment. Among the passaged virus isolates, only a few minor nucleotide changes were identified. One non-synonymous, conservative substitution in the S protein was explicitly enriched in the rocaglate-treated viruses at passage 15. Other mutations identified after p15 of HCoV-229E were not specifically associated with rocaglate treatment, indicating nonspecific selective pressure or cell culture adaptations. The fact that all p15 virus isolates showed no selective advantage in replication over p0 viruses and maintained their sensitivity towards rocaglate treatment, indicates a high barrier for escape mutations against these antiviral compounds targeting the host protein eIF4A. At this stage, we cannot formally exclude that viral adaptations emerge after prolonged passaging.

In comparison with our findings, 13 passages of SARS-CoV-2 in the presence of the DAA remdesivir, which inhibits the viral RNA-dependent-RNA polymerase (RdRp), were reported to lead to partial resistance due to a non-synonymous mutation in the RdRp (E802D) [41]. Similar findings were also reported for other coronaviruses, such as the mouse hepatitis virus (MHV). Here, an increased ability to replicate in the presence of remdesivir was observed after 23 passages. More specifically, two mutations in the RdRp (F476L and V553L) led to a 5.6-fold resistance to remdesivir, based on EC_{50} values. Likewise, homologous substitutions in the genome of SARS-CoV (F480L and V557L) conferred resistance to remdesivir as well [42]. Although these resistance mutations impaired (in the absence of remdesivir) the competitive fitness of the viruses in vitro (SARS-CoV-2 and MHV) and caused attenuation in vivo (SARS-CoV) [41,42], it should be emphasized that DAA-resistant virus mutants can emerge rapidly, which calls for short treatment windows and combination therapies. Against this background, continued efforts to develop HDAs are highly desirable.

We further compared three different rocaglates regarding their potency of translation inhibition in a viral 5′-UTR-sensitive reporter gene expression system. Moreover, we evaluated their capacity to clamp the eIF4A-polypurine $(AG)_5$ RNA complex using a thermal shift assay. In line with our results on the antiviral activities of rocaglates, we observed inhibition of translation in the presence of coronavirus 5′-UTRs with all three rocaglates (Figure 3A). Silvestrol, with its additional dioxane moiety, but surprisingly also zotatifin, were able to clamp stable RNA hairpin structures in a polypurine-independent manner, whereas CR-1-31-B only showed inhibition of translation in the presence of a polypurine stretch, which is in line with data obtained in previous studies [20,37] (Figure 3A and Figure S1). Apart from that, reduced RNA hairpin stability led to a loss of the inhibitory effects of all tested rocaglates, indicating that the thermodynamic stability of the RNA substrate is crucial for purine-independent inhibition (Figure 3A and Figure S1). The thermal shift assay results further revealed that eIF4A-polypurine $(AG)_5$ complexes are most stable with silvestrol and CR-1-31-B. In the presence of zotatifin, the complexes showed a slightly reduced thermal stability, which might explain the somewhat lower antiviral activity of zotatifin observed here. Our observation of polypurine-independent RNA-clamping, mediated by zotatifin and silvestrol in the reporter assay, might indicate a broader spectrum of viral and also cellular mRNA substrates that are affected by these rocaglates.

Regarding cellular toxicity in human immune cells, all three rocaglates showed no significant cytotoxicity in T cells, dendritic cells and M2 macrophages. Moreover, zotatifin seemed to be better tolerated than CR-1-31-B and silvestrol by monocytes and M1 macrophages. In general, silvestrol is known to influence the inflammatory status of immune cells depending on the cell type and activation status [34]. If this is also the case for zotatifin and CR-1-31-B has not been investigated so far. However, modulating the immune response after viral infection is of outstanding importance for the development of antiviral

drugs that can be applied in the later stages of a viral disease. Therefore, rocaglates might be very interesting therapeutic compounds due to their dual effects on virus replication and on modulation of the immune response.

The antiviral activities of all three tested rocaglates are very similar in MRC-5 cells infected with HCoV-229E or MERS-CoV (Figure 5). However, for Vero E6 cells infected with SARS-CoV-2, the EC_{50} value of zotatifin was about 20-fold higher than previously observed for CR-1-31-B. Further studies are required to determine if these differences are linked to the different cell systems used or result from specific properties of the SARS-CoV-2 isolate (Figure 5C) [43]. It should be noted that a previous study by Gordon et al. reported an EC_{90} for zotatifin of 37 nM against SARS-CoV-2 in Vero E6 cells [44].

To further assess the antiviral potential of the two synthetic rocaglates zotatifin and CR-1-31-B, we analyzed their effects in an infection-relevant ex vivo cell system, namely differentiated human bronchial epithelial cells. This system allows the investigation of inhaled pathogens, including respiratory viruses, on a pseudostratified epithelium, including goblet cells, ciliated cells, club cells and basal cells [45]. Notably, the antiviral effect of CR-1-31-B as well as of zotatifin against MERS-CoV replication could be confirmed in this model system. Interestingly, no major inhibition of MERS-CoV replication was observed for both synthetic rocaglates at a concentration of 10 nM, in contrast to HCoV-229E [20] and SARS-CoV-2 [21]. Our data suggest a lower sensitivity of MERS-CoV to rocaglate treatment in this ex vivo primary cell system. Overall, CR-1-31-B appears to be more effective but also slightly more toxic than zotatifin (Figure 6B,C).

5. Conclusions

Our results clearly show that treatment with rocaglates is a potent antiviral approach against different coronaviruses. Our findings support the notion that targeting the host factor eIF4A by rocaglates is associated with a low risk of rapidly emerging virus escape mutants. In addition, we were able to show that rocaglates have differential cytotoxic effects on different human immune cell subpopulations. Application via an aerosol into the respiratory tract of infected organisms (instead of a systemic application) may reduce the uptake of rocaglates into blood cells and thereby reduce the risk of potential toxic side effects. Another advantage of this application route is that the first-pass effect of the liver can be omitted. Therefore, a local application of rocaglates should be the preferred route for future studies that aim at combating respiratory viruses.

Supplementary Materials: The following supporting information can be downloaded at: https://www.mdpi.com/article/10.3390/v14030519/s1, Figure S1: (A) Effects of 5 nM and 10 nM Silvestrol, CR-1-31-B and Zotatifin on reporter gene expression. The 5′-UTR of the human ß-Globin mRNA and the unstructured $(AC)_{15}$ sequence serve as negative controls, while the $(AG)_{15}$ polypurine sequence servesas a positive control. Reporter gene expressions were normalized to transfection efficiencies and DMSO controls ($n > 3$). (B) Predicted RNA secondary structures of ß-Globin 5′-UTR, $(AC)_{15}$, $(AG)_{15}$ and HEVgt3c 5′-UTR constructs. The secondary structures were predicted using the RNAfold web server (University of Vienna) and structures with minimal free energy are shown.

Author Contributions: W.O., A.F., R.M., P.K., J.P.M., S.S. and C.M., performed experiments, analyzed and visualized the data; T.H. and J.P.M. sequenced HCoV-229E isolates; S.S., J.Z., C.M. and A.G. supervised the study and analyzed and visualized data; C.M. and A.G. wrote the initial paper draft, and S.P., H.-G.W., R.K.H. as well as all other authors helped to finalize the paper. All authors have read and agreed to the published version of the manuscript.

Funding: This research was funded by the LOEWE Center DRUID (projects A2 and B2, to A.G. and J.Z.), the German Center for Infection Research (DZIF), partner site Giessen-Marburg-Langen (TTU Emerging Infections, to J.Z. and S.P.), the Deutsche Forschungsgemeinschaft (SFB 1021 'RNA viruses: RNA metabolism, pathogenesis and host response'; projects A01 and A02, to J.Z. and R.K.H.; Z02, to T.H.; KFO309, project P3, to J.Z.; Z1 to J.P.M. and T.H.; GRK2581, project P10, to J.Z.), the German Federal Ministry for Education and Research (BMBF, COVINET, to J.Z.), the BMBF project HELIATAR (to A.G. and J.Z) and the von Behring-Roentgen Foundation (to J.Z.). Further support to H.G.W. was from the NCI Cancer Center Support Grant to MSKCC (CCSG, P30 CA08748), the

Starr Cancer Consortium (GC230724) and from NIH grants RO1CA183876-05, RO1CA207217–03, R35 CA252982-01, P50 CA192937-03, P50 CA217694), LLS 7014-17, LLS 1318-15.

Institutional Review Board Statement: Not applicable.

Informed Consent Statement: Not applicable.

Data Availability Statement: All data are available from the corresponding authors upon reasonable request.

Acknowledgments: We thank Nadja Karl for her excellent technical assistance.

Conflicts of Interest: The authors declare no conflict of interest.

References

1. Hu, B.; Guo, H.; Zhou, P.; Shi, Z. Characteristics of SARS-CoV-2 and COVID-19. *Nat. Rev. Microbiol.* **2021**, *19*, 141–154. [CrossRef] [PubMed]
2. Domingo, E.; Holland, J.J. RNA virus mutations and fitness for survival. *Annu. Rev. Microbiol.* **1997**, *51*, 151–178. [CrossRef] [PubMed]
3. Elena, S.F.; Sanjuan, R. Adaptive value of high mutation rates of RNA viruses: Separating causes from consequences. *J. Virol.* **2005**, *79*, 11555–11558. [CrossRef]
4. Hussain, M.; Galvin, H.D.; Haw, T.Y.; Nutsford, A.N.; Husain, M. Drug resistance in influenza A virus: The epidemiology and management. *Infect. Drug Resist.* **2017**, *10*, 121–134. [CrossRef] [PubMed]
5. Snijder, E.J.; Decroly, E.; Ziebuhr, J. The Nonstructural Proteins Directing Coronavirus RNA Synthesis and Processing. *Adv. Virus Res.* **2016**, *96*, 59–126.
6. Minskaia, E.; Hertzig, T.; Gorbalenya, A.E.; Campanacci, V.; Cambillau, C.; Canard, B.; Ziebuhr, J. Discovery of an RNA virus 3′->5′ exoribonuclease that is critically involved in coronavirus RNA synthesis. *Proc. Natl. Acad. Sci. USA* **2006**, *103*, 5108–5113. [CrossRef]
7. Harvey, W.T.; Carabelli, A.M.; Jackson, B.; Gupta, R.K.; Thomson, E.C.; Harrison, E.M.; Ludden, C.; Reeve, R.; Rambaut, A.; Genomics UK (COG-UK) Consortium; et al. SARS-CoV-2 variants, spike mutations and immune escape. *Nat. Rev. Microbiol.* **2021**, *19*, 409–424.
8. Maher, M.C.; Bartha, I.; Weaver, S.; Di Iulio, J.; Ferri, E.; Soriaga, L.; Lempp, F.A.; Hie, B.L.; Bryson, B.; Berger, B.; et al. Predicting the mutational drivers of future SARS-CoV-2 variants of concern. *Sci. Transl. Med.* **2022**, *14*, abk3445. [CrossRef]
9. Parums, D.V. Editorial: Current Status of Oral Antiviral Drug Treatments for SARS-CoV-2 Infection in Non-Hospitalized Patients. *Med. Sci. Monit.* **2022**, *28*, e935952. [CrossRef]
10. Ader, F.; Bouscambert-Duchamp, M.; Hites, M.; Peiffer-Smadja, N.; Poissy, J.; Belhadi, D.; Diallo, A.; Lê, M.-P.; Peytavin, G.; Staub, T.; et al. Remdesivir plus standard of care versus standard of care alone for the treatment of patients admitted to hospital with COVID-19 (DisCoVeRy): A phase 3, randomised, controlled, open-label trial. *Lancet. Infect. Dis.* **2021**, *22*, 209–221. [CrossRef]
11. Bauer, L.; Lyoo, H.; van der Schaar, H.M.; Strating, J.; van Kuppeveld, F.J. Direct-acting antivirals and host-targeting strategies to combat enterovirus infections. *Curr. Opin. Virol.* **2017**, *24*, 1–8. [CrossRef] [PubMed]
12. Kaufmann, S.H.E.; Dorhoi, A.; Hotchkiss, R.S.; Bartenschlager, R. Host-directed therapies for bacterial and viral infections. *Nat. Rev. Drug. Discov.* **2018**, *17*, 35–56. [CrossRef] [PubMed]
13. Taroncher-Oldenburg, G.; Müller, C.; Obermann, W.; Ziebuhr, J.; Hartmann, R.; Grünweller, A. Targeting the DEAD-Box RNA Helicase eIF4A with Rocaglates-A Pan-Antiviral Strategy for Minimizing the Impact of Future RNA Virus Pandemics. *Microorganisms* **2021**, *9*, 540. [CrossRef] [PubMed]
14. Toribio, R.; Diaz-Lopez, I.; Ventoso, I. New insights into the topology of the scanning ribosome during translation initiation: Lessons from viruses. *RNA Biol.* **2016**, *13*, 1223–1227. [CrossRef]
15. Biedenkopf, N.; Lange-Grünweller, K.; Schulte, F.W.; Weißer, A.; Müller, C.; Becker, D.; Becker, S.; Hartmann, R.K.; Grünweller, A. The natural compound silvestrol is a potent inhibitor of Ebola virus replication. *Antiviral Res.* **2017**, *137*, 76–81. [CrossRef] [PubMed]
16. Elgner, F.; Sabino, C.; Basic, M.; Ploen, D.; Grünweller, A.; Hildt, E. Inhibition of Zika Virus Replication by Silvestrol. *Viruses* **2018**, *10*, 149. [CrossRef]
17. Glitscher, M.; Himmelsbach, K.; Woytinek, K.; Johne, R.; Reuter, A.; Spiric, J.; Schwaben, L.; Grünweller, A.; Hildt, E. Inhibition of Hepatitis E Virus Spread by the Natural Compound Silvestrol. *Viruses* **2018**, *10*, 301. [CrossRef]
18. Henss, L.; Scholz, T.; Grünweller, A.; Schnierle, B.S. Silvestrol Inhibits Chikungunya Virus Replication. *Viruses* **2018**, *10*, 592. [CrossRef]
19. Müller, C.; Schulte, F.W.; Lange-Grünweller, K.; Obermann, W.; Madhugiri, R.; Pleschka, S.; Ziebuhr, J.; Hartmann, R.K.; Grünweller, A. Broad-spectrum antiviral activity of the eIF4A inhibitor silvestrol against corona- and picornaviruses. *Antivir. Res.* **2018**, *150*, 123–129. [CrossRef]

20. Müller, C.; Obermann, W.; Schulte, F.W.; Lange-Grünweller, K.; Oestereich, L.; Elgner, F.; Glitscher, M.; Hildt, E.; Singh, K.; Wendel, H.-G.; et al. Comparison of broad-spectrum antiviral activities of the synthetic rocaglate CR-31-B (-) and the eIF4A-inhibitor Silvestrol. *Antivir. Res.* **2020**, *175*, 104706. [CrossRef]
21. Müller, C.; Obermann, W.; Karl, N.; Wendel, H.G.; Taroncher-Oldenburg, G.; Pleschka, S.; Hartmann, R.K.; Grünweller, A.; Ziebuhr, J. The rocaglate CR-31-B (-) inhibits SARS-CoV-2 replication at non-cytotoxic, low nanomolar concentrations in vitro and ex vivo. *Antiviral Res* **2021**, *186*, 105012. [CrossRef] [PubMed]
22. Todt, D.; Moeller, N.; Praditya, D.; Kinast, V.; Friesland, M.; Engelmann, M.; Verhoye, L.; Sayed, I.M.; Behrendt, P.; Thi, V.L.D.; et al. The natural compound silvestrol inhibits hepatitis E virus (HEV) replication in vitro and in vivo. *Antivir. Res.* **2018**, *157*, 151–158. [CrossRef] [PubMed]
23. Slaine, P.D.; Kleer, M.; Smith, N.K.; Khaperskyy, D.A.; McCormick, C. Stress Granule-Inducing Eukaryotic Translation Initiation Factor 4A Inhibitors Block Influenza A Virus Replication. *Viruses* **2017**, *9*, 388. [CrossRef] [PubMed]
24. Chu, J.; Zhang, W.; Cencic, R.; Devine, W.G.; Beglov, D.; Henkel, T.; Brown, L.E.; Vajda, S.; Porco, J.A.; Pelletier, J. Amidino-Rocaglates: A Potent Class of eIF4A Inhibitors. *Cell Chem. Biol.* **2019**, *26*, 1586–1593. [CrossRef] [PubMed]
25. Ernst, J.T.; Thompson, P.A.; Nilewski, C.; Sprengeler, P.A.; Sperry, S.; Packard, G.; Michels, T.; Xiang, A.; Tran, C.; Wegerski, C.J.; et al. Design of Development Candidate eFT226, a First in Class Inhibitor of Eukaryotic Initiation Factor 4A RNA Helicase. *J. Med. Chem.* **2020**, *63*, 5879–5955. [CrossRef]
26. Bordeleau, M.-E.; Robert, F.; Gerard, B.; Lindqvist, L.; Chen, S.M.; Wendel, H.-G.; Brem, B.; Greger, H.; Lowe, S.W.; Porco, J.A.; et al. Therapeutic suppression of translation initiation modulates chemosensitivity in a mouse lymphoma model. *J. Clin. Investig.* **2008**, *118*, 2651–2660. [CrossRef]
27. Kogure, T.; Kinghorn, A.D.; Yan, I.; Bolon, B.; Lucas, D.M.; Grever, M.R.; Patel, T. Therapeutic potential of the translation inhibitor silvestrol in hepatocellular cancer. *PLoS ONE* **2013**, *8*, e76136. [CrossRef]
28. Patton, J.T.; Lustberg, M.E.; Lozanski, G.; Garman, S.L.; Towns, W.H.; Drohan, C.M.; Lehman, A.; Zhang, X.; Bolon, B.; Pan, L.; et al. The translation inhibitor silvestrol exhibits direct anti-tumor activity while preserving innate and adaptive immunity against EBV-driven lymphoproliferative disease. *Oncotarget* **2015**, *6*, 2693–2708. [CrossRef]
29. Nakabayashi, H.; Taketa, K.; Miyano, K.; Yamane, T.; Sato, J. Growth of human hepatoma cells lines with differentiated functions in chemically defined medium. *Cancer Res.* **1982**, *42*, 3858–3863.
30. Hoffmann, M.; Hannah, K.-W.; Simon, S.; Nadine, K.; Tanja, H.; Sandra, E.; Tobias, S.S.; Georg, H.N.-H.W.; Andreas, N.; Muller, M.; et al. SARS-CoV-2 Cell Entry Depends on ACE2 and TMPRSS2 and Is Blocked by a Clinically Proven Protease Inhibitor. *Cell* **2020**, *181*, 271–280. [CrossRef]
31. Wolfe, A.L.; Singh, K.; Zhong, Y.; Drewe, P.; Rajasekhar, V.K.; Sanghvi, V.R.; Mavrakis, K.J.; Jiang, M.; Roderick, J.E.; Van Der Meulen, J.; et al. RNA G-quadruplexes cause eIF4A-dependent oncogene translation in cancer. *Nature* **2014**, *513*, 65–70. [CrossRef] [PubMed]
32. Rodrigo, C.M.; Cencic, R.; Roche, S.P.; Pelletier, J.; Porco, J.J.A. Synthesis of rocaglamide hydroxamates and related compounds as eukaryotic translation inhibitors: Synthetic and biological studies. *J. Med. Chem.* **2012**, *55*, 558–562. [CrossRef] [PubMed]
33. Jin, C.; Rajabi, H.; Rodrigo, C.M.; A Porco, J.; Kufe, D. Targeting the eIF4A RNA helicase blocks translation of the MUC1-C oncoprotein. *Oncogene* **2013**, *32*, 2179–2188. [CrossRef] [PubMed]
34. Blum, L.; Geisslinger, G.; Parnham, M.J.; Grünweller, A.; Schiffmann, S. Natural antiviral compound silvestrol modulates human monocyte-derived macrophages and dendritic cells. *J. Cell Mol. Med.* **2020**, *24*, 6988–6999. [CrossRef]
35. Morris, G.M.; Huey, R.; Lindstrom, W.; Sanner, M.F.; Belew, R.K.; Goodsell, D.S.; Olson, A.J. AutoDock4 and AutoDockTools4: Automated docking with selective receptor flexibility. *J. Comput. Chem.* **2009**, *30*, 2785–2791. [CrossRef]
36. Trott, O.; Olson, A.J. AutoDock Vina: Improving the speed and accuracy of docking with a new scoring function, efficient optimization, and multithreading. *J. Comput. Chem.* **2010**, *31*, 455–461. [CrossRef]
37. Chu, J.; Zhang, W.; Cencic, R.; O'Connor, P.B.; Robert, F.; Devine, W.G.; Selznick, A.; Henkel, T.; Merrick, W.C.; Brown, L.E.; et al. Rocaglates Induce Gain-of-Function Alterations to eIF4A and eIF4F. *Cell. Rep.* **2020**, *30*, 2481–2488.e5. [CrossRef]
38. Iwasaki, S.; Iwasaki, W.; Takahashi, M.; Sakamoto, A.; Watanabe, C.; Shichino, Y.; Floor, S.; Fujiwara, K.; Mito, M.; Dodo, K.; et al. The Translation Inhibitor Rocaglamide Targets a Bimolecular Cavity between eIF4A and Polypurine RNA. *Mol. Cell.* **2019**, *73*, 738–748.e9. [CrossRef]
39. Srinivasan, B.; Kolli, A.R.; Esch, M.B.; Abaci, H.E.; Shuler, M.L.; Hickman, J.J. TEER measurement techniques for in vitro barrier model systems. *J. Lab. Autom.* **2015**, *20*, 107–126. [CrossRef]
40. Gupta, S.V.; Sass, E.J.; Davis, M.E.; Edwards, R.B.; Lozanski, G.; Heerema, N.A.; Lehman, A.; Zhang, X.; Jarjoura, D.; Byrd, J.C.; et al. Resistance to the translation initiation inhibitor silvestrol is mediated by ABCB1/P-glycoprotein overexpression in acute lymphoblastic leukemia cells. *AAPS J.* **2011**, *13*, 357–364. [CrossRef]
41. Szemiel, A.M.; Merits, A.; Orton, R.J.; MacLean, O.A.; Pinto, R.M.; Wickenhagen, A.; Lieber, G.; Matthew, L.T.; Wang, S.; Furnon, W.; et al. In vitro selection of Remdesivir resistance suggests evolutionary predictability of SARS-CoV-2. *PLoS Pathog.* **2021**, *17*, e1009929. [CrossRef] [PubMed]
42. Agostini, M.L.; Andres, E.L.; Sims, A.C.; Graham, R.L.; Sheahan, T.P.; Lu, X.; Smith, E.C.; Case, J.B.; Feng, J.Y.; Jordan, R.; et al. Coronavirus Susceptibility to the Antiviral Remdesivir (GS-5734) Is Mediated by the Viral Polymerase and the Proofreading Exoribonuclease. *mBio* **2018**, *9*, e00221-18. [CrossRef] [PubMed]

43. Dittmar, M.; Lee, J.S.; Whig, K.; Segrist, E.; Li, M.; Kamalia, B.; Castellana, L.; Ayyanathan, K.; Cardenas-Diaz, F.L.; Morrisey, E.E.; et al. Drug repurposing screens reveal cell-type-specific entry pathways and FDA-approved drugs active against SARS-Cov-2. *Cell Rep.* **2021**, *35*, 108959. [CrossRef] [PubMed]
44. Gordon, D.E.; Jang, G.M.; Bouhaddou, M.; Xu, J.; Obernier, K.; White, K.M.; O'Meara, M.J.; Rezelj, V.V.; Guo, J.Z.; Swaney, D.L.; et al. A SARS-CoV-2 protein interaction map reveals targets for drug repurposing. *Nature* **2020**, *583*, 459–468. [CrossRef] [PubMed]
45. Shaban, M.S.; Müller, C.; Mayr-Buro, C.; Weiser, H.; Meier-Soelch, J.; Albert, B.V.; Weber, A.; Linne, U.; Hain, T.; Babayev, I.; et al. Multi-level inhibition of coronavirus replication by chemical ER stress. *Nat. Commun.* **2021**, *12*, 5536. [CrossRef] [PubMed]